ABSTRACT

Title of dissertation: DEVELOPMENT OF A TIME-ACCURATE VISCOUS LAGRANGIAN VORTEX WAKE MODEL FOR WIND TURBINE APPLICATIONS

Sandeep Gupta, Doctor of Philosophy, 2006

Dissertation directed by: Minta Martin Professor J. Gordon Leishman, Department of Aerospace Engineering

A second-order accurate model has been developed and validated for modeling the unsteady aerodynamics of a wind turbine. The free-vortex wake method consists of the Lagrangian description of the rotor flow field and viscous effects were incorporated using a viscous splitting approach. The wake geometry solution was then integrated with the rotor aerodynamics model in a consistent manner. The analysis was then used to predict the performance and airloads on a wind turbine in the upwind configuration under unyawed and yawed flow conditions. The present work has demonstrated the versatility and robustness of the free-vortex wake method for wind turbine applications.

The understanding of the accuracy and the stability of the numerical method is very important in developing robust wake methodology. The accuracy of the straight-line segmentation method has been examined for a vortex ring and helical vortex, and it has been shown to be second-order accurate. However, a minimum discretization of ten degrees is shown to be required to obtain second-order accuracy and also keep the maximum error in the induced velocity field less than 10%. Lin-

ear and nonlinear numerical stability of various time-marching schemes were also examined, and a two-step backward differencing scheme was chosen. The overall numerical solution was demonstrated to converge with a second-order accuracy.

The nonlinear unsteady aerodynamics of the blade section was modeled using the Leishman–Beddoes dynamic stall model modified for wind turbine applications. The numerical simulations captured the dynamics of the unsteady flow over the airfoil surface for both attached and stalled flow conditions. Validation of the numerical predictions of the aerodynamic force coefficients against measurements obtained for the S809 airfoil showed overall good agreement. It has been shown that with a proper representation of the static stall characteristics, this model can be used to predict dynamic stall for airfoil sections typical of those used for wind turbine applications. The unsteady airfoil model coupled with the blade model also adequately represented the three-dimensionality of the unsteady flow field for a parked blade, under both steady and unsteady flow conditions.

The wake geometry solution integrated with the blade model was then used to predict the performance and airloads for a wind turbine tested under controlled conditions. It has been shown that it is important to accurately predict the transient wake aerodynamics to obtain accurate estimates of the unsteady airloads and power output. The skewed wake geometry behind an upwind wind turbine was successfully predicted in yawed flow conditions over a range of yaw angles and tip speed ratios. Measurements from the Phase VI of the NREL/NASA Ames wind tunnel test were used for validating the predictions of performance and airloads. The variation of the turbine thrust and the aerodynamic power output with wind speed was adequately predicted. Spanwise distributions of the aerodynamic coefficients were represented well, and encouraging agreement was obtained against the measured coefficients. The azimuthal variation of loads showed that the unsteady aerodynamic behavior of the the wind turbine was adequately represented, with some exceptions.

DEVELOPMENT OF A TIME-ACCURATE VISCOUS LAGRANGIAN VORTEX WAKE MODEL FOR WIND TURBINE APPLICATIONS

by

Sandeep Gupta

Dissertation submitted to the Faculty of the Graduate School of the
University of Maryland, College Park in partial fulfillment
of the requirements for the degree of
Doctor of Philosophy
2006

Advisory Commmittee:

Minta Martin Professor J. Gordon Leishman, Chairman/Advisor

Professor Inderjit Chopra

Associate Professor James D. Baeder

Associate Professor Norman Wereley

Professor James H. Duncan, Dean's Representative

DEDICATION

To my parents, whose efforts have brought me to this point.

ACKNOWLEDGMENTS

I owe my gratitude to all the people who have made this work possible, and because of whom my graduate experience has been one that I will cherish forever. First and foremost I would like to thank my advisor, Prof. Gordon Leishman, for his keen interest and critical evaluation of my work. Over the last four years, he has constantly motivated me to work harder, helped me better understand the underlying physical principles, and stay focused on the ultimate goal. Without his encouragement and constant guidance, this thesis would not have seen the possible.

Thanks are due to Professors Inderjit Chopra, James Baeder, Norman Wereley and Jim Duncan, for agreeing to serve on my thesis committee and for sparing their invaluable time reviewing the manuscript.

I would like to acknowledge the support I received from National Renewable Energy Laboratories, which sponsored this work. I am very grateful to Dr. Scott Schreck, technical monitor for this work. He provided immense help in getting the experimental data and answering my numerous questions regarding the experimental test data. I would also like to thank folks at NREL especially Jason Jonkman, Marshall Buhl and Lee Jay Fingersh. I would also like to acknowledge the help of Wouter Haans from Delft University in the Netherlands, who provided me with the wake data from his experimental measurements.

Many a thanks to my colleagues at the rotorcraft center, particularly Shreyas Ananthan, Jaynarayanan Sitaraman, Karthikeyan Duraisamy, Manikandan Ramasamy, Vineet Gupta, Arun Isaac Jose, Abhishek, Maria, and Carlos for providing a friendly atmosphere. It was my pleasure to interact with them. I thank Shreyas Ananthan for all the enlightening discussions, and for teaching me the basics of free-vortex wake method. We have shared many pleasant memories and some anxious moments over

the last four years. I am indebted to him for his help, support and encouragement which contributed greatly to the successful completion of this dissertation.

Many a thanks to my friends and roommates for making my stay in Maryland a pleasant and happy experience, so that I could better focus on my work. I am eternally grateful to my family - my mother and father who have provided me constant support while I pursued my dreams. I would like to dedicate this dissertation to them. I would like to thank my girlfriend, Vidita for being a pillar of strength during the course of this research work.

Last, but not least, I am thankful to God for showing me the right path.

TABLE OF CONTENTS

LIST OF TABLES

LIST OF FIGURES

Nomenclature

A	Area of the rotor disk, m^2
a	Axial induction factor, v_i/V_∞
a_1	Squire parameter
a'	Tangential induction factor, $v_t/\Omega r$
C_0	Mean offset of the aerodynamic center from the 1/4-chord
C_1, C_2	Coefficients for nonlinear variation of the center of pressure
C_d	Drag coefficient
C_{d_0}	Zero-lift drag coefficient
C_l	Lift coefficient
C_{l_α}	Sectional lift curve slope, rad^{-1}
C_m	Pitching moment coefficient
C_{m_0}	Zero-lift pitching moment coefficient
C_m^v	Vortex induced pitching moment coefficient
C_n	Normal force coefficient
C_n'	Normal force coefficient including pressure lag response
C_{n_1}	Critical normal force coefficient
C_n^c	Circulatory normal force coefficient
C_n^f	Normal force coefficient including trailing edge separation
C_n^{nc}	Non-circulatory normal force coefficient
C_n^p	Normal force coefficient under potential flow conditions
C_n^v	Vortex induced normal force coefficient
C_{n_α}	Normal force curve slope
C_P	Power coefficient, $P/\frac{1}{2}\rho A V_\infty^3$
$C_{P_{\mathrm{hel}}}$	Helicopter power coefficient, $P/\rho A(\Omega R)^3$
$C_{P_{\mathrm{wt}}}$	Wind turbine power coefficient, $P/\frac{1}{2}\rho A V_\infty^3$
C_t	Leading-edge thrust coefficient
C_T	Thrust coefficient, $T/\frac{1}{2}\rho A V_\infty^2$

$C_{T_{\text{hel}}}$	Helicopter thrust coefficient, $T/\rho A(\Omega R)^2$
$C_{T_{\text{wt}}}$	Wind turbine thrust coefficient, $T/\frac{1}{2}\rho A V_\infty^2$
c	Airfoil chord, m
D_f, D_p	Deficiency functions
D_ψ	Temporal difference operator
D_ζ	Spatial difference operator
$\mathbf{E}$	Legendre's elliptic integral of the second kind
F	Prandtl loss factor
F_{root}	Prandtl root loss factor
F_{tip}	Prandtl tip loss factor
f	Effective flow separation point
f'	Flow separation point including unsteady pressure lag
f''	Flow separation point including unsteady boundary layer response
f_{root}	Exponent in Prandtl root loss factor
f_{tip}	Exponent in Prandtl tip loss factor
h	Generic time step size, s
$\mathbf{K}$	Legendre's elliptic integral of the first kind
k	Reduced frequency $= \omega c/2V_\infty$
k_x	Longitudinal inflow weighting factor
k_y	Lateral inflow weighting factor
$L_2 - \text{norm}$	Second norm of the error vector
M	Number of divisions per revolution of helical wake
N	Number of turns in the helix
N_b	Number of blades
N_{f}	Number of vortex filaments in the helix
P	Turbine power output, kW
$P(\sigma)$	Characteristic polynomial
p	Helical pitch (distance between adjacent filaments normalized by radius)

Q	Turbine torque, Nm
q	Non-dimensional pitch rate , $\dot{\alpha}c/V_\infty$
R	Rotor radius or radius of vortex ring, m
Re	Reynolds number = $\rho V_\infty c/\mu$
Re_{v}	Vortex Reynolds number
$\mathbf{r}$	Position vector of vortex collocation point, m
r	Non-dimensional radial position
r_c	Non-dimensional root cut-out
r_{c_0}	Initial core radius, m
r, θ, z	Cylindrical polar coordinates, (m, rad, m)
s	Non-dimensional distance travelled by airfoil in semi-chords = $2V_\infty t/c$
T	Rotor thrust, N
T_f, T_p, T_v	Time constants (semi-chords)
T_{v_l}	Non-dimensional vortex traversal time
t	Time, s
U, V, W	Velocity components in Cartesian coordinates, (ms^{-1}, ms^{-1}, ms^{-1})
U_{b}	Binormal velocity, ms^{-1}
u	Generic variable
$\tilde{u}$	Intermediate value of generic variable
$u^{'}$	Time derivative of generic variable
u, v, w	Velocity components in Cartesian coordinates, (ms^{-1}, ms^{-1}, ms^{-1})
$\mathbf{V}$	Velocity vector, ms^{-1}
$\mathbf{V}_{\mathrm{ex}}$	Perturbation or external velocity vector, ms^{-1}
$\mathbf{V}_{\mathrm{ind}}$	Induced velocity vector, ms^{-1}
$\mathbf{V}_\infty$	Free stream velocity vector, ms^{-1}
V_{approx}	Velocity obtained using straight-line segmentation, ms^{-1}
V_{exact}	Exact velocity, ms^{-1}
V_r, V_θ, V_z	Velocity components in polar coordinates, (ms^{-1}, ms^{-1}, ms^{-1})

V_x, V_y, V_z	Velocity components in Cartesian coordinates, (ms^{-1}, ms^{-1}, ms^{-1})
v_h	Induced axial velocity (hovering rotor), ms^{-1}
v_i	Induced axial velocity, ms^{-1}
v_t	Induced tangential velocity, ms^{-1}
$X(s), Y(s)$	Deficiency functions
X_{TSR}	Tip-speed ratio, $\Omega R/V_\infty$
x, y, z	Cartesian coordinates, (m, m, m)
x_{ac}	Aerodynamic center, m
x_{cp}	Center of pressure, m
$\bar{x}_{cp_v}$	Non-dimensional vortex induced center of pressure
α	Geometric angle of attack, rad
α_1	Angle of attack corresponding to first break in lift, rad
α_2	Angle of attack corresponding to second break in lift, rad
α^c	Effective unsteady angle of attack, rad
α_f	Effective angle of attack with pressure lag, rad
$\dot{\alpha}$	Pitch rate, $\mathrm{rad\,s}^{-1}$
β	Prandtl–Glauert compressibility factor = $\sqrt{1-M^2}$
β	Wake skew angle, deg
Γ_{v}	Vortex strength (circulation), $\mathrm{m}^2\mathrm{s}^{-1}$
Δa	Differential axial induction factor
Δq	Step change in pitch rate, rad
$\Delta\alpha$	Step change in angle of attack, rad
$\Delta\theta$	Angular discretization of ring, rad
$\Delta\psi$	Angular discretization of wake, rad
δ	Cutoff angle, rad
δ	Effective eddy viscosity coefficient
ϵ_{abs}	Absolute error
ϵ_p	Phase error, rad

ϵ_{rel}	Relative error
ζ	Vortex wake age, rad
θ_{tip}	Blade tip pitch angle, deg
θ_{tw}	Blade twist rate, deg
Λ	Yaw angle of turbine, deg
λ	Eigenvalue of the space difference matrix
λ	Tip speed ratio, $\Omega R/V_\infty$
λ_h	Inflow coefficient in hover, $v_h/\Omega R$
μ	Viscosity, $\mathrm{kg\,m^{-1}s^{-1}}$
ν	Kinematic viscosity, $\mathrm{m^2s^{-1}}$
ρ	Air density, $\mathrm{kg\,m^{-3}}$
σ	Eigenvalue of the time-marching method
σ	Rotor solidity, $N_b c/\pi R$
σ_1	Principal eigenvalue
τ_v	Non-dimensional vortex time
ϕ^c	Circulatory part of the indicial response function
ϕ^{nc}	Non-circulatory part of the indicial response function
ϕ	Induced angle of attack, rad
ϕ_{FWi}	Induced angle of attack from far-wake, rad
ϕ_{NWi}	Induced angle of attack from near-wake, rad
χ	Wake skew angle, rad
ψ	Azimuthal angle, rad
Ω	Rotational speed of turbine rotor, rad $\mathrm{s^{-1}}$
ω	Circular frequency, $\mathrm{rad\,s^{-1}}$

Abbreviations

B3RFB	Strain gauge root flap bending moment
B3REB	Strain gauge root edge bending moment
BEM	Blade-element momentum
EAEROFB	Estimated aerodynamic root flap bending moment
EAEROTQ	Estimated aerodynamic torque
FVM	Free-vortex method
LSSTQCOR	Corrected strain gauge torque
NWS	Normal working state
TSR	Tip speed ratio
TWS	Turbulent wake state
VRS	Vortex ring state
WBS	Windmill brake state

Chapter 1

Introduction

1.1 Historical Development of Wind Turbines

Wind energy is one of the leading contenders among renewable sources of energy. The cost of wind energy has steadily decreased over the last few decades, mainly because of the improvement in design and reliability of wind turbines. Wind energy has been used for centuries in the form of windmills for milling grain and pumping water. Some authors maintain having discovered stone windmills used in Egypt, which are suspected to be 3,000 years old [1]. From the seventh to the eleventh century, windmills were developed in Persia, Afghanistan, and China; these were mainly vertical-axis windmills. The horizontal-axis windmill design, which is the most commonly used design in present times, was probably developed independently in Europe, with a lot of success in Germany, the Netherlands, and France. Figure 1.1 shows a photograph of a Dutch windmill used in the early 19th century.

In America, Daniel Halladay [1] is credited with the invention of the first commercially successful windmill. Initially, American "fan" windmills were small and were designed for pumping water. In the late 19th century, some larger windmills were designed for industrial water supply system. The transition of windmills to wind turbines for producing electricity happened somewhere at the end of the 19th century. Charles Brush, an industrialist in Ohio, is credited with erecting the first windmill [2] to supply 12 kW of DC power to charge storage batteries. The Brush windmill had an upwind rotor with 144 blades, and was 17 m in diameter mounted on an 18 m high tower.

Figure 1.1: A photograph of a Dutch windmill.

The improvement in windmills or wind turbines from medieval times to the 17th century was not a result of any systematic research, but more of trial and error. The fundamental physics of wind turbines technology was first developed by the end of the 17th century. Gottfried Leibniz, Daniel Bernoulli and Leonhard Euler were among the first researchers to apply the physical and mathematical principles in wind turbine design. However, Paul LaCour in Denmark was the first to conduct wind turbine research using engineering principles. He was probably the first to use a wind tunnel to study the aerodynamics of the blades of a wind turbine. LaCour also solved the problem of energy storage using the direct current produced by the wind turbine for electrolysis, and stored the hydrogen gas thus produced [1]. Figure 1.2 shows a four bladed LaCour Lykkegard wind turbine, with rectangular, twisted blades. In the early 20th century, LaCour wind turbines generating 5 to 25 kW of power were extensively used for agriculture.

The use of wind energy in the 20th century has always fluctuated with the price

Figure 1.2: A four bladed windmill designed by LaCour for generation of electricity.

of conventional sources of energy. It was during the Second World War (WWII) that F.L. Smith and several other companies began successfully producing two- and three-bladed wind turbines. In the early 1950s, the turbines were equipped with the first AC generators, rather than the conventional DC generators. The interest in wind turbines dropped again when the energy crisis of WWII had passed. Cheap oil and the development of nuclear power in the 1950s led to a decline of interest in wind turbine technology. However, the oil crisis of the 1970s again propelled renewed interest in wind energy. In the last few decades, the increasing cost of conventional sources of energy, compounded by increased realization of the effects of these energy sources on pollution, global warming, health, etc., have also propelled the development of renewable energy technologies. At present, wind energy is the fastest growing renewable energy technology, with an increase in the world wind energy capacity from 2,000 MW in 1990 to approximately 40,000 MW in 2004. The wind energy potential in the US is 10,777 billion KWh, which is twice that of the electricity generated in the US at the end of 2004.

Fuel	**Levelized costs (cents/kWh)**
Coal	4.8–5.5
Natural gas	3.9–4.4
Hydroelectric	5.1–11.3
Nuclear	11.1–14.5
Wind	4.0–6.0

Table 1.1: Comparison of the levelized cost of various energy options according to California Wind Energy Commission (CWEC) energy technology report. (Taken from Ref. 3).

Table 1.1 shows a comparison of the levelized costs of various energy options according to a California Wind Energy Commission energy technology report in 1996 [3]. It can be seen that the cost of wind energy is still relatively high as compared to the conventional sources of energy. Better and more reliable design of the various components of a wind turbine, such as the rotor blades, nacelle and the tower is, thus, very important for reducing the cost per unit of energy extracted from wind.

1.2 Energy Extraction Using a Wind Turbine

A wind turbine is a device that extracts the kinetic energy of the wind from the mass of air that flows through the turbine disk. Wind turbines can be classified according to their aerodynamic function or their conceptual design. The simplest type of wind turbines use aerodynamic drag surfaces to capture the power of the wind. However, the maximum power coefficient of a pure drag rotor is limited to only 0.2, which is less than 30% efficient. On the other hand, wind energy converters using aerodynamic lift can achieve considerably higher power coefficients. Approximately $80-90\%$ of modern wind turbines use aerodynamic lift to capture the power of the wind.

The second way to classify wind turbines is based on their design, and this is determined by the axis of rotation of the rotor plane: vertical axis or horizontal axis wind turbines. Vertical axis wind turbines (VAWT) have a vertical axis of rotation, and are really the oldest form of design. The first designs of VAWT were purely drag based rotors, such as the Savonius rotor. Purely drag based designs turn relatively slowly, but yield a high torque. They can be useful for grinding grain, pumping water, and many other tasks but are not as good for generating electricity. However, vertical axis wind turbines using aerodynamic lift concepts have also been designed. French engineer Darrieus proposed a design where the rotation of the blades follow a "spinning rope" or "eggbeater" pattern, with a vertical axis of rotation, as shown in Fig. 1.3. A variation of the Darrieus rotor is the H-rotor design [4], where straight blades connected to the shaft by struts are used. Even after the advantages such as simplicity of their design and elimination of the need for a yaw mechanism, VAWTs have not been very successful in the commercial wind turbine market. The disadvantages of this design include an inability to self-start, an inability to control power output by pitch of the rotor blades and aeroelastic issues for larger wind turbines.

The horizontal axis wind turbines (HAWT) have a horizontal axis of rotation. About 95% of the wind turbines, which are used to produce electricity, follow this design. There are several advantages of the HAWT design such as the ability to control power and rotational speed using blade pitch control. This design has the ability to achieve high efficiency using aerodynamically optimized blades. However, one of the main disadvantages of HAWTs is dependence of power output on the wind direction, and the need for a yaw control mechanism. Figure 1.4 is a schematic showing the components of a HAWT.

Figure 1.3: A 500 kw variable speed Darrieus wind turbine installed by the DOE.

1.3 Momentum Theory

In this section, the mechanism for energy extraction is discussed for horizontal axis wind turbines only. The axial momentum method in which the rotor is modeled as an actuator disk is used. This analysis was first developed for propellers by Froude [5], Betz [6] and Lanchester [7]. Assuming that the mass of air slowed down can be separated from the unaffected mass by a boundary, a streamtube can be formed by extending it upstream and downstream of the turbine disk, as shown in Fig. 1.5. The mass flow rate of the air will be constant across all cross-sections (with the assumption that no air crosses the streamtube boundary). This means that the streamtube expands behind the turbine disk, where the air is slowed down.

An actuator disk concept can be used to explain the energy extraction process. As shown in Fig. 1.5, the mass flow rate of the air through a given cross section of the stream-tube is given by

$$\dot{m} = \rho A U \tag{1.1}$$

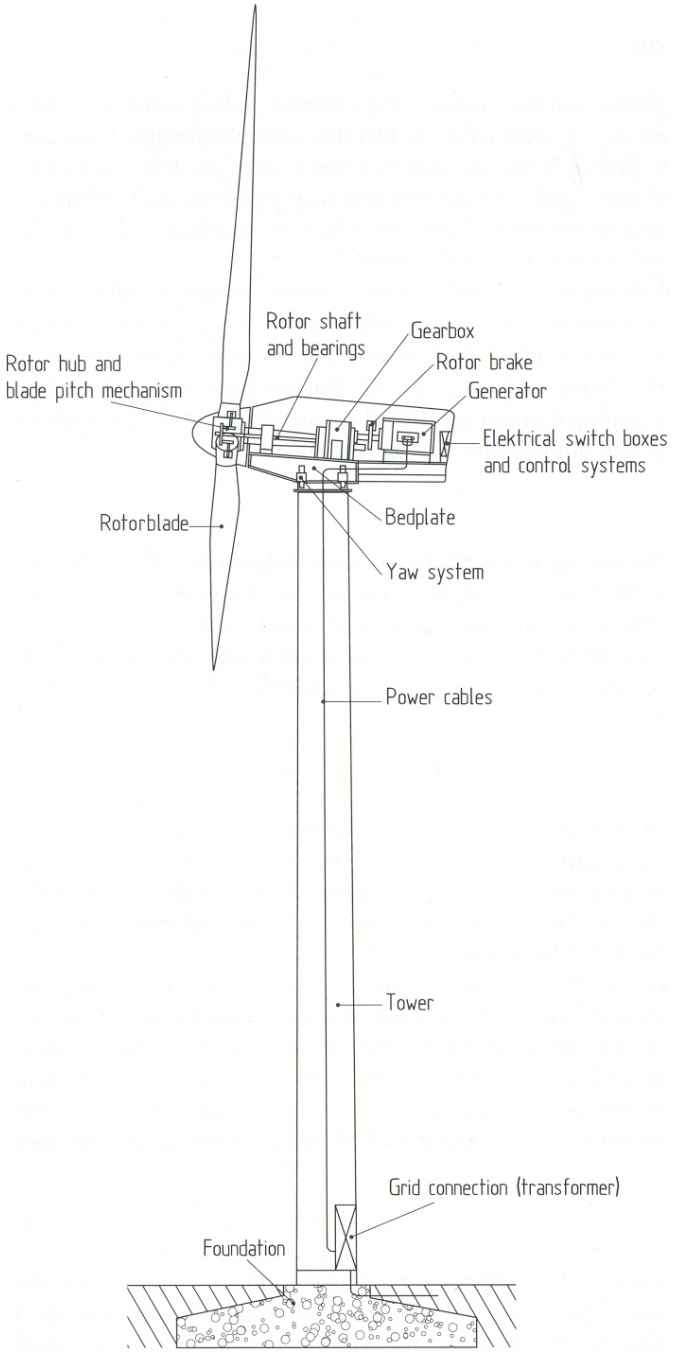

Figure 1.4: Schematic of a horizontal axis wind turbine showing the major components. (Taken from Ref. 1.)

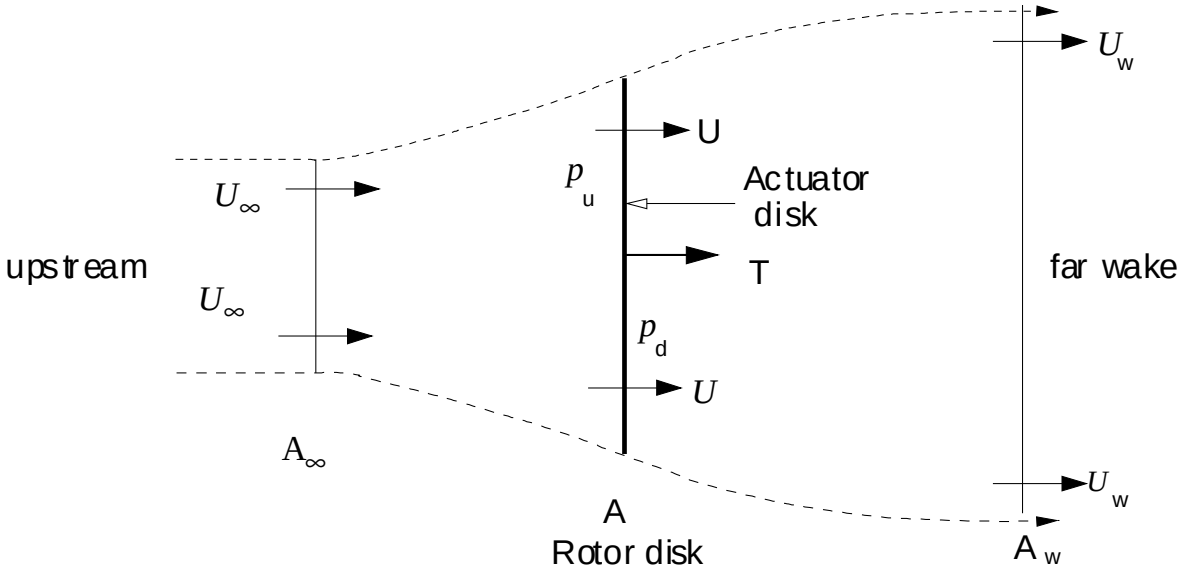

Figure 1.5: A simple schematic of the control volume showing the extraction of energy by a wind turbine.

The mass flow rate should be same everywhere along the streamtube so from continuity

$$\rho A_\infty U_\infty = \rho A U = \rho A_w U_w \tag{1.2}$$

where A_∞ and A_w are the areas of a cross-section upstream and downstream of the disk, respectively. Similarly, U_∞ is the free-stream velocity upstream of the turbine and U_w is the velocity of air in the wake of the turbine. Taking an axial induction factor a, the net streamwise velocity at the disk is given by

$$U = U_\infty(1-a) \tag{1.3}$$

The net rate of change of momentum is equal to the change in velocity times the mass flow rate. This change in momentum comes from the pressure difference across the actuator disk. Therefore,

$$(p^d - p^u)A = (U_\infty - U_w)\rho A U_\infty(1-a) \tag{1.4}$$

To obtain the pressure difference, the Bernoulli's equation is applied both upstream

and downstream of the turbine disk. Assuming incompressible flow and no change in height, the Bernoulli's equation upstream of the disk can be written as

$$\frac{1}{2}\rho U_\infty^2 + p_\infty = \frac{1}{2}\rho U^2 + p_u \tag{1.5}$$

Similarly, Bernoulli's equation on the downstream can be written as

$$\frac{1}{2}\rho U^2 + p_d = \frac{1}{2}\rho U_w^2 + p_\infty \tag{1.6}$$

Subtracting Eq. 1.5 from 1.6 gives

$$(p_d - p_u) = \frac{1}{2}\rho(U_\infty^2 - U_w^2) \tag{1.7}$$

Equation 1.4 then gives

$$\frac{1}{2}\rho(U_\infty^2 - U_w^2)A = (U_\infty - U_w)\rho A U_\infty(1-a) \tag{1.8}$$

which results in

$$U_w = (1-2a)U_\infty \tag{1.9}$$

This implies that the loss in the speed of the wind is equal upstream and downstream of the turbine disk. The net thrust on the turbine disk is then given by the rate of change of momentum and is equal to

$$T = (p_d - p_u)A = 2\rho A U_\infty^2 a(1-a) \tag{1.10}$$

Similarly, the power extracted from the wind turbine is given by

$$P = TU = 2\rho A U_\infty^3 a(1-a)^2 \tag{1.11}$$

The power coefficient, which defines the ratio of the power extracted to the power available in the air is defined as

$$C_P = \frac{P}{\frac{1}{2}\rho A U_\infty^3} \tag{1.12}$$

Substituting the expression for power from Eq. 1.11, then

$$C_P = 4a(1-a)^2 \tag{1.13}$$

The maximum value of C_P occurs when

$$\frac{dC_P}{da} = 4(1-a)(1-3a) = 0 \tag{1.14}$$

which gives $a = 1/3$. Therefore, the maximum value of the power coefficient is then

$$C_{P_{\max}} = 16/27 = 0.593 \tag{1.15}$$

The maximum value of power coefficient achievable by a wind turbine is called the Betz limit after German aerodynamicist, Albert Betz, who derived this theoretical limit [6]. This value of the power coefficient corresponds to 100% extraction of energy from the air. The same conclusion was drawn by Lanchester [7] independently, and this limit is sometimes called the Lanchester–Betz limit. However, it has been theorized by van Kuik [8] that the assumption of no radial force on the streamtube does not hold, and a slightly higher maximum power coefficient than the Betz limit can be achieved. In addition to this, the use of flow diffusers [9] or tip vanes [10] can increase the value of $C_{P_{\max}}$.

1.4 Factors Affecting the Power Output

The electricity produced from wind turbines is the cleanest form of energy with minimal environmental footprint. However, the higher cost of electricity produced from wind turbines is still a limiting factor in the acceptance of wind energy. Technical improvements in turbine design, new blade materials, electrical generators, etc., over the past two decades has helped to reduce the cost of wind energy by almost tenfold. Besides the technological development, government subsidies, transmission tax and the cost of financing, are also important factors in determining the cost of wind energy. In Europe, favorable policies and encouragement from the government has led to rapid developments in wind turbine technology. In Denmark, almost 20% of the electricity consumed is produced using the wind.

However, the improvement in the wind turbine technology areas still holds the key to reduction in the cost per unit of energy from the wind. This can be achieved,

in part, by developing a thorough understanding of the complicated aerodynamics and dynamics of a wind turbine. Various factors that play an important role in the design of wind turbine are now discussed.

1.4.1 Wind Regime

The mean annual wind speed at the hub height of the wind turbine is the most important parameter that determines the energy captured by a wind turbine. As shown in Eq. 1.11, the energy extracted by a turbine from the wind varies as the cube of the average wind speed. For example, a wind turbine site with average wind speed of 6 ms^{-1} theoretically produces 72% more power than at a site with average wind speed of 5 ms^{-1}. However, at higher wind speeds, the net power output of a wind turbine is either limited by the blade stall or otherwise regulated by the control system to prevent high loads on the turbine components.

Wind resource assessment is one of the most important aspects of a wind farm design. In the planning phase of a wind farm, wind speed is usually monitored over a range of 6 months to 1 year by obtaining several types of meteorological data from the planned site. The spatial and temporal variability of the wind at the site are important in the overall output from the turbine because it directly affects the annual energy production (AEP) and the structural fatigue life of the turbine.

Figure 1.6 shows a typical variation of the power output with increasing wind speed. As the average hub-height wind speed increases beyond 4 ms^{-1}, turbine starts to produce power. This speed is defined as the cut-in speed ($V_{\text{cut-in}}$) of a wind turbine. The cut-in wind speed is governed, in part, by the torque required to overcome friction and drive train losses. The power produced then increases as the cube of wind speed, and reaches a maximum power output at the rated wind speed (V_{rated}). At higher wind speeds, the loads on the turbine become very large, and it would have to be very heavy and expensive to carry the loads. Therefore, wind turbines are designed to reach a maximum power output, after which the

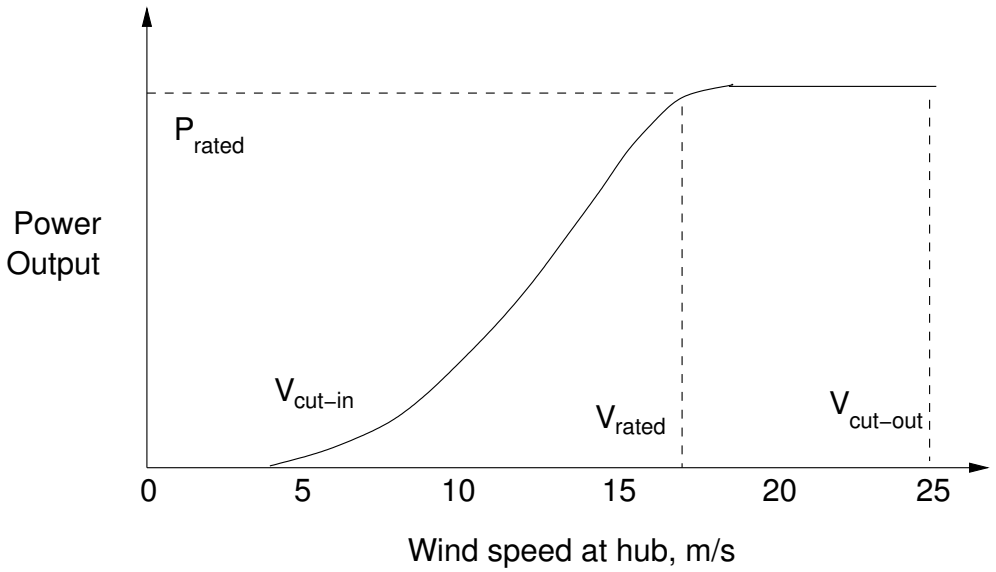

Figure 1.6: Typical variation of the power output of a wind turbine with the average wind speed at the hub.

power produced is controlled either by flow separation on the blades (stall controlled turbines) or pitch control (most of the larger wind turbines use this form of control). At very high wind speeds (usually more than 25 ms^{-1}), wind turbine blades are locked into a parked position to prevent excessive loads and subsequent damage to the turbine. This wind speed is defined as the cut-out speed ($V_{\mathrm{cut-out}}$).

1.4.2 Rotor Swept Area and Hub Height

The power output of a wind turbine is directly proportional to the area swept by the rotor blades, i.e., to the square of the rotor diameter, as can be seen from Eq. 1.11. Therefore, larger the blades the higher is the power output from a wind turbine. However, the blade mass also increases with increasing size of the turbine, and the blades become more expensive. For sites with very high wind speeds, such as offshore wind turbines, very large blades (with a diameter of up to 100 meters) are used. An increase in power output can also be achieved by increasing the hub height. With a greater hub height, the wind turbine operates out of the ground boundary layer, and so sees a higher annual mean wind speed. The minimum value

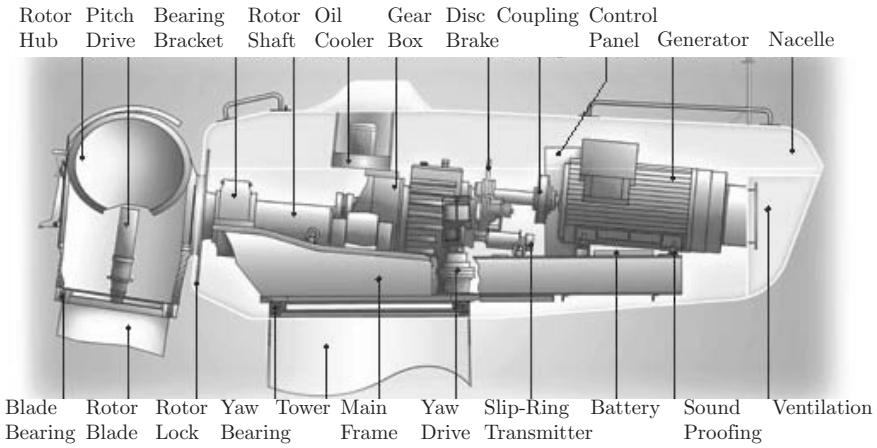

Figure 1.7: Layout of a modern wind turbine describing the various components.

of the hub height is obviously determined by the radius of the rotor.

1.4.3 Power Control and Electronic Monitoring

The power control mechanism also has an influence on the annual energy yield. Blade stall as a means of power control is usually only used for smaller wind turbines. However, this leads to non-optimal operation in the partial load regime, leading to approximately 1 to 3 % loss in the annual energy yield. Blade pitch control, on the other hand, is usually used for larger wind turbines. This form of power control provides better conditions for optimal energy capture, especially if it is combined with variable-speed operation. Wind turbines operate at maximum efficiency only at a given tip-speed ratio. In a variable speed turbine, the rotational speed of the rotor is adjusted so that it operates at this optimal tip-speed ratio. This improves the power captured from the wind, and is commonly used in most of the large wind turbines.

1.4.4 Layout of a Modern Wind Turbine

About 95% of the wind turbines producing electricity in the world are horizontal axis wind turbines. The hub is connected to the generator via a gearbox.

Both the generator and the gearbox are housed in a nacelle, as shown in Fig. 1.7, which shows the general layout of a wind turbine. The nacelle is mounted on the tower, which can be either a tubular or lattice tower. A tubular tower allows for access to the generator, the gearbox, and the rotor, from within the tower. This is advantageous in bad weather conditions. On the other hand, the lattice tower design is cheap with considerable material savings. The electric current produced by the generator is then distributed to the transformer through high voltage cables located inside the tower.

Two- and three-bladed turbines are the most commonly used designs for modern wind turbines. The blade cross section is made of an airfoil designed to produce lift as the blades rotate. Most large wind turbine blades are made from glass fiber reinforced plastic (GRP) or carbon fiber reinforced plastic (CFRP). Wood is also a light-weight, good strength, and fatigue-resistant material, but the sensitivity to moisture and processing costs are a drawback. However, blades for some small wind turbines are still made out of wood.

1.5 Aerodynamic Environment of a Wind Turbine

Wind turbines operate in a very complicated aerodynamic environment [11,12]. Turbulent winds, ground boundary layer, yawed flows, tower shadow effects, spatial and temporal shear layer, and the vortical wake behind the wind turbine compound the difficulties in predicting the aerodynamics of a wind turbine. With each revolution, a wind turbine rotor undergoes complete gravity stress reversal, along with out-of-plane cyclic loading as a result of these effects. Because of these unsteady loads on a wind turbine, it is subjected to a severe fatigue loading. Therefore, fatigue loads are one of the key criteria for the design of a wind turbine. Coupled with the elastic deformation of the blade, these unsteady loads can also cause aeroelastic instabilities. With modern wind turbines, which are flexible and bigger, understanding the coupling between the aerodynamics and the structural dynamics of

wind turbines becomes even more important. Figure 1.8 shows various components of the aerodynamic environment of a horizontal axis wind turbine.

1.5.1 Yawed Flow

Wind turbines experience yawed flow for a substantial amount of their operational time. Yawed flow operation means that the wind direction is not always perpendicular to the rotor disk. This is quite common as the wind direction on a site is not constant and changes continuously. A crossflow velocity leads to an asymmetry in the magnitude of wind speed over the azimuth. This leads to an asymmetry in the local airloads and fluctuations in the power output.

Operation in yawed flow results in a loss of power output from the turbine for a given wind speed. If Λ is the yaw error in tracking the wind speed, it can be easily shown that the power output will be proportional to the cube of the yaw angle, i.e., $P_{\text{output}} \propto \Lambda^3$. Most of the modern large wind turbines use yaw control to ensure that there is no yaw error. However, sudden changes in the wind direction or crossflow gusts cause the turbine to operate in yawed flow. Moreover, for smaller wind turbines, yawing the rotor out of the wind has also been used for power control in high wind speeds. Cyclic variation in the loads as a result of the asymmetry in flow conditions reduce the fatigue life of various mechanical components. The operation of the turbine blade sections beyond stall in yawed flow can also lead to dynamic stall. Dynamic stall is characterized by a considerable hysteresis in the airloads and reduced aerodynamic damping, particularly in torsion [13].

1.5.2 Turbulence

The wind speed, U, at any instant in time consists of two components: a mean speed, $\bar{U}$, that is determined by the seasonal, synoptic and diurnal effects, with a

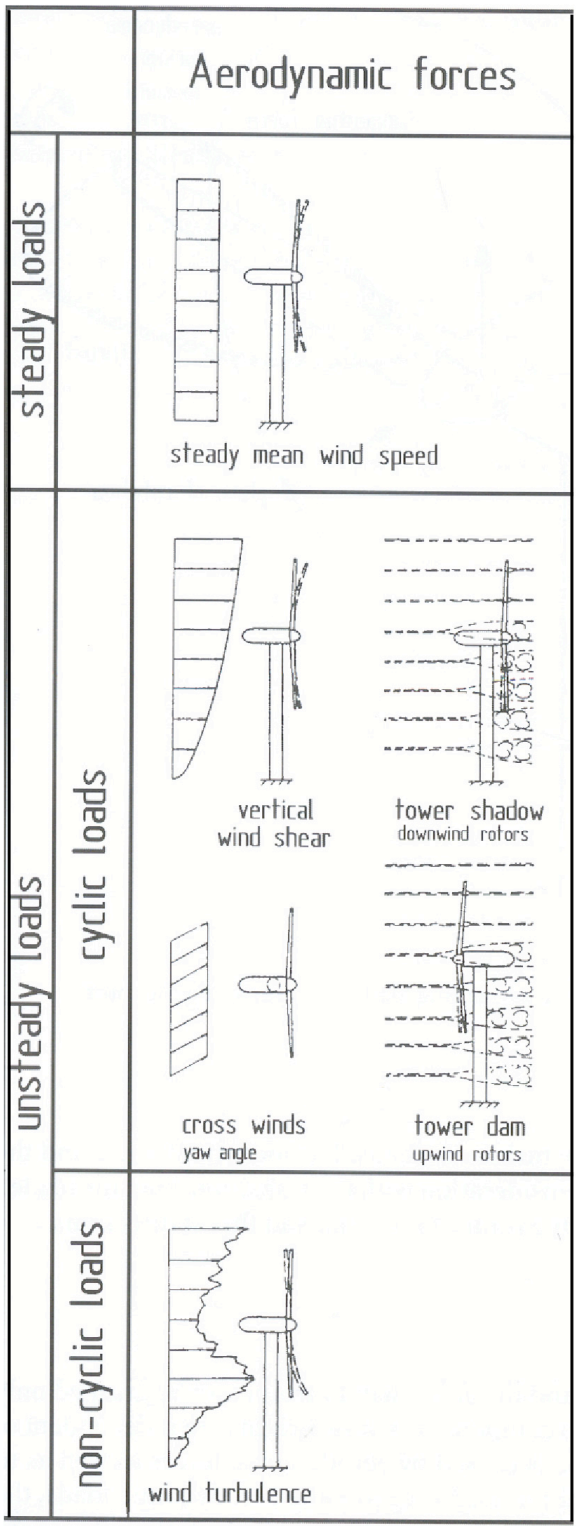

Figure 1.8: A schematic of the unsteady aerodynamic environment of a wind turbine. (Reproduced from Ref. 1.)

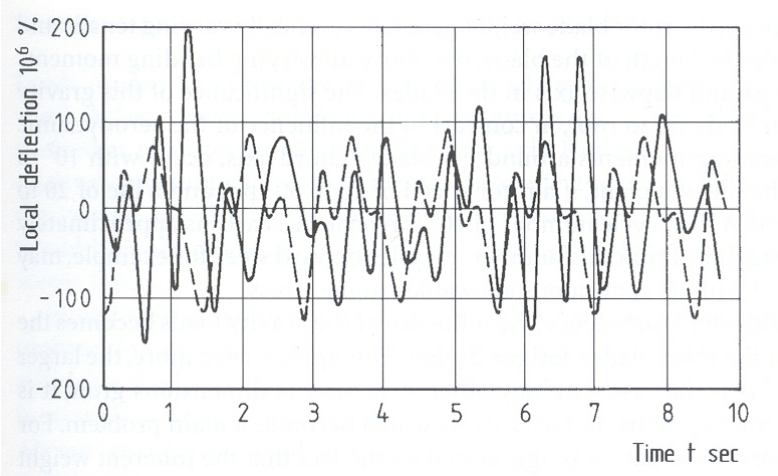

Figure 1.9: Rotor blade flapwise bending deflection without and with the inclusion of turbulence spectrum for a HWP-300 wind turbine. (Reproduced from Ref. 14.)

turbulent fluctuation part u', i.e.,

$$U = \bar{U} + u' \tag{1.16}$$

Turbulent fluctuations in the wind are a result of friction with the earth's surface and also thermal effects. The flow disturbances resulting from friction can be thought of as a result of the roughness of the earth's surface, and also because of topographical features such as hills, mountains, etc. Thermal effects cause the air mass to move vertically as a result of variations in temperature, which leads to the formation of turbulent eddies.

Turbulence can be described as a chaotic process, and can be described in terms of its statistical properties. Turbulence intensity, which is a measure of the overall level of turbulence, can be defined as

$$I = \frac{\sigma}{\overline{U}} \tag{1.17}$$

where σ is the standard deviation of the wind speed. The turbulent intensity varies with the wind speed, the earth's surface roughness, and topographic features [15]. The minimum value of turbulence intensity (about 5%) is usually found over the open sea and the maximum value (around 20%) is found in dense forests. Turbulent

fluctuations cause unsteady airloads on the turbine blades with sharp peaks in the load history. Fluctuating loads on different components of a wind turbine from the turbulent winds also leads to structural fatigue loads.

Figure 1.9 shows the effect of wind turbulence on a specific dynamic load situation showing the flapwise bending deflections with and without the inclusion of turbulence. Note that that the maximum deflection value is almost doubled after the inclusion of the turbulence spectrum.

1.5.3 Wind Shear and the Ground Boundary Layer

The presence of the ground boundary layer leads to vertical shear in the wind speed. The mean horizontal speed of the wind at the surface of the earth is zero and increases with the altitude. A ground boundary layer can be as large as 50 m above the earth's surface. An example of a typical wind speed profile is shown in Fig. 1.10. The instantaneous profile shows large peaks associated with gusts and turbulent eddies. The solid line shows the steady wind speed profile, which is obtained by time averaging the instantaneous speed. The principal effect that governs the properties of the boundary layer are the surface roughness, the strength of the geostrophic wind, thermal effects, and the Coriolis effects from earth's rotation. Thermal effects are the most important effect governing the strength and properties of the boundary layer.

The variation of wind speed with height above ground is important for both the assessment of the wind energy resource and the design of wind turbines. If the rotor disk is operating in the presence of the wind shear, wind impacts the rotor asymmetrically. During each revolution, a blade experiences higher wind speed in the upper rotational half than the lower half. This leads to cyclic varying loads on the blades with higher loads in the upper half than lower half. A representative result demonstrating the effect of the wind shear on the flapwise bending moment is shown in Fig. 1.11. The cyclic loading of the blades and other parts of the turbine

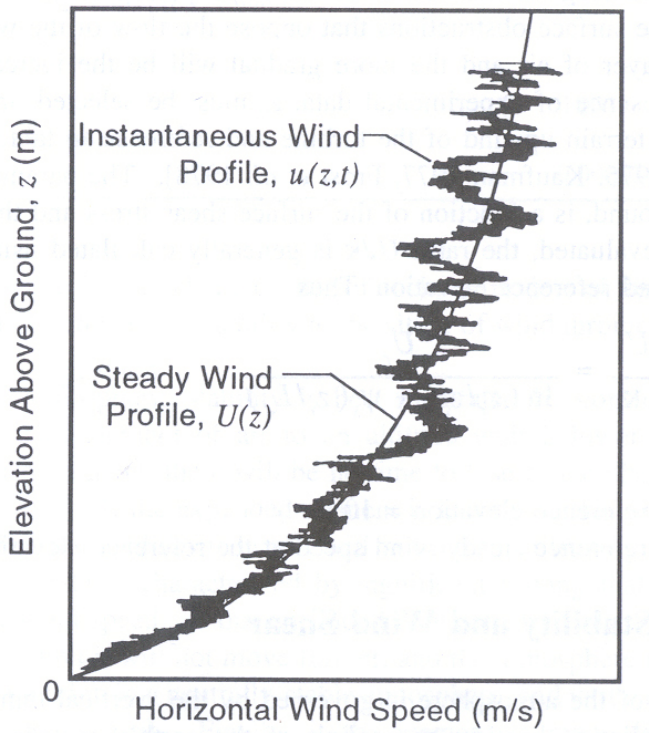

Figure 1.10: A typical profile of the wind speed, with both the instantaneous and steady components shown. (Reproduced from Ref. 16.)

causes considerable fatigue loads. Power output is also affected by the rotor above ground. The designer has to come up with an optimum hub height to balance the the excess energy captured against the cost of taller tower.

1.5.4 Tower Shadow Effects

The rotor of a horizontal axis wind turbine rotates very close to the support tower. To limit the size of the nacelle supporting the rotor, the clearance between the rotor and the tower is usually small. This leads to an aerodynamic flow around the tower and an influence of the turbine. These interference effects are minimized for the upwind configuration of a HAWT. In this configuration, the rotor is mounted upwind of the tower, and the tower shadow effect manifests as slowing of the flow in front of the tower. For modern wind turbines with slender towers, this effect is quite small. For downwind turbines, the tower is mounted upstream of the turbine disk.

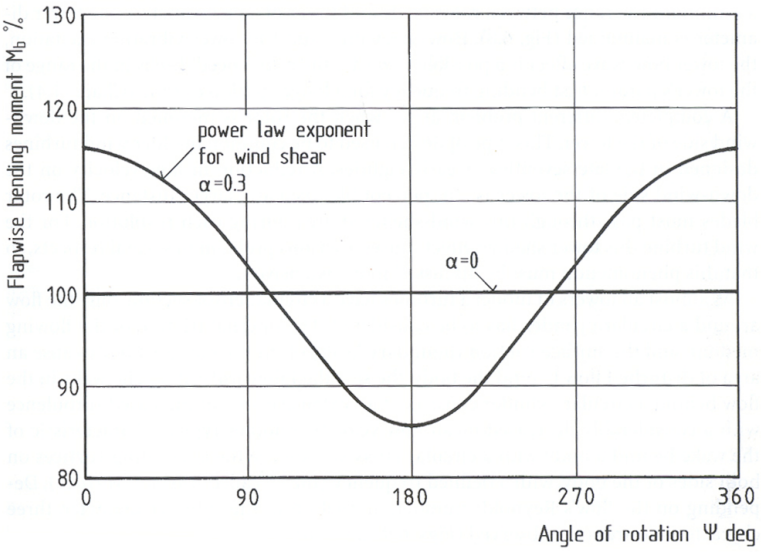

Figure 1.11: Cyclically varying flapwise bending moment with a high wind shear. (Reproduced from Ref. 1.)

Hence, the tower shadow effect is significant because the rotor blades encounter the wake of the tower during each revolution. The reduced wind speed near the tower changes the effective angle of attack at the rotor blades, which affects the forces and torque.

Figure 1.12 shows an example of the azimuthal variation of the torque output for a two-bladed wind turbine. The flow behind the cylindrical cross section of the tower is turbulent, with the alternative shedding of vortices from the cylindrical tower with a defined frequency (called as K*àrmàn* vortex sheet). This frequency can fall within the range of of some of the turbine's natural frequencies, especially those of the drive train. The aeroelastic problems caused by the rotor wake (which persists long enough), and the noise generated by the downwind wind turbines, has led to almost complete disappearance of downwind type wind turbines.

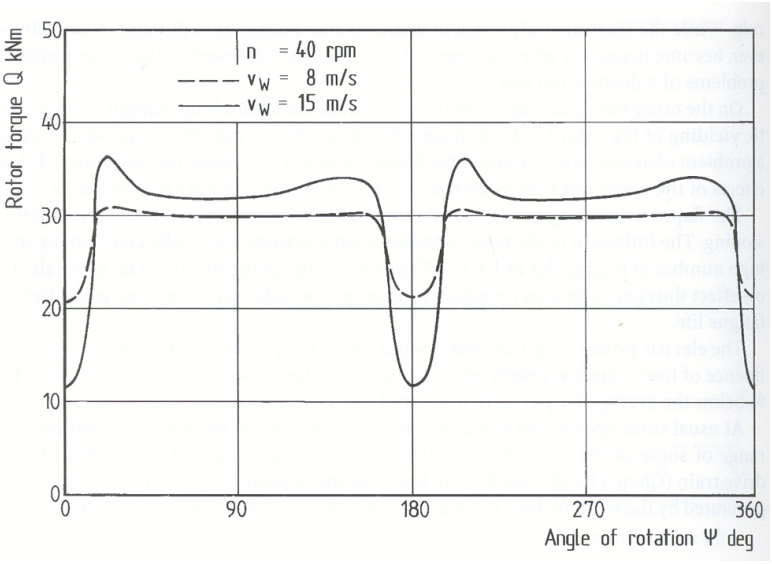

Figure 1.12: Influence of the tower shadow on the rotor torque for the experimental MOD-0 wind turbine. (Reproduced from Ref. 1.)

1.5.5 Wake Array Effects

For the economical use of wind energy, wind farms consist of a number of individual wind turbines arranged on a given site. The wind turbines situated upwind for a given wind direction affect the flow downwind of the turbine, causing significant turbulence mainly because of the strong vortical wake behind the turbine. This effect is called the *wake array* effect, and poses significant challenge for a wind farm designer. The optimum placement of wind turbines on the site is one of the major challenges in designing a wind farm because the loss in power capture from wake array effects can be significant.

Representative results of the energy loss for a 6×6 array of wind turbines spaced 10 diameters apart in the prevailing wind direction [17] is shown in Fig. 1.13 as a function of the crosswind spacing and the turbulence intensity. It can be seen that losses of almost $15 - 20\%$ is possible for a small crosswind spacing. The total losses also depend on the directionality of the wind; power losses from wake array effects are more dominant in a unidirectional wind than in the case of an

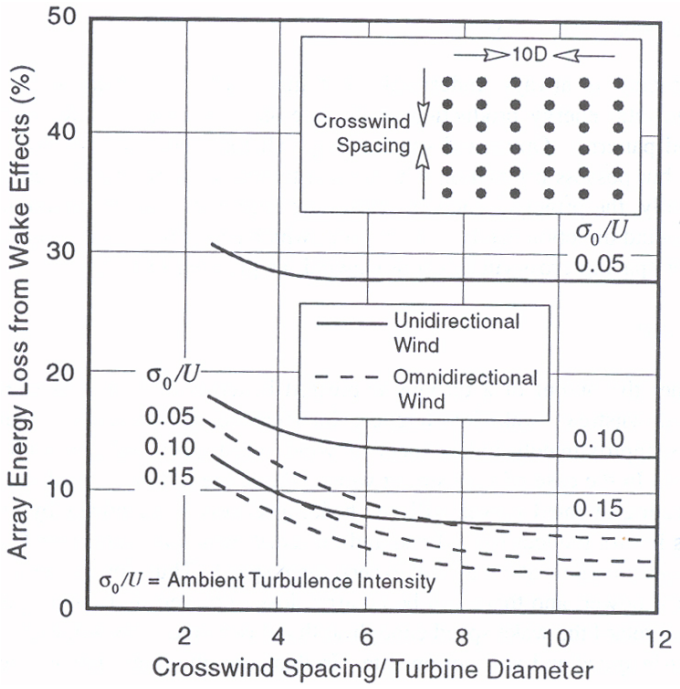

Figure 1.13: Influence of the crosswind spacing and turbulent intensity on the power output of a wind turbine. (Reproduced from Ref. 17.)

omnidirectional wind, as shown in Fig. 1.13.

An understanding of wake array effects requires an accurate understanding of the strong vortical wake behind a wind turbine and its effects on the local turbulence [18]. The turbulence generated by upstream turbines can affect the operation of a downwind turbine leading to a loss of fatigue life, exciting blade vibrations, and unfavorable control response.

1.6 Aerodynamic Modeling of Wind Turbines

The aerodynamics of a wind turbine are dominated by the aerodynamic flow around the rotor. Different approaches have been used to model the aerodynamics of a wind turbine, ranging from engineering models using the blade element momentum (BEM) theory, to solving the Navier–Stokes equations using computational fluid dynamics. However, for design purposes, the use of engineering models based on

BEM has been dominant. Another class of methods called vortex wake models have also been used, which use the potential, inviscid and irrotational flow approximation to the Navier–Stokes equations. These methods bridge the gap between the blade element models and CFD by giving a cost-effective but more physical solution, and a solution that is valid over a wide range of turbine operating conditions.

1.6.1 Blade Element Momentum Methods

Momentum theory, as discussed previously in Section 1.3, was developed independently by Betz [6] and Lanchester [7]. Also, see Ref. 19 for more details. The theory is based on an actuator disk concept, and provides a derivation for the theoretical maximum power that can be produced by a wind turbine. However, this theory assumes a constant inflow through the rotor disk, which does not precisely represent the actual flow physics. The theory also neglects the effects of viscous forces on the power extraction. However, momentum theory gives an upper limit to the aerodynamic power output available from a wind turbine.

Glauert [20] extended the basic theory to apply the momentum theory to an annular ring of the disk, and to match the results of thrust and torque derived from the blade element analysis. The theory was developed initially for propellers and also extended to wind turbines. Glauert also added the equation for the balance of change in angular momentum to the torque exerted by the rotor on the air. The application of momentum theory at the annular level then provides a tool for the design and analysis of wind turbine. Wilson and Lissaman [21] updated the blade element momentum method to account for finite number of blades by using the Prandtl tip and hub loss model. A detailed description of the blade element momentum method (BEM) is given later in Chapter 5.

The BEM method assumes independence of the annular sections. This assumption introduces a limitation in the BEM method for application in the case of yawed flow, i.e., when there exists a finite angle between wind direction and the

rotor axis. As mentioned earlier, yawed flow operation is common for wind turbines. Changes in the wind direction from gusts and turbulence are too rapid to be followed by the yaw control system. The BEM approach is often acceptably accurate for predicting the axisymmetric distribution of inflow in unyawed flow, but additional inflow estimates at the rotor disk are required to apply the BEM methods to yawed flows. However, this introduces empiricism into the calculations. Glauert proposed a simple sinusoidal distribution of inflow over the rotor disk,

$$u_i = \overline{u}_i \Big[1 - K_c f\left(\frac{r}{R}\right) \sin \phi_r \Big] \tag{1.18}$$

Here $\overline{u}_i$ is the induced velocity averaged over the whole disk. Various linear inflow models have been developed to approximate the cyclic variation of the inflow. These models mainly differ in the way they represent K_c, which is usually a function of the wake skew angle (the angle between the wake slipstream and the rotor axis). For the radial dependency function, $f(r/R)$, Glauert proposed a simple linear relation,

$$f\left(\frac{r}{R}\right) = \frac{r}{R} \tag{1.19}$$

The inflow equation used in most of the models are similar to Eq. 1.18, but differ in the coefficients and the radial dependency function. The coefficients of these inflow models are derived empirically from either experiments [22,23] or numerical simulations [24]. However, the applicability of these models is limited to a restricted range of wind turbine operating conditions. Another shortcoming of the BEM methods is their inability to capture the transient behavior of the power output in yawed flow. Moreover, these models have also not been validated for dynamically changing yaw angles, which happens frequently during the operational regime of wind turbines. Recent developments of inflow models for application to yawed flow have been discussed by Snel [25], and also by Snel and Schepers [26].

BEM also breaks down for very high rotor disk loading, i.e., when the inflow through the rotor disk is very high. This flow state usually arises for high tip speed ratios (low wind speeds), which are around 1.3 to 1.4 times the value for which

the maximum power output is attained. This flow state is known as the turbulent wake state (TWS), and a considerable amount of energy extracted from the wind is converted into large scale recirculating flow in the far wake of the turbine. In these conditions, the assumption of the existence of a streamtube does not hold. BEM methods have been modified based on empirical corrections [21, 27, 28] to overcome this limitation. However, these corrections are not applicable for all operating conditions, and often fail at higher tip-speed ratios. Some of the limitations of the BEM methods have been addressed in Refs. 29 and 30. For a variable speed wind turbine, this condition does not occur in practice. However, it has been estimated that about $15\% - 20\%$ of the yearly energy generation takes place in this region. Assuming the prediction error of 20%, the total error in the annual energy yield would be around 4% [31].

Blade element models forms the basis of most of the modern wind turbine design tools such as Aerodyn [32], BLADED [33], ADAMS [34], etc. A number of additional corrections are also made in the state-of-the-art models, such as a correction for 3D effects and dynamic stall. Blade element momentum theory uses 2D airfoil characteristics from wind tunnel tests. However, the flow field around a blade in a wind turbine is inherently 3D. The radial flow on the blade resulting from Coriolis forces modifies the pressure gradients on the flow about the blade section [35]. The 3D corrections in airfoil characteristics account for the changes in these pressure gradients resulting in the delayed stall and enhanced force coefficients. A number of 3D stall delay models [36–38] have been proposed. However, these models give acceptable prediction only in the case of unyawed flow.

Wind turbine blade sections undergo dynamic stall in an unsteady flow environment such as operation in turbulent winds, in the presence of a ground boundary layer, yaw error, etc. Dynamic stall is characterized by a delay in the onset of flow separation to a higher angle of attack than can be achieved statically [39]. Combined with the effects of a dynamic stall vortex, dynamic stall is responsible for

enhanced values of lift and increases in drag on the blade. In addition, there are a significant hysteresis in the airloads. In the BEM method, the effect of dynamic stall is accounted for by using several types of engineering models. However, most of these models have been developed for helicopter applications [40, 41] and cannot be directly applied to wind turbines.

1.6.2 CFD Based Methods

At the other end of the modeling spectrum are the computational fluid dynamics (CFD) methods. Using CFD methods to solve the time-dependent incompressible Navier–Stokes (N–S) equations provides the most comprehensive way of analyzing the flow field around the wind turbines. However, with the current computational power available, it is not possible to solve these equations. CFD methods, although more exact are computationally very expensive and have large memory requirements. In addition to this, the numerical issues associated with CFD methods such as turbulence modeling, wake diffusion, etc. have prevented the routine use of these methods. Various approximations are thus made to provide a more approximate and practical level of solution.

For an incompressible flow, the Navier–Stokes equations can be written as

$$\frac{\partial u_j}{\partial x_j} = 0 \tag{1.20}$$

$$\frac{\partial u_i}{\partial t} + u_j \frac{\partial u_i}{\partial x_j} = -\frac{1}{\rho}\frac{\partial p}{\partial x_i} + \nu \frac{\partial^2 u_i}{\partial x_j^2} + f_i, \quad i = 1, 2, 3 \tag{1.21}$$

Equation 1.20, known as the continuity equation represents mass conservation and Eq. 1.21 represents the balance of momentum. The momentum equations are nonlinear in velocity components through the convective acceleration terms. The exact solution of these nonlinear equations is available only for a few special cases. Direct numerical solution (DNS) of the N–S equations requires a numerical resolution, which is beyond the present levels of computational power. However, various ap-

proximations to the N–S equations have been used, which make the solutions more tractable.

The Euler equations are a non-viscous form of the N–S equations. Euler equations cannot represent the creation, diffusion, or dissipation of vorticity. Because of high Reynolds number in the global flow, and the absence of solid boundaries except near the rotor, this approximation is somewhat justified. However, the diffusion of vorticity in the wake of the turbine, and creation of turbulence and mixing because of strong tip vortices is not accounted for by the Euler equations. A detailed discussion on Euler solvers for wind turbines can be found in Ref. 42. Another approach, effectively also an Euler flow solver, is the use of asymptotic acceleration method developed at the Delft University of Technology. Although adapted for helicopter applications [43] initially, the method was extended to wind turbines by van Bussel [44]. This method extends Prandtl's lifting line theory to the case of rotating blades with unsteady flow. However, the small perturbation approximation is not always valid for wind turbines.

A simplification to the full N–S equations for high Reynolds number flows is done through the use of Reynolds Averaged Navier–Stokes equations (RANS). The RANS uses a time-averaged form of N–S equations, and averages the turbulent fluctuations in the flow field. This leads to a larger number of unknowns than equations. To resolve this issue, closure models called as turbulence models are used [45–48]. Many researchers have used this methodology for computing flow field around a wind turbine [49–51]. The RANS model has shown a lot of success in predicting the flow field under attached flow conditions. However, the uncertainity in prescribing the flow transition point has caused some problems in the separated flow regime and deep stall regimes. Wolfe and Ochs [52] noted that the poor predictions of the maximum lift coefficient for the S809 airfoil is probably caused by the deficiency of the $k - \epsilon$ model in a stalled flow. Chaviaropolous [53] also noted the problems regarding turbulence modeling for 2D unsteady and quasi-3D N–S modeling. Langtry

et al. [54] discuss the use of transition model for general CFD codes for 2D airfoil and 3D wind turbine rotor performance. Evaluation of turbulence models for predicting wind turbine aerodynamics in the realm of RANS solvers has been discussed in Ref. 55.

The use of hybrid codes has also been explored by some researchers. Sorenson and colleagues have developed Ellipsys3D [56], a steady N–S solver for flow about a wind turbine. The global flow field is computed by an axisymmetric Euler solver, with the rotor represented as an actuator disk. The rotor flow is solved by the solution of the RANS equations with a $k-\omega$ turbulence model developed by Menter [57]. Sankar and co-workers [58–60] have developed a hybrid Navier–Stokes/full potential/free-wake method for predicting 3D unsteady viscous flow around a horizontal axis wind turbine, which is a promising approach for the application of CFD to wind turbines.

1.6.3 Vortex Methods

A special case of the Euler equations comprise vortex wake methods. Vortex methods assume an incompressible potential flow, with the wake vorticity being confined to a finite number of nominally helical vortex elements. These vortex elements can be either straight lines or vortex blobs. Lagrangian fluid markers are placed along each vortex element and are linked together, usually with straight line segments. Using the principle of vorticity transport [61], the movement of the Lagrangian fluid markers is described by the advection equation

$$\frac{d\mathbf{r}}{dt} = \mathbf{V}(\mathbf{r}, t), \quad \mathbf{r}(t_0) = \mathbf{r_0} \tag{1.22}$$

where $\mathbf{r_0}$ is the initial position vector of the wake marker. One such equation holds for each marker. The governing equation in the blade fixed coordinates can be written as

$$\frac{\partial \mathbf{r}}{\partial \psi} + \frac{\partial \mathbf{r}}{\partial \zeta} = \frac{\mathbf{V}(\mathbf{r})}{\Omega} \tag{1.23}$$

where ψ is the azimuthal position of a blade defined from a reference datum, and ζ is the time (age) of the vortex filament since it was trailed into the flow. A numerical solution to the free-vortex problem dictates a discretization of both the left- and right-hand sides of Eq. 1.23. A time-marching method gives the force-free solutions of the wake for the given operating conditions of the wind-turbine.

Vortex methods were initially developed for helicopter applications [62, 63]. However, the early time marching methods suffered from numerical convergence problems. This problem motivated the development of steady state vortex wake methods, which can be classified into relaxation wake methods and prescribed wake methods. Both these methodologies have seen significant development over the last three decades.

1.6.4 Prescribed Vortex Wake Methods

Prescribed vortex methods assume a priori specification of the position of the vortex elements from experiments. Once the wake geometry has been prescribed, the induced velocity and circulation distribution along the blade can be calculated. Wake visualization of helicopter wake in hover [64] laid the foundation of such methods for helicopters operating in hover. Kocurek & Tangler [65] also proposed a semi-empirical model based on measurements made on a sub-scale hovering rotor. Egolf & Landgrebe [66] proposed a prescribed wake model for helicopters in forward flight.

Prescribed vortex wake models have been also been used for wind turbines applications. Kocurek [67] described a method featuring a detailed, prescribed wake solution. The wake model was extended to include the effect of the windmill brake state on the radial and axial displacement rates of the trailing vortex system. Performance calculations were made by coupling the lifting-surface circulation solution to a blade-element analysis. Coton and Wang [68] coupled a prescribed wake model with a semi-empirical unsteady aerofoil model to provide the unsteady aerodynamic

response of the blades to the cyclic variation of blade pitch. They showed good comparisons between the predictions from the model and experimental measurements, both in terms of gross performance prediction and detailed blade loads. A similar model was also used by Coton et al. [69] to model the tower shadow effect on downwind wind turbines. Dumitrescu and Cardos [70] used a prescribed wake model along with blades being represented by lifting lines. Predictions were shown to compare well with the existing numerical data from free vortex wake methods at much lower computational cost.

Despite their simplicity and computational efficiency, prescribed wake methods are limited in their formulation by the unavailability of experimental data for wind turbine wakes. To resolve this problem, recent flow visualization experiments have been performed to obtain vortex wake measurements. Laser sheet flow visualization was used by Grant et al. [71] to obtain wake positions for a HAWT in an open jet closed return wind tunnel under various conditions of turbine yaw and blade azimuth. Selected results obtained in the experimental study were compared with the predictions made by a prescribed wake model.

Experimental measurements of wake positions have also been obtained at the Delft University of Technology for unyawed [72] and yawed flow conditions [73]. The availability of wake position measurements resolves one limiting factor of prescribed vortex wake methods. However, these models cannot predict the distortion in the wake geometry and roll up of the tip vortices, and are also not useful for the prediction of transient loads and power output of wind turbines.

1.6.5 Free Vortex Wake Methods

Unlike prescribed wake methods, free-vortex wake methods do not require a priori specification of the position of the vortex elements. The vortex elements are allowed to distort freely under the influence of the local velocity field to force free locations. In this approach, the wake positions at each time step are calculated using

Biot–Savart law to obtain the induced velocities over all vortex filaments. These methods have fewer potential limitations, and are also applicable over a wider range of operating conditions.

Free-vortex methods can be classified into relaxation methods and time-marching methods. Relaxation methods assume that the steady state wake structure is periodic at the rotor frequency. The governing equations are modified to include a pseudo-time term, i.e.,

$$\frac{\partial \mathbf{r}}{\partial \tau} + \frac{\partial \mathbf{r}}{\partial \psi} + \frac{\partial \mathbf{r}}{\partial \zeta} = \frac{\mathbf{V}(\mathbf{r})}{\Omega} \tag{1.24}$$

This equation is solved in pseudo-time domain (τ) until a steady state is reached. The wake solution is relaxed until the vortex element positions remain unchanged over successive iterations. At this time, the τ derivative vanishes and Eq. 1.23 is recovered. The relaxation methods show rapid convergence. With earliest implementations in the early 1970s [74,75], relaxation based free wake methods have been developed by the helicopter community [76–78]. These methods have also been used for comprehensive rotorcraft analyses like CAMRAD [79] and UMARC [80].

One of the shortcomings of the relaxation based methods is their inability to capture the transient wake aerodynamics. On the other hand, a time-marching algorithm has that flexibility, which makes it suitable for the simulation of a wind turbine operating in unsteady aerodynamic environment. Despite their success for helicopter applications [81–83], and potential flexibility for wind turbine applications, the free-vortex method (FVM) has yet seen only limited use for wind turbines flow-field predictions. As mentioned earlier, either filaments or particles/blobs can be used as vortex elements in a free wake method.

Simoes et al. [84] and Wagner et al. [85] have used vortex filaments for FVM calculation. Voutsinas et al. [86] have developed a vortex particle method called GENUVP, which was used successfully to investigate the response of horizontal axis wind turbines during yawed operation [87]. The numerical results were validated against full-scale measurements made on the Tjareborg [88] wind turbine. ROVLM

was developed at the University of Stuttgart by Wagner et al. [85], and GENUVP was also used in the JOULE projects. Duque et al. [89] present a comparison of a blade element momentum method and a RANS solver with a free wake solver CAMRAD II developed by Johnson [90].

The solution of the equation governing the rotor wake problem given by Eq. 1.23 is quite challenging. This is because the right-hand side (RHS) of Eq. 1.23 is the velocity at each fluid marker, which is a highly nonlinear term. This velocity comprises of the free-stream velocity, any external or perturbation velocity, and the induced velocity from vortex filaments. The vortex induced velocities are governed by the Biot–Savart law, which gives a highly coupled system of equations. A practical disadvantage of the free vortex method is thus very large amount of computational time needed for the calculation. The CPU times for FVM are about two orders of magnitude higher than the BEM methods. However, at the same time, free-vortex wake can easily model the unsteady aerodynamics, and can be used to obtain transient loads on a wind turbine.

1.7 Objectives of the Dissertation

The motivation for the current research stems, in part, from a blind comparison study that was conducted in 2000 by National Renewable Energy Laboratory (NREL). In this experiment, a two-bladed wind turbine with twisted and tapered blades was tested over a wide range of operating conditions in the full-scale NASA Ames 80×120 ft wind tunnel [91, 92]. This experiment provided an extensive set of airloads and performance measurements, which can be used for thorough validation of predictive codes free of uncertainties caused by atmospheric effects. To ascertain the baseline capabilities of various competing predictive methodologies, NREL conducted a blind comparison study involving twenty participants, who used the gamut of methods for the prediction of the loads and performance of the NREL Phase VI turbine.

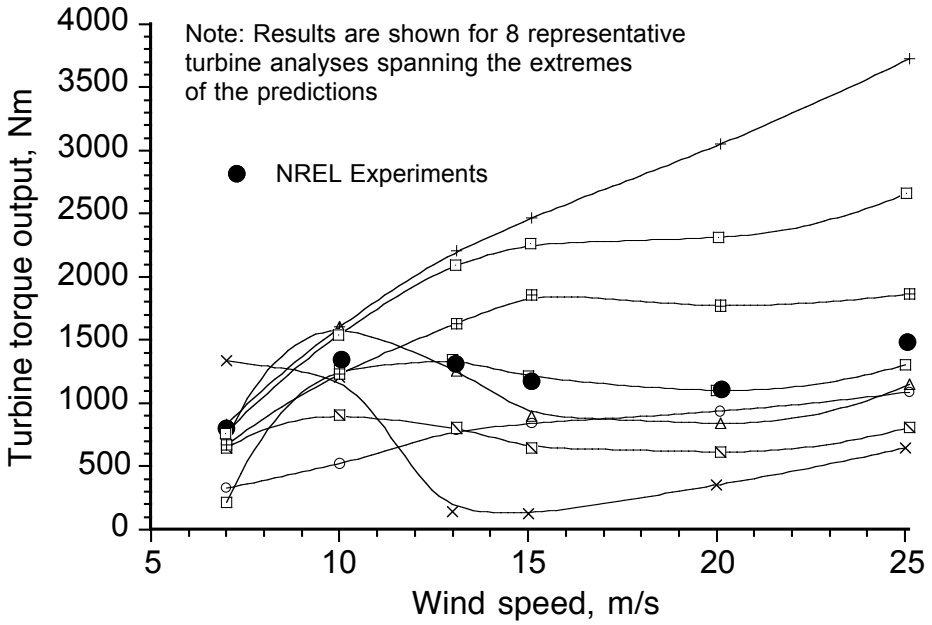

Figure 1.14: A comparison of the representative "in the blind" predictions of turbine low speed shaft torque output to experimental measurements. (Reproduced from Ref. 11.)

The results from the NREL blind comparison study showed unexpected large margins of disagreement between predicted and measured data [93]. In addition, no consistent trends were apparent regarding the magnitude or the sign of the deviations. Figure 1.14 depicts the prediction of the low speed shaft torque at zero yaw with various predictive codes, where the solid circles represent the measurements. The results of the torque output varied from 60% underprediction to more than 150% overpredictions. In addition, the predictive tools with essentially the same set of sub-models showed large differences in the predictions. This suggested both the inconsistencies in the assumptions made in certain predictive tools [94], as well as errors in the coupling between various sub-models [11].

The gross failure of the state-of-the-art tools to predict the aerodynamics loads and performance of the NREL wind turbine, even for the simplest of operating cases underlined the need for a careful study of the assumptions made in various

methodologies and in the assumption made in the coupling of the sub-models. In the present research, a time-accurate free-vortex wake method has been developed for the aerodynamic modeling of wind turbines. Vortex methods have a great potential to provide a high fidelity aerodynamic model with reasonable computational cost for wind turbine applications.

The development of a robust free wake methodology requires understanding of the stability characteristics and the overall accuracy of the numerical scheme. Numerical instabilities can mimic the growth of physical disturbances, which makes it harder to recognize the origin of these instabilities. One objective of this dissertation was to develop and carefully examine the stability characteristics of the numerical scheme. In addition to this, the present work also examines the accuracy of using straight-line vortex segmentation in a detailed manner. The objective was to ensure that an overall second-order predictive accuracy was maintained for the numerical solution.

The numerical method also needs to be validated against experimental data for a wide range of operating conditions. The coupled blade and wake model includes empiricism in the numerical method in the form of the viscous core growth model and dynamic stall model. One objective of the present work was to validate the empirical model with available experimental data. Finally, the long term objective of the current work is to develop an aerodynamic model that can be integrated with a structural dynamics code to provide a high fidelity aeroelastic tool and to help in the more efficient and less expensive design of wind turbines.

1.8 Organization of the Dissertation

An introduction to the origin and evolution of modern wind turbines, along with a discussion of the complicated operating aerodynamic environment of the wind turbine has been introduced in Chapter 1. The current state-of-the-art in aerodynamic modeling strategies were then discussed in Section 1.6. The motivation

and objectives of the current research were then discussed.

Chapter 2 describes the methodology for solving the governing wake equations. The blade lift solution methodology is also discussed. Wind turbine airfoil characteristics especially for the stall controlled turbines are unique, and a detailed description of the steady and unsteady airfoil modeling is also given.

The remainder of the dissertation follows a building-block strategy. Each submodel of the numerical method is analyzed and validated before moving on to the next step. Chapter 3 discusses the accuracy of the straight-line segmentation of the vortex wake behind a wind turbine. The stability and accuracy of the numerical algorithm used for the time integration of the rotor wake equations is also discussed in Chapter 3.

Chapter 4 compares the predictions of the power and thrust for unyawed and yawed flows from the blade element momentum and the proposed free-vortex wake method for a wind turbine with hyperbolically twisted rotor in the absence of a stall model.

Chapter 5 describes the validation of the stall model modified for wind turbine applications. The model is first validated against the 2D steady airfoil lift and drag measurements. The comparison is then extended to unsteady measurements from an oscillating S809 airfoil. The coupling between the airfoil model and the blade model is comprehensively validated with the parked blade measurements from the NREL tests.

Chapter 6 discusses the validation of the coupled free-vortex wake model against the experimental measurements. The wake geometry validation against wake measurements is presented. Finally, the validation of the predicted power and aerodynamic loads against the NREL wind tunnel measurements is presented for a wide range of conditions to demonstrate the robustness of the method for wind turbine applications. Finally, Chapter 7 summarizes the conclusions drawn from the present work, and provides some suggestions for future research.

Chapter 2

Methodology

This chapter describes the details of the methodology used in the present study. Various sub-models are involved in the aerodynamic modeling of a horizontal axis wind turbine, including a time-accurate free-vortex wake method. In the following sections, the governing equations and the numerical methodology are explained in detail. A strategy to account for the viscous diffusion of the wake is then presented. Modification of the vorticity field because of filament stretching is also discussed. A one panel lifting surface model, called the Weissinger-L model, is used to represent the blade, and its coupling with the wake model is discussed. The 2D blade airfoil model is then discussed, with an emphasis on the modification of an existing dynamic stall model for wind turbine applications.

2.1 Governing Equations of the Downstream Wake

A vortex wake approach represents the vortical structure of the downstream wake in the form of vortex lines that exist in a potential flow. In vortex theory, the mathematical representation of the wake can be done in variety of ways, such as by means of constant vorticity straight-line filaments, curved vortex filaments, or vortex blobs [95]. The straight-line segment approximation approach is most often used because the induced velocity contribution of each segment can be evaluated exactly.

Lagrangian markers placed on the vortex filaments are linked together, usually with straight line segments. These markers and the associated vorticity are

then convected naturally through the flow field at the local flow velocity to force free locations. The incompressible Navier–Stokes equations in the velocity–vorticity form describe the convection these wake filaments. The governing equations can be written as

$$\frac{D\vec{\omega}}{Dt} = (\vec{\omega} \cdot \vec{\nabla})\mathbf{V} + \nu\vec{\Delta} \cdot \vec{\omega} \tag{2.1}$$

The left-hand side of the equation is the material derivative of vorticity. The first term on the right hand side represents the strain term. This term represents the change in the length of the vortex filament as well as the change in the orientation of the vorticity vector. The second term accounts for the diffusion of vorticity because of the viscosity of the fluid.

The global flow field can be assumed to be essentially inviscid as the viscous effects are confined to much smaller length scales compared to the potential flow field. Assuming an inviscid flow field Eq. 2.1 can be written as

$$\frac{D\vec{\omega}}{Dt} = (\vec{\omega} \cdot \vec{\nabla})\mathbf{V} \tag{2.2}$$

It has been shown that under the assumptions of an inviscid, incompressible and irrotational flow, the elements on the vortex lines move convect with the fluid particles [96]. In other words, the rate of change of the position vector of an element on a vortex filament is equal to its local velocity. With these assumptions, Eq. 2.2 reduced to a convection equation.

In the present formulation, the vorticity is assumed to be concentrated in a finite number of vortex filaments with a singularity at the center of each filament. The convection of the Lagrangian markers (or vorticity) on a free-vortex filament is then described by the equation

$$\frac{d\mathbf{r}(\psi, \zeta)}{dt} = \mathbf{V}(\mathbf{r}(\psi, \zeta), t), \quad \mathbf{r}(t_0) = \mathbf{r}_0 \tag{2.3}$$

In Eq. 2.3, ψ is the azimuthal position of a blade defined from a reference datum, and ζ is the time (age) of the vortex filament since it was trailed into the flow – see

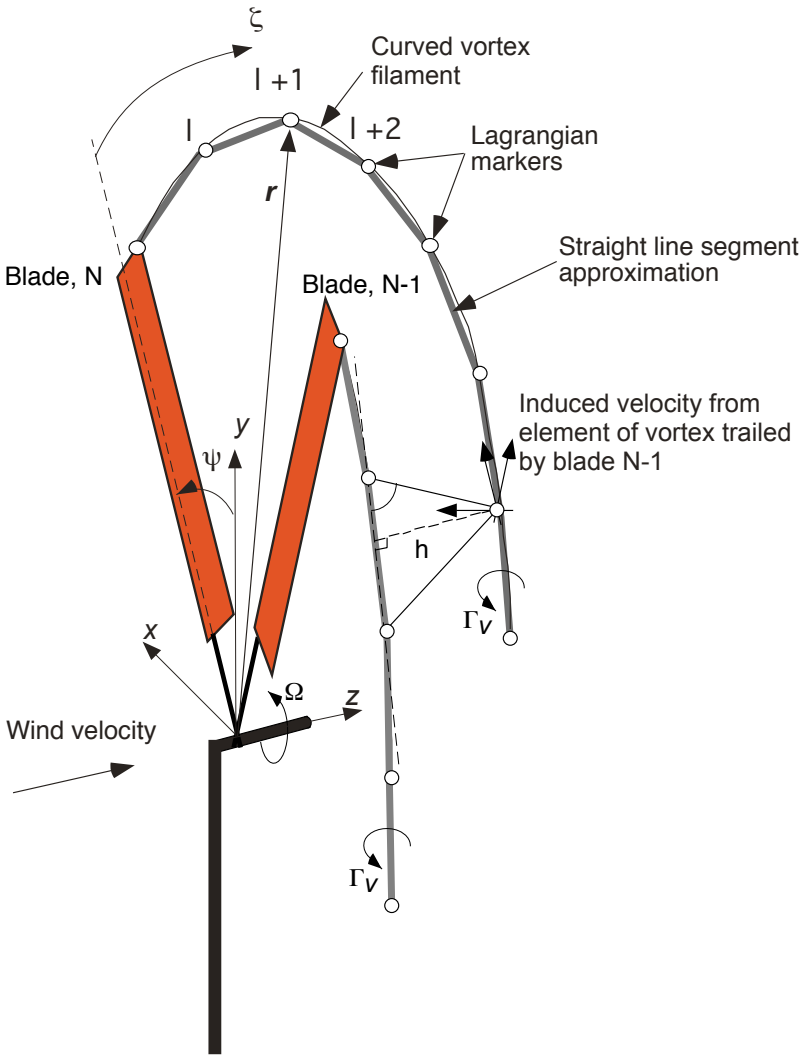

Figure 2.1: A schematic of the free-vortex wake strategy for modeling the aerodynamics of a wind turbine wake.

Fig. 2.1. The symbol $\mathbf{r}$ is the position vector of marker lying on a vortex filament that is trailed from a rotor blade located at an azimuth ψ at time t, $\mathbf{V}$ is the local velocity of that marker and $\mathbf{r}_0$ is the initial position vector.

Let t_0 denote the time when the vortex element was first formed and the blade was located at $(\psi - \zeta)$, i.e.,

$$(\psi - \zeta) = \Omega t_0 \tag{2.4}$$

Because $\psi = \Omega t$, it can be written

$$\zeta = \Omega(t - t_0) \tag{2.5}$$

Using the chain rule of differentiation, the time derivative of Eq. 2.3 can be written in terms of ψ, ζ and Ω [97, 98], i.e.,

$$\frac{d\mathbf{r}(\psi,\zeta)}{dt} = \frac{\partial \mathbf{r}(\psi,\zeta)}{\partial \psi}\frac{d\psi}{dt} + \frac{\partial \mathbf{r}(\psi,\zeta)}{\partial \zeta}\frac{d\zeta}{dt} \tag{2.6}$$

Because $d\zeta/dt = d\psi/dt = \Omega$, the time derivative can be written as

$$\frac{d\mathbf{r}(\psi,\zeta)}{dt} = \Omega\Big(\frac{\partial \mathbf{r}(\psi,\zeta)}{\partial \psi} + \frac{\partial \mathbf{r}(\psi,\zeta)}{\partial \zeta}\Big) \tag{2.7}$$

In blade fixed coordinates, this latter equation can be then written as the partial differential equation

$$\frac{\partial \mathbf{r}(\psi,\zeta)}{\partial \psi} + \frac{\partial \mathbf{r}(\psi,\zeta)}{\partial \zeta} = \frac{\mathbf{V}(\mathbf{r})(\psi,\zeta)}{\Omega} \tag{2.8}$$

The velocity term on the right-hand side is the sum of the free stream velocity $\mathbf{V}_\infty$, any external sources of perturbation $\mathbf{V}_{\text{ex}}$, such as the atmospheric boundary layer, wind turbulence, etc., and the wake induced velocity $\mathbf{V}_{\text{ind}}$. Therefore, $\mathbf{V}$ can be written as

$$\mathbf{V} = \mathbf{V}_\infty + \mathbf{V}_{\text{ex}} + \mathbf{V}_{\text{ind}} \tag{2.9}$$

The induced velocity term is comprised of the self- and mutually-induced velocities in the wake, mainly from the tip and root vortex filaments, but also the induced

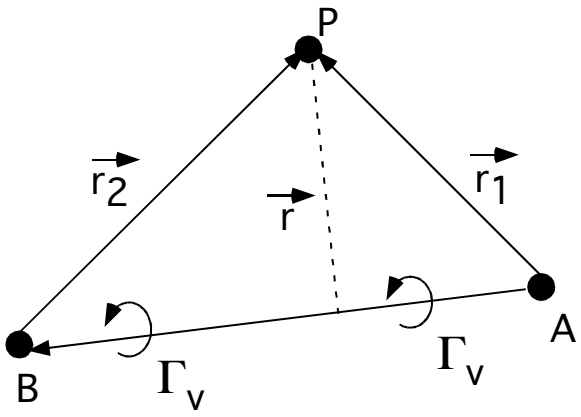

Figure 2.2: A finite length vortex segment and the application of the Biot–Savart law.

velocity contribution of the bound vortex. This term is highly nonlinear function of the spatial and temporal locations of the vortices, as dictated by the Biot–Savart law. The left-hand side of Eq. 1.23 is essentially a one dimensional wave equation. The equation is solved numerically using finite difference approximations, which will be discussed later in this chapter.

2.1.1 Nonlinear Induced Velocity

The wake induced velocity, $\mathbf{V}_{\text{ind}}$ on the right-hand side of Eq. 2.25, is a highly nonlinear term. It is the most difficult element of the wake problem to calculate accurately and the most expensive to compute. The solution to the wake induced velocity is evaluated by the repeated application of the Biot–Savart law as an integral along the complete length of each vortex wake filament. This integral is, in general, not available in analytic form for curvilinear vortex filaments. To overcome this, straight-line segmentation of the vortex filament is normally used. The induced velocity contribution for each segment can then be analytically calculated.

Consider a vortex segment of infinitesimal length dl and a point P at a distance

r from the line segment AB, as shown in Fig. 2.2. By means of the Biot–Savart law, the velocity induced, $d\mathbf{V}$, at point P by the vortex segment is given by

$$d\mathbf{V} = \frac{\Gamma_v}{4\pi} \frac{d\mathbf{l} \times \mathbf{r}}{|\mathbf{r}|^3} \tag{2.10}$$

For a finite segment as shown in Fig. 2.2, where $\mathbf{r}_1$ and $\mathbf{r}_2$ are the distances of the end point of the line segment from a point P, the induced velocity $d\mathbf{V}$ can be written as [99]

$$d\mathbf{V} = \frac{\Gamma_v}{4\pi} (\mathbf{r}_1 \times \mathbf{r}_2) \left(\frac{1}{r_1} + \frac{1}{r_2}\right) \left(\frac{1}{r_1 r_2 + \mathbf{r}_1 \cdot \mathbf{r}_2}\right) \tag{2.11}$$

One of the disadvantages of all types of vortex methods is the relatively large number of individual vortex filaments necessary to fully resolve the vortical flow, and the associated high computational cost of evaluating the Biot–Savart law for each and every filament. This often prevents the use of very fine discretization in the free-vortex wake calculations. Unfortunately, the use of smaller number of segments can compromise the accuracy of the induced velocity field reconstruction. Therefore, there is a need to carefully evaluate the accuracy of the straight-line segmentation approach, and to establish thresholds of discretization that will provide good accuracy while still containing computational costs (see Section 3.1).

The viscous diffusion and stretching of the vortex filaments have been neglected in Eq. 2.1. This assumption is valid in most operating conditions for wind turbines because these effects are usually confined to a much smaller scale. However, the detailed structure of the tip vortices can become important even at large scales away from the blades. The wake induced loads, especially when the vortex filaments interact with the blades, depend on the exact viscous structure of the tip vortex filaments. For wind turbines, this is not a common problem unless the turbine is yawing dynamically in and out of the wind. The modeling of the viscous and strain effects is also important when the turbine is operating in yawed flow because the wake filaments come close together at points in the downstream wake, and begin to roll up and bundle around each other. An improved modeling capability of tip

vortices will directly translate into the improved prediction of the wind turbine transient loads and power output.

In this study, the vortex filament positions are updated along with the consideration of viscous and strain effects by using a sequential treatment of the convective, viscous and strain effects, as shown in Figure 2.3. The approach is formulated as a time-marching process with three sub-component models. This approach follows the classical concepts to distinguish viscous and inviscid phenomenon developed by Prandtl [100], Chorin [101], Ananthan et al. [102] and others.

The first step in the process is a convection process, where the filaments are moved to new positions under the influence of the local velocity field as described above. In the second step, viscous effects associated with diffusion of the filaments are calculated based on the age of the filaments relative to the time at which they originated in the flow, and the vorticity field is thus modified accordingly. The third step accounts for the stretching effects, which uses the position vectors from the first step and serves to modify the vorticity field. In this study, each step of this process has been implemented as a predictor-corrector sequence to improve the accuracy of the solution.

2.1.2 Viscous Core Model

The motion of the Lagrangian marker on each vortex filament to a force free position is described by Eq. 2.1. The induced velocity at each marker position in the wake is calculated using the Biot–Savart law. However, the self-induced velocity has a logarithmic singularity at the axis of each filament. Unusually large wake induced velocities can cause the evolving tip vortex geometries to over-react to self- and mutually-induced effects, and will cause convergence problems. The same problem occurs when a collocation point moves very close to the vortex line segment and ejects at a very high induced velocity.

To desingularize the calculation of the induced velocity, a constant viscous

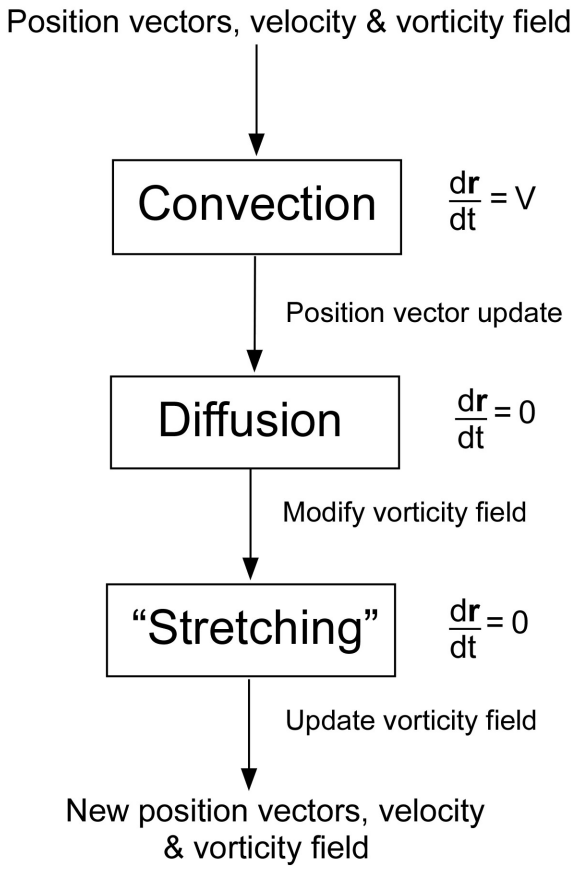

Figure 2.3: Schematic of the sequential treatment of the convective, viscous diffusion, and strain effects in the free-vortex model.

core size or a diffusive viscous core can be used. The "cutoff method," similar to the one used by Saffman [103], has been proposed by some to exclude the logarithmic singularity in vortex filaments. In this correction, for collocation points at a distance smaller than the "cut-off" length from a vortex filament, the induced velocity contribution from that vortex filament is zero. However, the solution then becomes a function of the cut-off length. To overcome this limitation in the present wake, the cut-off distance or the viscous core radius is prescribed based on experimental measurements.

Several empirical models have been developed to model the viscous diffusion of the tip vortex. The simplest model for a viscous vortex is the Rankine vortex [104]. Rankine vortex has a finite core, with a solid body-like rotation near the vortex center, and a potential vortex away from the center. The swirl velocity of a Rankine vortex can be written as

$$V_\theta(\bar{r}) = \begin{cases} \left(\dfrac{\Gamma_v}{2\pi r_c}\right)\bar{r} & 0 < \bar{r} < 1 \\ \left(\dfrac{\Gamma_v}{2\pi r_c}\right)\dfrac{1}{\bar{r}} & \bar{r} > 1 \end{cases} \tag{2.12}$$

where $\bar{r} = r/r_c$ is the non-dimensional radial location normalized by the core radius, r_c. However, the swirl velocity distribution and the circulation are discontinuous at the vortex core radius. The classical Lamb–Oseen [105] model is a solution to the one-dimensional N–S equations. It is assumed that the axial and radial velocity components are zero, and analytical solution of the swirl velocity can thus be obtained. The swirl velocity according to the Lamb–Oseen model is given by

$$V_\theta(\bar{r}) = \frac{\Gamma}{2\pi r}\left[1 - \exp\left(-\frac{r^2}{4\nu t}\right)\right] \tag{2.13}$$

The viscous core radius is the radial location where the swirl velocity is a maximum. The core radius can be obtained by setting the derivative of Eq. 2.13 to zero and is given by

$$r_c = \sqrt{4\alpha\nu t} \tag{2.14}$$

where $\alpha = 1.25643$. The Lamb–Oseen model can then be written in the form

$$V_\theta(\bar{r}) = \frac{\Gamma}{2\pi r_c}\left(\frac{1 - e^{-\alpha \bar{r}^2}}{\bar{r}}\right) \tag{2.15}$$

Using a vortex length scale of $\bar{r}_c = \sqrt{4\nu t}$, the Lamb vortex model can be written as

$$V_\theta(\bar{r}) = \frac{\Gamma}{2\pi r_c \bar{r}}\left(1 - e^{-\bar{r}^2}\right) \tag{2.16}$$

Using a series expansion for the exponential term and ignoring higher order terms, the model can be reduced a model proposed by Scully [62], which can be written as

$$V_\theta(\bar{r}) = \frac{\Gamma}{2\pi}\left(\frac{\bar{r}}{1 + \bar{r}^2}\right) = \frac{\Gamma}{2\pi}\left(\frac{r}{r^2 + r_c^2}\right) \tag{2.17}$$

In this work, a generalized swirl velocity profile given by Vatistas [106] has been used, which can be written in the form

$$V_\theta(r) = \frac{\Gamma_v}{2\pi}\left(\frac{r}{(r_c^{2n} + r^{2n})^{1/n}}\right) \tag{2.18}$$

For $n = 1$, Vatistas model reduces to the Scully model given by Eq. 2.17. In this study, a value of 2 was used for n because this has been found to give better correlation with experimental measurements.

The swirl velocity given by the Lamb–Oseen model in Eq. 2.13 is singular at the formation of the tip vortex, i.e., at $t = t_0$, and unrealistically high velocities are obtained at young wake ages compared to measurements. In addition, the core growth given by Eq. 2.14 has been found to be unrealistically slow. Therefore, an effective origin offset was further proposed by Squire [107] to give a finite core size and finite induced velocity field at the origin of the vortex filament. Squire also proposed the inclusion of a turbulent eddy viscosity parameter δ to account for the effects of turbulence on the net rate of viscous diffusion. In this work, a core growth model similar to the Lamb–Oseen model [105], and modified according to empirical observations by Bhagwat et al. [82], has been used to account for the average viscous and turbulent diffusion of the vortex core with time as given by

$$r_c(t) = \sqrt{r_{c_0}^2 + \frac{4\alpha\delta\nu\zeta}{\Omega}} \tag{2.19}$$

where r_{c_0} is the vortex core radius at zero wake age. However, the effect of turbulence on the vortex core radius is not well understood. Some researchers [108, 109], have shown a negligibly small effect of turbulence on the diffusion of the vortex core and claim that the vortex diffusion is dominated by viscous effects. From the rotating-wing measurements in Ref. 109, it has been shown that the core growth rate is inversely proportional to the vortex Reynolds number, which suggests laminar viscous diffusion. Iversen [110] reported that the turbulent effects of the vortex core are visible only for high vortex Reynolds number ($Re_v > 10^5$), which partly explains the laminar core growth achieved in the experiments, which used small scale models.

The eddy viscosity coefficient (δ) is formulated in terms of the vortex Reynolds number ($Re_v = \Gamma_v/\nu$) as given by

$$\delta = 1 + a_1 Re_v \tag{2.20}$$

which implies that vortex diffusion increases with increasing vortex Reynolds number. From experimental measurements, it has been observed that the rotary-wing results show a slightly higher viscous diffusion corresponding to an average value of $a_1 = 2 \times 10^{-4}$, while the fixed-wing results show a lower diffusion with $a_1 = 5 \times 10^{-5}$. However, these empirical value of a_1 comes from experiments performed on helicopter blades. No experiments data is available about the detailed viscous structure of the tip vortices for wind turbines.

2.1.3 Effect of Vortex "Stretching"

Distortion of the wake in the free-vortex wake solution causes three-dimensional strain in the vortex filaments, which in turn modifies the core vorticity and the resulting induced velocity field. In addition, the vortical wake behind a wind turbine expands, which stretches the vortex filaments. It is thus important to consider the effects of stretching of the vortex filaments for wind turbine applications. In the

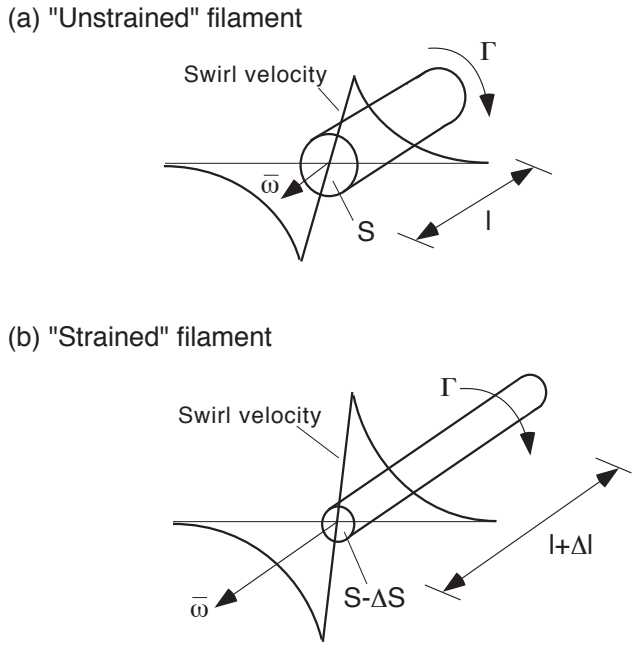

Figure 2.4: Schematic showing stretching of a vortex filaments and vorticity intensification that results in an increase in the induced swirl velocity from the filament core. (Schematic taken from Ref. 102.)

present formulation, stretching effects have been accounted for by an application of a model developed by Ananthan and Leishman [102].

Assuming that the flow is incompressible, net circulation of any vortex filament remains constant according to Helmholtz's third law. The circulation in a vortex filament is given as

$$\Gamma = \int_s \vec{\omega}\, d\mathbf{S} \tag{2.21}$$

In an incompressible flow field, an increase in the length of the cylindrical filament must be accompanied with a corresponding decrease in the cross-sectional area of the filament. This implies that as the vortex filament is stretched, the net vorticity increases to maintain a constant circulation – see Fig. 2.4

Consider a vortex filament, where the vorticity is assumed to be concentrated inside a cylinder of length l and core radius r_c. Assuming a change in the length because of filament straining to be $\epsilon = \Delta l/l$, which occurs over a time step $\Delta t = \Delta\zeta/\Omega$,

the conservation of the filament volume (using an incompressible flow assumption) states

$$\pi r_c^2 l = \pi(r_c - \Delta r_c)^2(l + \Delta l) \tag{2.22}$$

The change in the effective core radius can then be given as

$$\Delta r_c = r_c\Big(1 - \frac{1}{\sqrt{1+\epsilon}}\Big) \tag{2.23}$$

Combining Eqs. 2.19 and 2.23, the effective core radius at time $t = \zeta/\Omega$ can be written as

$$r_c(\zeta, \epsilon) = \sqrt{r_{c_0}^2 + \frac{4\alpha\delta\nu\zeta}{\Omega}\int_0^{\zeta}(1+\epsilon)^{-1}d\zeta} \tag{2.24}$$

The above equation gives the effective core radius at any time and includes the integral effects of the strain field from the point of the origin of the vortex. The modified core radius obtained from Eq. 2.24 is then used to compute the induced velocities from the vortex segments.

2.1.4 Time Marching Solution of Left-Hand Side

A numerical solution to the free-vortex problem dictates a discretization of both the left- and right-hand sides of Eq. 2.1. The discretization scheme should however ensure a consistent order of approximation between both sides. The left-hand side of the equation is essentially a one-dimensional wave equation. The discretized equation can be written as

$$(D_\psi + D_\zeta)\mathbf{r} = \frac{1}{\Omega}\sum \mathbf{V} \tag{2.25}$$

where D_ψ and D_ζ are the temporal and spatial finite difference operators. This discretization results in a set of finite difference equations, which can be solved using various types of numerical integration techniques [111]. A study of the stability of various time-marching schemes will be described in detail in Section 3.2.

Special discretization algorithm based on 5-point central differencing in space and 2-point backward differencing in time (PC2B scheme) developed by Bhagwat

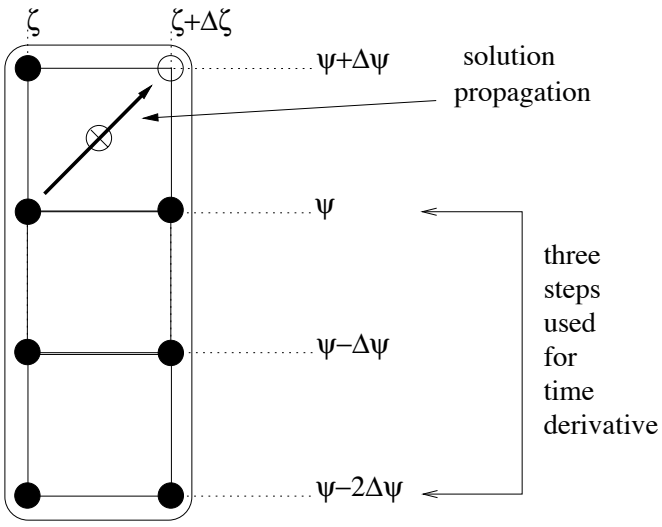

Figure 2.5: Stencil for the second-order two-step backward differencing scheme used in the PC2B algorithm. (Reproduced from Ref. 112.)

and Leishman [112] has been used in the present study. The governing equations are solved at the midpoints $(\psi + \Delta\psi/2, \zeta + \Delta\zeta/2)$ of the computational grid cell. The velocity at the center of the grid cell is approximated by averaging the velocities at the four surrounding grid points, which gives a second-order accurate approximation of the induced velocity.

The spatial derivative, D_ζ is approximated by a five-point central difference scheme, i.e.,

$$D_\zeta|_{\psi++\Delta\psi/2,\zeta+\Delta\zeta/2} = \frac{r(\psi+\Delta\psi,\zeta+\Delta\zeta) + r(\psi,\zeta+\Delta\zeta) - r(\psi+\Delta\psi,\zeta) - r(\psi,\zeta)}{2\Delta\psi} \tag{2.26}$$

The PC2B time-accurate algorithm uses a second-order backward difference approximation for the time (ψ) derivative. In this case, three previous time steps are used in approximating the temporal derivative – see Fig. 2.5. This approximation is given by

$$D_\psi|_{\psi+\Delta\psi/2,\zeta} = \frac{3r(\psi+\Delta\psi,\zeta) - r(\psi,\zeta) - 3r(\psi-\Delta\psi,\zeta) + r(\psi-2\Delta\psi,\zeta)}{4\Delta\psi} \tag{2.27}$$

The spatial operator is the same as in the PCC scheme. Using a Taylor series

expansion around the mid-point of a cell at $r(\psi + \Delta\psi/2, \zeta + \Delta\zeta/2)$ and expressing all the extra terms in terms of spatial derivatives, the modified equation for the PC2B scheme is obtained as [112]

$$\frac{\partial r}{\partial \psi} + \frac{\partial r}{\partial \zeta} = V + \Delta\zeta^2 \left[\begin{array}{l} \text{nonlinear dissipative} \\ \text{and dispersive terms} \end{array} - \frac{\Delta\zeta}{4} r_{4\zeta} \right] \tag{2.28}$$

The $-r_{4\zeta}$ term in the modified equation is a dissipative term, and is independent of the velocity field. This dissipative term acts like an energy sink and is stabilizing, and so this makes the overall PC2B scheme stable. This term is also a third-order term, so the overall second-order accuracy of the scheme is preserved.

2.1.5 Blade Model

In this work, the turbine was modeled as N_b rigid blades. The simplest representation of the blade model in terms of vortex singularities is the classical lifting line model. However, this model does not capture the three-dimensional effects on a wind turbine blade. Using a lifting surface model, where the blade is divided into a matrix of spanwise and chordwise panels, has been shown to better represent the three-dimensionality of the flow on the blade. However, the computational cost of using a a lifting surface model is much higher than a simple lifting line model. A good compromise between the lifting line and lifting surface models is the Weissinger-L model [113]. It is essentially a lifting surface model with one chordwise panel – see Fig. 2.6. Bound vortices are located at the 1/4-chord and the control points are located at 3/4-chord at the center of each panel. The trailed wake vortices extend downstream from the 1/4-chord forming a a series of horseshoe filaments. A Weissinger-L blade model has been shown to give much better representation of the aerodynamics of a blade as compared to a lifting-line model and at the same time with a much lower computational cost than a lifting-surface model.

The rotor blade is divided into N spanwise panels. The strength of the trailed vortices is determined using Helmholtz's law of circulation conservation and is given

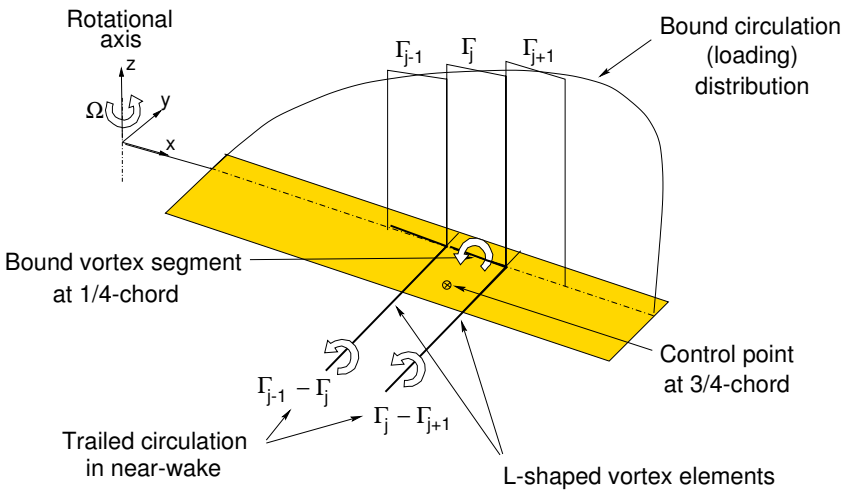

Figure 2.6: Schematic of the Wissinger-L blade model used in free-vortex wake modeling of wind turbines.

by

$$\Gamma_{\text{trailed}}|_i = \Gamma_{\text{bound}}|_i - \Gamma_{\text{bound}}|_{i+1} \tag{2.29}$$

The contribution of bound vortices to the induced velocity is added to the contribution from the trailing vortices and the flow tangency condition is satisfied at the 3/4-chord. The immediate near wake is assumed to be in the same plane as the blade, and is geometrically constrained relative to the blade control points. The induced velocity is, therefore, normal to the blade plane, and so changes the effective angle of attack. The flow tangency condition for the i^{th} blade segment at the 3/4-chord is given by

$$V_{b_i} = V_{\infty i}(\theta_i - \phi_{FW\,i} - \phi_{NW\,i}) \tag{2.30}$$

where θ_i is the geometric angle of attack and $\phi_{FW\,i}$ and $\phi_{NW\,i}$ are the induced angles of attack from the far wake and near wake, respectively. Equation 2.30 can be rewritten as

$$V_{b_i} = V_{\infty i}(\theta_i - \phi_{FW\,i}) - V_{NW_i} \tag{2.31}$$

The induced inflow from the far wake is calculated using the free-vortex wake solution. The bound circulation and the near wake are, however, geometrically con-

strained relative to the blade control points. The induced velocity from the bound circulation and the near-wake are written as

$$V_{b_i} = \sum_j I_{b_{i,j}} \Gamma_j \tag{2.32}$$

$$V_{NW_i} = \sum_j I_{NW_{i,j}} \Gamma_j \tag{2.33}$$

Here I_b and I_{NW} are the influence coefficient matrices for the bound vortex and the near wake, respectively. The governing equation for the blade circulation can then be written as

$$\sum_{j=1}^{N} (I_{b_{i,j}} + I_{NW_{i,j}}) \Gamma_j = V_{\infty j} (\theta_i - \phi_{FW\,i}) \tag{2.34}$$

This linear system of equations is then solved by standard methods to obtain the bound circulation on the blade. In this study, the near wake is truncated at after a short azimuthal distance, typically $\Delta\psi = 30°$. It is assumed that, beyond this point, the vortex sheet has completely rolled up and all the circulation in the flowfield is concentrated in the free trailers, which comprise the far-wake.

In the case of a geometrically twisted blade, which is very typical for wind turbines, the near wake trailers are not in the same plane. This implies that the velocity induced by the near wake is not exactly normal to the blade sections at the control point. The effect of twist is accounted for by evaluating the component of near wake induced velocity normal to the blade sections.

The lift produced by each blade segment can be computed directly once the blade bound circulation is determined. The rotor forces and moments can then be calculated by numerically integrating the segment loads along the blade span using

$$T = \int_e^R N_b \left(dL \cos\phi - dD \sin\phi \right) dr \tag{2.35}$$

$$Q = \int_e^R N_b \left(-dL \sin\phi + dD \cos\phi \right) r dr \tag{2.36}$$

where e is the distance of the root cut-out from the root of the blade. The instantaneous values of thrust and torque are then averaged over the azimuth to obtain the average thrust and torque.

Coupling of the Blade Model with the Wake Solution

The far-wake or tip vortex release point and initial strength depend on the near-wake solution. Beyond the assumed 30° of near-wake, extends a far-wake comprised of a single tip vortex filament. From visualization experiment performed for the helicopter and wind turbine rotors, the tip vortex has been found to be fully developed within a few chords behind the rotor blades. The initial strength and radial location from which the tip vortex is trailed by the blades into the wake is required as a boundary condition for the free-wake analysis.

The strength of the tip vortex was determined by assuming that the sum of the blade bound vorticity outboard of the maximum is trailed into the tip vortex. It can be shown that this results in a tip vortex of strength equal to the global maximum bound vorticity over the span of the blade at any given azimuth location. The release point of the tip vortex is usually the tip of the blade. It has been shown in some experimental studies of helicopter rotors [114] that the tip vortex release point is somewhat inboard of the tip. However, this has not been shown in the visualization experiments performed on wind turbine blades [73, 115].

2.2 Blade Section Model

Wind turbine blade sections can stall when the turbine operates at high wind speeds. Because of the low rotational speed of the turbine rotor, the inboard regions of the blades on a stall controlled wind turbine are stalled for much of their operational time. Thus, It is very important to model accurately the detailed aerodynamic characteristics of the airfoils being considered over a wide range of angles of attack.

Most of the numerical methods used to model the aerodynamics of wind turbines (see Ref. 1.6), with the exception of CFD based methods, require empirical modeling of airfoil behavior in the post-stall regime. CFD methods model the

physics of the flow over a wind turbine blade from the first principles using the Navier–Stokes equations. However, there are numerous unresolved numerical issues in the application of CFD methods to practical problems such as turbulence closure models, excessive numerical diffusion, etc. In addition, the computational expense involved is very high.

Various experimental studies [116, 117] have been conducted to understand the complex aerodynamics of a wind turbine in the attached and the separated flow regimes. A post-stall model proposed by Viterna [118] based on flat-plate theory has been used extensively in wind turbine research. Stall delay models have also been formulated [36, 37] to account for the influence of the three-dimensional flow [35] on the blade stall. Pierce and Hansen [119] applied the Leishman–Beddoes model [40, 120] to predict the blade loads with dynamic stall [121]. The use of two-dimensional measurements with BEM methods to predict the performance of wind turbines in attached and separated flows has been discussed by Tangler [122]. Most of the methods obtain a reasonable agreement with measurements for low angles of attack and attached flows, but the agreement is not always as good at or in stall or in the post-stall region.

In addition to this, the inherent unsteady nature of aerodynamic environment poses further problems. An airfoil section undergoes dynamic stall when it is subjected to any form of unsteady angle of attack motion (like pitching, plunging etc.), which takes the effective angle of attack beyond its normal static stall angle [39]. Dynamic stall of an airfoil is characterized by the shedding of a strong vortical disturbance from its leading edge, which is called a dynamic stall vortex. The onset of flow separation is also delayed to a higher angle of attack than the static stall angle, and combined with the effects of the dynamic stall vortex, is responsible for elevated values of lift. The aft movement of the center of pressure during the vortex shedding causes a large nose-down pitching moment (moment stall). When the angle of attack decreases, flow reattachment is found to be delayed to an angle of

attack lower than the static stall angle. This leads to significant hysteresis in the airloads and reduced aerodynamic damping, particularly in torsion [13]. This can cause torsional aeroelastic instabilities on the blades. Therefore, the consideration of dynamic stall is important to predict the unsteady blade loads, and also to define the operational boundaries of a wind turbine.

Modeling of dynamic stall through the numerical solution of the unsteady Navier–Stokes equations with CFD techniques has shown some recent success [123, 124], and has become increasingly feasible with the increase in computational power. CFD solutions are, however, still computationally very expensive, and are basically prohibitive for the routine engineering analyses of wind turbines. In addition, there are numerous issues such as turbulence modeling that still need to be understood. In the absence of less approximate and cost effective solutions, researchers have used various semi-empirical models to represent dynamic stall [40, 41, 120, 125] - see Ref. 95 for a discussion on dynamic stall and alternative models. The advantage of using these models is their relative simplicity and low computational expense. These models have met with good success, and have been shown to improve the predictive capability for blade airloads. Some of these models have also been used for wind turbine applications [119, 126].

In this formulation, the complex post-stall behavior of the wind turbine airfoil sections is modeled by dividing the problems into smaller and more physically identifiable aerodynamic sub-systems. These are then connected in the form of a Kelvin chain, when the output from one sub-systems defines the input to the other sub-system. All these effects are represented in such a way as to allow progressive transition between the static stall and dynamic stall characteristics. Figure 2.7 shows the components involved in calculating the unsteady airloads on an airfoil.

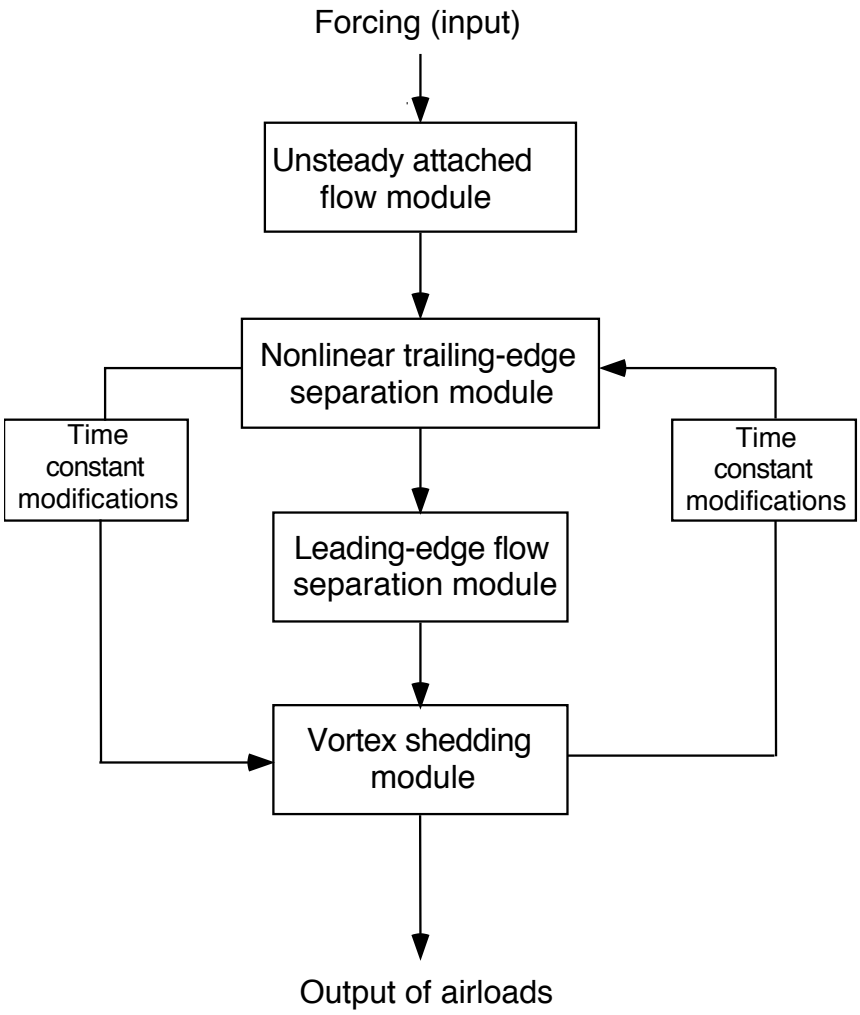

Figure 2.7: Flow chart of the elements of the unsteady airfoil model.

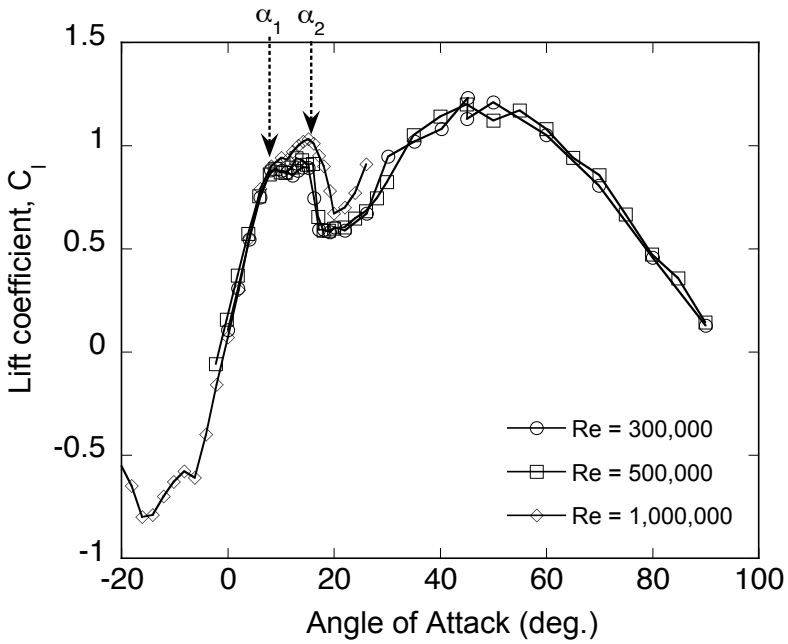

Figure 2.8: Variation of the lift coefficient with angle of attack for the S809 airfoil at different Reynolds number.

2.2.1 Nonlinear Static Airfoil Model

The normal force coefficient C_n is expressed in terms of the trailing-edge flow separation point f using two exponential curves to obtain a continuous functional form similar to that used in the Leishman–Beddoes model. Stall controlled wind turbine sections have unique nonlinear airfoil characteristics. S809 airfoil, which was used in the NREL wind tunnel tests [91] has a characteristic lift curve (see Fig. 2.8) where the lift coefficient C_l changes slowly over a range of angle of attack just before stall, i.e., between α_1 and α_2. The Leishman–Beddoes (L–B) model has been modified for use with the S809 airfoil, and the variation of the trailing-edge separation point with angle of attack is expressed in terms of three exponential curves.

Trailing-edge flow separation causes a loss of circulation and introduces nonlinearities into the lift, drag, and pitching moment. To represent the static (quasi-

steady) nonlinear post-stall behavior, the Kirchhoff/Helmholtz formulation [127] for modeling the lift on a flat plate is used. The relationship between the normal force coefficient and a fixed trailing-edge flow separation point is given by

$$C_n = C_{n_\alpha}\left(\frac{1+\sqrt{f}}{2}\right)^2 \alpha \tag{2.37}$$

where f is the effective flow separation point on the chord non-dimensionalised by the chord length. This formulation is strictly valid only up to moderate angles of attack. To model the airfoil behavior at very high angles of attack, as seen in wind turbines, the Kirchhoff formulation is modified to read

$$C_n = C_{n_\alpha}\left(\frac{1+\sqrt{f}}{2}\right)^2 \sin\alpha \tag{2.38}$$

In either case, the variation of the separation point f with angle of attack α can be obtained from the experimental measurements of static C_n by rearranging Eq. 2.38 to solve for f in terms of the measured values of C_n and α.

As an extension to this approach, the leading-edge thrust coefficient can be approximated by [40]

$$C_t = \begin{cases} C_{n_\alpha}\sqrt{f}\ \alpha\sin\alpha & C_n < C_n(\alpha_2) \\ K_1 + C_{n_\alpha} f\ \alpha\sin\alpha & C_n > C_n(\alpha_2) \end{cases} \tag{2.39}$$

Here α_2 is the static stall angle for S809 airfoil. The parameter K_1 is a constant required to fit the C_t curve from 2D static test data. The leading-edge thrust coefficient varies as $\sqrt{f}$ below $C_n(\alpha_2)$ and is proportional to f above $C_n(\alpha_2)$. The lift and drag coefficients are then obtained from the normal force and leading-edge thrust coefficients.

It is, however, not possible to define a general expression for the pitching moment variation from the Kirchhoff formulation so an empirical relation is used. This relation is derived from static airfoil measurements by expressing the center of pressure variation C_m/C_n as a function of the effective flow separation point [40]. The empirical relation for C_m/C_n (accounting for the zero-lift moment) for the S809

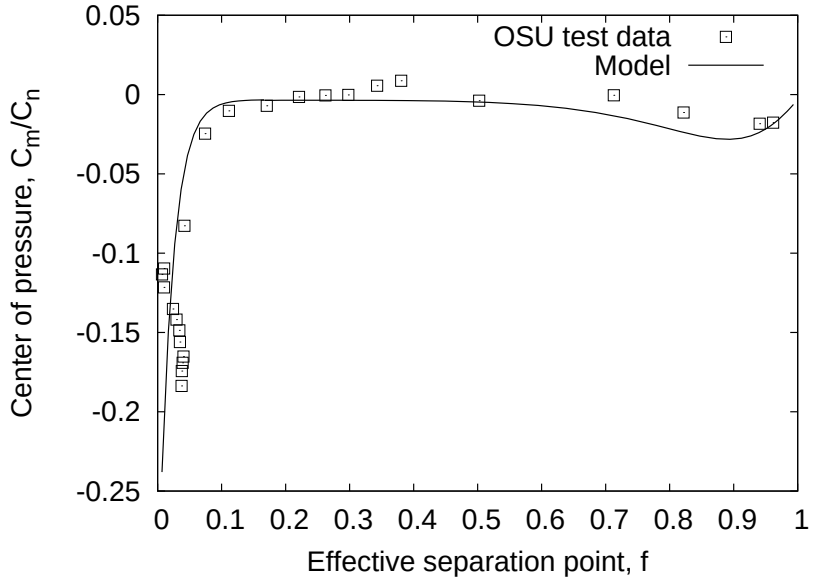

Figure 2.9: Variation of the center of pressure with the effective trailing-edge flow separation point for the S809 airfoil.

airfoil is fitted to the form

$$C_m = \begin{cases} C_{m_0} + \Big(C_0 + C_1(1-f) + C_2 \sin(\pi f^m)\Big) C_n & \text{for } \alpha < \alpha_2 \\ C_{m_0} + \Big(C_0 + C_1 \exp(C_2 f^m)\Big) C_n & \text{for } \alpha > \alpha_2 \end{cases} \tag{2.40}$$

Here C_{m_0} is the zero-lift moment and C_0 is the mean offset of the aerodynamic center from the 1/4-chord ($C_0 = x_{ac}/c - 1/4$). The coefficients C_1 and C_2 describe the nonlinear variation of the center of pressure. Figure 2.9 shows the variation of the steady center of pressure for the S809 airfoil versus the separation point, f, and Fig. 2.10 shows the reconstructed pitching moment curve according to Eq. 2.40.

2.2.2 Unsteady Attached Flow

The mathematical root of the L–B model lies within the classical, incompressible unsteady thin airfoil theory, but it is modified semi-empirically to represent compressibility effects in subsonic flow. The ability to accurately predict the unsteady aerodynamic forces and moments in attached flows is critical to the prediction of the onset of nonlinear aerodynamic effects, such as dynamic stall. The unsteady

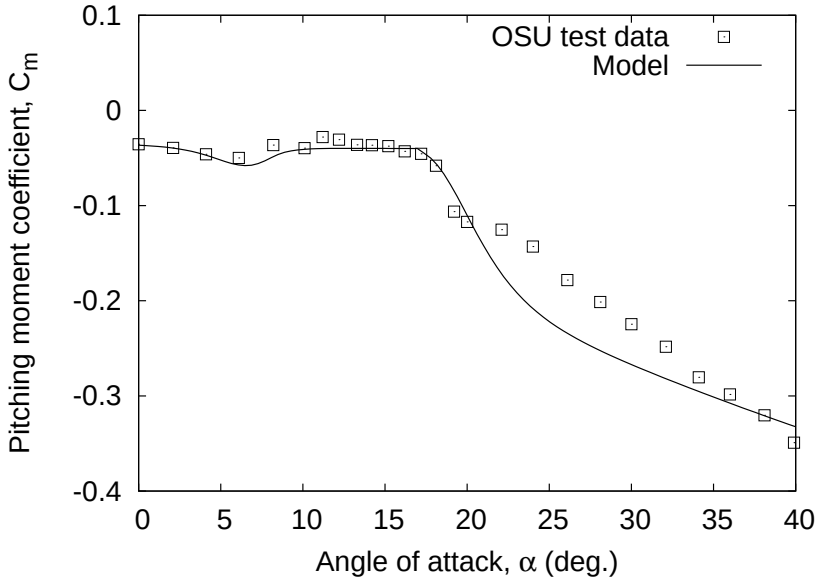

Figure 2.10: Variation of the pitching moment coefficient about 1/4-chord with angle of attack for the S809 airfoil.

attached flow response is computed in the L–B model in terms of a superposition of indicial aerodynamic responses. The indicial functions were derived for the Mach number range appropriate to helicopter rotors, but they can be applied to lower Mach numbers as well. The indicial responses are composed of the non-circulatory and circulatory loading components, which are written in functional form as exponential series.

The indicial response for the normal force and 1/4-chord pitching moment (in terms of the relative distance travelled by airfoil in semi-chords) for a step change in angle of attack $\Delta\alpha$ is given by

$$\Delta C_n(s) = \left(C_{n_\alpha}\phi_\alpha^c(s,M) + \frac{4}{M}\phi_\alpha^{nc}(s,M)\right)\Delta\alpha \tag{2.41}$$

$$\Delta C_m(s) = \left((0.25 - x_{ac})C_{n_\alpha}\phi_\alpha^c(s,M) - \frac{1}{M}\phi_\alpha^{nc}(s,M)\right)\Delta\alpha \tag{2.42}$$

The indicial responses from a step change in non-dimensional pitch rate about 1/4-chord is given by

$$\Delta C_n(s) = \left(\frac{C_{n_\alpha}}{2}\phi_q^c(s,M) + \frac{1}{M}\phi_q^{nc}(s,M)\right)\Delta q \tag{2.43}$$

$$\Delta C_m(s) \;=\; \Big(-\frac{C_{n_\alpha}}{16}\phi_q^c(s,M) - \frac{7}{12M}\phi_q^{nc}(s,M)\Big)\Delta q \tag{2.44}$$

where the ϕ^{nc} refers to the non-circulatory part of the response, and ϕ^c refers to the circulatory part. The indicial response from the circulatory part [120] can be approximated by

$$\phi^c(s,M) = 1.0 - A_1\exp(-b_1\beta^2 s) - A_2\exp(-b_2\beta^2 s) \tag{2.45}$$

where the constants are $A_1 = 0.3$, $A_1 = 0.7$, $b_1 = 0.14$ and $b_2 = 0.53$, and $\beta = \sqrt{1-M^2}$ is the Glauert factor. The non-circulatory indicial functions for step change in angle of attack and pitch rate about 1/4-chord are also approximated by exponential functions (see Ref. 128).

The above step response can then be superimposed using finite-difference approximation to Duhamel's integral (for details see Ref. 125) to take into account the time history of the change in angle of attack and pitch rate. For a continuously changing angle of attack, the effective unsteady angle of attack of the airfoil is given by

$$\alpha_e^c(s,M) = \alpha(s) - X(s) - Y(s) \tag{2.46}$$

where $X(s)$ and $Y(s)$ are deficiency functions written in terms of the exponential series representation of the indicial functions as given by

$$X(s) = A_1\int_{s_0}^{s}\frac{d\alpha}{ds}(\sigma)\exp(-b_1(s-\sigma)d\sigma) \tag{2.47}$$

$$Y(s) = A_2\int_{s_0}^{s}\frac{d\alpha}{ds}(\sigma)\exp(-b_2(s-\sigma)d\sigma) \tag{2.48}$$

These integral equations can be solved using a special finite-difference approximation to Duhamel's integral that is formulated as a set of recurrence equations [95]. A second-order algorithm can be written as

$$X(s) \;=\; X(s-\Delta s)\exp(-b_1\beta^2\Delta s) + A_1\Delta\alpha\exp(-b_1\beta^2\Delta s/2) \tag{2.49}$$

$$Y(s) \;=\; Y(s-\Delta s)\exp(-b_2\beta^2\Delta s) + A_2\Delta\alpha\exp(-b_2\beta^2\Delta s/2) \tag{2.50}$$

Here A_1, A_2, b_1 and b_2 are the coefficients of indicial functions, and are a function of the airfoil and the Mach number. These recurrence relations account for the circulatory time-history effects in the airloads.

A similar recurrence relation is used for the non-circulatory part of the airloads (see Refs. 40 & 125 for details). The non-circulatory normal force coefficients are given by

$$C^{nc}_{n_\alpha} = \frac{4}{M}\phi^{nc}_{\alpha} = \frac{4}{M}\exp\left(\frac{-s}{T'_\alpha}\right) \tag{2.51}$$

$$C^{nc}_{n_q} = \frac{q}{M}\phi^{nc}_{q} = \frac{1}{M}\exp\left(\frac{-s}{T'_q}\right) \tag{2.52}$$

Matching the correct initial value and the slope of the the total indicial response as given by the exact theory, the values of constants T'_α and T'_q are given by

$$T'_\alpha = \frac{2M}{(1-M)+\pi\beta M^2(A_1b_1+A_2b_2)} \tag{2.53}$$

$$T'_q = \frac{2M}{(1-M)+2\pi\beta M^2(A_1b_1+A_2b_2)} \tag{2.54}$$

A Duhamel recurrence solution can also be written for the non-circulatory terms. For a change in effective angle of attack $\Delta\alpha$, the non-circulatory component of normal force coefficient is given as

$$C^{nc}_{\Delta\alpha}|_s = C^{nc}_{\Delta\alpha}|_{s-\Delta s}e^{-\Delta s/T'_\alpha} + (\Delta\alpha|_s - \Delta\alpha|_{s-\Delta s})\left(\frac{2V}{c\Delta s}\right)e^{-\Delta s/2T'_\alpha} \tag{2.55}$$

$$C^{nc}_{n_\alpha} = \frac{4T_\alpha}{M}\left[\left(\frac{2V}{c\Delta s}\right)\Delta\alpha - C^{nc}_{\Delta\alpha}\right]_s \tag{2.56}$$

Similarly, for a pitch rate q, the recurrence relation for C_n can be written as

$$C^{nc}_{\Delta q}|_s = C^{nc}_{\Delta q}|_{s-\Delta s}e^{-\Delta s/T'_q} + (\Delta q|_s - \Delta q|_{s-\Delta s})\left(\frac{2V}{c\Delta s}\right)e^{-\Delta s/2T'_q} \tag{2.57}$$

$$C^{nc}_{n_q} = \frac{4T_q}{M}\left[\left(\frac{2V}{c\Delta s}\right)\Delta q - C^{nc}_{\Delta q}\right]_s \tag{2.58}$$

This linear unsteady aerodynamic model then forms the root for the upper level part of the overall nonlinear aerodynamic model, as shown in Fig. 2.7.

2.2.3 Unsteady Separated Flow

Defining the onset of leading-edge flow separation is the most important aspect of modeling dynamic stall. The criterion in the L–B model for static leading-edge flow separation can be represented in terms of the critical leading-edge pressure and the associated pressure gradient. This is equivalent to defining a critical value of normal force coefficient C_{n_1}, which corresponds to the critical pressure for the onset of flow separation [120]. Under unsteady conditions, there is a lag in the leading-edge pressure with increasing angle of attack, which can be expressed as a first-order lag as given by

$$C'_n = C_n - D_n^p \tag{2.59}$$

where D_n^p is given by

$$D_{n_k}^p = D_{n_{k-1}}^p \exp\Big(-\frac{\Delta s}{T_p}\Big) + (C_{n_k}^p - C_{n_{k-1}}^p) \exp\Big(-\frac{\Delta s}{2T_p}\Big) \tag{2.60}$$

The attainment of $C'_n \geq C_{n_1}$ causes leading edge flow separation. The time constant T_P is determined from unsteady airfoil data. Based on correlation with various airfoils, T_P has been found to be largely independent of airfoil shape [125, 129]. Trailing-edge separation is modeled as described in Section 2.2.1.

Under unsteady flow conditions, the value of f is modified because of the previously mentioned temporal effects on the airfoil pressure distribution and the boundary layer response. The effective angle of attack after incorporating the unsteady pressure response is given by

$$\alpha_f = C'_n / C_{n_\alpha} \tag{2.61}$$

This value of α_f is used to obtain a new value of the effective flow separation point called f'. The additional effects of the boundary layer response are incorporated as a first-order lag as given by

$$f'' = f' - D_{f_k} \tag{2.62}$$

where

$$D_{f_k} = D_{f_{k-1}} \exp\Big(-\frac{\Delta s}{T_f}\Big) + (f'_k - f'_{k-1}) \exp\Big(-\frac{\Delta s}{2T_f}\Big) \tag{2.63}$$

Using the final modified separation point, f'', the effective normal force coefficient is then obtained by

$$C_n^f = C_{n_\alpha}\Big(\frac{1+\sqrt{f''}}{2}\Big)^2 \sin\alpha \tag{2.64}$$

Similar to Eq. 2.39, the leading-edge thrust coefficient on the airfoil for the unsteady separated flow can be approximated by [40]

$$C_t = \begin{cases} C_{n_\alpha}\sqrt{f}\ \alpha \sin\alpha & C'_n \le C_{n_1} \\ K_1 + C_{n_\alpha}\sqrt{f} f^\Phi\ \alpha \sin\alpha & C'_n > C_{n_1} \end{cases} \tag{2.65}$$

Here C'_n is the so-called lagged value of the normal force and C_{n_1}, is the critical normal force value. The parameter K_1 is a constant required to fit the C_t curve from 2D static test data. C_t varies as $\sqrt{f}$ below C_{n_1}, and is proportional to $\sqrt{f}f^\Phi$ beyond stall. The parameter Φ is given by

$$\Phi = D_f(C'_n - C_{n_1}) + E_f(f'' - f) \tag{2.66}$$

where f is the quasi-static separation point, f'' is the lagged separation point at C_{n_1} and E_f and D_f are constants. The lift and drag coefficients are obtained by force resolution from the normal force and leading-edge thrust coefficients (see Fig. 2.11) using

$$C_l = C_n^f \cos\alpha + C_t \sin\alpha \tag{2.67}$$

$$C_d = C_n^f \sin\alpha - C_t \cos\alpha + C_{d_0} \tag{2.68}$$

where C_{d_0} is the zero-lift drag coefficient of the airfoil.

2.2.4 Vortex Lift

Dynamic stall is characterized by the formation of a vortical disturbance near the leading-edge of the airfoil, which separates from the surface at some critical point

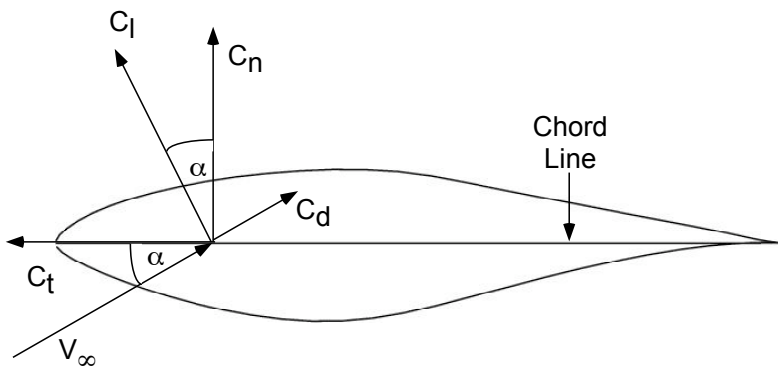

Figure 2.11: A schematic of the S809 airfoil and the various aerodynamic force coefficients.

and is then convected downstream along the chord. The effect of the vortex shedding is accounted in the L–B model by defining the vortex lift as the difference between the linearized value of the unsteady circulatory lift and the unsteady nonlinear lift obtained from the Kirchhoff approximation, i.e., by using

$$C_n^v = C_n^c(1 - K_n) \tag{2.69}$$

where

$$K_n = (1 + \sqrt{f''})^2/4 \tag{2.70}$$

At the same time, the vortex lift is allowed to decay with time, but it can be updated by a new increment in lift based on prior forcing conditions, i.e.,

$$C_{n_k}^v = C_{n_{k-1}}^v \exp\Big(-\frac{\Delta s}{T_v}\Big) + (C_{v_k} - C_{v_{k-1}}) \exp\Big(-\frac{\Delta s}{2T_v}\Big) \tag{2.71}$$

where T_v is the vortex time decay constant. When the critical conditions for leading-edge flow separation are reached (i.e., $C_n' > C_{n_1}$), the accumulated vortex lift starts to convect over the airfoil chord. During vortex convection process, the vortex lift continues to accumulate but ends when the vortex reaches the airfoil trailing-edge (i.e., when the non-dimensional vortex time, τ_v, is equal to the vortex traversal time, T_{vl}).

The center of pressure produced on the airfoil also varies with the convection of the leading-edge vortex over the chord, and is represented by the empirical relation

$$\bar{x}_{cp_v} = 0.20\Big(1 - \cos\left(\frac{\pi\tau_v}{T_{vl}}\right)\Big) \tag{2.72}$$

The increment in pitching moment about 1/4-chord resulting from the aft movement of the center of pressure is given by

$$C_m^v = -\bar{x}_{cp_v}\ C_n^v \tag{2.73}$$

The total loading on the airfoil is then obtained by adding the vortex induced contributions using

$$C_n = C_n^f + C_n^{nc} + C_n^v \tag{2.74}$$

$$C_m = C_m^c + C_m^{nc} + C_m^v \tag{2.75}$$

$$C_d = C_d^c + C_{d_0} \tag{2.76}$$

Although the above components have been described in an open loop sense, the elements are coupled, which are represented by temporary modifications of the appropriate time constants [125].

2.2.5 Tower Shadow Model

Tower shadow manifests as a velocity deficit in the flow behind the support tower. This leads to a reduction in the net lift and torque produced by the blade. In the FVM, the tower shadow effect is modeled as a velocity deficit normal to the surface of the blade, centered around an azimuth angle of $\psi = 180°$, i.e.

$$V_z(\psi) = V_{z_\infty} - \Delta v_z \exp\left(-\frac{(\psi - \psi_0)^2}{2\sigma_{tower}^2}\right) \tag{2.77}$$

The velocity deficit normal to the surface of the blade Δv_z and the azimuthal span of the velocity deficit σ_{tower} are determined empirically from experiment. The effect of the change in the velocity field on the lift and torque, as a function of the azimuthal location, is then accounted by the unsteady airfoil model.

2.3 Summary

In this chapter, the methodology used in the present research has been discussed. The governing equations of the vortex wake were reviewed. The free-vortex wake methodology for the solution of the wind turbine wake dynamics was developed. Straight-line segmentation was used to discretize the vortical wake. This gives a second-order accurate reconstruction of induced velocity. A second-order, time-accurate, two-step backward, predictor-corrector algorithm was used to numerically solve the inviscid, incompressible form of the governing equations for the convection of the wake markers.

Assuming incompressible. inviscid and irrotational flow, the governing equations of the wake were reduced to sets of convection equations. A sequential approach was adopted to include the viscous and stretching effects. The viscous diffusion and the filament strain effects were accounted for by using a viscous core growth model that was corrected for filament strain effects. The modified position vectors and the vorticity field were then marched to the next time step.

The Weissinger-L method was used for the blade lift solution. It is lifting surface method with only one chordwise panel. The Weissinger-L solution for blade bound circulation is related to the blade lift through an application of the Kutta–Joukowski theorem. Although the theoretical basis for the model is inviscid incompressible flow, compressibility and viscous effects can be included using an empirical airfoil lift and drag model.

A nonlinear airfoil characteristics model was formulated for wind turbines. The model is based on a the the Kirchhoff/Helmholtz formulation for modeling the lift on a flat plate, and a continuous functional representation was developed for the normal force coefficient. The original formulation was, however, modified to extend its validity to large angles of attack. A semi-empirical model was formulated for expressing the leading-edge thrust and the pitching moment coefficient.

Chapter 3

Accuracy and Stability of Numerical Scheme

A numerical solution provides an approximate representation of the real physical solution. Two kinds of errors are introduced into the numerical solution: round-off errors or discretization errors. The round-off errors are a result of non-exact representation of real numbers in floating-point arithmetic. These errors mainly depend on the floating-point precision used by the computer program. For the double precision arithmetic used in the present work, these errors have a relative magnitude of approximately 10^{-16}. Therefore, the round-off errors are not a real concern for most practical problems. On the other hand, discretization errors are the errors introduced during the discretization of the original governing equations, and depend on the grid size. The discretization errors are much larger in magnitude, and are more important to the problem of the aerodynamic numerical solution.

The discretized governing equation of the vortical wake is given by Eq. 2.25. The right-hand side of the governing equation is the nonlinear velocity field. It includes the self- and mutually-induced field from the helicoidal vortex filament behind the turbine. The approximate representation of the continuous vortex filament using straight-line segments gives an approximate solution of the induced velocity field. Similarly, the left-hand side of the governing equations for the wake is discretized and solved using a time-marching method, which is an approximate representation of the physical solution.

The overall order of accuracy of the numerical solution is governed by the order of accuracy of the lowest order accurate term. Hence, it is important to analyze the order of accuracy of both sides of the governing equation to ensure a consistent

level of accuracy. A numerical solution with a higher order of accuracy is also more computationally expensive. Therefore, there is a need to carefully evaluate the accuracy of the numerical solution for the engineering analysis of wind turbines, and to establish thresholds of discretization that will provide acceptable levels of accuracy while still containing computational costs.

3.1 Accuracy of the Induced Velocity Reconstruction

Vortex methods model the vortical structure of the rotor wake in the form of continuous vortex lines that exist in a potential flow. As discussed in Section 2.1, the mathematical representation of a vortex wake can be done in variety of ways, such as constant vorticity straight-line filaments, curved vortex filaments, and vortex blobs [95]. Straight-line segment approximation is commonly used because the induced velocity contribution of each separate vortex segment can be evaluated exactly using the Biot–Savart law.

Bhagwat & Leishman [112] used the problem of calculating the induced velocity of an inviscid vortex ring to estimate the accuracy of straight-line segment approximation. The induced velocity calculations from the numerical integration of the Biot–Savart law were compared with the analytical result for a vortex ring derived in terms of elliptic integrals [130]. The error analysis was done by calculating the L_2-norm and L_∞-norm of the relative error in the induced velocity across the plane of a vortex ring. It was shown that the straight-line segmentation gives a second-order accurate reconstruction of the velocity field.

Wood & Li [131] have suggested a helical vortex as more appropriate and stringent case for estimating the accuracy of straight-line segmentation. They considered three test cases for various helical pitch values of a singly-infinite helical vortex. They showed a second-order accuracy for a control point away from the filament and a dependence on helical pitch for control points near the singularity. Asymptotic results for the binormal velocity of a singly-infinite helical vortex de-

rived by Boersma & Wood [132, 133] were used where an analytic solution is not available. Wood & Li also argued that a vortex ring is not a special case of a helical vortex as its helical pitch tends to zero.

In this section, the accuracy of the induced velocity reconstruction using a straight-line segmentation of the vortex filaments has been discussed. The induced velocity distribution and error behavior of a vortex ring and a helical vortex are also compared.

3.1.1 Vortex Ring

A vortex ring can be thought of as one revolution of the helicoidal wake with the helical pitch equal to zero. The velocity induced by a vortex ring is given by the integration of the velocity induced by each straight line segment (given by Eq. 2.11) over the perimeter of the ring, which is given in polar coordinates r and z by the equations

$$\begin{aligned} V_r(r,z) &= -\frac{\Gamma}{4\pi}\int_{\delta}^{2\pi-\delta} \frac{Rz\cos\theta}{(R^2+r^2-2rR\cos\theta+z^2)^{3/2}}d\theta \\ V_z(r,z) &= -\frac{\Gamma}{4\pi}\int_{\delta}^{2\pi-\delta} \frac{R(R-r\cos\theta)}{(R^2+r^2-2rR\cos\theta+z^2)^{3/2}}d\theta \end{aligned} \tag{3.1}$$

Here δ is the cutoff angle which is equal to the angular discretization of the vortex ring.

An exact solution for the velocity induced by a vortex ring at any point can be found in terms of elliptic integrals [130]. For a vortex ring with strength Γ and radius R, the axial and radial velocity components are given by

$$\begin{aligned} V_z(r,z) &= \frac{-\Gamma}{2\pi\sqrt{z^2+(r+R)^2}}\left[\mathbf{K}(x)+\frac{R^2-r^2-z^2}{z^2+(R-r)^2}\mathbf{E}(x)\right] \\ V_r(r,z) &= \frac{-\Gamma z}{2\pi\sqrt{z^2+(r+R)^2}}\left[\mathbf{K}(x)-\frac{R^2+r^2+z^2}{z^2+(R-r)^2}\mathbf{E}(x)\right] \end{aligned} \tag{3.2}$$

respectively, where $\mathbf{K}(x)$ and $\mathbf{E}(x)$ are the elliptic integrals of the first and second

kind respectively. The argument x is defined by the equation

$$x = \sqrt{\frac{4rR}{z^2 + (r+1)^2}} \tag{3.3}$$

The velocity induced by the discretized vortex ring was calculated along a diameter across the plane of the vortex ring. All the calculations were done using double precision arithmetic. In the plane of the vortex ring, the radial component of the induced velocity is zero and only the axial component exists. The azimuthal discretization level was varied from a coarse azimuthal segmentation of 30° to a fine resolution of 0.01°.

Figure 3.1 shows the numerical results for the axial velocity, V_z, for various discretization levels, as compared to the exact solution given by Eq. 3.2. The exact solution is not defined at $|\vec{r}| = 1$, which is where a logarithmic singularity exists. For all other points in the plane of the ring, the numerical results show very good agreement with the exact solution. For $\Delta\theta = 0.01°$, the two values agree numerically up to 7 decimal places. Figure 3.2 shows the relative error distribution along the radius of the vortex ring. The magnitude of the relative error is maximum near the singularity at $|\vec{r}| = 1$, and decreases away from the singularity.

To estimate the accuracy of the reconstruction of induced velocity, a plot of L_2-norm versus the discretization level is shown in Fig. 3.3. In the first case, the error is calculated with respect to the exact solution, and in the second case with respect to the numerical solution from finest discretization. The two values were found to coincide for all discretization levels. A quadratic fit is also shown, indicating a second-order accuracy. For coarse discretizations, ($\Delta\theta > 10°$), the maximum error is more than 10%, and the order of accuracy appears to be lower. The above results show that for fine discretizations, the induced velocity calculation is at least second-order accurate.

The fact that the induced velocity calculation from the finest discretization compares so well with the exact solution will be used in the analysis of helical vortex. The induced velocity from the finest discretization will be used as an approximation

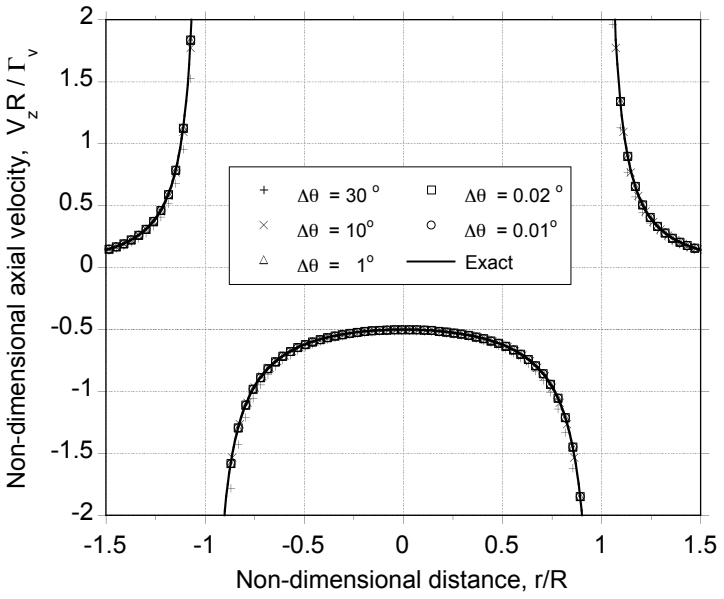

Figure 3.1: Induced velocity in the plane of a vortex ring.

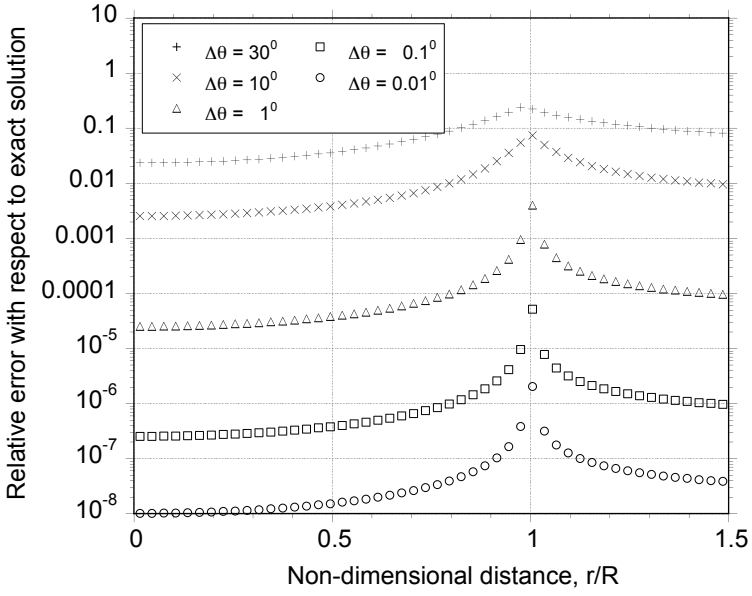

Figure 3.2: Numerical error distribution in the plane of a vortex ring.

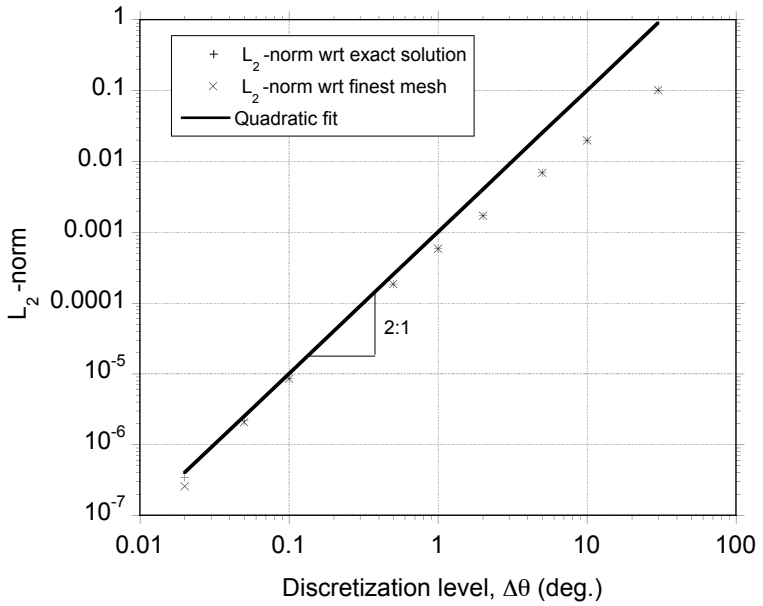

Figure 3.3: L_2-norm versus discretization for a vortex ring showing a second-order accuracy.

to the exact solution to calculate the error for a helical vortex, which does not have an analytical solution.

3.1.2 Comparison of a Vortex Ring and a Helical Vortex

A vortex ring can be thought of as helical vortex of pitch equal to zero laid down by one revolution of the rotor. It has been argued by Wood and Li [131], that the vortex ring is not a special case of a helical vortex with helical pitch, $p \rightarrow 0$. To understand this problem and compare the two cases quantitatively, the induced velocity distribution, scaled by the number of turns, from a singly-infinite and a doubly-infinite helical vortex with very small helical pitch was examined and compared to that of a vortex ring. Three cases were considered.

1. The spatial extent of the helical vortex ($N \times p$) was held constant.

2. Number of turns in the helical vortex, N, for different values of helical pitch, p was held constant.

3. Number of turns of the helix was varied for a constant helical pitch, p.

The results are presented for an azimuthal discretization of $\Delta\theta = 0.1°$. In Section 3.1.1, it was shown that the numerical evaluation of the Biot–Savart integral using an azimuthal discretization of $\Delta\theta = 0.1°$ to obtain induced velocity field gives a maximum error of less than 0.01%, which is essentially exact for any practical purpose.

Case 1: $N \times p$ is constant

In this case, the spatial extent of the helical vortex is kept constant. For $p = 0.01$, a total of 20 and 40 turns were used for singly-infinite and doubly-infinite helical vortices, respectively. For decreasing helical pitch, the number of turns was increased to keep the product $N \times p$ constant, and hence the spatial extent of the helix constant.

Figure 3.4 shows the induced velocity distribution across the $z = 0$ plane of a singly-infinite helical vortex. Notice that the induced velocity in this case is scaled by the number of turns. Also shown, is the induced velocity distribution from a vortex ring across the same plane. With decreasing helical pitch, the induced velocity distribution remains the same and does not approach the induced velocity distribution from a vortex ring. Figure 3.5 shows the error distribution of the induced velocity as compared to the exact solution for a vortex ring. For various helical pitch values, the error distribution was found to be the same.

The induced velocity distribution from a doubly-infinite helical vortex, scaled by the number of turns, is shown in Fig. 3.6. In this case, the velocity distribution was similar to the velocity induced by a singly-infinite helical vortex, and did not change for decreasing pitch. Figure 3.7 shows the error in induced velocity as compared to vortex ring. The magnitude of the error at all points was, again, the same as for the singly-infinite vortex.

Case 2: Constant N

For the second case, the number of turns of the helical vortex was kept constant for different helical pitch values, and the spatial extent of the helical vortex decreased with decreasing pitch. A total of 20 and 40 turns were used for the singly-infinite and doubly-infinite helical vortices, respectively. The induced velocity distribution for singly-infinite helical vortex is shown in Fig. 3.8. In this case, with decreasing helical pitch the induced velocity distribution approached the velocity distribution from a vortex ring, as shown by the solid line.

Figure 3.9 shows the magnitude of the error in the induced velocity calculated with respect to the induced velocity from a vortex ring. The magnitude of this error decreased as the value of helical pitch decreased. Similarly, the induced velocity distribution for a doubly infinite helical vortex (shown in Fig. 3.10), also approached the vortex ring result. For this case, the induced velocity scaled by number of turns for the singly-infinite and doubly-infinite helical vortices are the same. The error distribution for a doubly-infinite helical vortex, is similar to singly-infinite helical vortex, as shown in Fig. 3.11.

Case 3: Constant p

The variation in the induced velocity distribution for a fixed helical pitch, p, but with an increasing number of turns was also studied. Figure 3.12 shows the induced velocity distribution from a singly-infinite helical vortex with $p = 0.001$ for increasing N. It can be seen that the velocity distribution differs more and more from the vortex ring case, as N is increased. A doubly-infinite vortex ring also behaves in a similar way, as shown in Figure 3.13.

All of the above results show that a helical vortex reduces to a vortex ring as the helical pitch $p \to 0$, provided the number of turns, N, is kept constant. If the spatial extent of the helical vortex is kept constant, the velocity distribution does

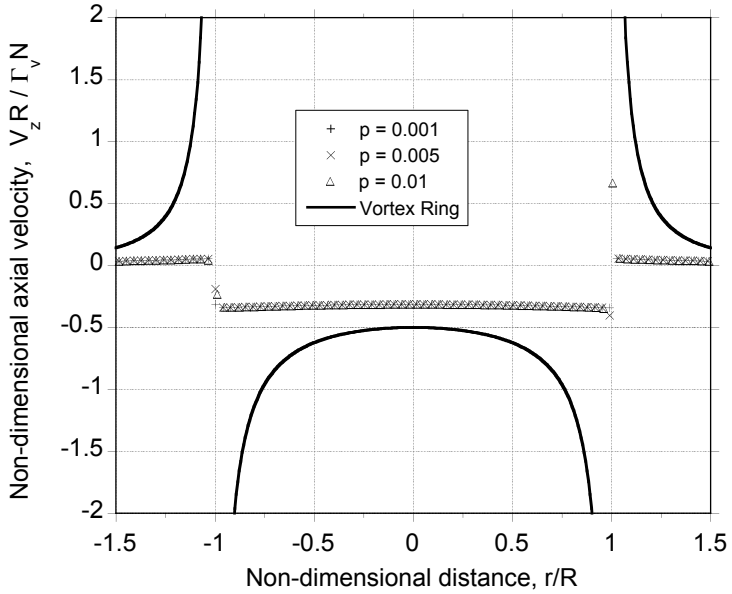

Figure 3.4: Induced velocity distribution from a singly-infinite helical vortex for decreasing helical pitch with $N \times p$ constant. An azimuthal discretization of $\Delta\theta = 0.1^\circ$ is used. The velocity induced by a vortex ring is also shown.

not depend on the helical pitch. When the helical pitch is reduced for a constant N, the case of a vortex ring is approached. If the number of turns is increased for small but finite helical pitch (Figs. 3.12 and 3.13), the induced velocity distribution becomes less like the vortex ring case.

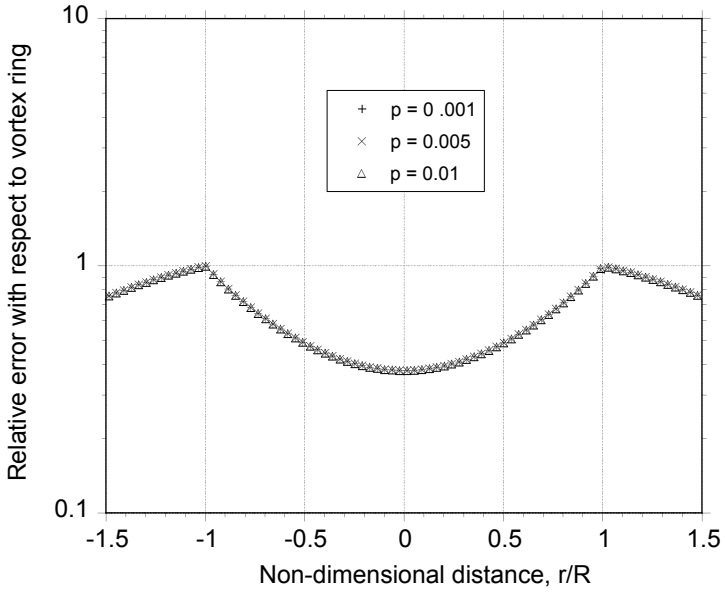

Figure 3.5: Error distribution in induced velocity from a singly-infinite helical vortex for decreasing helical pitch with $N \times p$ constant, compared to a vortex ring. An azimuthal discretization of $\Delta\theta = 0.1°$ is used.

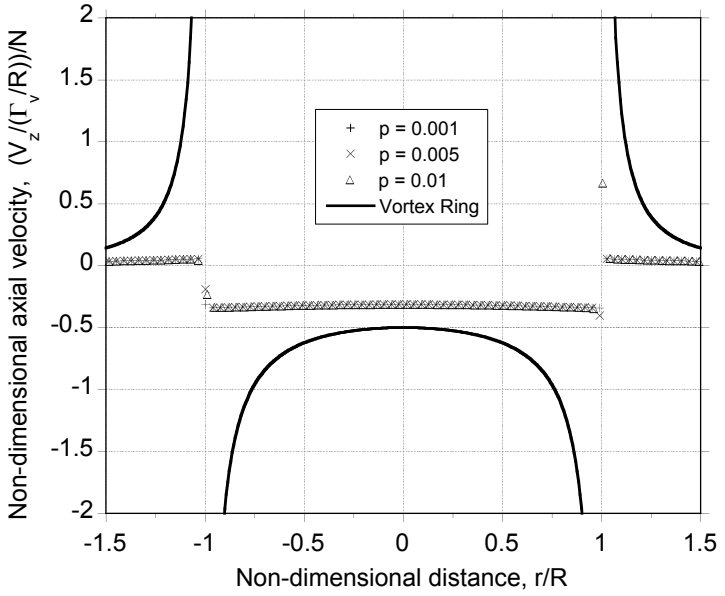

Figure 3.6: Induced velocity distribution from a doubly-infinite helical vortex for decreasing helical pitch with $N \times p$ constant. An azimuthal discretization of $\Delta\theta = 0.1°$ is used. The velocity induced by a vortex ring is also shown.

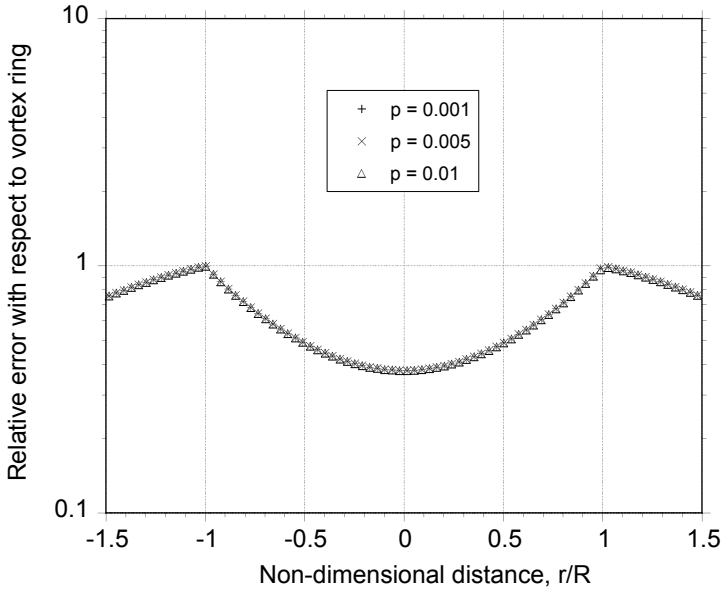

Figure 3.7: Error distribution in induced velocity from a doubly-infinite helical vortex for decreasing helical pitch with $N \times p$ constant, compared to a vortex ring. An azimuthal discretization of $\Delta\theta = 0.1^\circ$ is used.

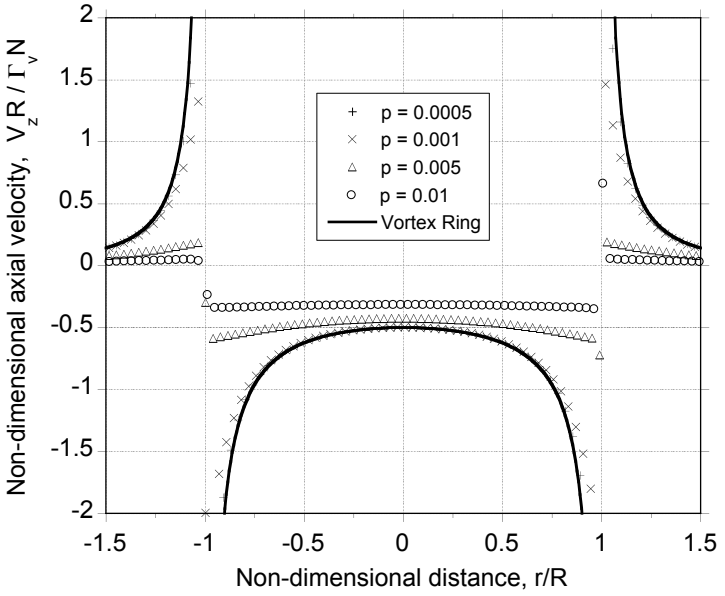

Figure 3.8: Induced velocity distribution from a singly-infinite helical vortex for decreasing helical pitch with N constant. An azimuthal discretization of $\Delta\theta = 0.1^\circ$ is used. The velocity induced by a vortex ring is also shown.

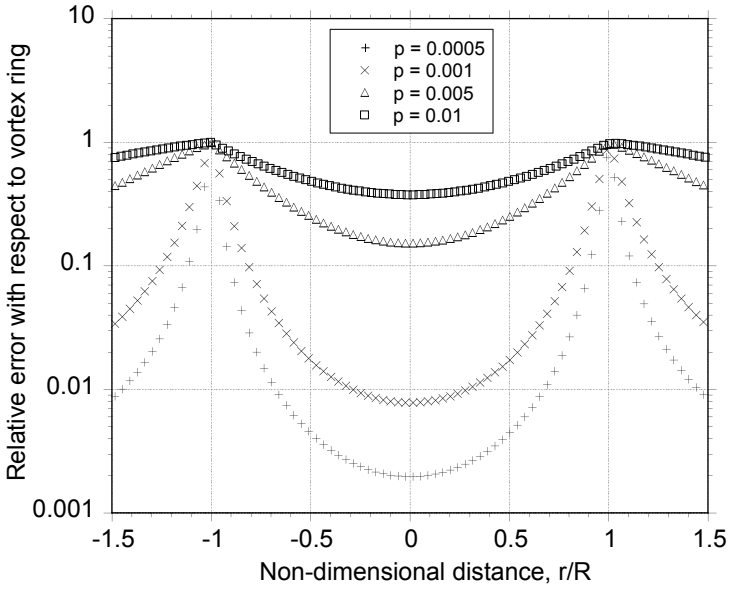

Figure 3.9: Error distribution in induced velocity from a singly-infinite helical vortex for decreasing helical pitch with N constant, compared to a vortex ring. An azimuthal discretization of $\Delta\theta = 0.1^\circ$ is used.

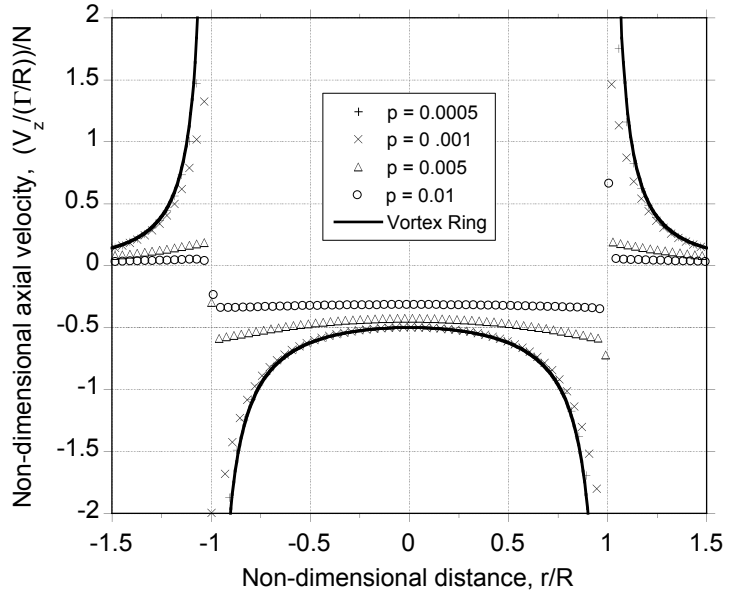

Figure 3.10: Induced velocity distribution from a doubly-infinite helical vortex for decreasing helical pitch with N constant. An azimuthal discretization of $\Delta\theta = 0.1^\circ$ is used. The velocity induced by a vortex ring is also shown.

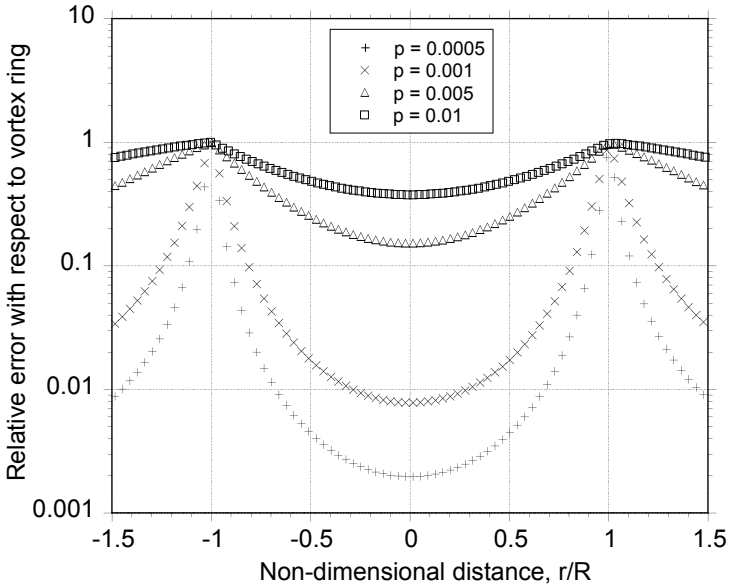

Figure 3.11: Error distribution in induced velocity from a doubly-infinite helical vortex for decreasing helical pitch with N constant, compared to a vortex ring. An azimuthal discretization of $\Delta\theta = 0.1^\circ$ is used.

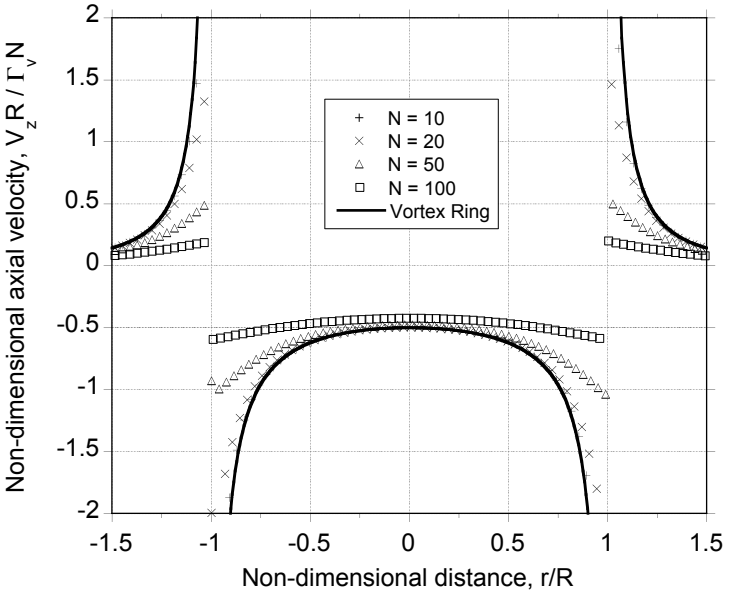

Figure 3.12: Comparison of the induced velocity distribution from a vortex ring and a singly-infinite helical vortex for increasing number of turns and constant helical pitch $p = 0.001$. An azimuthal discretization of $\Delta\theta = 0.1^\circ$ is used.

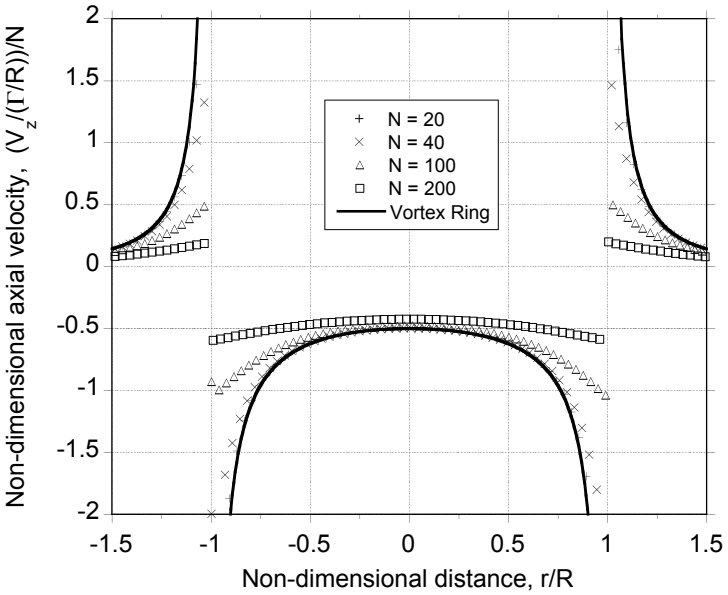

Figure 3.13: Comparison of the induced velocity distribution from a vortex ring and a doubly-infinite helical vortex for increasing number of turns and constant helical pitch $p = 0.001$. An azimuthal discretization of $\Delta\theta = 0.1^\circ$ is used.

3.1.3 Accuracy of Straight-Line Segmentation of Helical Vortex

In Section 3.1.2, the induced velocity distribution and error distribution for singly-infinite and doubly-infinite helical vortex with very small pitch were compared with that of a vortex ring. The vortex ring has been established as a special case of helical vortex with the helical pitch tending to zero, but only if number of turns is held constant. In this section, the accuracy of the induced velocity reconstruction from a helical vortex will be considered.

It was shown in Section 3.1.1 that the numerical results from the finest discretization for the induced velocity reconstruction of the vortex ring agree very well with the exact solution. This result will be used in assessing the accuracy of the induced velocity from both singly-infinite and doubly-infinite helical vortices, and so the errors were calculated with respect to the numerical results from the finest discretization level. Results were studied for a range of values of helical pitch, p. All the calculations were done in double precision arithmetic.

Figure 3.14 shows the induced velocity from a singly-infinite helical vortex with a helical pitch of $p = 0.05$. The induced velocity distribution has a singularity at $\vec{r} = +1$, but the variation near $\vec{r} = -1$ is smoother. The error distribution in the induced velocity calculated with respect to the finest discretization is shown in Fig. 3.15. The error distribution has a maximum at $\vec{r} = -1.2$. The induced velocity near $\vec{r} = -1.2$ is close to zero, which causes an increase in the relative error at this point. However, the absolute maximum error still occurs at the singularity $\vec{r} = 1$. The solid line shows the relative error in the induced velocity for a vortex ring for a discretization of $\Delta\theta = 0.02°$. It can be seen that the magnitude of the relative error for the vortex ring is greater than the corresponding case of a helical vortex at all points. The position of minimum error is governed by the cancellation of errors from the successive turns of the helix.

Figure 3.16 shows the velocity distribution for a helical pitch of $p = 0.1$. The velocity distribution is essentially the same, except for the value of constant velocity

near $|r| = 0$. The error distribution (Fig. 3.17) has only one minima at $\vec{r} = -0.2$ and a maxima near the singularity at $|r| = 1.0$. For $p = 1.0$ (Fig. 3.18), the vortex element nearest to $\vec{r} = -1.0$, is relatively far, and the induced velocity distribution is flat. The minima in the error distribution moves to $\vec{r} = 0.0$ (Fig. 3.19).

Figure 3.20 shows the L_2-norm versus discretization level for various values of helical pitch. A curve fit is also shown to bring out the nature of the numerical errors. For all values of helical pitch, the errors decreased quadratically with grid discretization. The results were similar to the case of vortex ring, as discussed previously in Section 3.1.1. The magnitude of the L_2-norm (computed from the relative error) for $p = 0.05$ was more than the other cases because of the reasons cited earlier. The accuracy is less than second-order for coarse discretizations, and as found for the vortex ring case, a discretization of at least $\Delta\theta = 10^\circ$ was required to keep the maximum error less than 10%.

Next, the case of a doubly-infinite vortex was considered. It was shown previously in Section 3.1.2 that the induced velocities (scaled by the number of turns), and the error behavior of both the doubly-infinite vortex and the singly-infinite vortex were similar. Figure 3.21 shows the velocity induced by a doubly-infinite vortex for $p = 0.05$. Notice that, in this case, the velocity is not scaled by the number of turns, and the magnitude of the induced velocities is almost twice that of the singly-infinite case. The error behavior (Fig. 3.22) was the same as for the singly-infinite vortex with $p = 0.05$. The minima is at $\vec{r} = -0.7$ and a maxima is at $\vec{r} = -1.2$.

Figure 3.23 shows the velocity induced by a doubly-infinite vortex with helical pitch of $p = 0.1$. Again, the magnitude of the velocity is twice the magnitude of the velocity induced by a singly-infinite helical vortex with the same pitch. The error distribution for this case is shown in Fig. 3.24.

The convergence trend (L_2-norm versus grid discretization) is shown in Fig. 3.25. A quadratic fit is also shown, which indicates a second-order accuracy for all values of helical pitch. For different helical pitch values, it is clear that the reconstruction

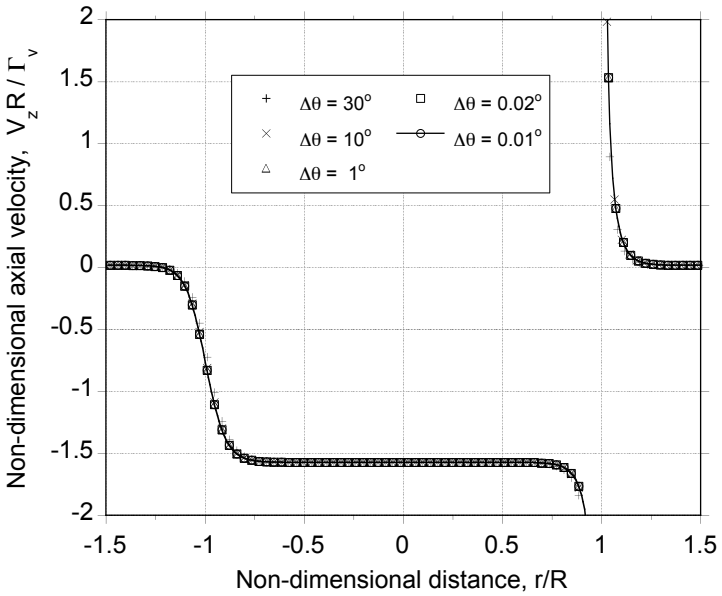

Figure 3.14: Induced velocity in the plane of a singly-infinite helical vortex with pitch $p = 0.05$ calculated using straight-line segmentation.

of the induced velocity field from both the singly-infinite and the doubly-infinite helical vortex by straight-line segmentation is at least second-order accurate.

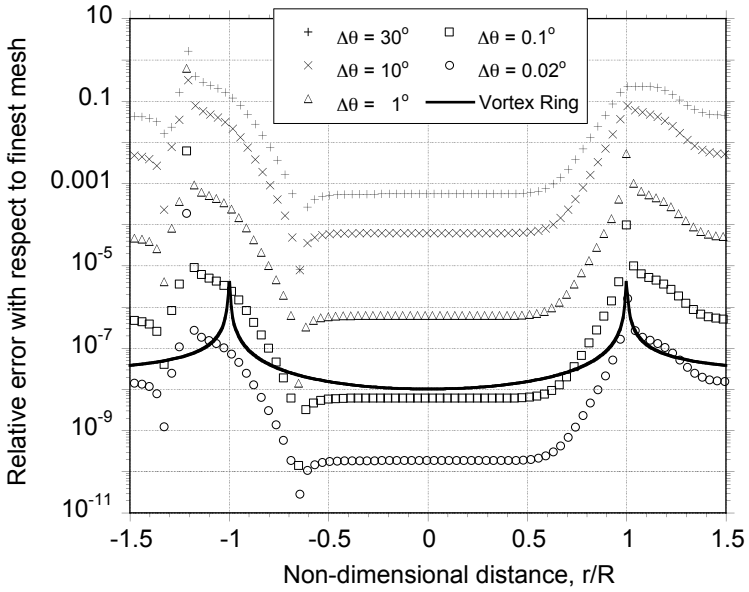

Figure 3.15: Error distribution in the induced velocity in the plane of a singly-infinite helical vortex ($p = 0.05$) with respect to the finest discretization. The error distribution for the case of vortex ring with discretization level of $\Delta\theta = 0.02°$ is also shown.

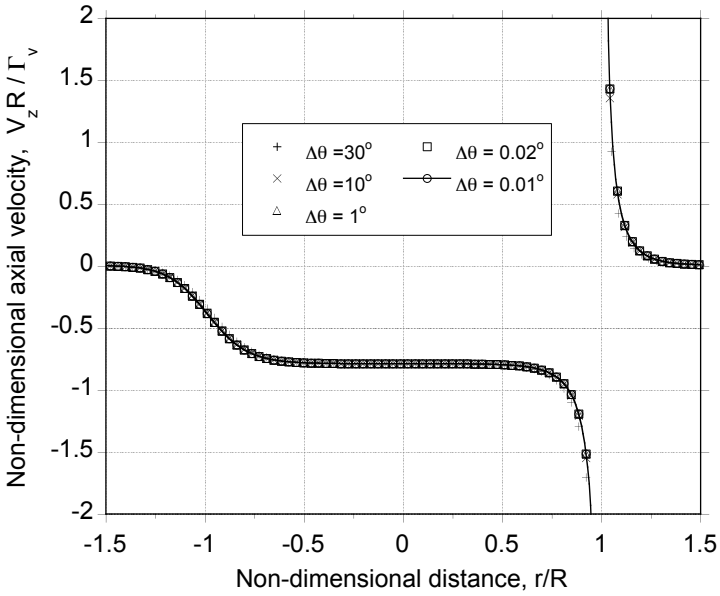

Figure 3.16: Induced velocity in the plane of a singly-infinite helical vortex with pitch $p = 0.1$ calculated using straight-line segmentation.

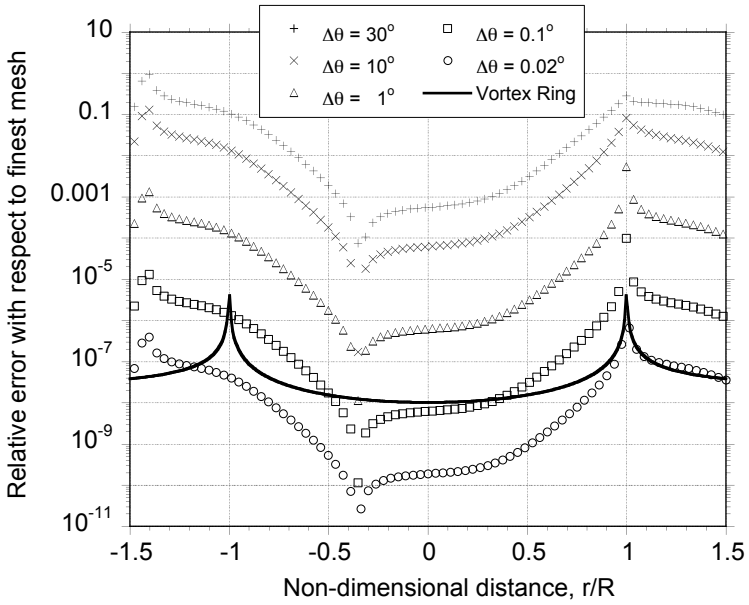

Figure 3.17: Error distribution in the induced velocity in the plane of a singly-infinite helical vortex ($p = 0.1$) with respect to the finest discretization. The error distribution for the case of vortex ring ($\Delta\theta = 0.02°$) is also shown.

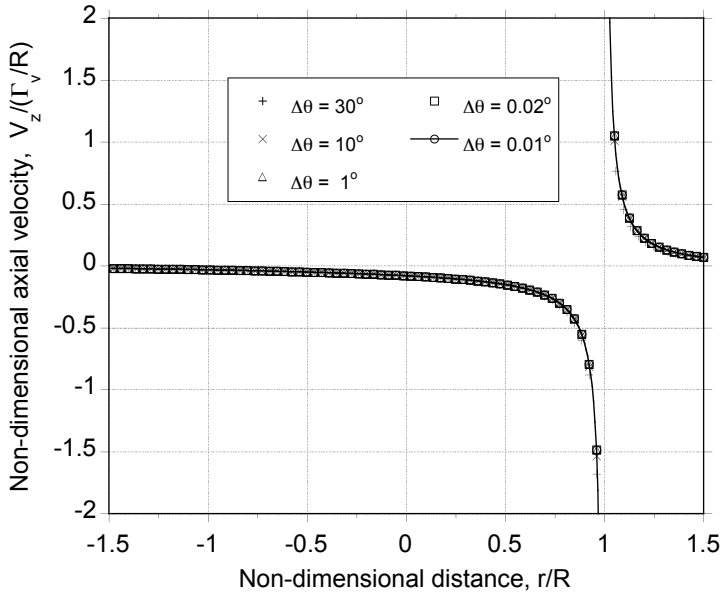

Figure 3.18: Induced velocity in the plane of a singly-infinite helical vortex with pitch $p = 1.0$ calculated using straight-line segmentation.

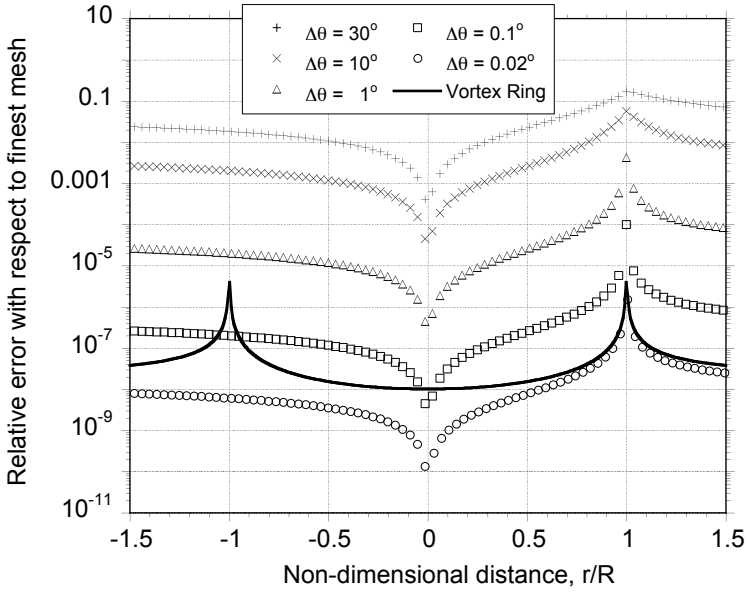

Figure 3.19: Error distribution in the induced velocity in the plane of a singly-infinite helical vortex ($p = 1.0$) with respect to the finest discretization. The error distribution for the case of vortex ring ($\Delta\theta = 0.02°$) is also shown.

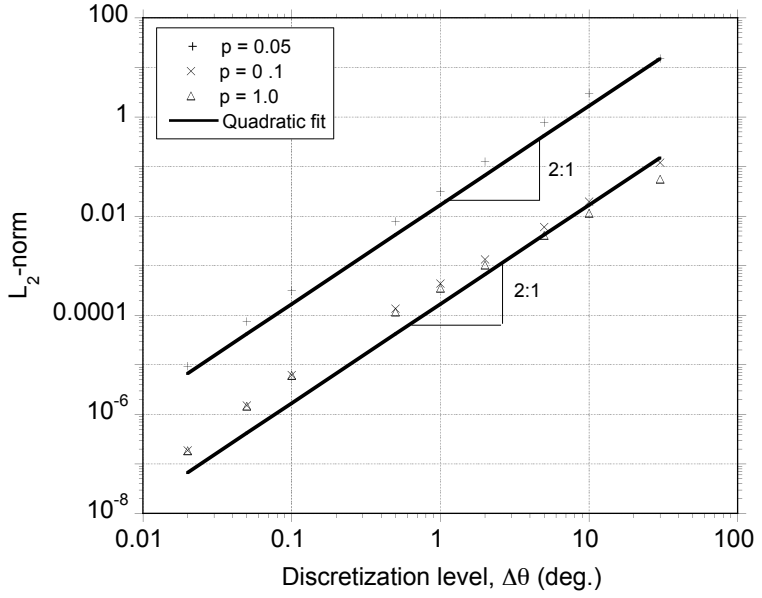

Figure 3.20: L_2-norm versus discretization level for various pitch values showing the convergence trend for the numerical scheme for the accuracy of induced velocity calculation by straight-line segmentation of doubly-infinite helical vortex.

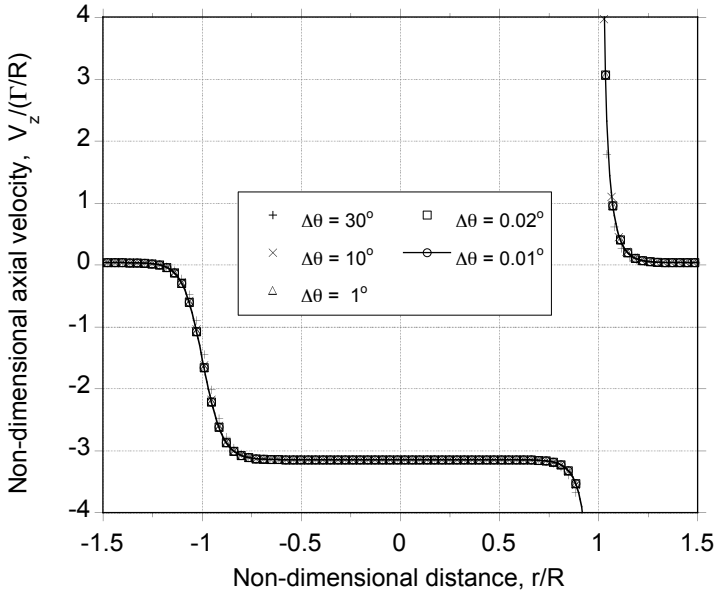

Figure 3.21: Induced velocity in the plane of a doubly-infinite helical vortex with pitch $p = 0.05$ calculated using straight-line segmentation.

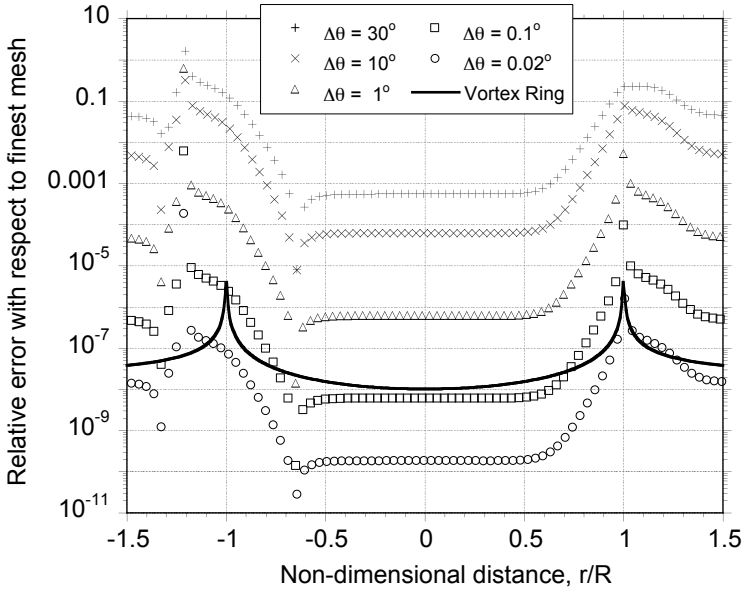

Figure 3.22: Error distribution in the induced velocity in the plane of a doubly-infinite helical vortex ($p = 0.05$) with respect to the finest discretization. The error distribution for the case of vortex ring ($\Delta\theta = 0.02°$) is also shown.

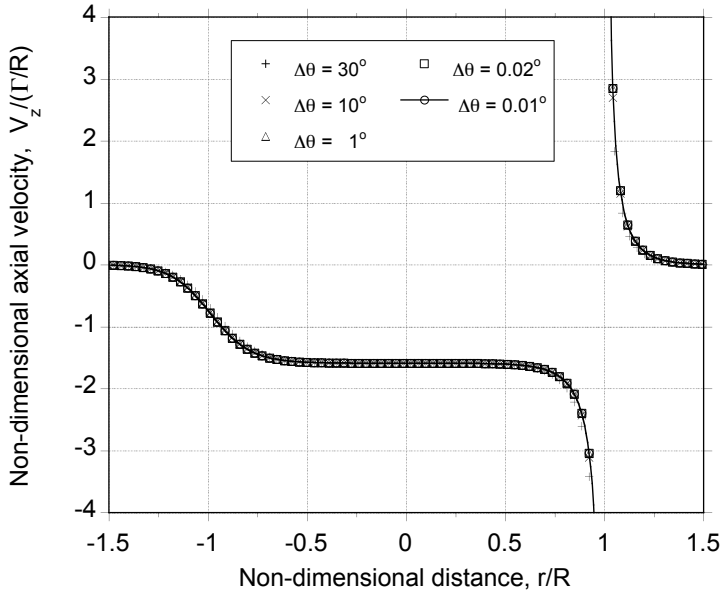

Figure 3.23: Induced velocity in the plane of a doubly-infinite helical vortex with pitch $p = 0.1$ calculated using straight-line segmentation.

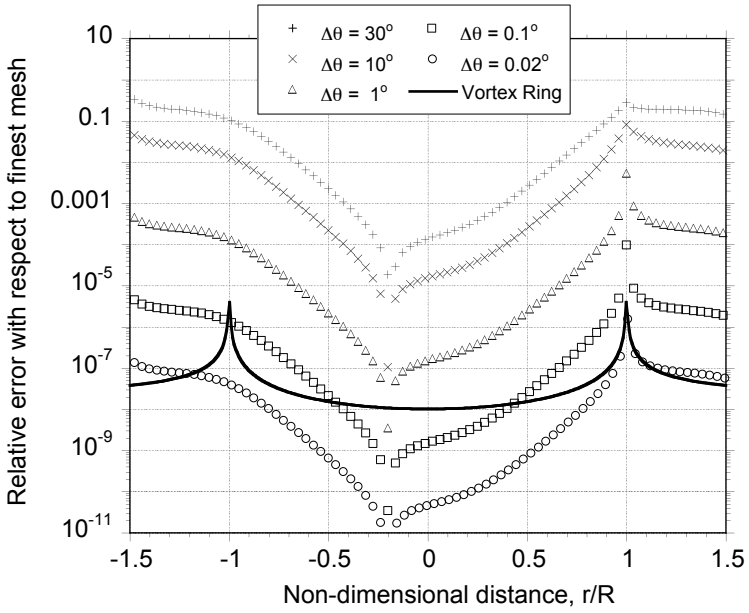

Figure 3.24: Error distribution in the induced velocity in the plane of a doubly-infinite helical vortex ($p = 0.1$) with respect to the finest discretization. Error distribution for the case of vortex ring ($\Delta\theta = 0.02°$) is also shown.

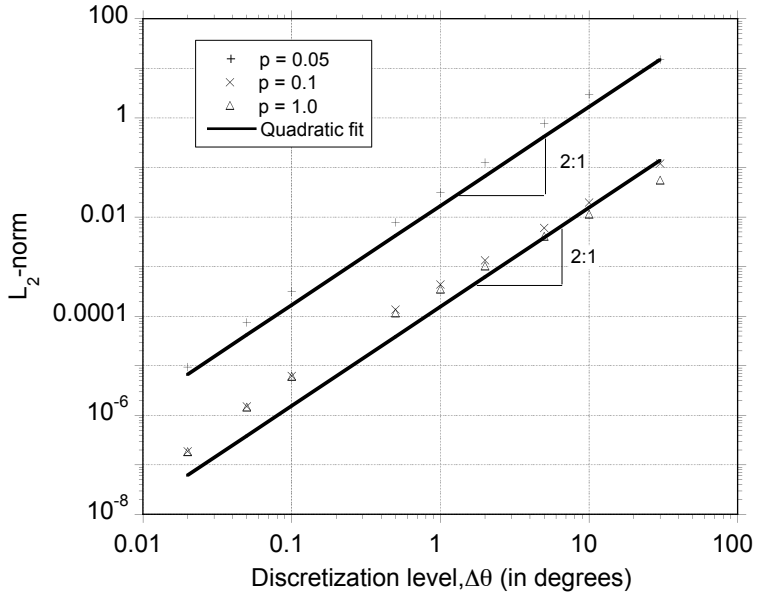

Figure 3.25: L_2-norm versus discretization level for various pitch values showing the convergence trend for the numerical scheme for the accuracy of induced velocity calculation by straight-line segmentation of doubly-infinite helical vortex.

3.1.4 Comparison of Results With Wood & Li

In this section, the accuracy of the reconstruction of the induced velocity field from a singly-infinite helical vortex using straight-line segmentation is considered. The approach follows the procedure of Wood & Li [131]. Three cases were considered. First case is the induced velocity on the axis of the helix at Point 1:$(x, y, z = 0, 0, 0)$, for which an analytic solution is available. The second case is the velocity at Point 2:$(x, y, z = 0, -1, 0)$ in Fig. 3.26, which is at the same radius as the vortex but displaced from the vortex by a distance $pR\pi$. Third case is the self-induced velocity at Point 3:$(x, y, z = 0, 1, 0)$.

The accuracy of the numerical scheme is analyzed locally at each point in [131]. An exact solution $U = p^{-1}$ is available for Point 1. For Points 2 and 3, a binormal velocity is available from the analysis performed in [132, 133], which was obtained using asymptotic expansions for small and large pitch. The results for the binormal velocity from Boersma & Wood [132, 133] are accurate up to six significant figures for all values of helical pitch. In this study, the binormal velocity is calculated numerically using the Biot–Savart law.

The error behavior with respect to the exact solution for Point 1, and binormal velocity given in Table 1 in Wood & Li [131] for Point 2, and Point 3 is compared with that of [131] for a wide range of helical pitch values. The binormal velocity, U_b, is calculated from the x and z direction velocities U and W using

$$U_b = \frac{U \pm pW}{(p^2 + 1)^{1/2}} \tag{3.4}$$

where pW is added for Point 2 and subtracted for Point 3. The components U and W are the sum of induced velocities contribution from each straight-line segment obtained by the Biot–Savart law.

In the first method, the singly-infinite helical vortex was approximated by a large number of helical turns (1000 turns), which is constant for different discretization levels. This is different than the procedure of Wood & Li, which will be analyzed

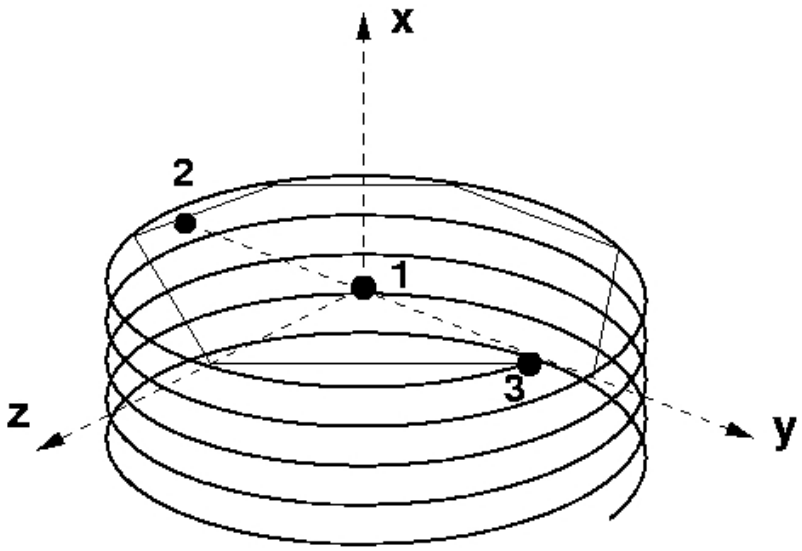

Figure 3.26: Schematic of a singly-infinite helical vortex discretized by straight-line segments, showing the three control points.

later in this section. The "analytic remainder", which approximates the remaining contribution from the infinite integral, is not calculated. According to Wood & Li [131], the analytic remainder, in any case, does not contribute significantly to the calculation of the induced velocities.

Figure 3.27 shows the absolute error plotted against discretization level for Point 1. This figure corresponds to Fig. 4 in Wood & Li [131]. The error for a particular value of helical pitch stays constant, and is not sensitive to the discretization level. The value of induced velocity is very close to the analytic result of $1/p$, even for very coarse discretization, and does not change with discretization level.

The variation of absolute error with discretization level for Point 2 is shown in Fig. 3.28. The thick solid line is a quadratic fit (M^{-2} fit), indicating that the accuracy of the induced velocity reconstruction for Point 2 is second-order, and does not change for large values of M. The increase in error, at large M for $p = 0.05$ and $p = 0.1$, as shown in [131], is not present here. Figure 3.29 shows the error variation for Point 3. A cutoff method proposed by Saffman [103], to exclude the logarithmic singularity, is used to obtain the induced velocity at this point. For small value of

helical pitch ($p = 0.01$ and $p = 0.05$), the absolute error decreases with increasing discretization level. For higher values of pitch, the absolute error increases with increasing values of M. This variation is consistent with the results in Fig. 6(a) in Wood & Li [131].

The second method proposed by Wood & Li [131], approximates the singly-infinite helical vortex with a finite number of number of turns, depending upon the number of divisions per revolution, M (or the discretization level) and the helical pitch, p, which is given by

$$N = \frac{5M}{\pi p} \tag{3.5}$$

An error analysis using this value of N was done for the three control points. As shown in Fig. 3.30 and Fig. 3.31, this approach gives a second-order trend for the variation of error in Point 1 and Point 2. Results for small helical pitch ($p = 0.01$ and $p = 0.05$) are not included because of the large number of turns required according to the results given by Eq. 3.5, yet Fig. 3.30 shows very good agreement with Fig. 4 of [131]. The dashed line shows a M^{-2} fit, indicating second-order accuracy. The solid line shows the variation of error for a vortex ring with discretization level, and the magnitude of the error for Point 1 is always more than the helical vortex with finite pitch.

From Fig. 3.27 and Fig. 3.30, it is clear that the second-order error trend seen in the second approach is a result of the small number of turns used for small M, pushing up the error. Consider the case for $p = 0.1$. When using 1000 turns, the error at $M = 10$ is $1e^{-5}$, whereas in the second approach, number of turns used is 16, and the magnitude of the error is $1e^{-3}$. For larger M, the magnitude of the error is smaller in the second approach because of a large number of turns used. For Point 2 (Fig. 3.31), the error variation is second-order, as indicated by a quadratic fit. The increase in the accuracy for large values of M, as reported in Ref. 131 is not seen here. Figure 3.32 shows the error behavior for Point 3, which is very similar to the results of Fig. 6(b) in Ref. 131.

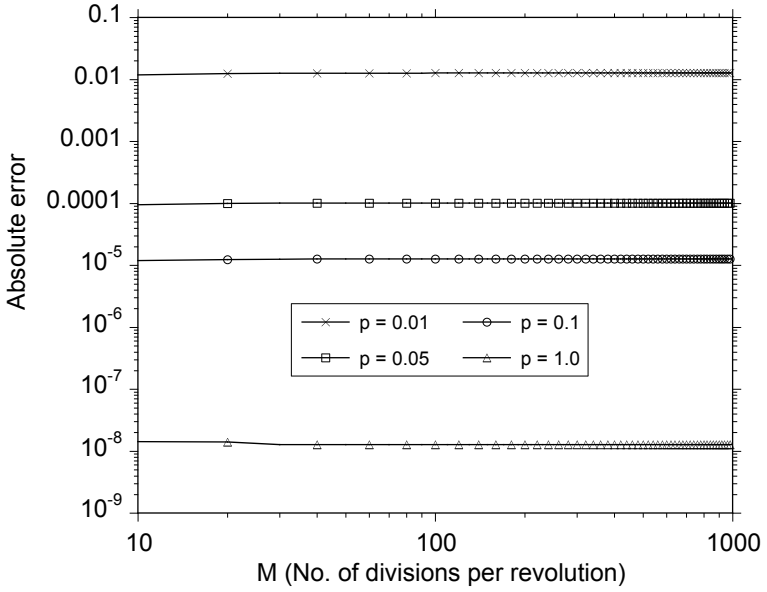

Figure 3.27: Absolute error in the induced velocity for Case 1 with respect to the exact solution $(1/p)$ for a singly-infinite helical vortex.

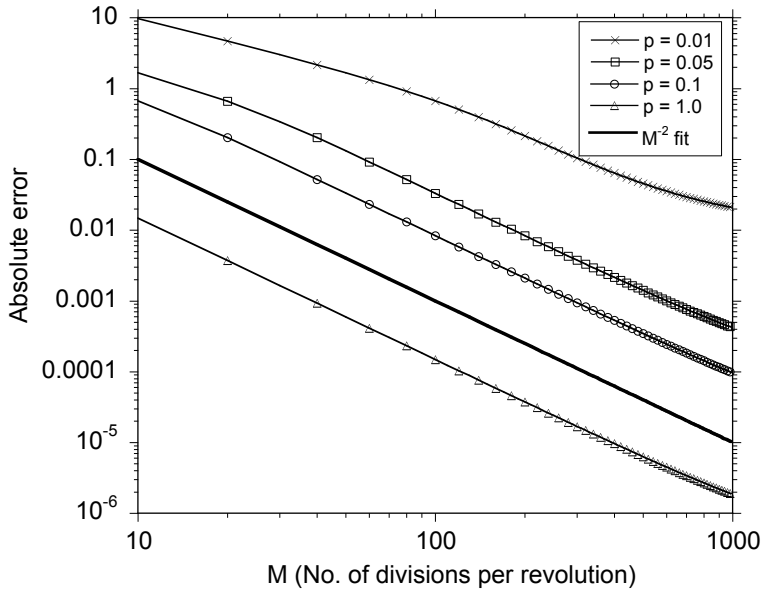

Figure 3.28: Absolute error in the induced velocity for Case 2 with respect to the numerical solution of binormal velocity U_b given in Table 1 of Ref. 131.

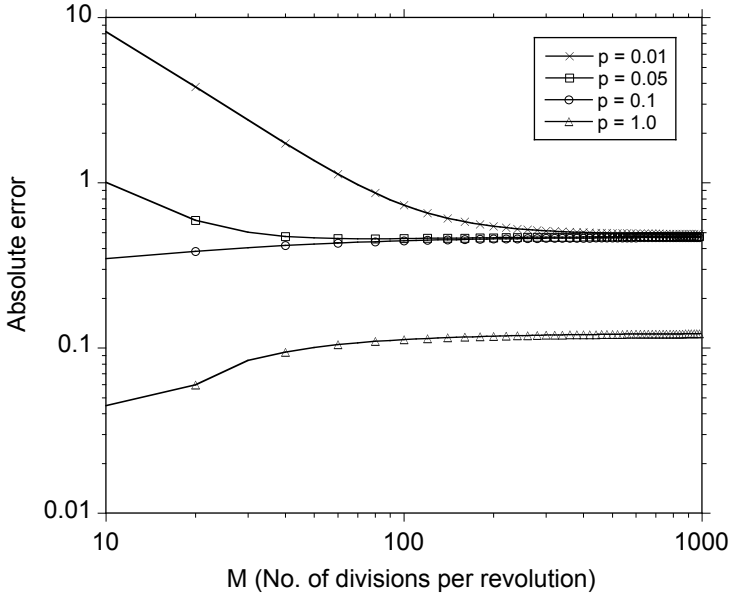

Figure 3.29: Absolute error in the induced velocity for Case 3 with respect to the numerical solution of binormal velocity U_b given in Table 1 of Ref. 131.

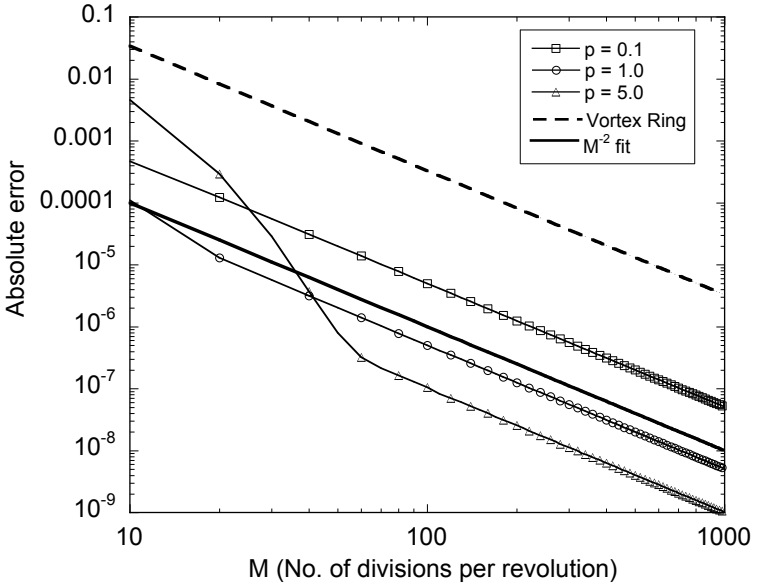

Figure 3.30: Absolute error in the induced velocity for Case 1 with respect to the exact solution $(1/p)$ for a singly-infinite helical vortex and number of turns given by Eq. 3.5.

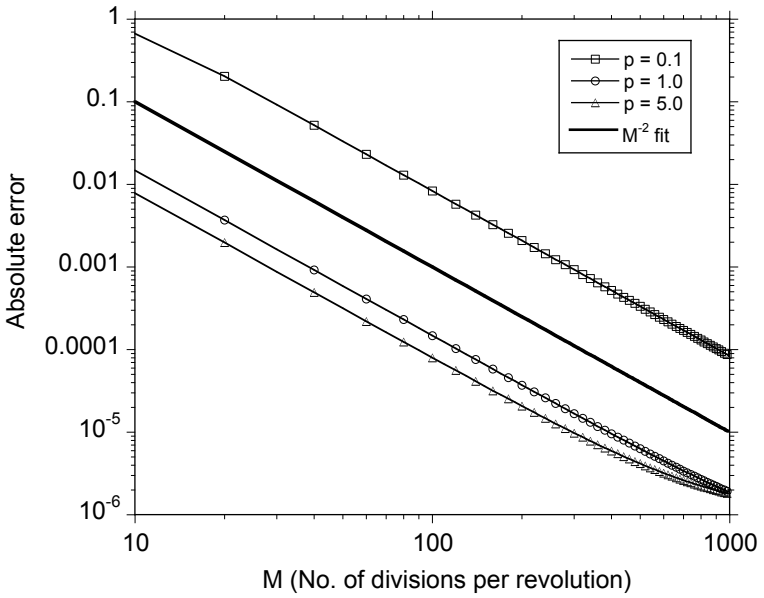

Figure 3.31: Absolute error in the induced velocity for Case 2 with respect to the numerical solution of binormal velocity U_b given in Table 1 of Ref. 131 and number of turns given by Eq. 3.5.

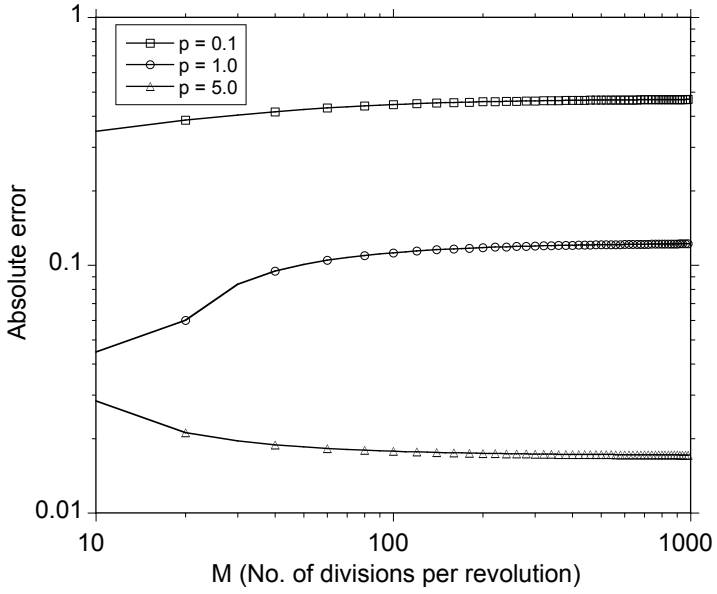

Figure 3.32: Absolute error in the induced velocity for Case 3 with respect to the numerical solution of binormal velocity U_b given in Table 1 of Ref. 131 and number of turns given by Eq. 3.5.

3.1.5 Accuracy of Induced Velocity Field for a Skewed Helix

The wake of a wind turbine in yawed operation resembles that of a skewed helical vortex. It is, therefore, important to understand the accuracy of the reconstruction of induced velocity of a skewed helical vortex using straight-line segmentation. In this section, the accuracy of this approach is studied, and the error behavior is compared with the unskewed case. In Section 3.1.3, it was seen that the behavior of singly-infinite and doubly-infinite unskewed helical vortex is very similar. Therefore, in this section only a singly-infinite skewed helical vortex will be analyzed.

Figure 3.33 shows a schematic of a skewed helical vortex, which is skewed along the x-axis. As in the unskewed case, using straight-line segmentation to discretize the vortex, the induced velocities are calculated in the $z = 0$ plane as the sum of the contribution from each vortex segment. Errors in the calculation of the induced velocity for each discretization level are calculated with respect to the induced velocity for the finest level of discretization ($\Delta\theta = 0.01°$).

Figure 3.34 shows the induced velocity for a helical pitch of $p = 0.05$ (which is typical of wind turbine wakes) for different skew angles. Figure 3.35 shows the distribution of the relative error across the disk plane for different skew angles. The induced velocity near $x = -1.2$ for the unskewed case is close to zero (see Section 3.1.3), which causes an increase in the magnitude of the error. The distribution of absolute error across the $z = 0$ plane is shown in Figure 3.36. Notice that the peak near $x = -1.2$ vanishes in this case, and the maximum error is found at the singularity ($\vec{r} = 1.0$), which is the same for the skewed and unskewed case. There are some additional minima in the skewed case which are a result of the cancellation of errors from adjacent turns of the helix.

Figure 3.37 shows the convergence trend (L_2-norm calculated from the relative error). The unskewed case has relatively higher errors because of the reasons stated above. The L_2-norm for the absolute error is plotted in Fig. 3.38, and the the values are similar for the skewed and unskewed case. A quadratic fit for both cases,

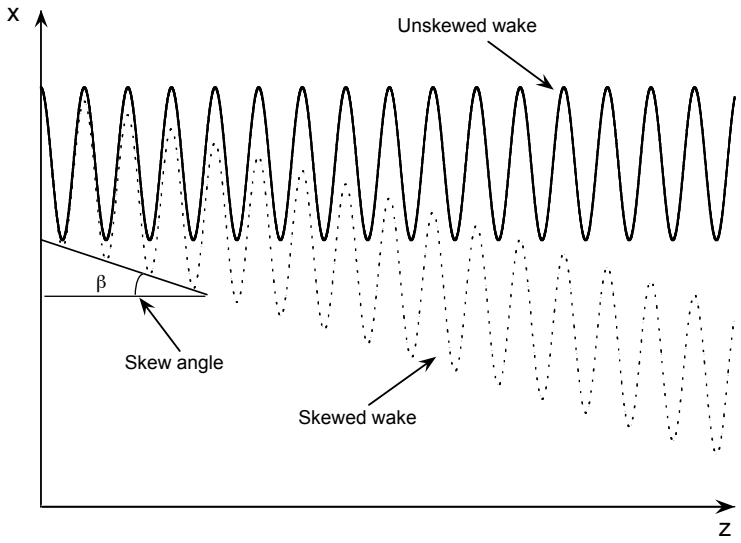

Figure 3.33: A schematic of a singly-infinite skewed helical vortex. The helical pitch of the vortex is $p = 1.0$ and the skew angle is 30° along the x-axis.

indicates the second-order accuracy of the straight-line approximation.

The free wake models used in practice normally use an azimuthal discretization of between 5° and 20° for efficiency considerations. This is because to convect and track a large number of vortex filaments is not computationally practical. Figures 3.39 and 3.40 show the relative errors in the calculation of induced velocity, for a practical range of azimuthal discretization of a singly-infinite helical vortex ($p = 0.05,\ \beta = 30°$). The errors were calculated with respect to a discretization of $\Delta\theta = 0.01°$. Figure 3.39 shows that at least a 10° discretization is required to keep the magnitude of the maximum error below 10%. An azimuthal discretization of less than 2.5° is required to keep maximum error less than 1%. The order of accuracy of straight-line segmentation is less than two for most practical values of $\Delta\theta$ (Fig. 3.40), and it is only for $\Delta\theta < 5°$ that a second-order accuracy is achieved.

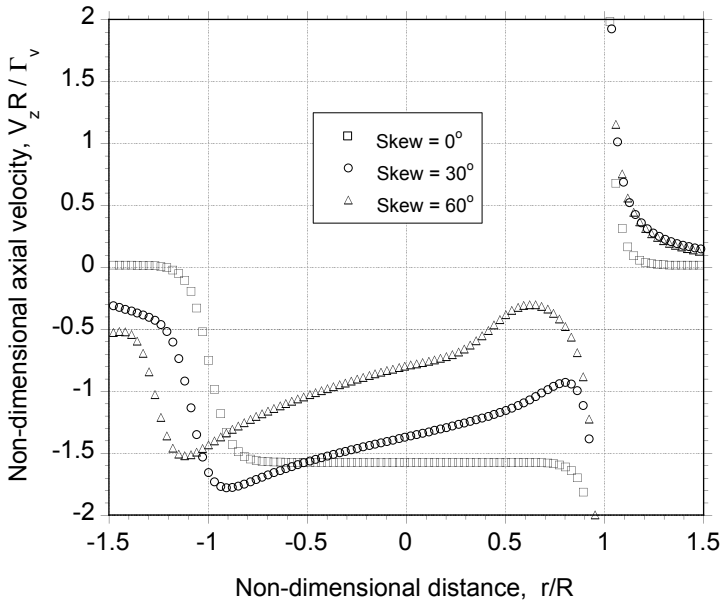

Figure 3.34: Non-dimensional induced axial velocity in the $z = 0$ plane of a skewed helical vortex with pitch $p = 0.05$ and skew angle $\beta = 0°$, $\beta = 30°$ and $\beta = 60°$.

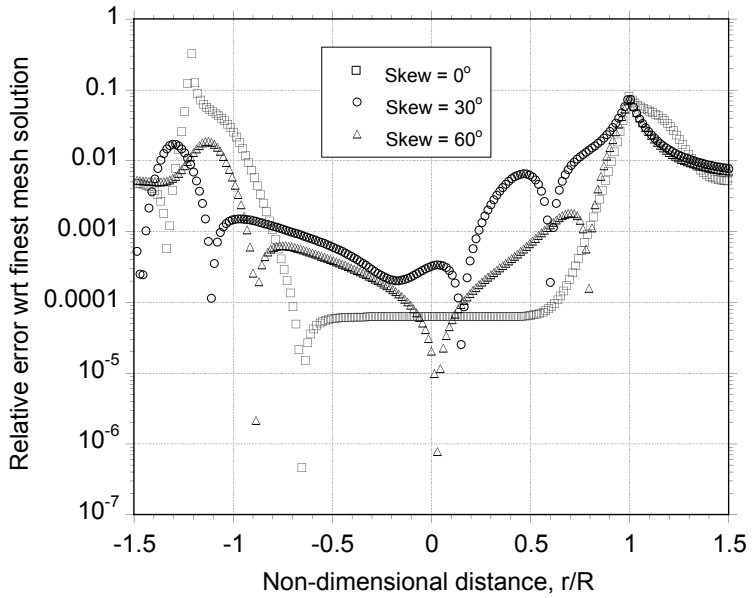

Figure 3.35: Relative error in the induced axial velocity in the $z = 0$ plane of a skewed helical vortex with pitch $p = 0.05$ and skew angle $\beta = 0°$, $\beta = 30°$ and $\beta = 60°$.

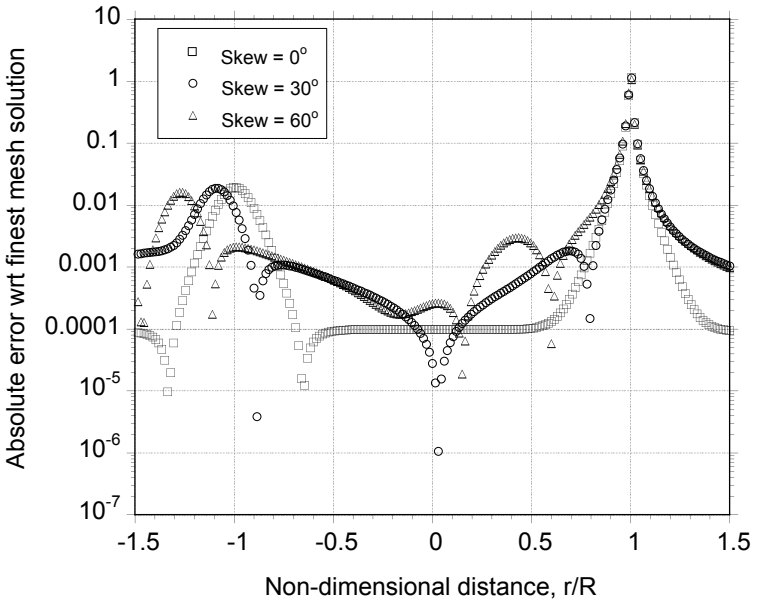

Figure 3.36: Absolute error in the induced axial velocity in the $z = 0$ plane of a skewed helical vortex with pitch $p = 0.05$ and skew angle $\beta = 0°$, $\beta = 30°$ and $\beta = 60°$.

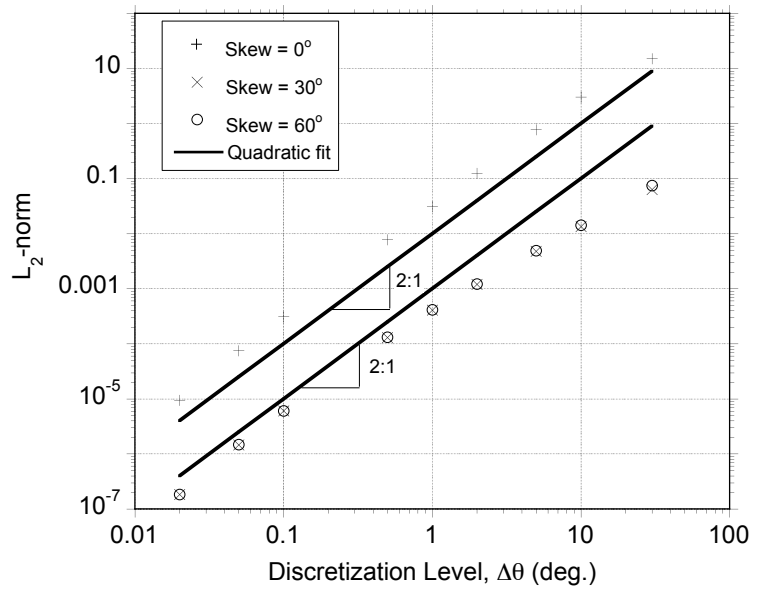

Figure 3.37: L_2-norm for the relative error in the induced axial velocity in the $z = 0$ plane of a skewed helical vortex with pitch $p = 0.05$ and skew angle $\beta = 0°$, $\beta = 30°$ and $\beta = 60°$.

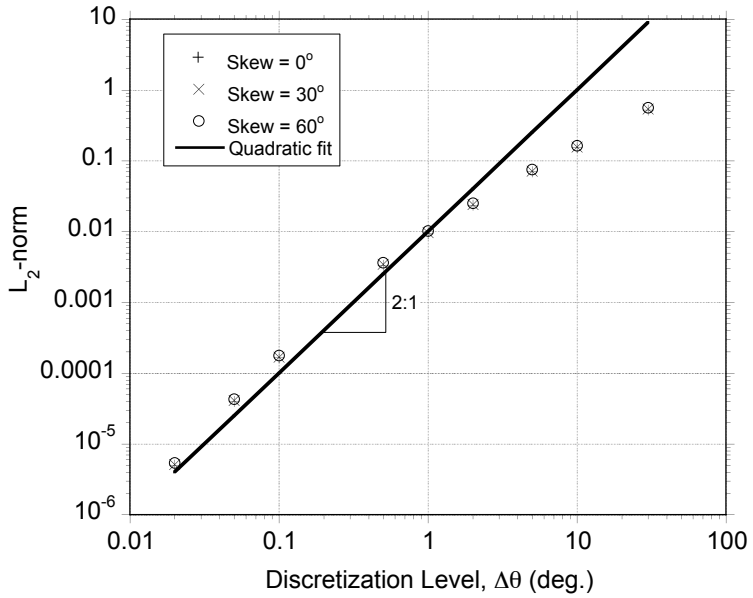

Figure 3.38: L_2-norm for the absolute error in the induced axial velocity in the $z = 0$ plane of a skewed helical vortex with pitch $p = 0.05$ and skew angle $\beta = 0°$, $\beta = 30°$ and $\beta = 60°$.

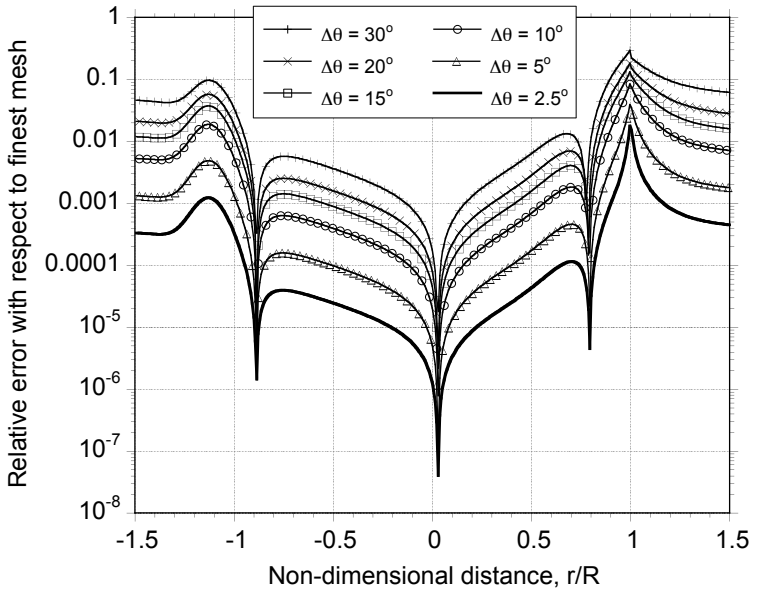

Figure 3.39: Relative error distribution in the induced axial velocity in the $z = 0$ plane of a skewed helical vortex with pitch, $p = 0.05$, and skew angle, $\beta = 30°$ for practical values of $\Delta\theta$.

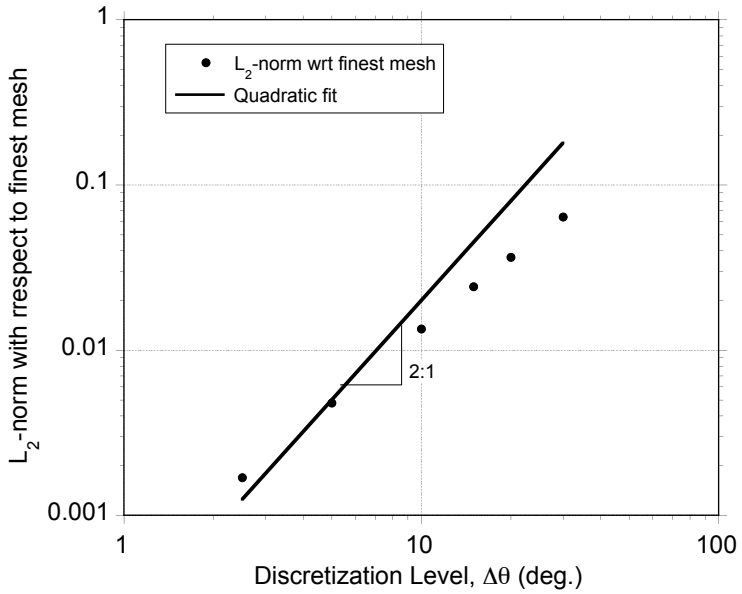

Figure 3.40: Convergence trend for straight-line segmentation of a skewed helical vortex with pitch $p = 0.05$ and skew angle $\beta = 30°$ for practical values of $\Delta\theta$.

3.2 Stability of Time-Marching Scheme

Time marching free-vortex wake methods track the discretized wake filaments to force-free locations in a time-accurate manner. The time-marching free-vortex wake methods are more flexible in representing the unsteady operating environment encountered by wind turbines.

This section examines the stability and accuracy of the numerical methods that can be used to solve the free-vortex wake problem for a wind turbine. This approach is used to quantify the source of potential numerical errors, and to ultimately help identify sources of discrepancies between numerical results and experimental measurements of turbine loads and performance. Both a linear and nonlinear stability analysis of the various methods has been conducted. Numerical convergence can be ensured by requiring that the discretized equations be (linearly) stable and also consistent with the governing equations. Yet, these two criteria alone may not guarantee convergence. It is further shown that the equations governing the behav-

ior of the turbine wake are highly nonlinear because of the induced velocities in the wake, which can affect the stability of the scheme. The optimum choice of numerical integration method is not an obvious one.

3.2.1 Linear Stability Analysis

The linear stability of the time-marching scheme has been studied using the method of representative equations [134]. Consider the first-order representative differential equation defined by

$$\frac{du}{dt} = \lambda u + ae^{\mu t} \tag{3.6}$$

The exact solution to Eq. 3.6 is given by

$$u(t) = u(0)e^{\lambda t} + a\left(\frac{e^{\mu t} - e^{\lambda t}}{\mu - \lambda}\right) \tag{3.7}$$

Applying various time-marching schemes to the representative equation in Eq. 3.7, a linear ordinary differential equation (ODE) can be converted to a linear ordinary difference equation (OΔE). The use of an Euler explicit time-marching method gives

$$u_{n+1} = u_n + hu'_n \tag{3.8}$$

where h is the time step. Applying this to the representative equation gives

$$P(\sigma) = Q(\sigma)ae^{\mu hn} \tag{3.9}$$

where $P(\sigma)$ is known as the characteristic polynomial. The values of σ are the roots of this polynomial, and their magnitudes determine the stability of the method. For numerical stability, the criterion that

$$|\sigma(\lambda = i\omega h)| \leq 1 \tag{3.10}$$

must be met, where ω is the spatial wave number. For the Euler explicit time-marching method, the characteristic polynomial is

$$P(\sigma) = \sigma - 1 - \lambda h \tag{3.11}$$

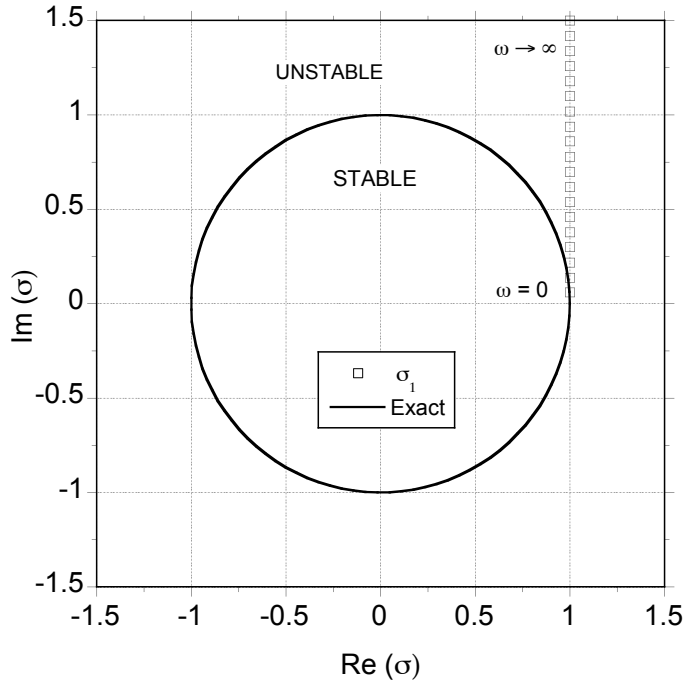

Figure 3.41: The eigenvalues for the Euler explicit method in the complex σ plane.

In this case, it gives the single (principal) eigenvalue as

$$\sigma_1 \;=\; 1 + \lambda h \tag{3.12}$$

which is $\mathcal{O}(h)$ and confirms that this scheme is only first-order accurate. The linear stability criterion requires that $|\sigma| < 1$, which implies that the eigenvalues for $\lambda = i\omega h$ must lie within the unit circle in the complex σ plane. Figure 3.41 shows the principal eigenvalue for the Euler explicit method, and this method is always unstable for all values of ωh. This means that based on this simple linear analysis, the Euler explicit method would always be an inappropriate choice for the integration of the wake equations.

Various other time-marching schemes have been proposed and used in free-vortex wake methods. Bhagwat & Leishman [112] have used a Predictor-Corrector Central (PCC) and a Predictor-Corrector second-order Backward (PC2B) scheme. A fourth-order Adams–Moulton method was used by Kini & Conlisk. [81]. A second-

order Adams–Bashforth method has also been analyzed in this study. For predictor-corrector and multi-step methods, multiple eigenvalues exist. One of the eigenvalues is the principal eigenvalue, and this dictates the accuracy of the numerical method. The other eigenvalues are called spurious roots. These do not affect the accuracy of the numerical scheme but may affect the overall stability of the time-marching method.

Applying Bhagwat & Leishman's PCC difference algorithm to the representative equation (Eq. 3.6) gives

$$\begin{aligned} \tilde{u}_{n+1} &= u_n + \frac{1}{2}\lambda h(\tilde{u}_{n+1} + u_n) + \frac{1}{2}ahe^{\mu hn} \\ u_{n+1} &= u_n + \frac{1}{2}\lambda h(u_{n+1} + u_n) + \frac{1}{2}ah\left(e^{\mu hn} + e^{\mu h\widetilde{(n+1)}}\right) \end{aligned} \tag{3.13}$$

The characteristic polynomial in this case is given by

$$P(\sigma) = (1 - \frac{1}{2}\lambda h)\sigma - (1 + \frac{1}{2}\lambda h) \tag{3.14}$$

and the principal eigenvalue by

$$\sigma_1 = \frac{1 - \frac{1}{2}\lambda h}{1 + \frac{1}{2}\lambda h} = 1 + \lambda h + \frac{1}{2}\lambda^2 h^2 + \cdots \tag{3.15}$$

The $\mathcal{O}(h^2)$ term in this latter equation indicates that the PCC algorithm is second-order accurate. The second eigenvalue, which in this case is zero, is the spurious root. Figure 3.42 shows the eigenvalues for the PCC scheme in the complex σ plane. Notice that the principal eigenvalue follows the exact solution, whereas the second eigenvalue is zero. This result shows that the PCC method is neutrally stable for all values of ωh.

Bhagwat & Leishman's PC2B method uses backward differencing with three previous time steps. This scheme adds additional effective damping, making it more stable whilst retaining the second-order accuracy. In this case, the PC2B scheme applied to the representative equation (Eq. 3.6) gives

$$\begin{aligned} \tilde{u}_{n+1} &= u_n + \frac{1}{2}\lambda h(\tilde{u}_{n+1} + u_n) + \frac{1}{2}ahe^{\mu hn} \\ 3u_{n+1} &= u_n + 3u_{n-1} - u_{n-2} + 2\lambda h(u_{n+1} + u_n)2ah\left(e^{\mu hn} + e^{\mu h\widetilde{(n+1)}}\right) \end{aligned} \tag{3.16}$$

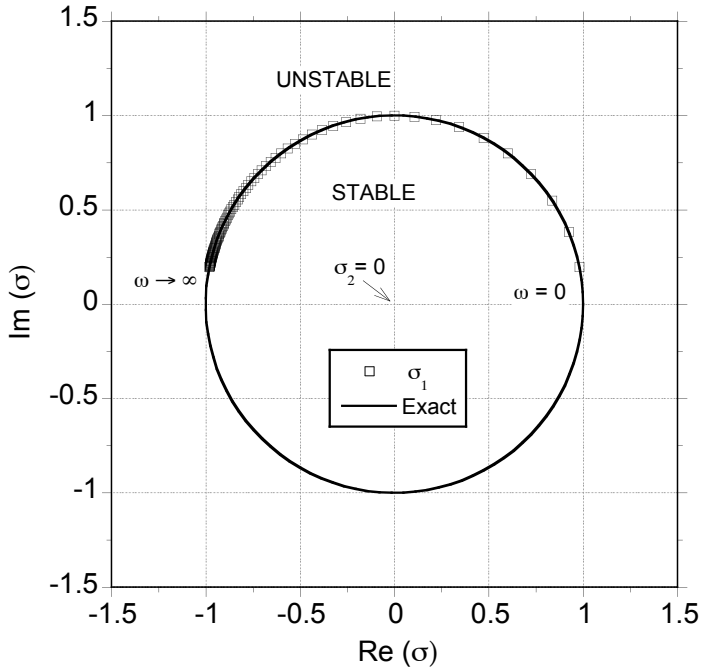

Figure 3.42: The eigenvalues for the PCC scheme in the complex σ plane.

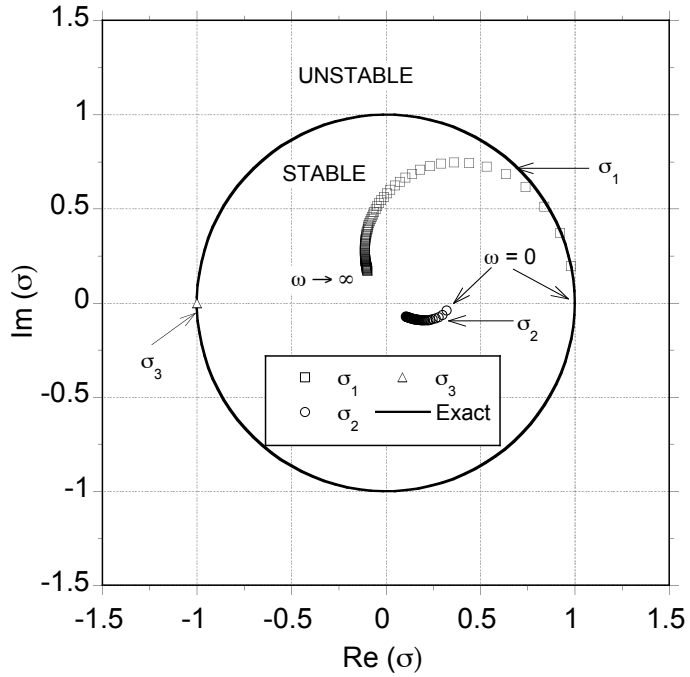

Figure 3.43: The eigenvalues for PC2B scheme in the complex σ plane.

Notice that like the PCC scheme, this scheme is more expensive because it uses two velocity field evaluations per time step. The characteristic polynomial for the PC2B scheme is

$$(3 - 2\lambda h)\sigma^3 - (1 + 2\lambda h)\sigma^2 - 3\sigma + 1 = 0 \tag{3.17}$$

The PC2B scheme uses three time steps in the integration algorithm, so there are three eigenvalues. These are given by

$$\begin{aligned} \sigma_1 &= 1 + \lambda h + \frac{1}{2}\lambda^2 h^2 + \frac{1}{2}\lambda^3 h^3 + \cdots \\ \sigma_2 &= \frac{1}{3} - \frac{1}{9}\lambda h + \frac{5}{54}\lambda^2 h^2 + \frac{17}{162}\lambda^3 h^3 + \cdots \\ \sigma_3 &= -1 \end{aligned} \tag{3.18}$$

Figure 3.43 shows the eigenvalues for the PC2B scheme. The principal eigenvalue follows the exact solution for smaller values of ωh and deviates from it only at higher values because of implicit dissipation in the scheme. In particular, notice that the PC2B scheme is stable for all values of ωh.

Generalized Adams–Bashforth type schemes for the time-marching solutions can be written in the form

$$u^{n+1} = u^n + \Delta t \left(\alpha u'^n + \beta u'^{n-1} + \gamma u'^{n-2} \right) \tag{3.19}$$

where α, β and γ are constants. By developing a Taylor series expansion and imposing a second-order accuracy requirement, the above equation reduces to a one parameter family of AB2 schemes as given by

$$u^{n+1} = u^n + \Delta t \Big(\alpha(u'^n - 2u'^{n-1} + u'^{n-2}) + (5u'^{n-1} - 3u'^{n-2})/2 \Big) \tag{3.20}$$

Applying this scheme to the representative equation (Eq. 3.6) gives

$$\begin{aligned} u^{n+1} &= u^n + h \left(\alpha(\lambda u^n + a e^{\mu h n} - 2(\lambda u^{n-1} + a e^{\mu h (n-1)}) + \lambda u^{n-2} + a e^{\mu h (n-2)}) \right. \\ &+ \left. (5(\lambda u^{n-1} + a e^{\mu h (n-1)} - 3(\lambda u^{n-2} + a e^{\mu h (n-2)})/2 \right) \end{aligned} \tag{3.21}$$

In particular, the characteristic polynomial for the case of $\alpha = 1.5$ is given by

$$P(\sigma) = \sigma^3 - \sigma^2(1 + \frac{3}{2}\lambda h) + \frac{\sigma}{2}\lambda h \tag{3.22}$$

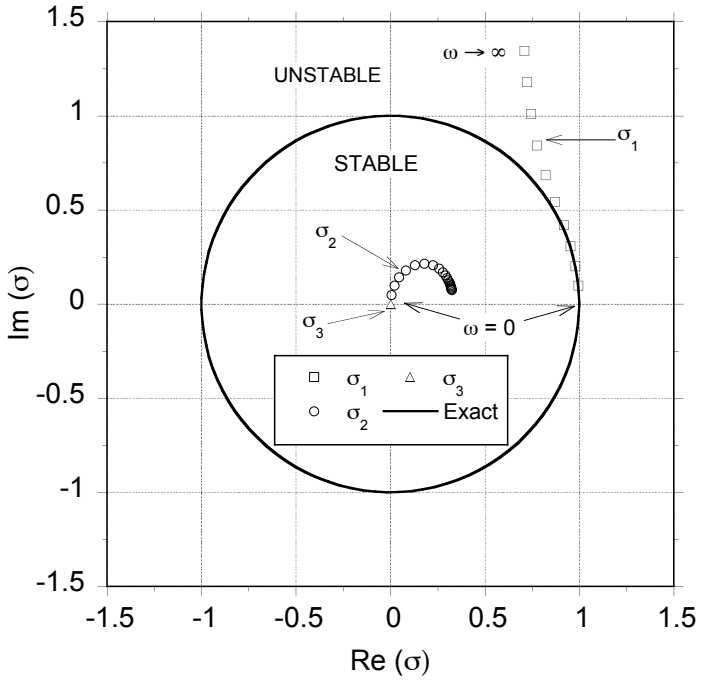

Figure 3.44: The eigenvalues for one-parameter, second-order Adams–Bashforth family of time-marching methods with $\alpha = 1.5$.

The roots of Eq. 3.22 can be obtained analytically. Figure 3.44 shows the variation of the eigenvalues with ωh for $\alpha = 1.5$. The principal eigenvalue falls outside the unit circle for all values of ωh, and so the scheme is unstable. The spurious eigenvalue stays within the unit circle.

The Adams–Moulton scheme is implicit, and so computationally very expensive. The fourth-order accurate Adams–Moulton (AM4) scheme can be written as

$$u_{n+1} = u_n + h\left(\frac{9}{24}u'_{n+1} + \frac{19}{24}u'_n - \frac{5}{24}u'_{n-1} + \frac{1}{24}u'_{n-2}\right) \tag{3.23}$$

Applying this scheme to the representative equation (3.6) gives

$$\begin{aligned} u^{n+1} &= u^n + h\left(\frac{9}{24}(\lambda u^{n+1} + ae^{\mu h(n+1)}) + \frac{19}{24}(\lambda u^n + ae^{\mu hn})\right. \\ &- \left.\frac{5}{24}(\lambda u^{n-1} + ae^{\mu h(n-1)}) + \frac{1}{24}(\lambda u^{n-2} + ae^{\mu h(n-2)})\right) \end{aligned} \tag{3.24}$$

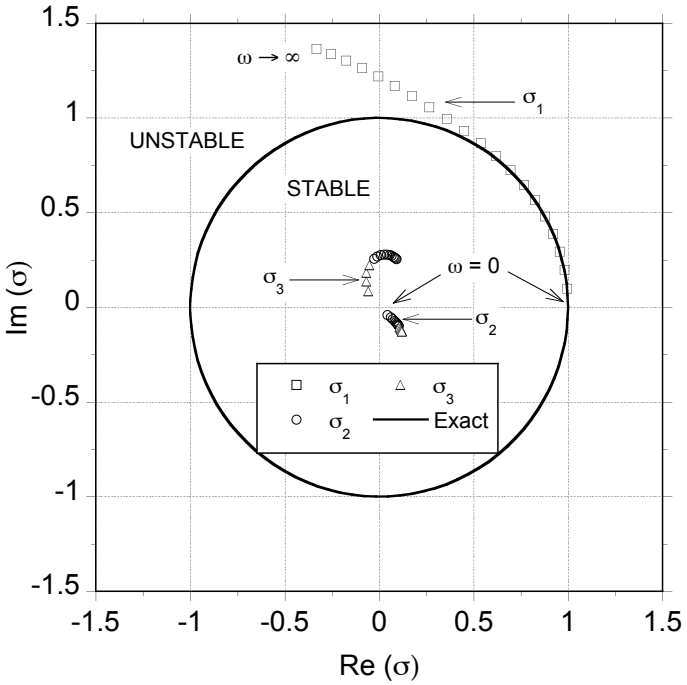

Figure 3.45: The eigenvalues for fourth-order Adams–Moulton method.

The characteristic equation in this case is given by

$$P(\sigma) \;=\; (1-\frac{9}{24}\lambda h)\sigma^3 - (1+\frac{19}{24}\lambda h)\sigma^2 + \frac{5}{24}\lambda h\sigma - \frac{\lambda h}{24} \tag{3.25}$$

The roots of this equation are plotted in Fig. 3.45. Notice that the principal eigenvalue follows the exact solution for smaller values of ωh. The spurious roots always stay within the unit circle. In this case the scheme is only stable for $\omega h < 0.7$.

Figure 3.46 shows a summary of the variations of the magnitude of the principal eigenvalue for all the previously considered schemes. When $|\sigma| = 1$, the exact amplitude of the solution is recovered. If the magnitude of the principal eigenvalue is smaller than unity then the scheme is stable, otherwise the scheme is unstable. It can be seen that the PC2B scheme is stable for all values of ωh, whereas the Adams–Bashforth (AB2) and the Euler explicit schemes are unstable. The PCC scheme is neutrally stable.

Figure 3.47 shows the corresponding variation of the phase errors introduced

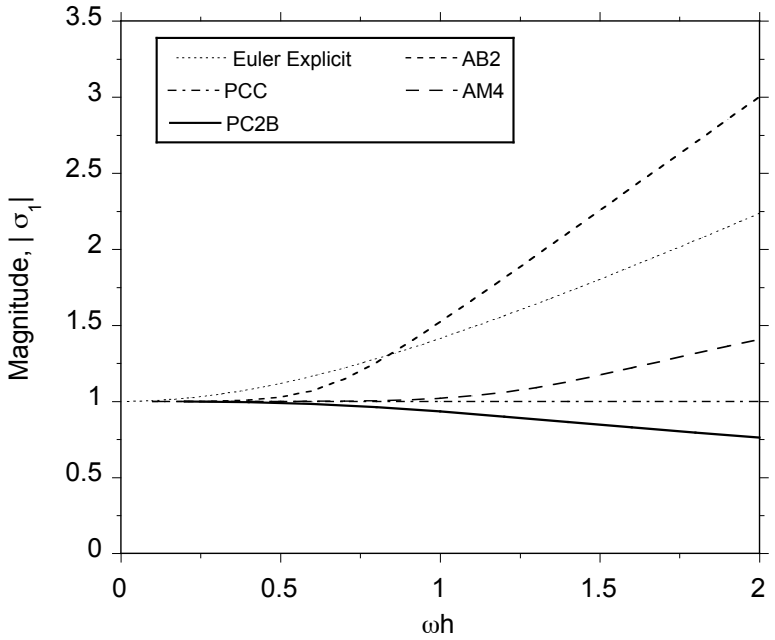

Figure 3.46: Variation of the magnitude of the principal eigenvalue with ωh for various time-marching methods.

with the various time-marching methods. The phase error is defined as

$$\epsilon_p = \omega h - \tan^{-1}\left[(\sigma_1)_{Im}/(\sigma_1)_{Re}\right] \tag{3.26}$$

where σ_1 is the principal eigenvalue. A positive value of the phase error ϵ_p corresponds to a phase lag, while a negative value corresponds to a phase lead. It can be seen from Fig. 3.47 that ϵ_p is a maximum for the Euler explicit scheme, and the AM4 method has the lowest phase error. For small values of ωh, both the PCC and PC2B schemes give comparable phase lags, whereas for higher values of ωh, the PCC scheme is better. Notice that the phase error for the second-order AB2 scheme changes from a phase-lead to a phase-lag, which thereafter increases rapidly with increasing ωh. From a linear stability point of view, the AM4 scheme seems to be the best scheme. However, it is an implicit scheme and, therefore, computationally expensive for a free-vortex wake analysis.

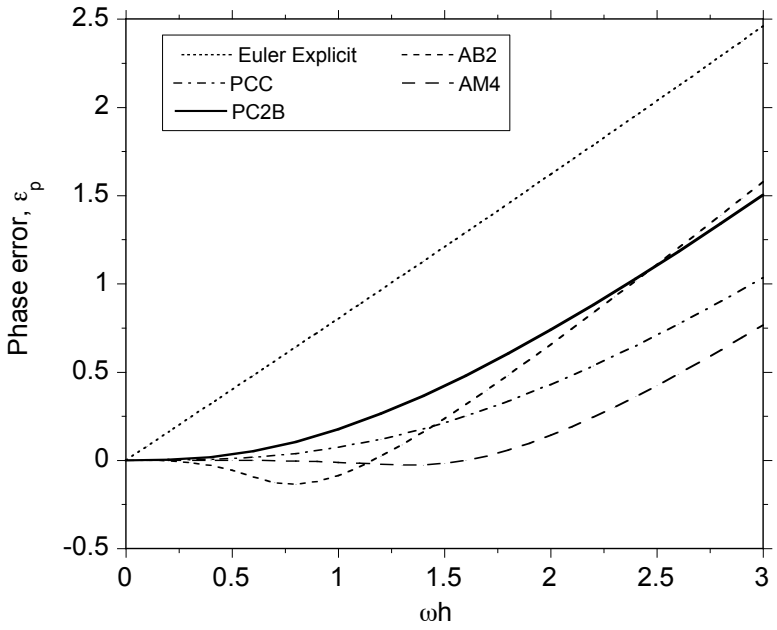

Figure 3.47: Variation of the phase error with ωh for various time-marching methods.

3.2.2 Nonlinear Stability Analysis

Linear stability of the scheme is a necessary but an insufficient condition for nonlinear problems. A linear analysis gives an upper bound for the time step size that can be used with different time-marching methods, and a quantification of the associated amplitude and phase errors. The governing equation of the wake dynamics involves the highly nonlinear velocity term, $\mathbf{V}$, which also must affect the stability of the overall time-marching scheme [112]. Therefore, a more detailed nonlinear stability analysis of the various schemes is required.

Two approaches are used to study the nonlinear stability characteristics: 1. The modified equation approach. 2. A direct examination of numerical convergence. The modified equation is the equation resulting from the discretization and averaging of all the terms in the governing equation. A modified equation can be used to help better understand the influence of any nonlinearities. The second approach is based on the philosophy used in traditional CFD analyses, in that a numerical

scheme is stable if the errors start out small and then remain small with increasing time. Linear stability requires that the numerical errors be properly bounded. For linear equations this is synonymous to the behavior being convergent. For nonlinear equations, the solution may exhibit spurious oscillations, although these may still be bounded. However, the solution may not be convergent because, although bounded for a given discretization, it may also depend on the grid discretization itself.

3.2.3 Modified Equation Approach

The modified equations are the equations obtained after discretizing and averaging all the terms in the original governing equations. The numerical method approximately solves the original governing equation but exactly solves the modified equation. Therefore, the modified equations provide key insight into the nonlinear behavior of the numerical solution.

As previously shown, the governing equation for the convection of the wake markers can be written as

$$\frac{\partial \mathbf{r}}{\partial \psi} + \frac{\partial \mathbf{r}}{\partial \zeta} = \mathbf{V}(\mathbf{r}) \tag{3.27}$$

where Ω has now been absorbed in the velocity term. The modified equations are obtained by discretizing Eq. 3.27 (see Fig. 3.48) and taking all extra terms to the right-hand side except those in the governing equation, and expressing them in terms of the spatial derivative of the solution. In the following analysis, equal discretization ($\Delta\psi = \Delta\zeta$) is assumed, and only terms up to $\mathcal{O}(\Delta\zeta^2)$ are shown for conciseness.

Euler Explicit Scheme

Dropping the vector notation for simplicity, the Euler explicit scheme as applied to Eq. 3.27 is given by

$$r(\psi + \Delta\psi, \zeta + \Delta\zeta) = r(\psi, \zeta) + V(\psi, \zeta)\Delta\psi \tag{3.28}$$

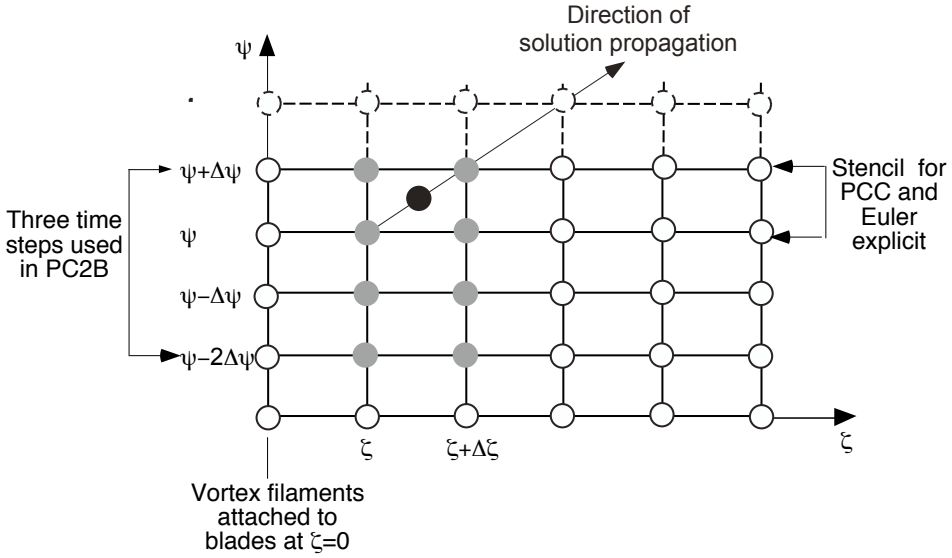

Figure 3.48: A schematic of the computational stencil for different time-marching methods

The right-hand side of Eq. 3.28 contains the highly nonlinear velocity field. This is the sum of the free-stream velocity, induced velocity from the turbine and any other form of perturbation velocity such as gusts and turbulence. Straight-line segmentation is used to evaluate the Biot–Savart integral to calculate the induced velocity, which has been shown to be second-order accurate. [112]

In the Euler explicit scheme, the induced velocity at the mid-point $r(\psi + \frac{\Delta\psi}{2}, \zeta + \frac{\Delta\zeta}{2})$ is approximated by the velocity at the neighboring point, $r(\psi, \zeta)$. A Taylor series expansion shows that

$$\begin{aligned} V(\psi,\zeta) &= V\Big(\psi + \frac{\Delta\psi}{2}, \zeta + \frac{\Delta\zeta}{2}\Big) - \frac{\Delta\psi}{2}V_\psi - \frac{\Delta\zeta}{2}V_\zeta \\ &\quad + \frac{1}{8}\Big(\Delta\psi^2 V_{\psi\psi} + \Delta\zeta^2 V_{\zeta\zeta} + 2\Delta\psi\Delta\zeta V_{\psi\zeta}\Big) \end{aligned} \tag{3.29}$$

Assuming $\Delta\psi = \Delta\zeta$ and adding the Biot–Savart approximation error, the discretized right-hand side term gives the modified equation

$$\frac{\partial r}{\partial\psi} + \frac{\partial r}{\partial\zeta} = V - \frac{\Delta\zeta}{2}(V_\psi + V_\zeta) + \frac{1}{12}V_{\zeta\zeta}\Delta\zeta^2 + \frac{\Delta\zeta^2}{8}(V_{\psi\psi} + 2V_{\psi\zeta} + V_{\zeta\zeta}) \tag{3.30}$$

The discretized equation for the left-hand side results in a further error. The Euler explicit scheme approximates the left-hand side by $r(\psi + \Delta\psi, \zeta + \Delta\zeta) - r(\psi, \zeta)$. Expanding these terms around the mid-point of the cell gives

$$\begin{aligned} r(\psi + \Delta\psi, \zeta + \Delta\zeta) - r(\psi, \zeta) &= \frac{\partial r}{\partial \psi} + \frac{\partial r}{\partial \zeta} \\ &\quad + \Delta\zeta^2 \left(\frac{1}{24} r_{3\psi} + \frac{1}{8} r_{\psi\psi\zeta} + \frac{1}{8} r_{\psi\zeta\zeta} + \frac{1}{24} r_{3\zeta} \right) \end{aligned} \tag{3.31}$$

The last term in above equation can be written as

$$\frac{1}{24}(r_{3\psi} + r_{3\zeta}) + \frac{1}{8}(r_\psi + r_\zeta)_{\psi\zeta} = \frac{1}{24}(V_{\psi\psi} + 2V_{\psi\zeta} + V_{\zeta\zeta}) \tag{3.32}$$

Therefore, the complete modified equation for the Euler explicit algorithm is given by

$$\frac{\partial r}{\partial \psi} + \frac{\partial r}{\partial \zeta} = V - \frac{\Delta\zeta}{2}(V_\psi + V_\zeta) + \Delta\zeta^2 \left(\frac{1}{12} V_{\zeta\zeta} + \frac{1}{12}(V_{\psi\psi} + 2V_{\psi\zeta} + V_{\zeta\zeta}) \right) \tag{3.33}$$

Using the governing equation (Eq. 3.27), the extra terms on the right-hand side of Eq. 3.33 can be written in terms of the spatial derivatives of the solution. Using Eq. 26 from Ref. 112, the modified equation for the Euler explicit algorithm is

$$\frac{\partial r}{\partial \psi} + \frac{\partial r}{\partial \zeta} = V - \frac{\Delta\zeta}{2} V_r V + \frac{\Delta\zeta^2}{12} \Big[V_{rr} r_\zeta^2 + V_r r_{\zeta\zeta} + (V_{rr} V + V_r^2) V \Big] \tag{3.34}$$

The dominant error terms in the modified equation are $\mathcal{O}(\Delta\zeta)$, which shows that the algorithm is only first-order accurate. The modified equation reduces to the original governing equation (Eq. 3.27) when $\Delta\zeta = 0$, so the scheme is consistent. The first-order term and the last of the extra second-order terms are the source terms, and have no direct impact on the numerical stability. The first term in the second-order extra term is the dispersive term, which may lead to phase errors in the numerical calculations, and perhaps to some spurious oscillations. The second term is the nonlinear implicit dissipation term, which is dependent on the velocity gradients (V_r, V_{rr}, etc.) in the flow. If this term is negative, it acts as an energy source, and the solution will be unstable.

PCC Scheme

The PCC scheme uses a five-point central difference approximation [135] for both the spatial and temporal derivatives. The governing equation is solved at the mid-point and the temporal difference operator is given by

$$\begin{aligned} D_\psi &\approx \frac{dr}{d\psi}|_{\psi+\Delta\psi/2,\zeta+\Delta\zeta/2} \\ &= \frac{r(\psi+\Delta\psi,\zeta+\Delta\zeta)-r(\psi,\zeta+\Delta\zeta)+r(\psi+\Delta\psi,\zeta)-r(\psi,\zeta)}{2\Delta\psi} \end{aligned} \tag{3.35}$$

The spatial operator is also given by an analogous expression. Expanding each term as a Taylor series around the mid-point of the cell gives

$$\begin{aligned} (D_\psi + D_\zeta) r(\psi+\Delta\psi/2,\zeta+\Delta\zeta/2) &= \frac{\partial r}{\partial\psi} + \frac{\partial r}{\partial\zeta} + \left(\frac{1}{24} r_{3\psi} + \frac{1}{8} r_{\psi^2\zeta}\right)\Delta\psi^2 \\ &\quad + \left(\frac{1}{8} r_{\zeta^2\psi} + \frac{1}{24} r_{3\zeta}\right)\Delta\zeta^2 \end{aligned} \tag{3.36}$$

Following the procedure outlined above for the Euler explicit scheme, the modified equations for the PCC algorithm are

$$\frac{\partial r}{\partial\psi} + \frac{\partial r}{\partial\zeta} = V + \frac{\Delta\zeta^2}{12}\Big[4(V_r r_\zeta)_\zeta - 3(V_{rr}V + V_r^2) r_\zeta - (V_{rr}V + V_r^2)V\Big] \tag{3.37}$$

The extra terms in the modified equation are all $\mathcal{O}(\Delta\zeta^2)$, i.e., the algorithm is second-order accurate.

In the manner found for the Euler explicit method, it is noted that the implicit dissipation term depends on the velocity gradients. Bhagwat & Leishman [112] have shown that the velocity gradients can be negative in the rotor wake. Therefore, the artificial dissipation term in Eqs. 3.34 and 3.37 can be negative and therefore, destabilizing. Although, the PCC scheme was found to be neutrally stable from the linear stability analysis, the modified equation shows that for certain operating conditions the scheme could, in fact, be unstable. Therefore, it is apparent that it will be desirable for a time-marching algorithm to contain some implicit dissipation that will compensate for the potentially destabilizing effects of the nonlinear velocity field.

PC2B Scheme

As previously explained, the PC2B scheme uses a second-order backward difference approximation to the temporal derivative. The temporal difference operator in this case is given as

$$\begin{aligned} D_\psi &\approx \frac{dr}{d\psi}|_{\psi+\Delta\psi/2,\zeta} \\ &= \frac{3r(\psi+\Delta\psi,\zeta) - r(\psi,\zeta) - 3r(\psi-\Delta\psi,\zeta) + r(\psi-2\Delta\psi,\zeta)}{4\Delta\psi} \end{aligned} \tag{3.38}$$

The spatial operator is the same as in the PCC scheme. Using a Taylor series expansion around the mid-point of a cell at $r(\psi+\Delta\psi/2, \zeta+\Delta\zeta/2)$ and expressing all the extra terms in terms of spatial derivatives, the modified equation for the PC2B scheme is obtained [112].

$$\frac{\partial r}{\partial \psi} + \frac{\partial r}{\partial \zeta} = V + \Delta\zeta^2 \left[\begin{array}{l} \text{nonlinear dissipative} \\ \text{and dispersive terms} \end{array} \; - \frac{\Delta\zeta}{4} r_{4\zeta} \right] \tag{3.39}$$

The $-r_{4\zeta}$ term in the modified equation is a dissipative term, and is independent of the velocity field. This dissipative term acts like an energy sink and is stabilizing, and so this makes the overall PC2B scheme stable. This term is also a third-order term, so the overall second-order accuracy of the scheme is preserved.

AB2 Scheme

The Adams–Bashforth (AB2) scheme solves the discretized governing equation at the grid points. This is unlike the schemes described in previous sections, which solve the equation at the mid-points of the cell. A five-point central difference operator is used to approximate the spatial difference operator. The discretized equation using the Adams–Bashforth scheme is then given by

$$\begin{aligned} r(\psi+\Delta\psi,\zeta+\Delta\zeta) = r(\psi-\Delta\psi,\zeta-\Delta\zeta) + \frac{4\Delta\psi}{3}\Big(3V(\psi,\zeta) - V(\psi-\Delta\psi,\zeta)\Big) \\ -\frac{8}{3}\Big(r(\psi+\Delta\psi,\zeta) - r(\psi,\zeta)\Big) \end{aligned}$$

$$+\Big(r(\psi+\Delta\psi,\zeta-\Delta\zeta)-r(\psi-\Delta\psi,\zeta+\Delta\zeta)\Big)$$
$$+\frac{1}{3}\Big[r(\psi,\zeta+\Delta\zeta)-r(\psi,\zeta-\Delta\zeta)-r(\psi-2\Delta\psi,\zeta+\Delta\zeta)$$
$$-r(\psi-2\Delta\psi,\zeta-\Delta\zeta)\Big] \tag{3.40}$$

Using a Taylor series expansion around the grid point (ψ,ζ) in the computational grid, and expressing all the extra terms in terms of spatial derivatives, the modified equation for the AB2 scheme is obtained as

$$\frac{\partial r}{\partial\psi}+\frac{\partial r}{\partial\zeta}=V+\frac{\Delta\zeta^2}{12}\Big[(V_r r_\zeta)_\zeta-7(V_{rr}V-V_r^2)r_\zeta-5(V_{rr}V+V_r^2)V-5r_{3\zeta}\Big] \tag{3.41}$$

The extra terms on the right are all $\mathcal{O}(\Delta\zeta^2)$, i.e. the algorithm is second-order accurate. The first term is the dissipation term, which depends on the velocity gradients. The second and fourth terms are dispersion terms, which introduce phase errors. The third term is the source term, which does not affect the stability of the numerical scheme.

3.2.4 Wake Convergence

To better understand the concept of the nonlinear stability of the time-marching method in the free-vortex wake method, a series of numerical experiments were performed. These calculations were performed using a representative three-bladed Grumman wind turbine with a nominal power output of 15 kW. Table 3.1 gives the geometrical and operational parameters of the turbine. The actual blade twist is hyperbolic. The present calculations were performed for a steady wind speed of 13 ms^{-1}.

The numerical experiments were performed using each of the Euler explicit, PCC, and PC2B schemes with a wake discretization of $\Delta\psi=\Delta\zeta=10^\circ$ for both the unyawed and the yawed cases. Figure 3.49 show the front view and the top view of the turbine wake after 40 revolutions when using the Euler explicit scheme for the unyawed case. It can be seen that the wake exhibits significant numerical

Number of blades, N_b	3
Radius, R	5.0290 m
Chord, c	0.457 m
Airfoil	S809
Twist, θ_{tw}	Hyperbolic
Rotational speed, Ω	7.53 rad/s
Wind speed, V_∞	13.0 m/s
Nominal power output at V_∞, P_{out}	15 kW

Table 3.1: Geometry of wind turbine and operational parameters

instabilities along the length of each vortex filament, especially at older wake ages. Recall from earlier that the linear stability analysis showed the Euler explicit method to be unstable for all time steps. However, the discretization of r_ζ (see Eq. 3.34) and the averaging errors introduces some implicit dissipation. Nevertheless, the Euler scheme produces a non-physical result compared to what would be expected based on experimental observations, such as those shown in Fig. 3.50, which suggests a much more smoothly expanding and relatively undisturbed helicoidal wake downstream of the turbine disk. The loss of axisymmetry in the experiment is partly a result of the ground boundary layer and the tower shadow. While there is perhaps some experimental evidence of wake instabilities in Eq. 3.50, they are relatively mild and seem to be excited by perturbations introduced by the tower shadow.

Figure 3.51 shows that PCC scheme gives a significant improvement in the numerical stability of the wake compared to the Euler explicit scheme. In this case there are still wake instabilities, but these grow more slowly. It could be argued that this particular result more closely resembles the result in Fig. 3.50 in the near wake region, although in this case the modeling does not represent the ground boundary layer or the tower shadow. Clearly, there are issues that must be fully explored in the future to help properly distinguish numerical versus physical wake instabilities.

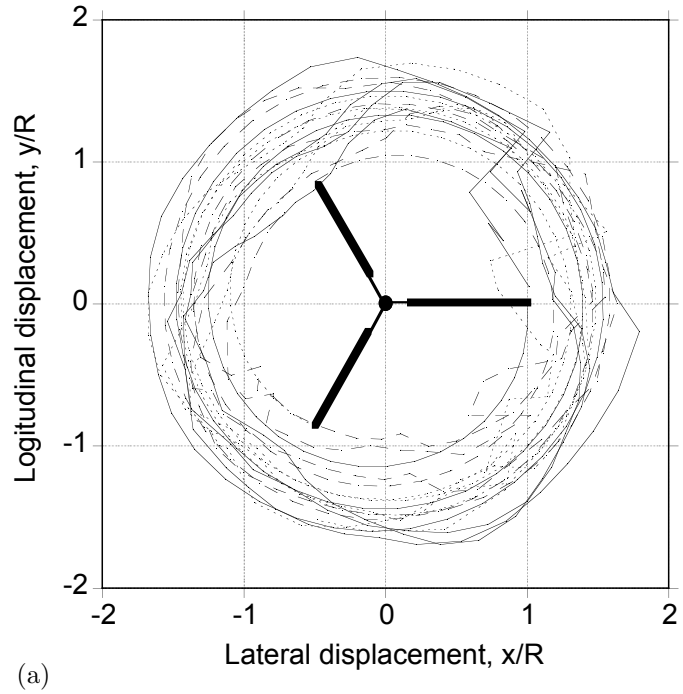

(a)

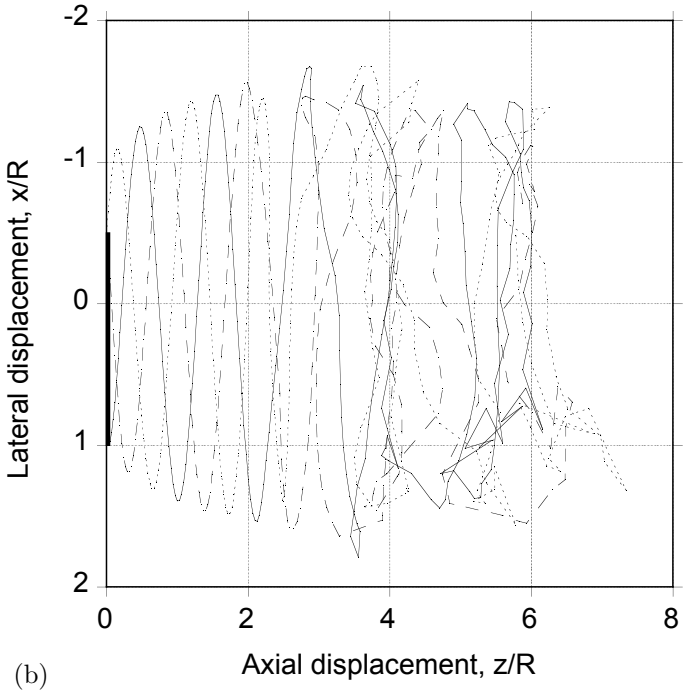

(b)

Figure 3.49: Time-marching free-vortex wake geometry for a three-bladed unyawed Grumman wind turbine using the Euler explicit scheme: (a) Front view, (b) Top view.

Figure 3.50: Photograph of the expanding vortical wake downstream a horizontal axis wind turbine rendered visible using smoke injection. Photo courtesy of NREL.

The wake obtained using the PC2B scheme (as shown in Fig. 3.52) gives a smoothly expanding structure with almost no evidence of disturbances, and is more consistent with the experimental observations of the wind turbine wake (Fig. 3.50).

Figure 3.53 shows a time-history of the L_2-norm of the change in the wake geometry using all three schemes. Notice that the result for the Euler explicit scheme initially reduces, but then continues to fluctuate. At later times, the L_2-norm begins to increase, suggesting that the result will eventually diverge. This is further evidence that, despite its simplicity and computational efficiency, the Euler method produces a non-physical solution, even for this relatively simple test case. The PCC scheme shows a converging trend, but there is still an accumulation of numerical errors. This is because the discrete approximation of the temporal and spatial derivatives results in a larger error as compared to the PC2B scheme. Notice that the wake geometry stabilizes very quickly when using the PC2B scheme. This is because the implicit dissipation in the method damps-out any numerical errors.

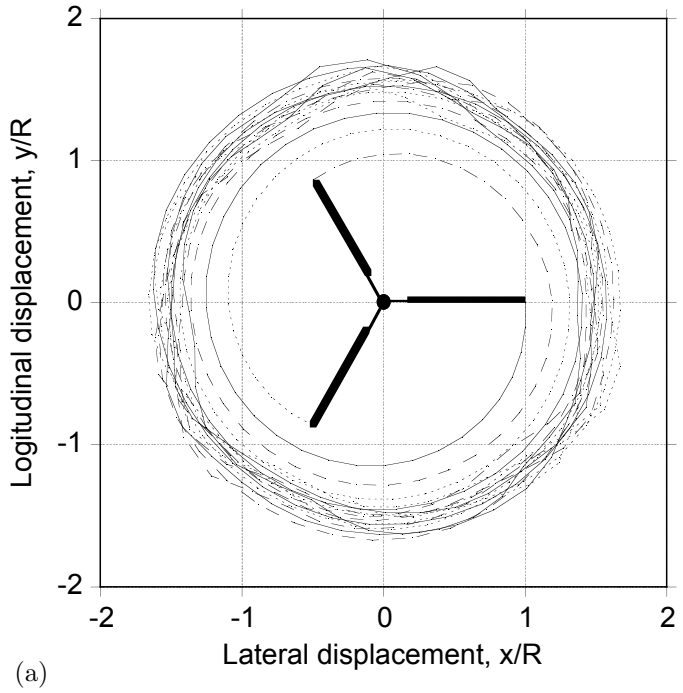

(a)

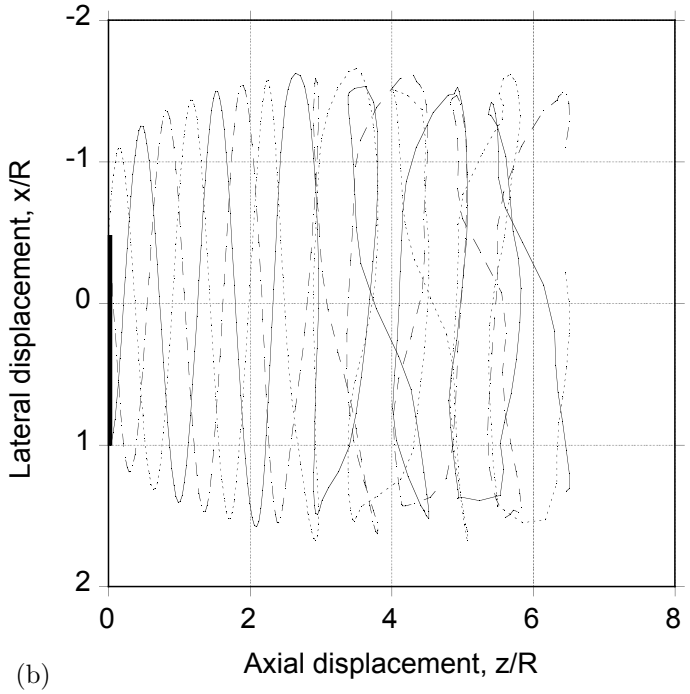

(b)

Figure 3.51: Time-marching free-vortex wake geometry for a three-bladed unyawed Grumman wind turbine using the PCC scheme: (a) Front view, (b) Top view.

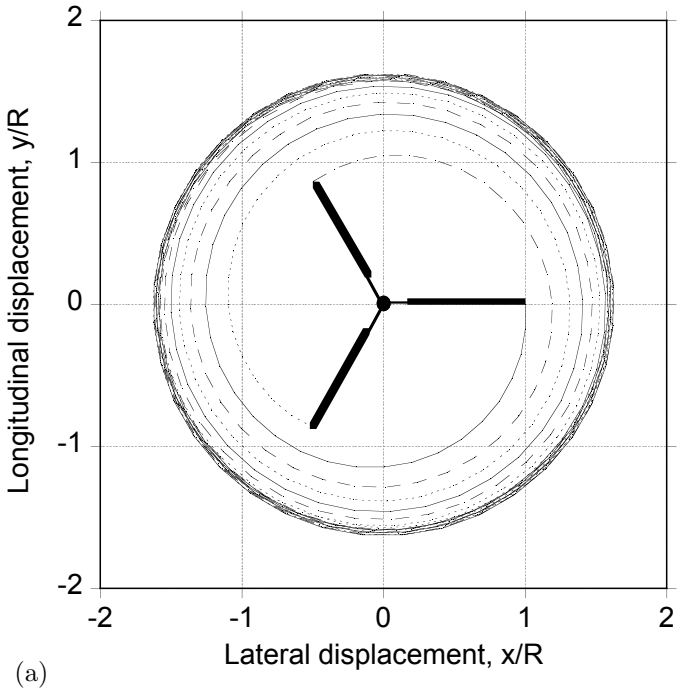

(a)

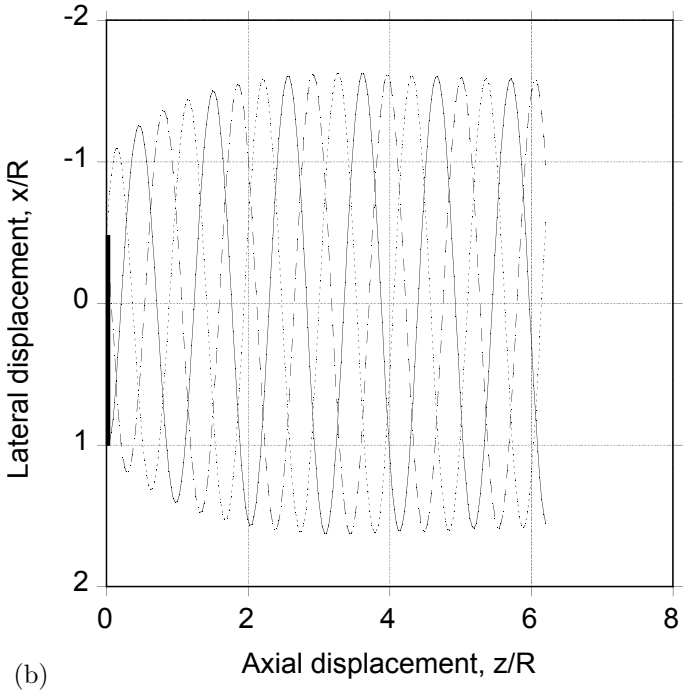

(b)

Figure 3.52: Time-marching free-vortex wake geometry for a three-bladed unyawed Grumman wind turbine using PC2B scheme: (a) Front view, (b) Top view.

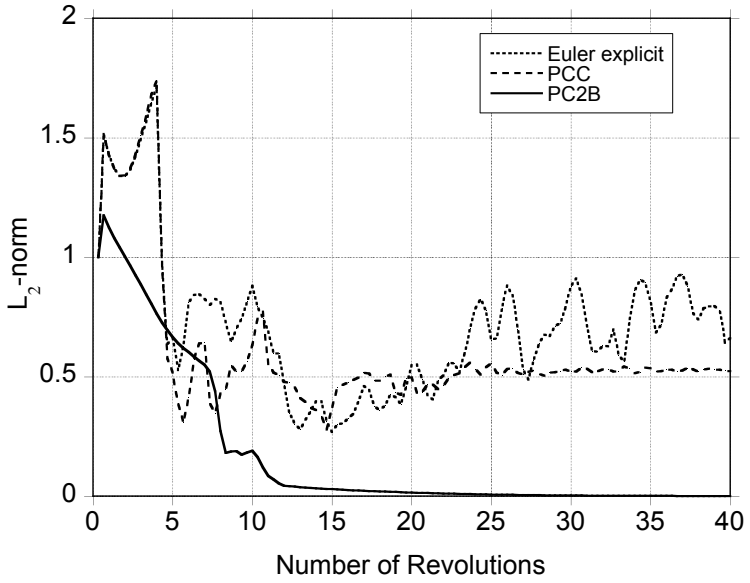

Figure 3.53: Time history of the L_2-norm of the error in wake geometry for the unyawed wind turbine.

It is common for wind turbines to operate in the yawed flow condition. Even though larger turbines have yaw control, sudden changes in the wind direction during gusts can cause yawed flow condition. For smaller wind turbines, turning the rotor out of the wind is used to limit the power captured from the wind. Operation in a yawed flow condition causes unsteady airloads (N_b/rev) on the rotor blades. The wind turbine has to be designed to account for these unsteady loads. To predict these unsteady airloads correctly, it is very important to capture the rotor wake accurately. The changes in the wake geometry affect the induced velocity in the rotor plane, which causes significant change in the angle of attack on the blade because of its low rotational speed. The Grumann wind turbine described previously was yawed 30° out of the wind, and a time-accurate calculation was performed using the three time-marching schemes. The unyawed wake obtained from the PC2B scheme was used to initialize the wake, and a yaw angle of 30° was then imposed. Figure 3.54

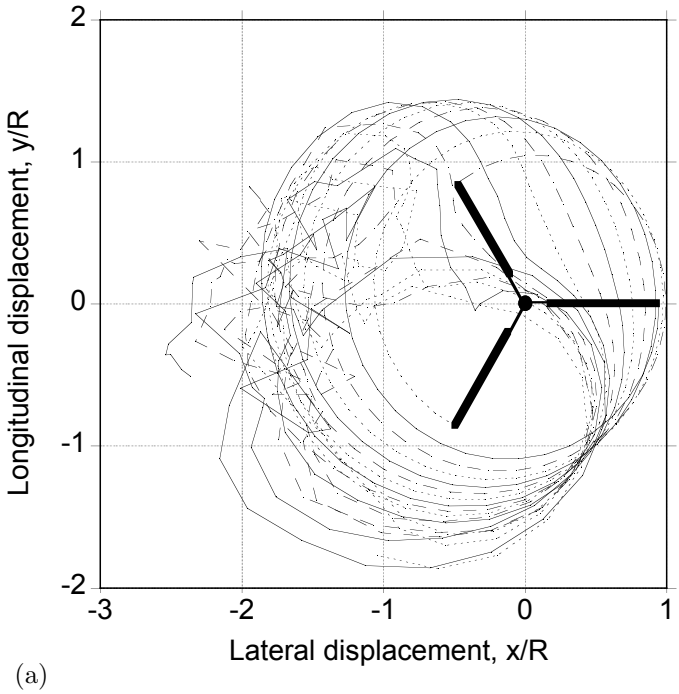

(a)

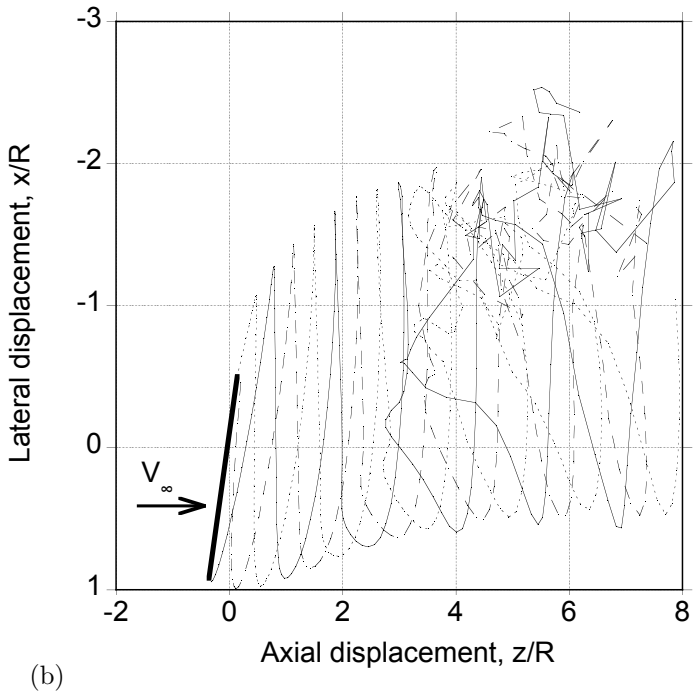

(b)

Figure 3.54: Time-marching free-vortex wake geometry for a three-bladed Grumman wind turbine yawed 30° out of the wind using the Euler explicit scheme: (a) Front view, (b) Top view.

shows the front view and the top view of the rotor wake after 60 rotor revolutions that was obtained using the Euler explicit scheme. Notice that the wake structure shows significant disturbances at later wake ages. Unlike the unyawed case, the PCC scheme (Fig. 3.55) does not show any improvement over the Euler explicit scheme whereas the wake geometry obtained using the PC2B scheme (Fig. 3.56) is free of any numerical disturbances.

Figure 3.57 shows the L_2-norm of the change in wake geometry with time. The error in all cases increases as the wake tries to readjust to the yawed flow but for the Euler explicit and the PCC schemes the error continues to fluctuate even after 50 revolutions. Notice that the wake geometry stabilizes quickly when using the PC2B scheme.

3.3 Summary

A systematic study of the accuracy of the reconstruction of the induced velocity from helical vortices was performed for a range of values of helical pitch, number of turns and wake skew angles. The accuracy of the straight-line segmentation approach of discretizing a helical vortex was found to be second-order for different combinations of pitch, skew and number of turns. A minimum discretization of $\Delta\theta = 10^\circ$ is required to keep the maximum error in the induced velocity field less than 10%. To keep the maximum error less than 1%, a discretization of $\Delta\theta < 2.5^\circ$ is required, which may be less practical for routine engineering use of vortex wake models.

A vortex ring can be viewed as a special case of helical vortex with its helical pitch tending to zero. The induced velocity from helical vortices with a helical pitch $p \to 0$ and scaled by number of turns was shown to reduce to that of a vortex ring. A vortex ring was found to be a more challenging case to model accurately using the straight-line segmentation approach than for the helical vortex. In the case of a vortex ring, the magnitude of the errors in the induced velocity for a particular level

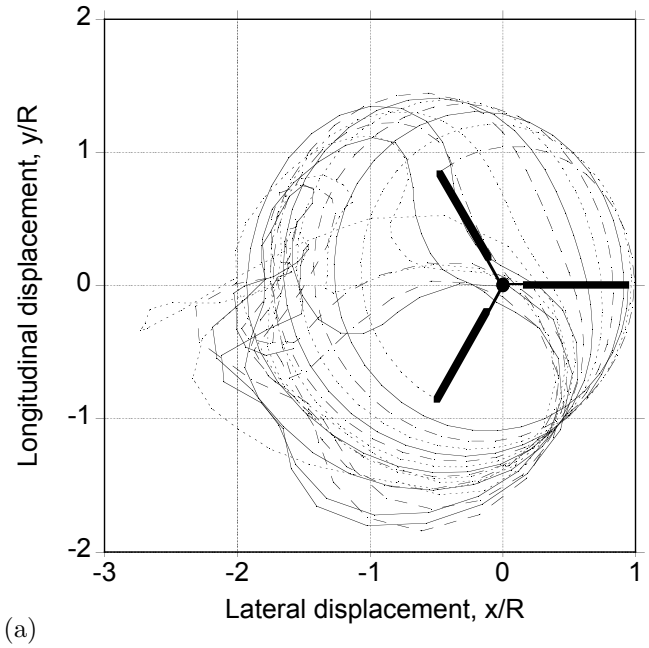

(a)

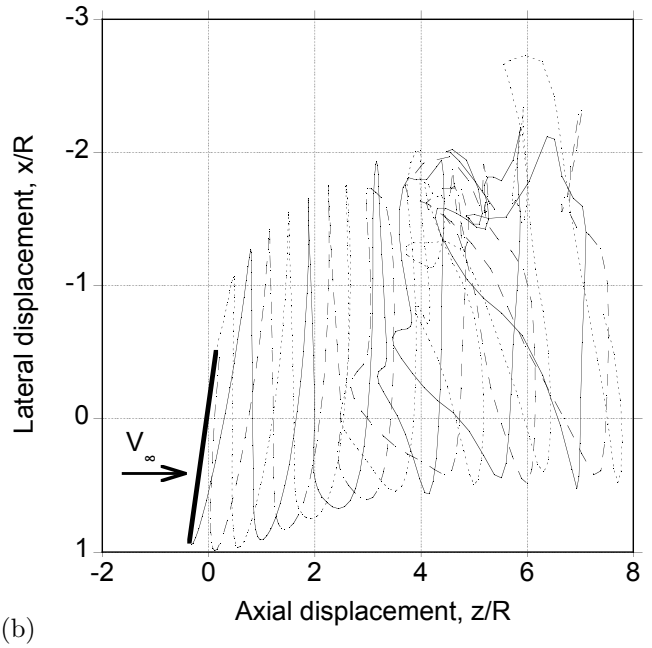

(b)

Figure 3.55: Time-marching free-vortex wake geometry for a three-bladed Grumman wind turbine yawed 30° out of the wind using the PCC scheme: (a) Front view, (b) Top view.

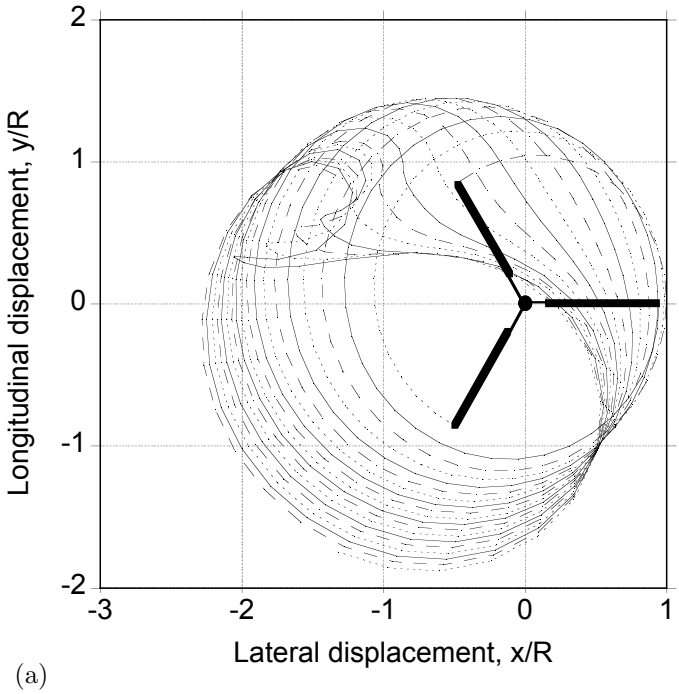

(a)

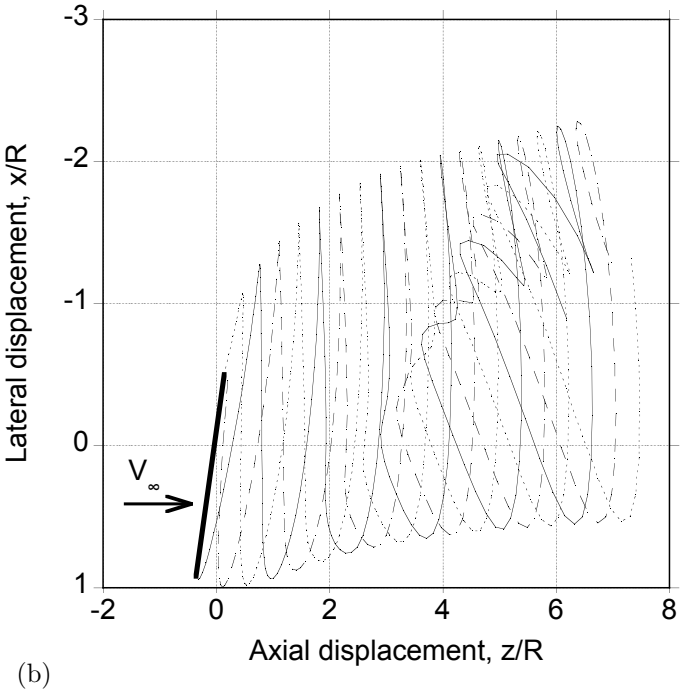

(b)

Figure 3.56: Time-marching free-vortex wake geometry for a three-bladed Grumman wind turbine yawed 30° out of the wind using PC2B scheme: (a) Front view, (b) Top view.

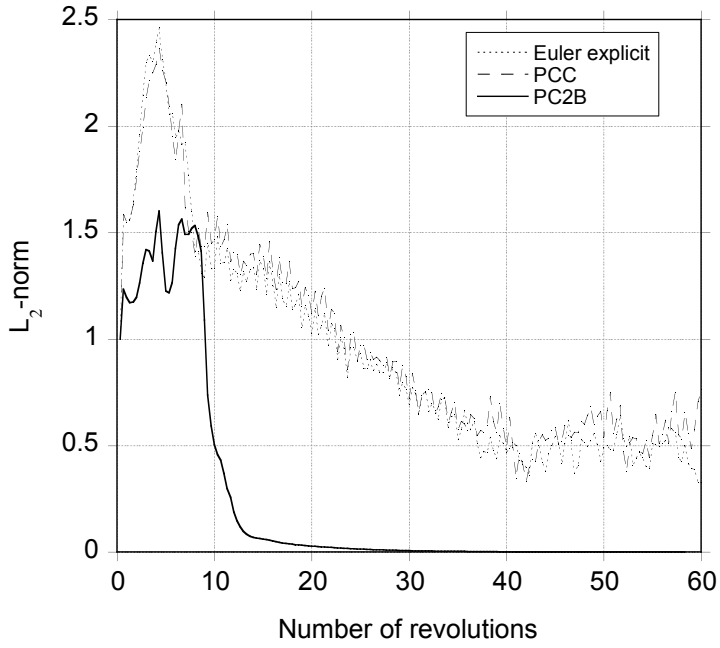

Figure 3.57: Time history of the L_2-norm of the error in wake geometry for a wind turbine yawed 30° out of the wind.

of discretization has been found to be larger than the corresponding helical vortex. The reconstruction of induced velocity by straight-line approximation of a skewed helical vortex was also found to be second-order accurate, and the magnitude of the errors were found to be comparable to those of the unskewed case.

The linear and nonlinear stability of various time-marching methods used in free-vortex wake methods has been analyzed. The linear stability analysis has shown that the PCC and PC2B schemes are stable for all values of time discretization. The Euler explicit and second-order Adams–Bashforth schemes are unstable for all values of discretization. The fourth-order Adams–Moulton scheme is stable for values of $\omega h < 0.7$. The fourth-order AM4 scheme produces the lowest phase error and the Euler explicit scheme has the largest error. From a linear stability point of view, the AM4 scheme seems to be the best scheme. However, the Adams–Moulton scheme is implicit and computationally expensive especially for a free-vortex wake analysis.

Any linearization or approximation to make this scheme explicit or semi-implicit will change the stability and dispersion characteristics of the scheme.

Considering the stability and dispersion characteristics as well as the computational cost, the PC2B algorithm seems to be the ideal scheme. The modified equation approach showed that the PC2B scheme introduces extra implicit dissipation that is independent of the velocity gradients. The dissipation term in all other schemes (Euler explicit, PCC and Adams–Bashforth) is affected by the induced velocity field gradients. The presence of the negative velocity gradients then introduces an anti-dissipation, which has a destabilizing effect on the developing wake geometry.

Numerical experiments were performed for a three-bladed Grumman wind turbine in the zero yaw condition and 30° yawed out of the wind. The Euler explicit method produces and non-physical unstable wake system. The PCC scheme showed a modest growth of numerical errors with time, albeit bounded. The PC2B scheme was found to produce a stable and convergent wake system free of any types of disturbances.

Chapter 4

Stall Modeling

Because of the low rotational speed of a turbine, the inboard regions of the blades are stalled for much of their operational time. Additionally, stall regulation is one of the methods used to control peak power output for smaller wind turbines. For the larger wind turbines, which use pitch control for power regulation, stall conditions can occur during wind gusts. Thus, predicting blade loads and the power output during stall (and in the post-stall region) is fundamental to the improved design of all types of wind turbines. It is, therefore, very important to model accurately the detailed aerodynamic characteristics of the airfoils being considered over a wide range of angles of attack.

In addition to this, a wind turbine blade section can undergo dynamic stall [39] when it is subjected to the unsteady aerodynamic environment. In the present formulation, a modified version of the Leishman–Beddoes (L–B) dynamic stall model [125] has been used to predict the aerodynamic characteristics of S809 airfoil under incipient and deep dynamic stall conditions. Several key modifications to the base model required to improve its validity over a wider range of angle of attack and operating Reynolds number representative of wind turbines have been discussed in Section 2.2.2.

Three data sets are available that document the 2D lift and profile drag coefficients for the S809 airfoil. The CSU test [136] is available for the low Reynolds number range (up to 650,000), whereas the higher Reynolds number data ($Re > 10^6$) is available from OSU [137] and the Delft University tests [138]. In this section, the aerodynamic coefficients for the S809 airfoil at $Re = 10^6$, as obtained from the OSU

tests are used as the 2D static test data. Although the aerodynamic coefficients were measured only up to an angle of attack of 40°, the results show relative insensitivity to Reynolds number at the higher angles of attack, as shown in Fig. 4.1. Once the static and unsteady stall model was validated against the experimental measurements, the airfoil model was coupled with the Weissinger-L blade model. The numerical results are then validated using the NREL static and oscillating parked blade measurements.

OSU Experimental Test Setup

The OSU 3×5 subsonic open circuit wind tunnel was used to conduct the tests on the S809 airfoil section. The test section dimensions were 1.0 m high by 1.4 m wide by 2.4 m long. An airfoil model with a constant chord of 457 mm was used in the experiment. A shaker system was incorporated to oscillate the airfoil for the unsteady airfoil measurements. The trailing-edge of the airfoil was thickened to 1.25 mm, and this thickness was added to the upper surface over the last 10% of the chord. Pressure measurements were obtained from 60 surface pressure taps. The distribution of pressure taps was dense near the leading-edge, and scarce near the trailing-edge. Wind tunnel wall corrections were applied to the pressure data. The corrected pressure data were integrated around the chord and thickness to obtain aerodynamic lift and profile drag, respectively.

4.1 2D Static Airfoil Coefficients

The S809 airfoil was designed by Somers [138] for applications in the wind turbines using stall as a method for power regulation. This airfoil has unique aerodynamic characteristics. The S809 airfoil was designed to have a pronounced trailing–edge separation and reduced sensitivity to increases in drag. With the low rotational speeds of a wind turbine, the inboard sections of the blade operate at

relatively high angles of attack. The lift coefficient for the S809 airfoil is found to be relatively constant for a range of angle of attack near the maximum lift coefficient. This ensures that loss in lift is not abrupt, and the inboard sections of the turbine blades also produce useful torque. Figure 4.1 shows the lift versus angle of attack curves for different chord Reynolds numbers.

For the numerical stall modeling, the variation of the effective trailing-edge separation point, f was estimated using the normal force coefficient values from the 2D static test data by rearranging Eq. 2.38. The deduced values of f were then fitted in a least-square sense by three exponential curves by using an implementation of a nonlinear least-squares Marquardt–Levenberg algorithm. These exponential curves are defined as

$$f = \begin{cases} c_1 + a_1 \exp(S_1 \alpha) & \alpha \leq \alpha_1 \\ c_2 + a_2 \exp(S_2 \alpha) & \alpha_1 \leq \alpha \leq \alpha_2 \\ c_3 + a_3 \exp(S_3 \alpha) & \alpha \geq \alpha_2 \end{cases} \tag{4.1}$$

where c_1, c_2, c_3, a_1, a_2, a_3, S_1, S_2 and S_3 are constants, which all depend on the

Table 4.1: Variation of airfoil section curve fit coefficients with the chord Reynolds number.

Re	300,000	500,000	650,000	10^6
c_1	1.0	1.0	1.0	1.0
c_2	0.0	0.0	0.0	0.0
c_2	0.02	0.01	0.005	0.02
a_1	0.02539	0.00250	0.02168	0.04995
a_2	4.5278	4.5503	3.4934	2.8844
a_3	8.61×10^7	4.76×10^6	4.97×10^8	4.08×10^4
S_1	15.618	19.829	18.269	12.066
S_2	-12.499	-11.299	-11.324	-9.82694
S_3	-74.270	-64.93	-78.675	-43.0635

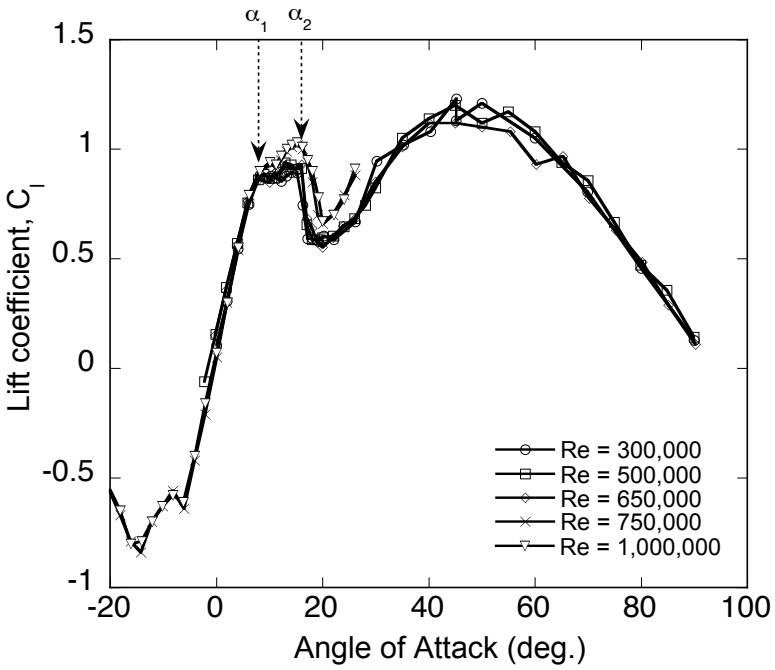

Figure 4.1: Variation of the lift coefficient with angle of attack for the S809 airfoil for different chord Reynolds number.

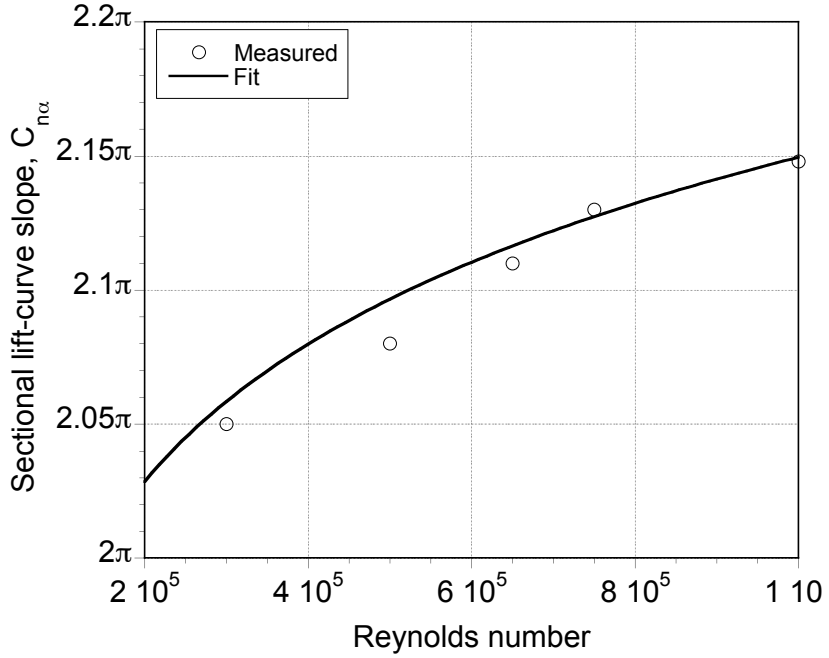

Figure 4.2: Lift-curve slope variation of the S809 airfoil for different chord Reynolds number.

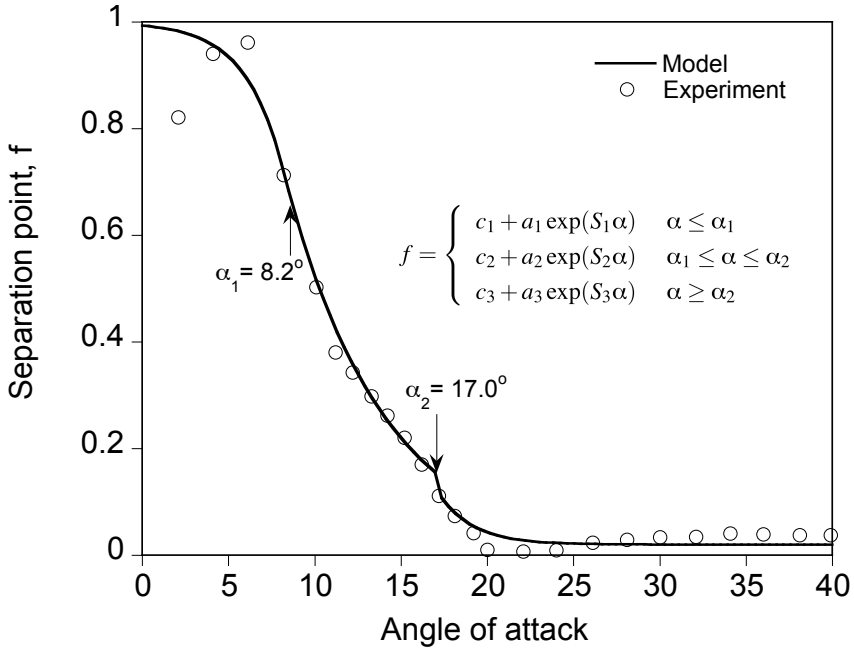

Figure 4.3: Variation of the effective flow separation point with angle of attack along with a functional fit at $Re = 10^6$.

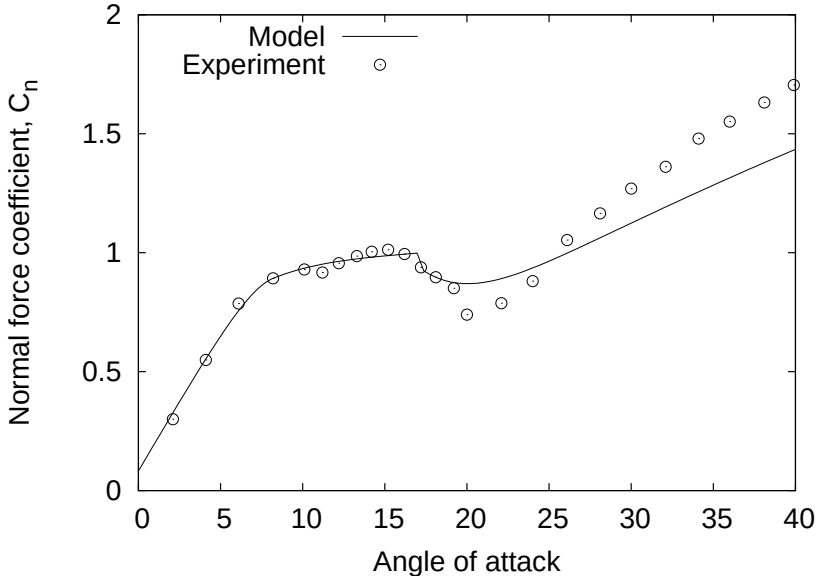

Figure 4.4: Variation of the measured and the predicted C_n with angle of attack at $Re = 10^6$.

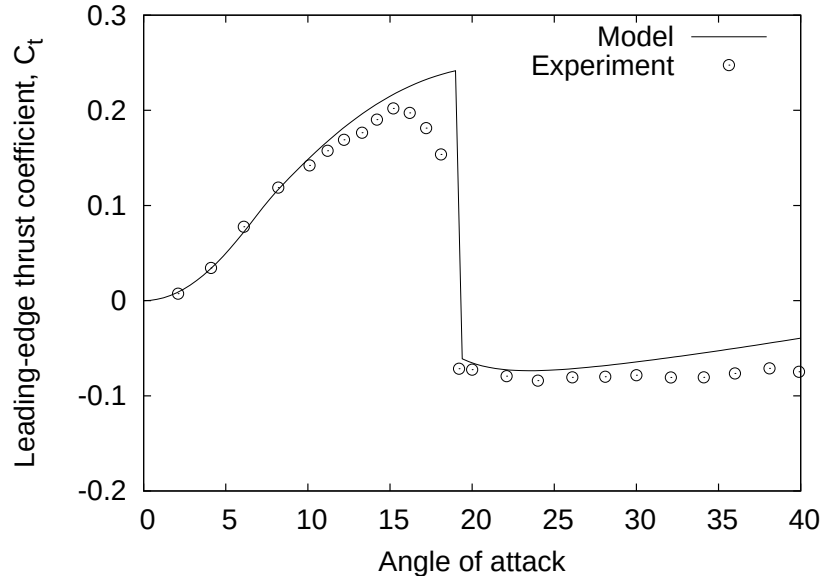

Figure 4.5: Variation of the measured and the predicted C_t with angle of attack at $Re = 10^6$.

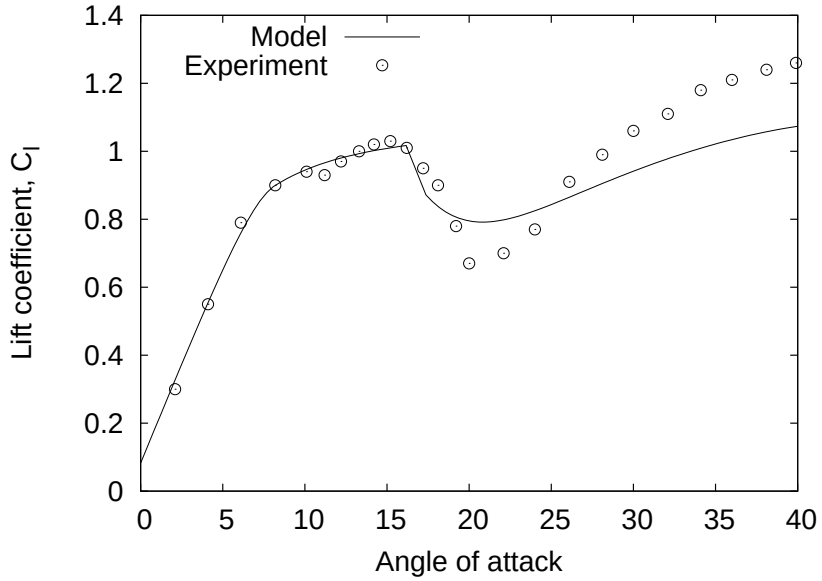

Figure 4.6: Variation of the measured and the predicted C_l with angle of attack at $Re = 10^6$.

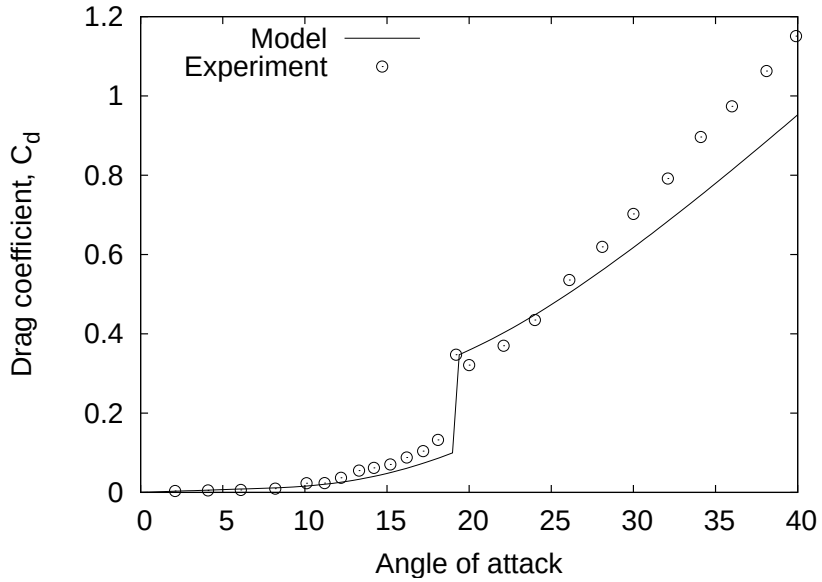

Figure 4.7: Variation of the measured and the predicted C_d with angle of attack at $Re = 10^6$.

Reynolds number (see Table 4.1). The constants α_1 and α_2 are the angles of attack corresponding to the first and second breaks in lift curve slope, as denoted by α_1 and α_2 in Fig. 4.1. The values of α_1 and α_2 were found to be fairly constant for different Reynolds numbers. However, the lift curve slope, C_{l_α} also varies with the chord Reynolds number; the variation of C_{l_α} with Re obtained from the experimental data, along with a smooth fit to the measured values is shown in Fig. 4.2.

The variation of the measured and reconstructed effective flow separation point f with the angle of attack is shown in Fig. 4.3. It can be seen that the flow separation point is close to the trailing-edge at low angle of attack. This shows that the flow is attached over most of the airfoil. With an increase in the angle of attack, there is in an increase in the adverse pressure gradient. The flow starts separating near the trailing-edge, and the separation point moves towards the leading-edge. At very high angles of attack, the flow separates over most of the airfoil, and the effective separation point stablizes very close to the leading-edge. Using the reconstructed effective flow separation point, C_n and C_t are obtained using the relations described in Section 2.2.1, i.e.,

$$C_n = C_{n_\alpha}\left(\frac{1+\sqrt{f}}{2}\right)^2 \sin\alpha \tag{4.2}$$

and

$$C_t = \begin{cases} C_{n_\alpha}\sqrt{f}\ \alpha\sin\alpha & C_n < C_n(\alpha_2) \\ K_1 + C_{n_\alpha} f\ \alpha\sin\alpha & C_n > C_n(\alpha_2) \end{cases} \tag{4.3}$$

The variation of the reconstructed C_n and C_t using the mathematical is shown in Figs. 4.4 and 4.5, respectively. In the attached flow region ($\alpha < \alpha_1$), good agreement was obtained from the model against the experimental values. The range of the angle of attack where C_n stays relatively constant is captured well by the model. In the post-stall regime, C_n was only slightly underestimated at very high values of angle of attack. The agreement between the modeled and measured C_t was seen to be very good for the attached flow regime. The increase in C_t with angle of attack was also captured well by the model. Airfoil stall is accompanied by a sudden

drop in C_t. As the angle of attack increases further, the airfoil stalls completely and the leading-edge thrust becomes negative. C_t stays relatively constant in the deep stall regime ($\alpha > 20°$). Notice that C_t is slightly over-predicted in the deep stall regime.

Figures 4.6 and 4.7 show the modeled static lift and drag coefficients. Good agreement is obtained with the experimental data at low to moderate angles of attack. The lift coefficient C_l is, however, underpredicted at high angle of attack. Variation of C_d is captured very well and the increase in drag with the onset of airfoil stall is represented accurately. However, the drag is slightly underpredicted at very high angles of attack. The reconstruction of the aerodynamic coefficients for the S809 airfoil at other Reynolds numbers was also equally good. However, results for only $Re = 1$ million have been shown here.

4.2 2D Unsteady Airfoil Coefficients

Unsteady airfoil model as described in Section 2.2.2 was used in conjunction with the static stall model modified for wind turbine applications. It has been shown in the previous section, that the static stall model provides a good reconstruction against the measured aerodynamic coefficients. For the validation of the unsteady airfoil model, the aerodynamic coefficient measurements from the OSU tests on an oscillating S809 airfoil at $Re = 10^6$ were used for validation [137]. The experimental data is available for sinusoidal pitch oscillations for various reduced frequencies, k, mean angles of attack, α_{mean}, and for two angle of attack amplitudes, α_{amp}, of 5.5° and 10°.

Table 4.2 shows the values of various parameters used for the S809 airfoil in the modified L–B model. These parameters were, remarkably, found to be close to the values used in the original model, which was formulated for the NACA0012 airfoil. The robustness of the L–B model has been demonstrated by its application to S809 airfoil (21% thick airfoil).

Table 4.2: Various parameters used in the model for the S809 airfoil.

C_0	C_1	C_2	C_{m_0}	m	C_{n_1}	T_p	T_f	T_v	T_{vl}	C_{d_0}	D_f	E_f
-0.0032	-0.001	-0.025	-0.036	6	1.9	1.7	3.0	6.0	11.0	0.012	2.0	1.0

The variation of the predicted unsteady lift coefficient C_l is shown in Fig. 4.8 for a reduced frequency of $k = 0.026$, angle of attack amplitude $\alpha_{\text{amp}} = 5.5°$ and three values of α_{mean}. Four cycles of extracted data are plotted to show both the cycle-to-cycle repeatability as well as its variability. For a mean angle of attack of 8°, the lift hysteresis loop was predicted well by the model. Notice that stall is delayed to a slightly higher angle of attack than the static case, and the lift curve is almost linear up to $\alpha = 10°$. As the angle of attack decreases during the pitch oscillation cycle, the onset of flow reattachment is delayed to lower angle of attack than in the static case. For $\alpha_{\text{amp}} = 14°$, the airfoil section is operating near the maximum lift coefficient. The hysteresis in the lift coefficient is much more pronounced and is well predicted by the model. For the higher mean angle of attack of $\alpha_{\text{mean}} = 20°$, the experimental data shows some deviations over the three cycles but the airloads are predicted well by the model, on average.

The corresponding variation of C_m is shown in Fig. 4.9. Good agreement was obtained with the experimental values for all mean angles of attack. For $\alpha_{\text{mean}} = 8°$, the flow is mostly attached, and the model easily predicts C_m. For the higher values of $\alpha_{\text{mean}} = 14°$, there is some evidence of dynamic stall and an abrupt increase in the nose-down pitching moment. However, the model and the experimental results show some differences. In particular, the model slightly underpredicts the angle of attack corresponding to the moment stall during the upstroke. Experimental measurements of C_m for $\alpha_{\text{mean}} = 20°$ are seen to have oscillations, which are a result of the unsteady, aperiodic flow field in deep stall. The average pitching moment distribution is, however, represented well by the model.

The variation of C_d is shown in Fig. 4.10. Again, the agreement between the

model and the experiment was reasonably good for $\alpha_{\text{mean}} = 8°$ and $14°$, but C_d is underpredicted on average for $\alpha_{\text{mean}} = 20°$. However, it should be noted that the measurements of C_d were obtained by integrating the pressure data across thickness of the airfoil, which is known to be very sensitive to the number of chordwise pressure points. Therefore, the measurements of C_t must have a higher degree of uncertainty in the deep stall regime than in C_n.

For the higher reduced frequencies ($k = 0.05$ and $k = 0.077$), the hysteresis in the airloads is larger than at the lower reduced frequency, as would be expected. The agreement between the experiments and the model for the C_l, C_m and C_d is reasonably good (see Figs. 4.11 through 4.16). For a reduced frequency $k = 0.077$, the hysteresis behavior in C_m was seen to be more pronounced in the experimental results compared to the predictions made by the model. The sudden decrease in C_m during moment stall is also slightly underpredicted by the model for $\alpha_{\text{mean}} = 20°$, but the overall agreement with the measurements is good enough for engineering purposes, especially bearing in the mind the simplicity of the L–B model.

Measurements were also available at $Re = 10^6$ for $\alpha_{\text{amp}} = 10°$ for the same mean angle of attack and reduced frequencies as the $\alpha_{\text{amp}} = 5.5°$ case. Figure 4.17 shows the variation of C_l for a reduced frequency of $k = 0.026$. The agreement between the predictions and measurements was found to be good for low mean angles of attack. For the higher values of α_{mean}, some transient overshoots and undershoots shown in the C_l measurements were present, however, those were not predicted by the model. The angle of attack in the experiments also showed deviations from the prescribed nominal angle of attack history. The agreement between the experiment and C_m predictions for $k = 0.026$ (see Fig. 4.18) was again very good, as seen for $\alpha_{\text{amp}} = 5.5°$ case. The drag coefficient (see Fig. 4.19) was also well predicted for the lowest mean angle of attack, but was underpredicted for $\alpha_{\text{mean}} = 14°$ and $20°$.

Figure 4.20 shows the variation of C_l with angle of attack for a reduced frequency of $k = 0.77$ and the three values of α_{mean}. The hysteresis in the value of

C_l during the cycle is predicted reasonably well except for the flow reattachment regime, where C_l is overpredicted. For all three values of α_{mean}, the variation of C_m is predicted well (Fig. 4.21). The contribution of the dynamic stall vortex to C_m can be clearly seen for $\alpha_{\text{mean}} = 14^\circ$ and 20°. The variation in C_m and the pitching moment stall is predicted well. Good agreement was also achieved in the prediction of C_d (Fig. 4.22). However, the predicted maximum drag during the cycle is somewhat lower than the experimental measurements.

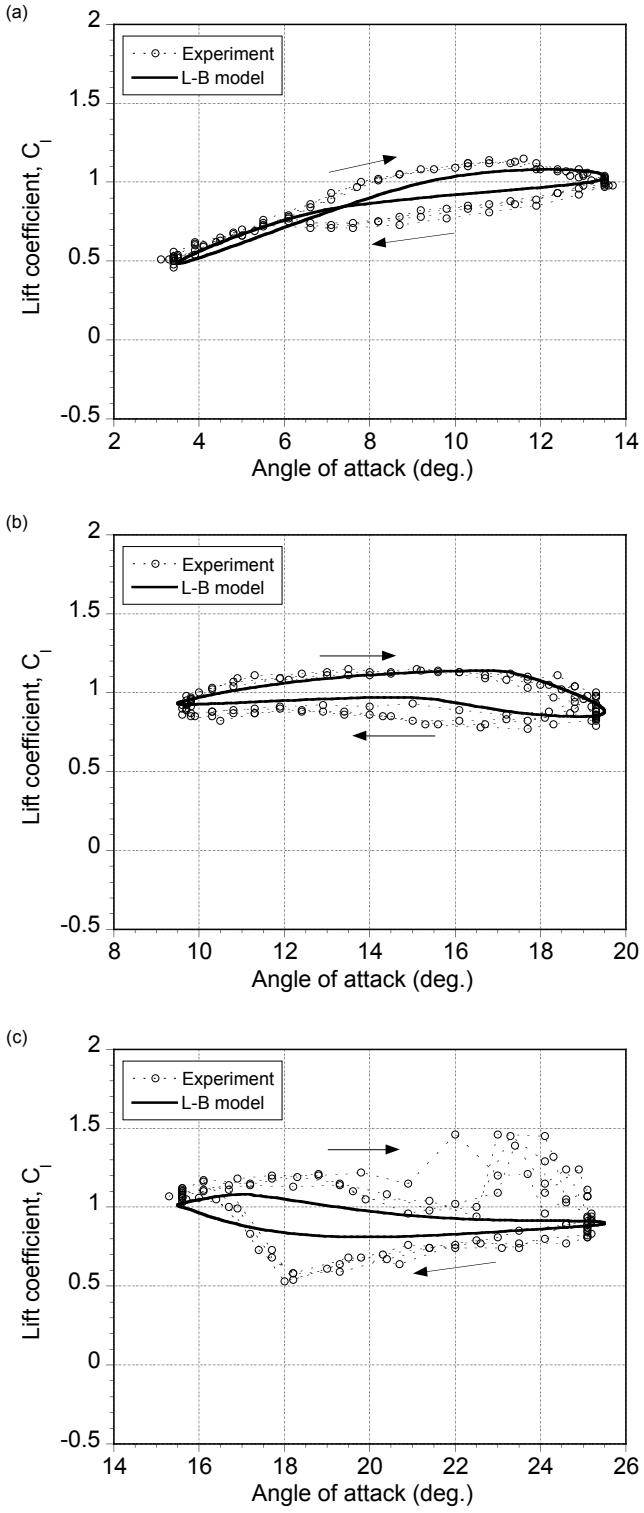

Figure 4.8: Variation of the lift coefficient with angle of attack for a reduced frequency $k = 0.026$ and angle of attack amplitude $\alpha_{\text{amp}} = 5.5°$ (a) $\alpha_{\text{mean}} = 8°$, (b) $\alpha_{\text{mean}} = 14°$, and (c) $\alpha_{\text{mean}} = 20°$.

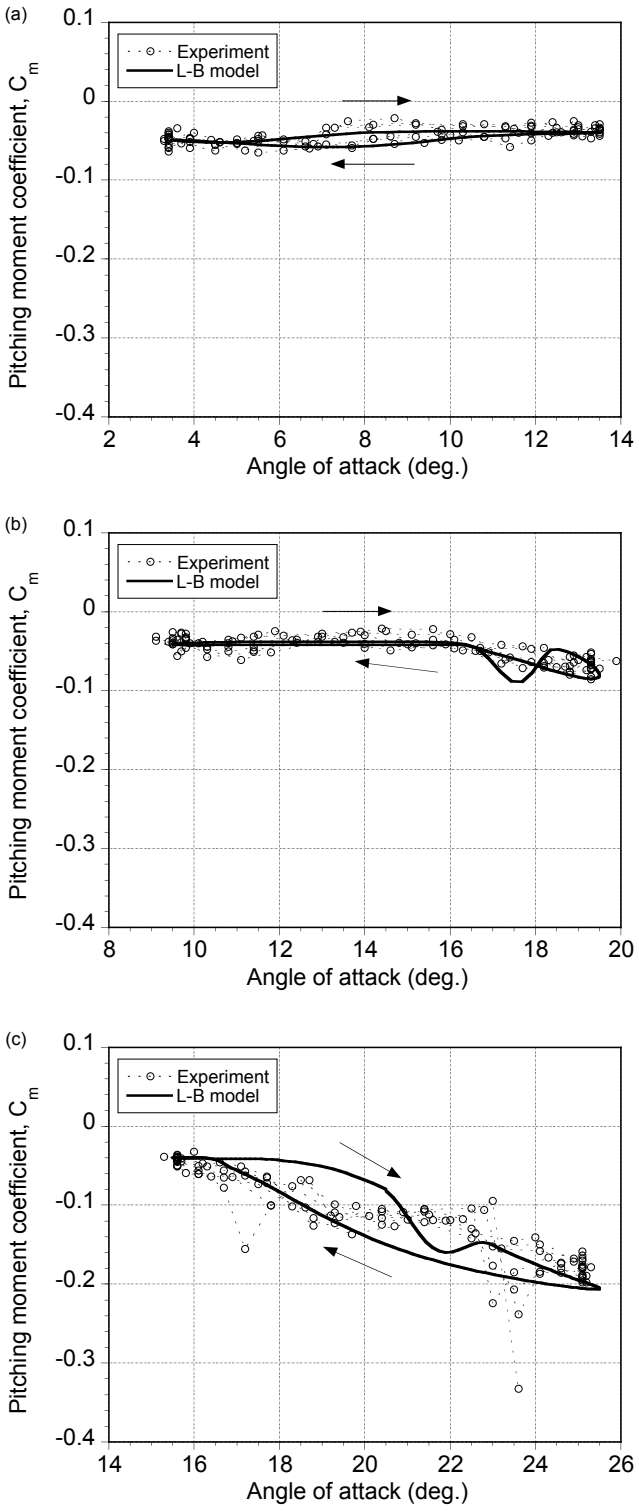

Figure 4.9: Variation of the pitching moment coefficient with angle of attack for a reduced frequency $k = 0.026$ and angle of attack amplitude $\alpha_{\text{amp}} = 5.5°$ (a) $\alpha_{\text{mean}} = 8°$, (b) $\alpha_{\text{mean}} = 14°$, and (c) $\alpha_{\text{mean}} = 20°$.

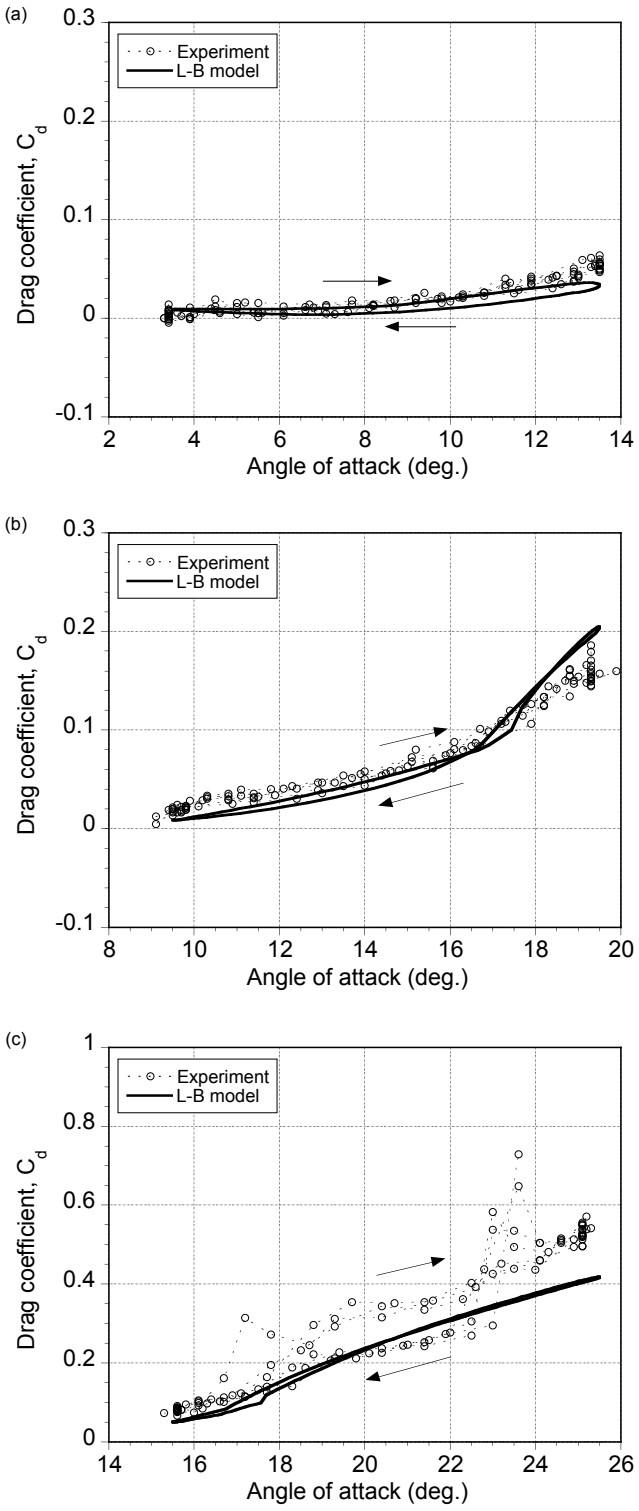

Figure 4.10: Variation of the drag coefficient with angle of attack for a reduced frequency $k = 0.026$ and angle of attack amplitude $\alpha_{\text{amp}} = 5.5^\circ$ (a) $\alpha_{\text{mean}} = 8^\circ$, (b) $\alpha_{\text{mean}} = 14^\circ$, and (c) $\alpha_{\text{mean}} = 20^\circ$.

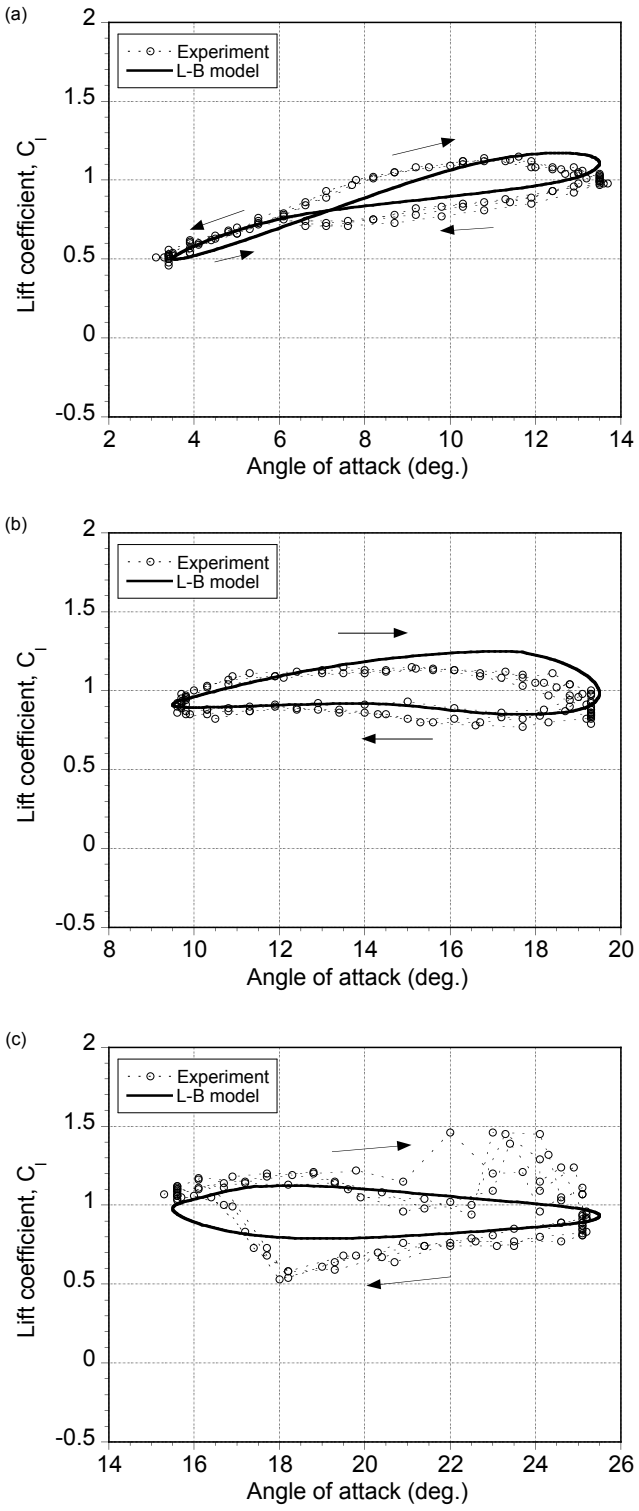

Figure 4.11: Variation of the lift coefficient with angle of attack for a reduced frequency $k = 0.05$ and angle of attack amplitude $\alpha_{\text{amp}} = 5.5^\circ$ (a) $\alpha_{\text{mean}} = 8^\circ$, (b) $\alpha_{\text{mean}} = 14^\circ$, and (c) $\alpha_{\text{mean}} = 20^\circ$.

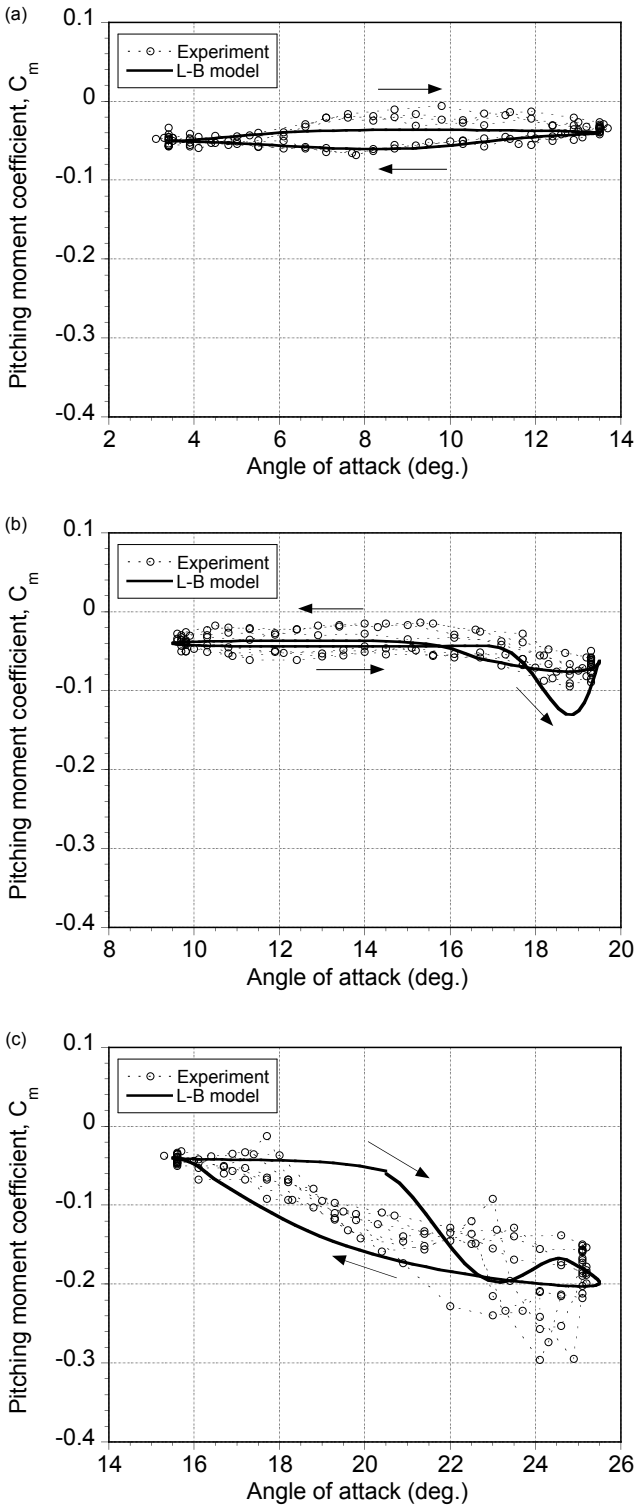

Figure 4.12: Variation of the pitching moment coefficient with angle of attack for a reduced frequency $k = 0.05$ and angle of attack amplitude $\alpha_{\text{amp}} = 5.5^\circ$ (a) $\alpha_{\text{mean}} = 8^\circ$, (b) $\alpha_{\text{mean}} = 14^\circ$, and (c) $\alpha_{\text{mean}} = 20^\circ$.

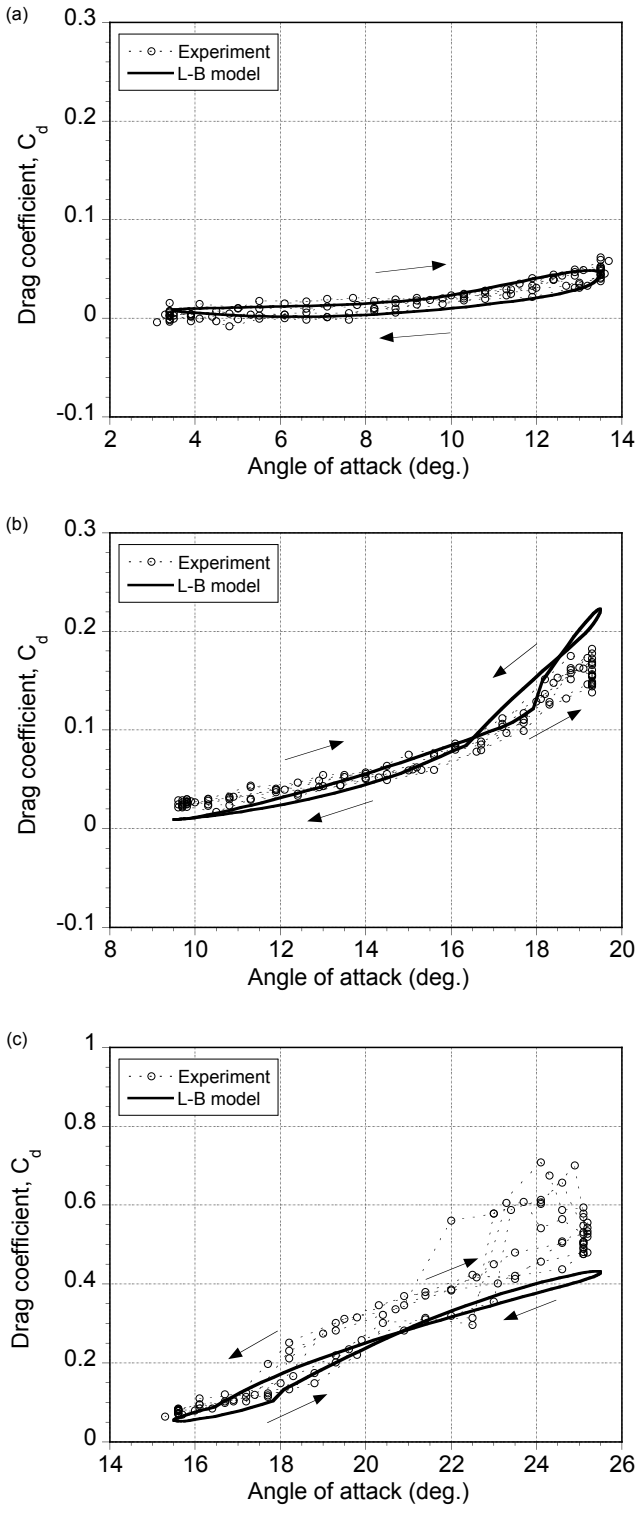

Figure 4.13: Variation of the drag coefficient with angle of attack for a reduced frequency $k = 0.05$ and angle of attack amplitude $\alpha_{\text{amp}} = 5.5^\circ$ (a) $\alpha_{\text{mean}} = 8^\circ$, (b) $\alpha_{\text{mean}} = 14^\circ$, and (c) $\alpha_{\text{mean}} = 20^\circ$.

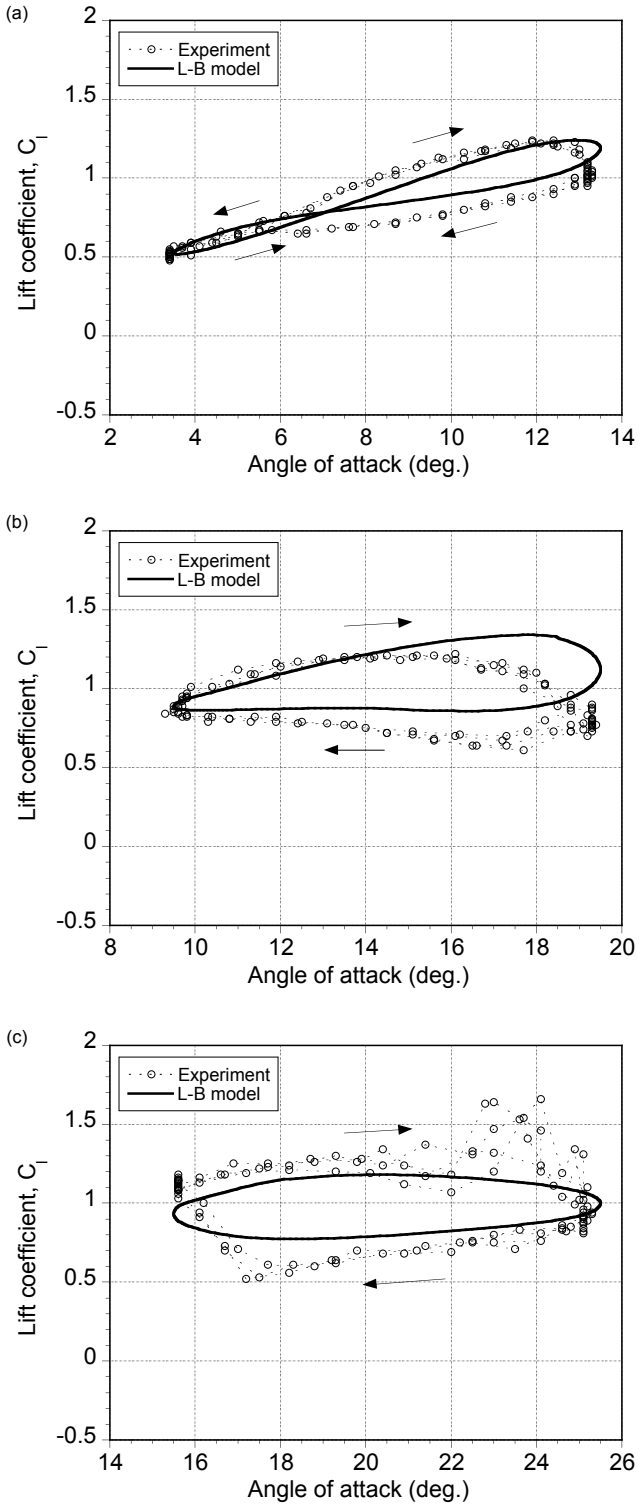

Figure 4.14: Variation of the lift coefficient with angle of attack for a reduced frequency $k = 0.077$ and angle of attack amplitude $\alpha_{\text{amp}} = 5.5^\circ$ (a) $\alpha_{\text{mean}} = 8^\circ$, (b) $\alpha_{\text{mean}} = 14^\circ$, and (c) $\alpha_{\text{mean}} = 20^\circ$.

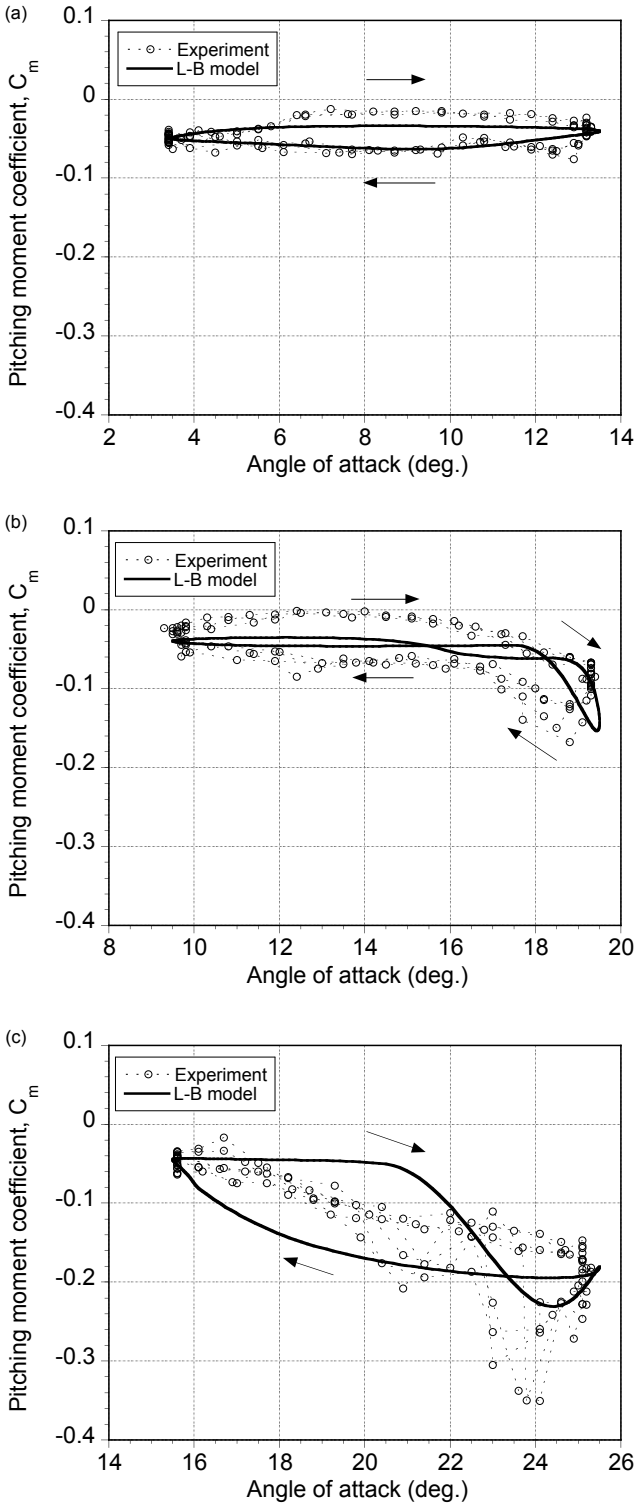

Figure 4.15: Variation of the pitching moment coefficient with angle of attack for a reduced frequency $k = 0.077$ and angle of attack amplitude $\alpha_{\text{amp}} = 5.5°$ (a) $\alpha_{\text{mean}} = 8°$, (b) $\alpha_{\text{mean}} = 14°$, and (c) $\alpha_{\text{mean}} = 20°$.

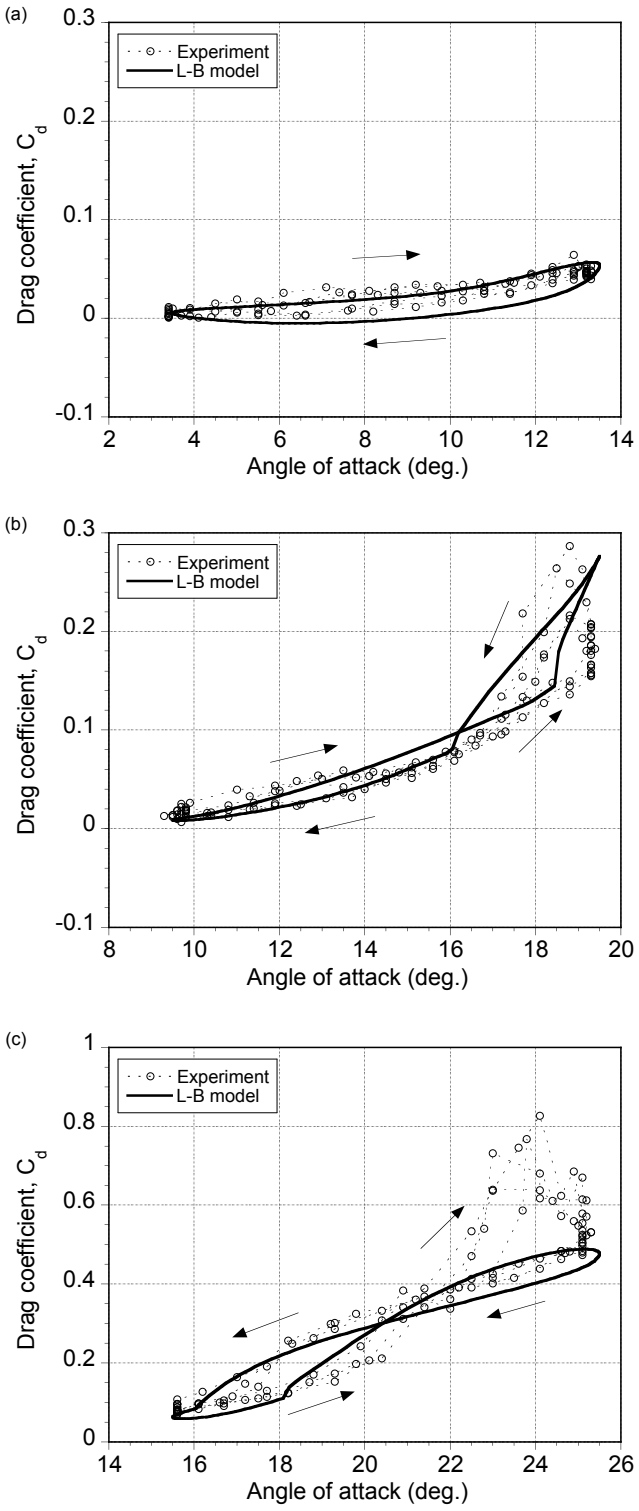

Figure 4.16: Variation of the drag coefficient with angle of attack for a reduced frequency $k = 0.077$ and angle of attack amplitude $\alpha_{\text{amp}} = 5.5^\circ$ (a) $\alpha_{\text{mean}} = 8^\circ$, (b) $\alpha_{\text{mean}} = 14^\circ$, and (c) $\alpha_{\text{mean}} = 20^\circ$.

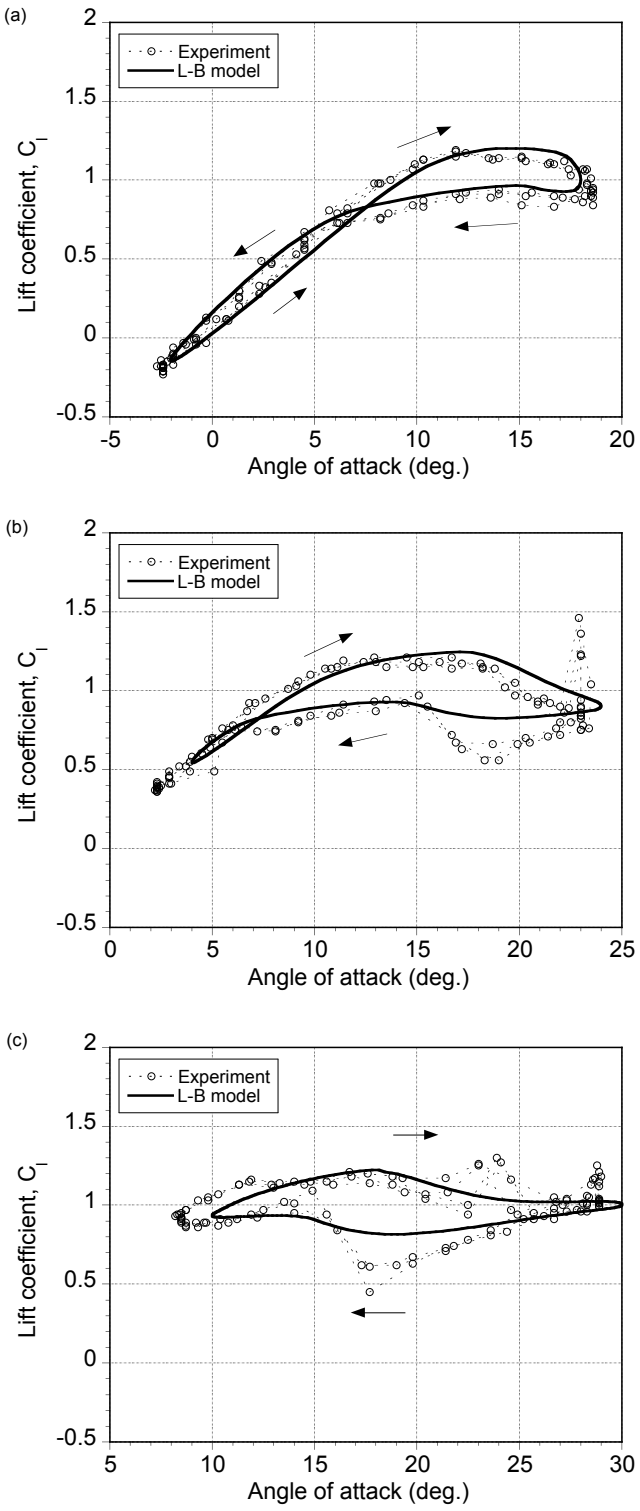

Figure 4.17: Variation of the lift coefficient with angle of attack for a reduced frequency $k = 0.026$ and angle of attack amplitude $\alpha_{\text{amp}} = 10^\circ$ (a) $\alpha_{\text{mean}} = 8^\circ$, (b) $\alpha_{\text{mean}} = 14^\circ$, and (c) $\alpha_{\text{mean}} = 20^\circ$.

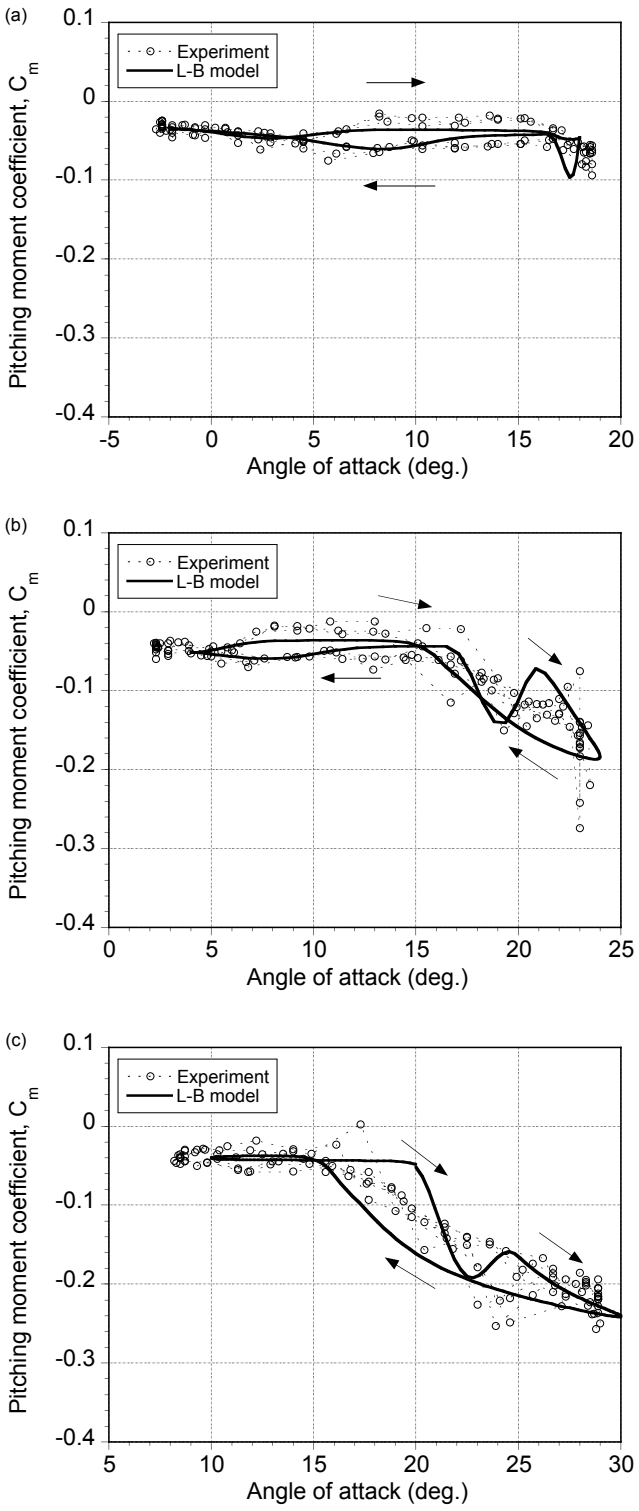

Figure 4.18: Variation of the pitching moment coefficient with angle of attack for a reduced frequency $k = 0.026$ and angle of attack amplitude $\alpha_{\text{amp}} = 10^\circ$ (a) $\alpha_{\text{mean}} = 8^\circ$, (b) $\alpha_{\text{mean}} = 14^\circ$, and (c) $\alpha_{\text{mean}} = 20^\circ$.

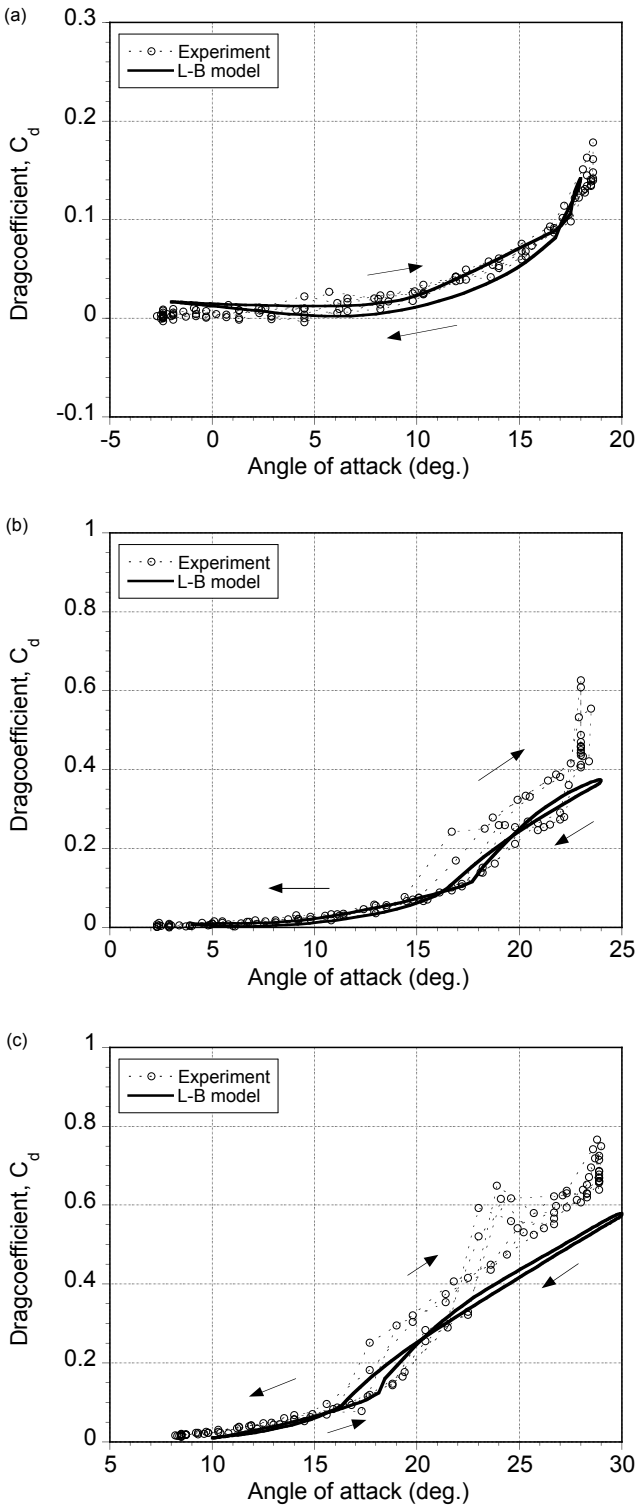

Figure 4.19: Variation of the drag coefficient with angle of attack for a reduced frequency $k = 0.026$ and angle of attack amplitude $\alpha_{\text{amp}} = 10^\circ$ (a) $\alpha_{\text{mean}} = 8^\circ$, (b) $\alpha_{\text{mean}} = 14^\circ$, and (c) $\alpha_{\text{mean}} = 20^\circ$.

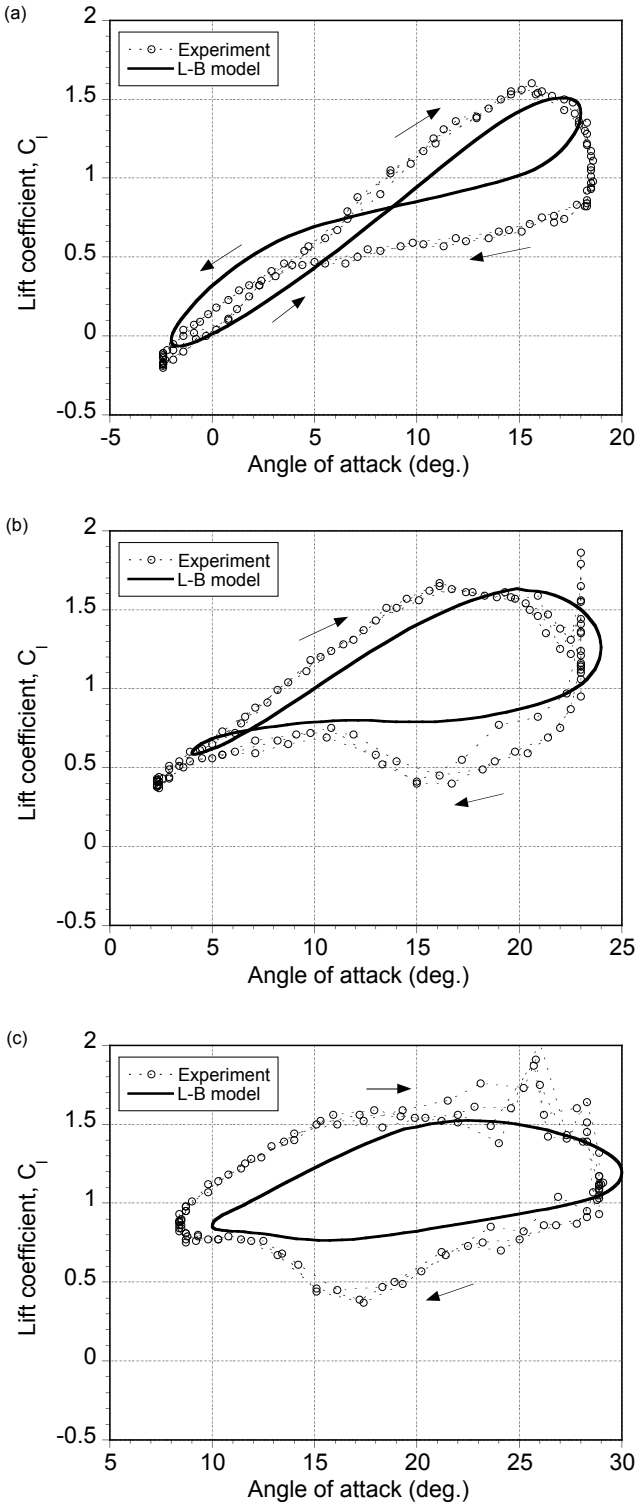

Figure 4.20: Variation of the lift coefficient with angle of attack for a reduced frequency $k = 0.077$ and angle of attack amplitude $\alpha_{\text{amp}} = 10^\circ$ (a) $\alpha_{\text{mean}} = 8^\circ$, (b) $\alpha_{\text{mean}} = 14^\circ$, and (c) $\alpha_{\text{mean}} = 20^\circ$.

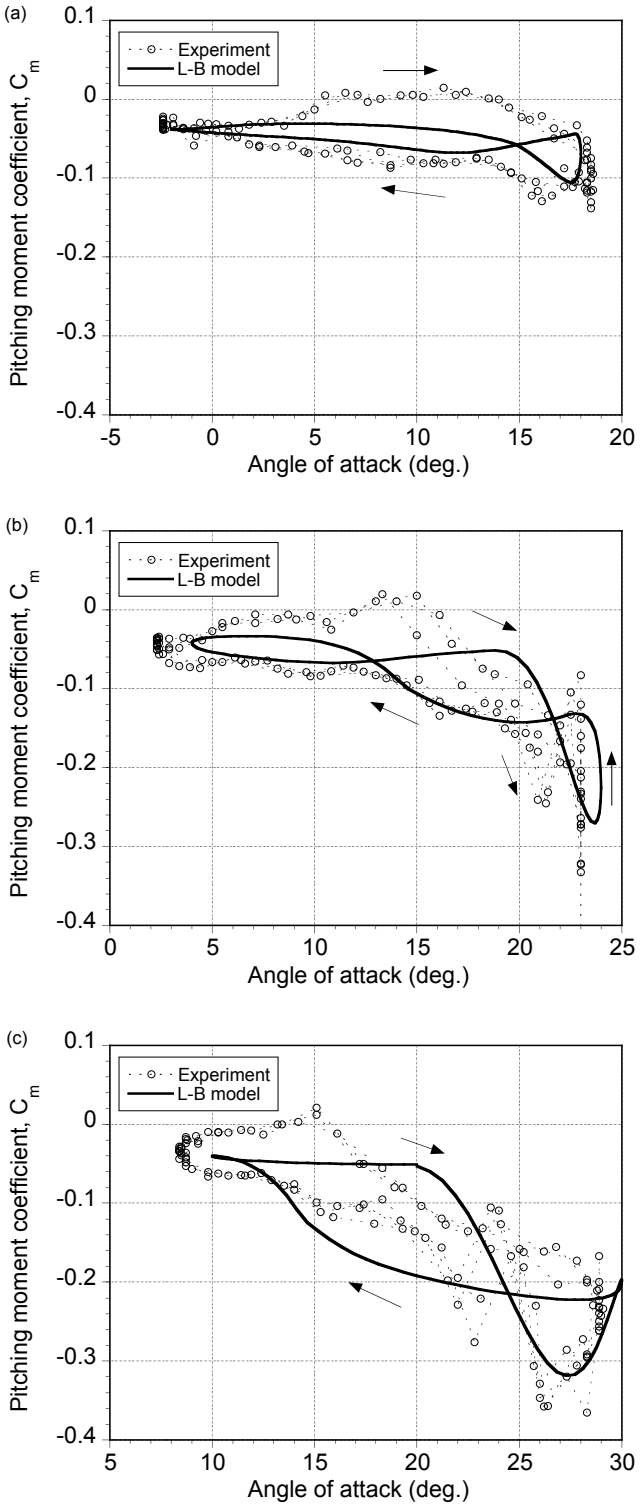

Figure 4.21: Variation of the pitching moment coefficient with angle of attack for a reduced frequency $k = 0.077$ and angle of attack amplitude $\alpha_{\text{amp}} = 10^\circ$ (a) $\alpha_{\text{mean}} = 8^\circ$, (b) $\alpha_{\text{mean}} = 14^\circ$, and (c) $\alpha_{\text{mean}} = 20^\circ$.

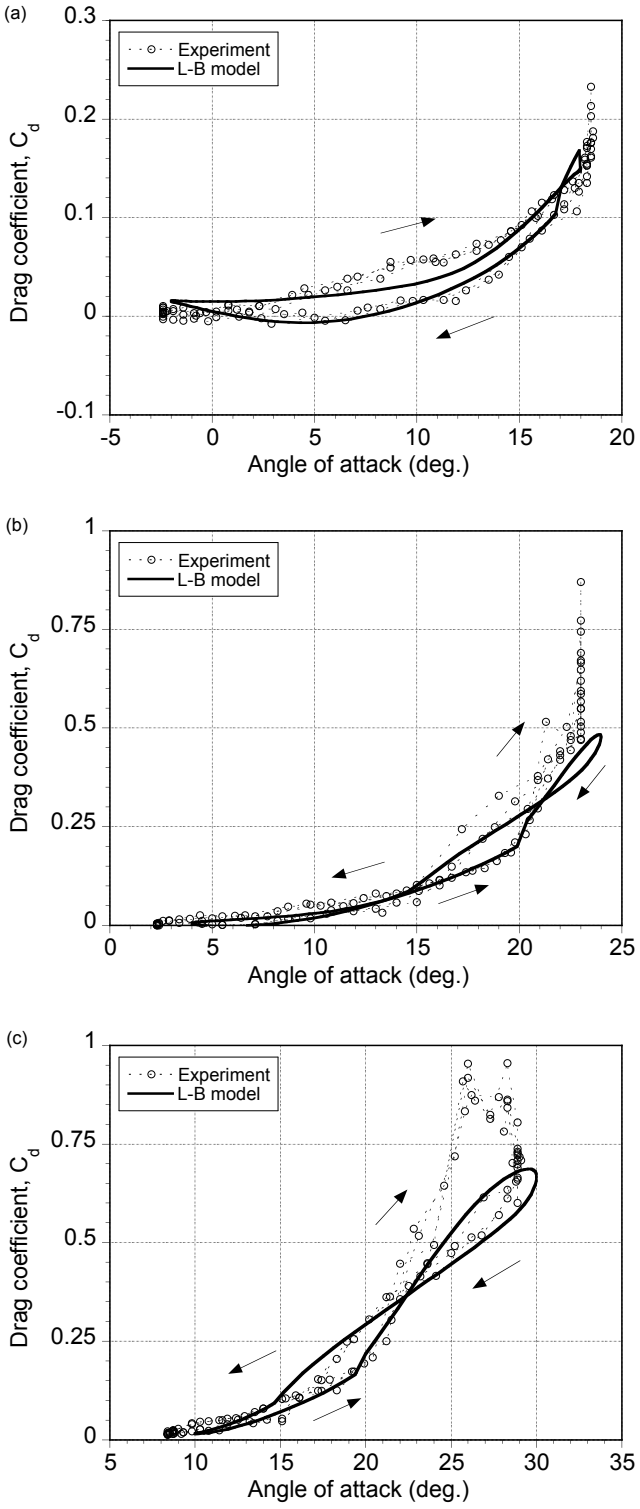

Figure 4.22: Variation of the drag coefficient with angle of attack for a reduced frequency $k = 0.077$ and angle of attack amplitude $\alpha_{\text{amp}} = 10^\circ$ (a) $\alpha_{\text{mean}} = 8^\circ$, (b) $\alpha_{\text{mean}} = 14^\circ$, and (c) $\alpha_{\text{mean}} = 20^\circ$.

4.3 NREL Parked Blade Test Validation

In the previous two sections, the airfoil model used to represent the nonlinear aerodynamic characteristics of the S809 airfoil has been validated against experimental measurements. After the unsteady 2D model was defined, the stall model was coupled with the 3D Weissinger–L blade model to account for the three-dimensionality of the flow. The effective angle of attack obtained from the Weissinger–L model is then used as an input to the nonlinear airfoil stall model. The output gives the nonlinear aerodynamic coefficients for the blade. In the next two sections, the coupled stall and blade model will be validated against the measurements from the static and oscillating NREL parked blade test.

In the comprehensive wind turbine tests conducted by NREL [91], experiments were also performed on a blade in the parked position. The parked blade has a linear taper and a nonlinear twist distribution, as shown in Fig. 4.23. A non-aerodynamic attachment is used for sections inboard of $0.25R$, where there is a cylindrical section and then a fairing, which joins with the S809 airfoil. However, a root cut-out of $0.175R$ was used in the numerical study and the S809 airfoil continues up to this root cut-out. The blade pitch is defined with respect to the tip. The geometric angle of attack is defined as the angle between the tunnel center-line and the section chord. To obtain the static parked blade pressure measurements, a 5° step change was made in the blade pitch and then held constant for 8 seconds, after which the measurements were made (see Ref. 91 for the details of the experiment). For oscillating parked blade experiment, the parked blade was pitched sinusoidally, and the pressure measurements were acquired for successive pitch cycles.

4.4 Static Parked Blade Validation

Static parked blade measurements were available for wind speeds of 20 ms^{-1} and 30 ms^{-1}. In this section, the comparison between the predicted loads and

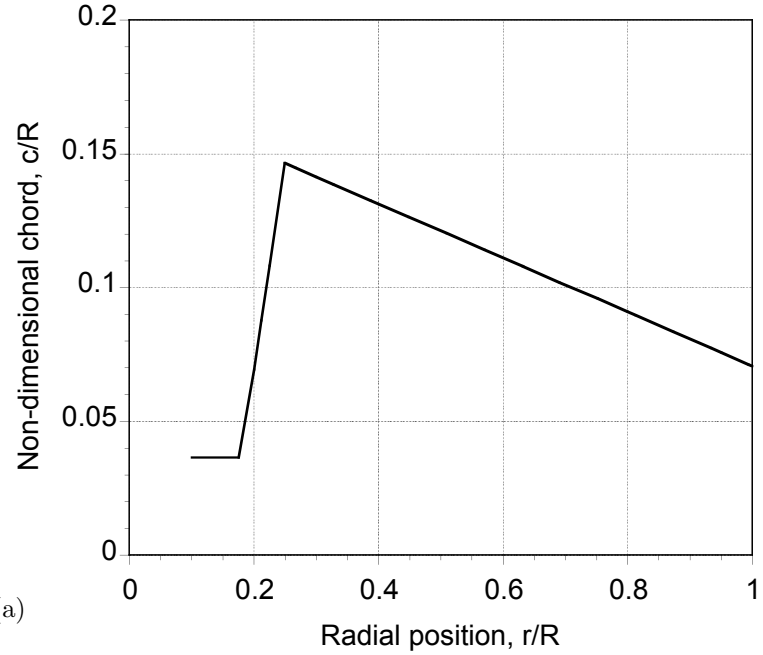

(a)

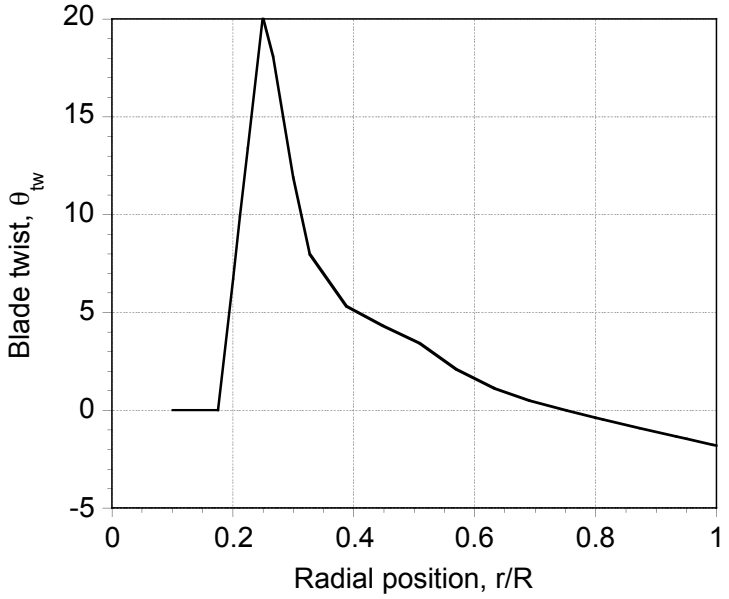

(b)

Figure 4.23: Distribution of (a) chord and (b) nonlinear twist for the Phase VI NREL wind turbine blade.

the experimental measurements will be shown, and the capability of the model to capture the 3D flow physics will be demonstrated. In this section, comparison will be made only for 20 ms^{-1} case as it represents both attached and separated flow conditions on the blade. The higher wind speed case, i.e., 30 ms^{-1} was found to show similar results and did not represent any additional flow physics.

Figures 4.24 through 4.28 show the variation of the C_n with the geometric angle of attack for the 2D tests at $Re = 10^6$. Clearly, the onset of stall and the corresponding values of C_n in the post-stall region are predicted well. It can be seen that the agreement between the model and the measurements is good in the attached flow region for all spanwise sections, except at the furthest inboard section at $0.3R$. This can be attributed to the changes in the blade planform near this spanwise station, and the potential effects of the non-aerodynamic blade attachments. The aerodynamic interference resulting from the geometrical modifications has not been modeled, and this is probably the reason for the over-prediction of the lift-curve slope here. The maximum C_n is, however, slightly under-predicted for most of the blade stations. In the deep stall region, the predicted C_n from the model is higher than the experimental values for all sections except at the outermost section at $0.95R$, where the predicted C_n is smaller.

The variation of C_t is shown in Figs. 4.29 through 4.33. The agreement between the predicted and the experimental C_t values is again good in the attached flow region, except at $0.3R$ and $0.95R$. Notice that the C_t is over-predicted at $0.3R$, again most likely because the effects of the non-aerodynamic blade attachment are not being modeled correctly. The predicted C_t also shows an offset compared to the experimental values for the section at $0.95R$. In the post-stall region, the predicted C_t stays relatively constant for all sections compared to an increase in C_t that was obtained in the experiment. The reason for this discrepancy is not yet fully understood. The increase in C_t for the parked blade compared to the constant values of C_t found in the 2D airfoil tests could be an artifact of the sensitivity of the

method of calculation of the integrated C_t from the measured pressure at discrete points, and the relatively sparse number of pressure taps used in the experiment.

The variation of C_n with blade pitch angle is shown in Fig. 4.34. The effects of the blade twist and the three-dimensionality of the flow on the blade can now be more clearly seen. For the outermost section ($0.95R$), the lift-curve slope is markedly less than the inboard sections. The maximum normal force coefficient is, however, almost the same for all the sections. Figure 4.35 shows the spanwise distribution of lift coefficient on the blade at different pitch angles. For a pitch angle of 90°, it is apparent that most of the blade produces negative lift. With decreasing blade pitch (increasing angle of attack), the outboard sections start producing positive lift. With further increase in the blade pitch, the outer sections begin to stall and the flow separation progresses from tip to root, which is predicted well by the model.

Figure 4.36 shows the corresponding chordwise and spanwise movement of the trailing-edge separation point from the trailing-edge to the leading-edge with a decrease in the blade pitch (increase in geometric angle of attack). At $\theta = 90°$, the flow is fully attached along the entire blade span. At $\theta = 80°$ the flow begins to separate near the blade tip. The separation point then moves towards the leading-edge near the tip while the flow is still attached at the inboard sections of the blade. With further reduction in the pitch angle, the flow separates completely and most of the blade operates with stall.

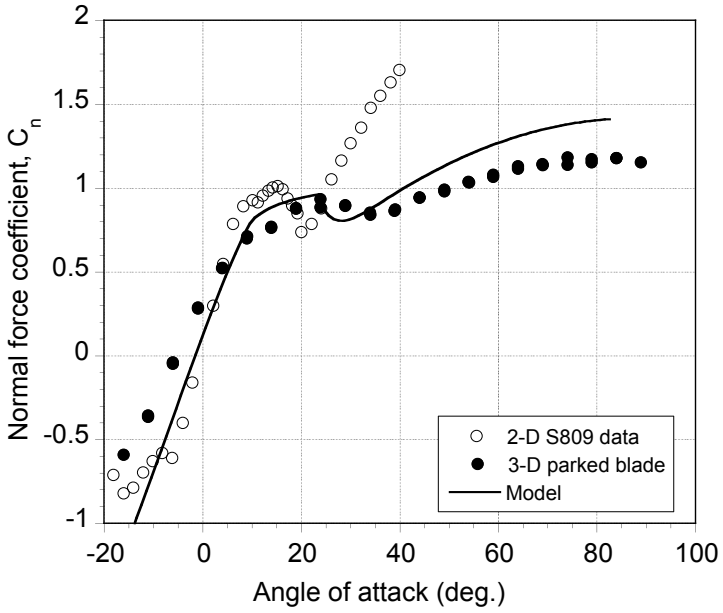

Figure 4.24: Variation of the normal force coefficient of the parked blade with geometric angle of attack at $0.3R$, $Re = 10^6$.

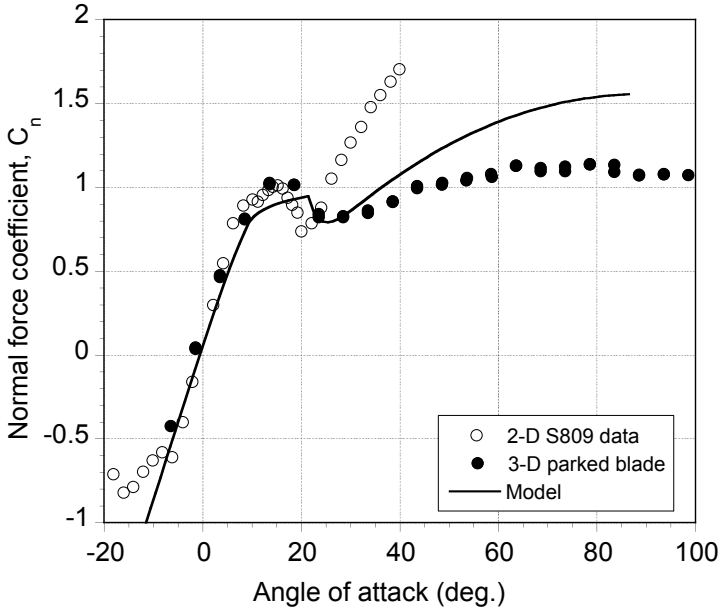

Figure 4.25: Variation of the normal force coefficient of the parked blade with geometric angle of attack at $0.466R$, $Re = 10^6$.

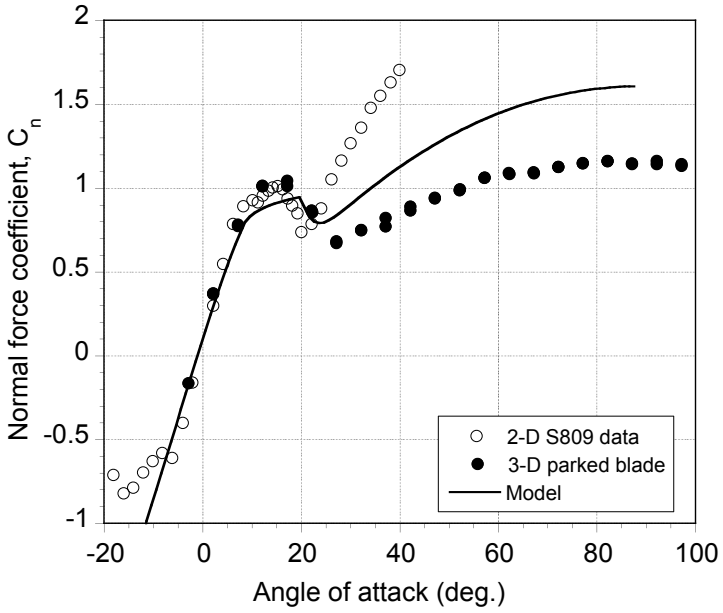

Figure 4.26: Variation of the normal force coefficient of the parked blade with geometric angle of attack at $0.63R$, $Re = 10^6$.

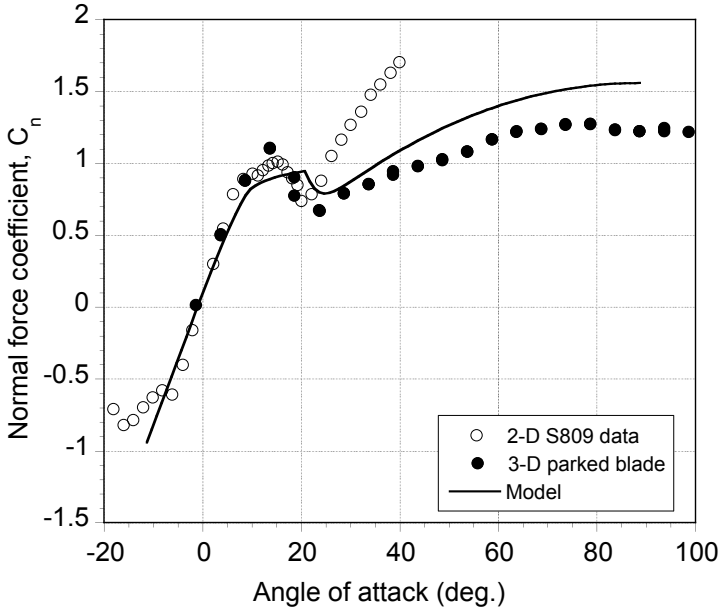

Figure 4.27: Variation of the normal force coefficient of the parked blade with geometric angle of attack at $0.8R$, $Re = 10^6$.

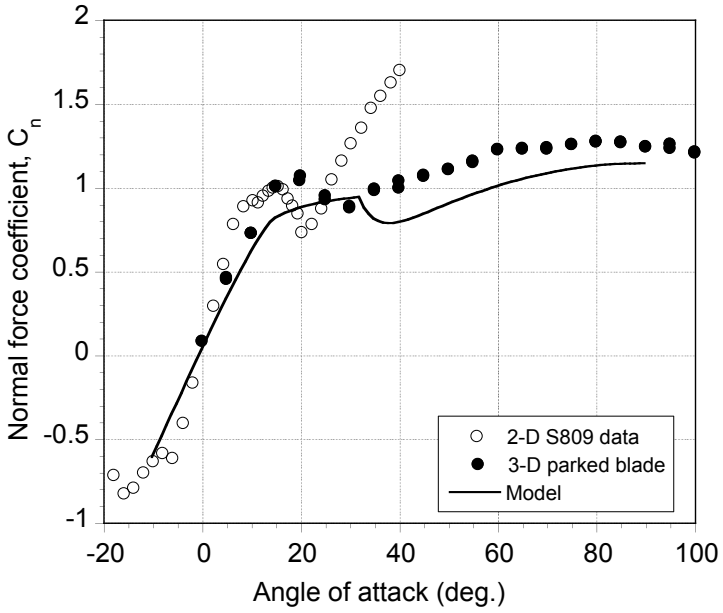

Figure 4.28: Variation of the normal force coefficient of the parked blade with geometric angle of attack at $0.95R$, $Re = 10^6$.

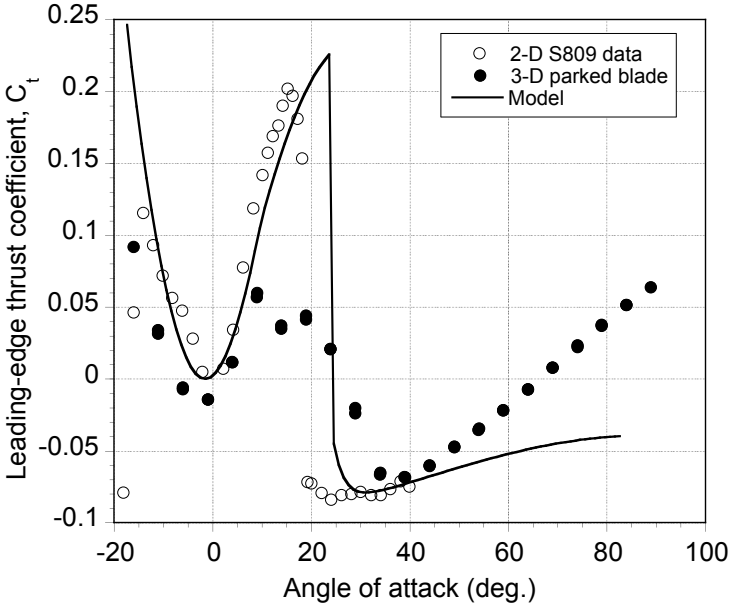

Figure 4.29: Variation of the leading-edge coefficient of the parked blade with geometric angle of attack at $0.3R$, $Re = 10^6$.

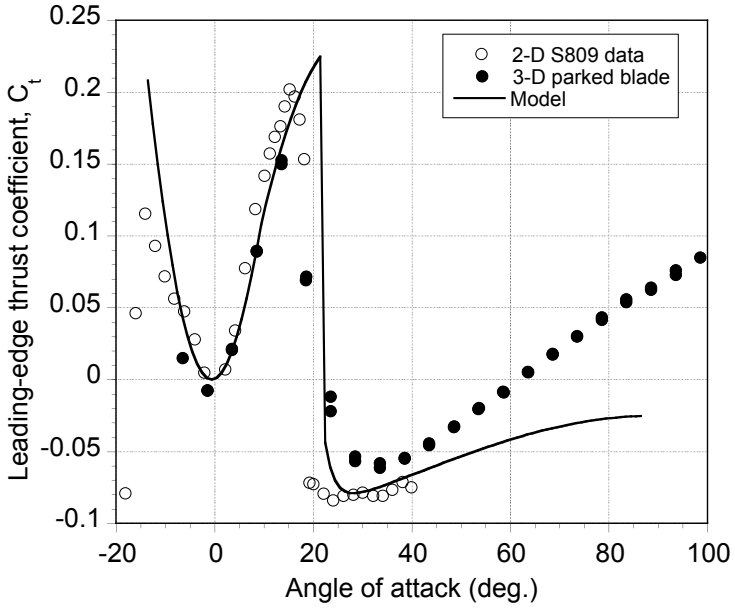

Figure 4.30: Variation of the leading-edge coefficient of the parked blade with geometric angle of attack at $0.466R$, $Re = 10^6$.

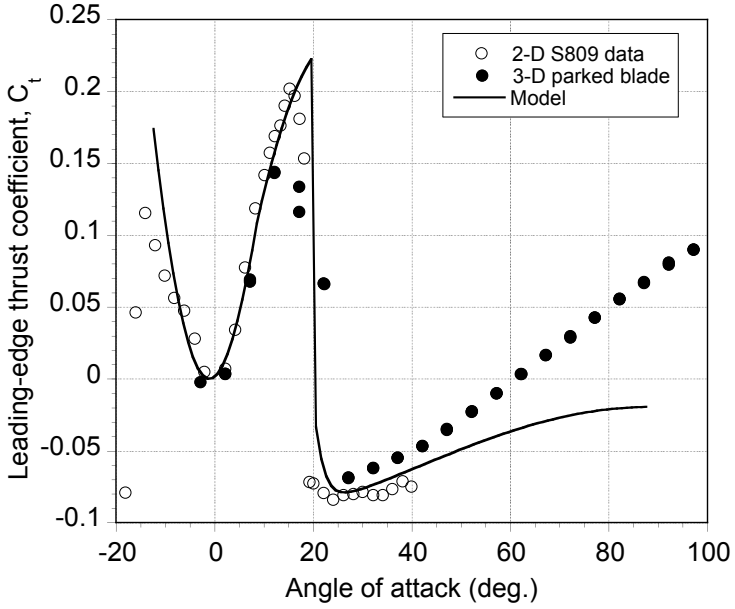

Figure 4.31: Variation of the leading-edge coefficient of the parked blade with geometric angle of attack at $0.63R$, $Re = 10^6$.

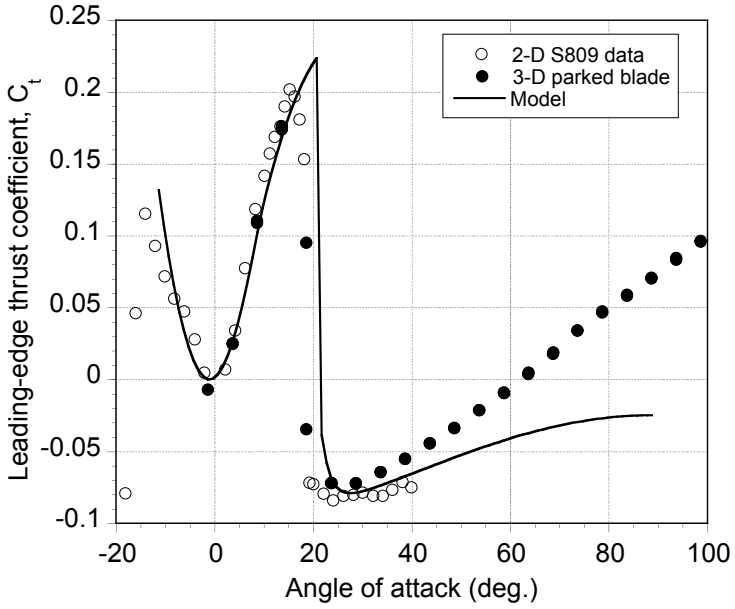

Figure 4.32: Variation of the leading-edge coefficient of the parked blade with geometric angle of attack at $0.8R$, $Re = 10^6$.

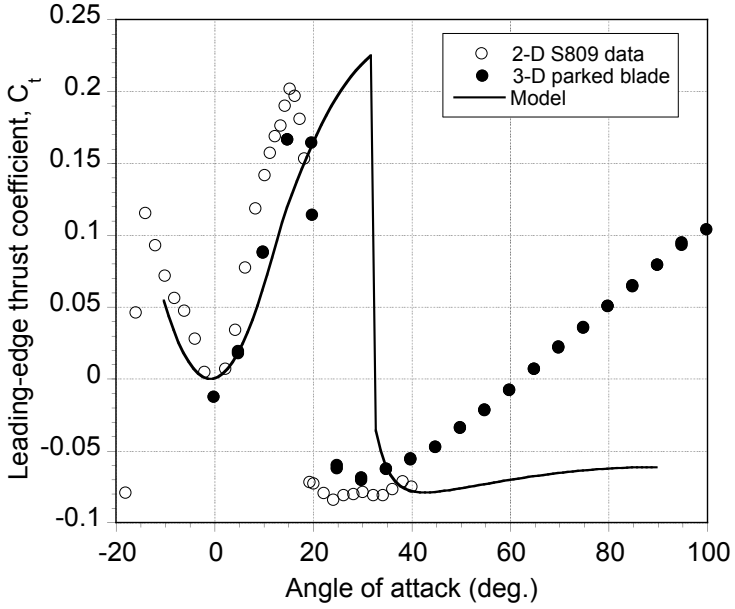

Figure 4.33: Variation of the leading-edge coefficient of the parked blade with geometric angle of attack at $0.95R$, $Re = 10^6$.

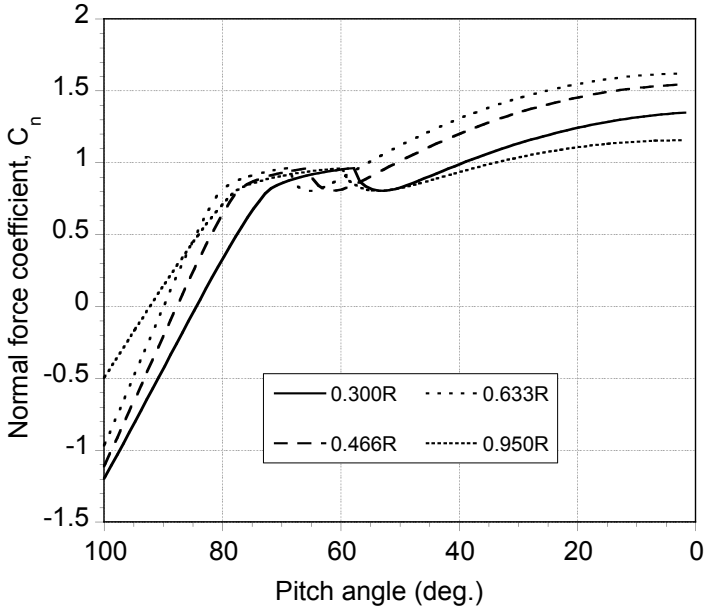

Figure 4.34: Variation of the normal force coefficient of the parked blade with the blade tip pitch angle at the four radial stations.

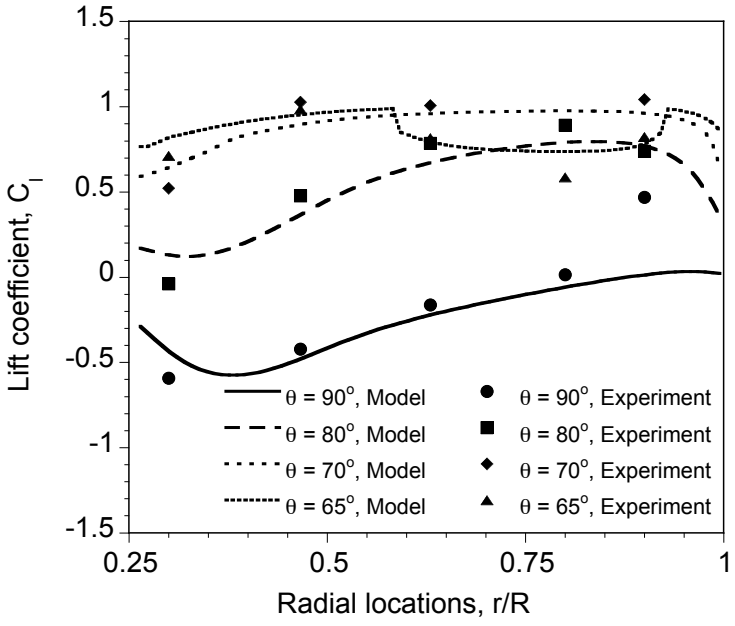

Figure 4.35: Spanwise distribution of the lift coefficient of the parked blade for various blade pitch angles.

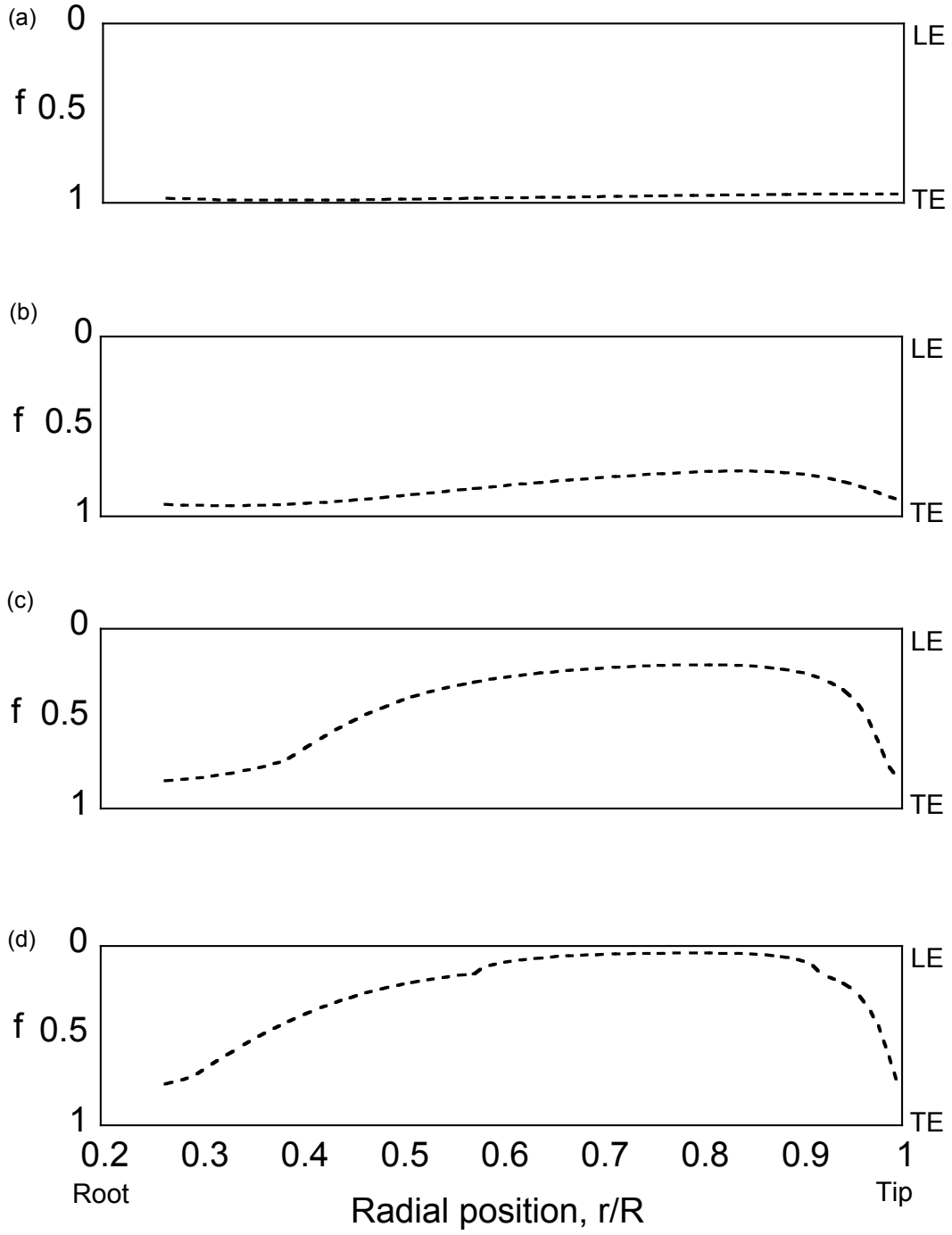

Figure 4.36: Variation of the separation point, f, along the radius of the blade for different pitch angles: (a) 90°, (b) 80°, (c) 70°, (d) 65°.

4.5 Oscillating Parked Blade Validation

The next step in the validation study of the coupled airfoil and blade model was to compare the predictions with the unsteady load measurements. Integrated aerodynamic coefficients obtained from the NREL parked blade test [91] for various reduced frequencies k, mean angles of attack α_{mean}, and angle of attack amplitudes α_{amp} were used to validate the numerical predictions. An extensive dataset from the NREL test is available for five spanwise stations, i.e., at $r/R = 30\%,\ 46\%,\ 63\%,\ 80\%$ and 95%. In this study, only the combinations of k, α_{mean}, and α_{amp} corresponding to those tested at OSU using the S809 airfoil section were used for validation. As described earlier, the blade used in the experiment has a nonlinear, hyperbolic twist distribution. To understand three-dimensionality of the unsteady flow, the oscillating parked blade was tested under a wide range of forcing conditions. In this section, only the cases where the prescribed angle of attack oscillations are enforced at $r/R = 80\%$ by varying the tip pitch angle will be shown.

The variation of C_n against the tip pitch angle is shown in Fig. 4.37 for $k = 0.025$, $\alpha_{\text{amp}} = 5.5^\circ$ and $\alpha_{\text{mean}} = 8^\circ$. Tip pitch angle has been used because the angle of attack measurements were not available. A few representative cycles are plotted for the experimental data to show both the variability and repeatability of the measurements. The flow is mostly attached along the blade span. Because the blade has a hyperbolic twist towards feather (i.e. nose-down) at most of the blade span, inboard stations of the blade are operating at negative angles of attack.

The predictions of C_n were found to be in good agreement with the experimental measurements. As was observed in the static parked blade case, the slope of the lift curve is slightly over-predicted at $r/R = 30\%$, which can be attributed to the non-aerodynamic attachments near the root. The effective angle of attack increases from inboard to outboard sections. Figure 4.38 shows the variation of the pitching moment coefficient at each spanwise station for the same forcing condition. Prediction of the pitching moment is good at inboard sections. The incipient dy-

namic stall can be observed for $r/R = 80\%$, which is not predicted by the model. For $r/R = 95\%$, the pitching moment is underpredicted. However, the reason for this discrepancy is not entirely clear.

For the higher mean angle of attack $\alpha_{\text{mean}} = 14^\circ$ (Fig. 4.39) at $r/R = 80\%$, the outboard sections of the blade are operating in the light stall region but the flow is still attached at the inboard blade sections. The agreement between the predicted and the measured values is reasonably good, except for the outermost station i.e., at $r/R = 95\%$. For $\alpha_{\text{mean}} = 20^\circ$ (see Fig. 4.41), most of the blade is in deep stall. Significant dynamic stall is observed on the outboard blade sections, as is clear from the pitching moment variation shown in Fig. 4.42. Good agreement is obtained between the experimental data and the predictions. The discrepancy in the pitching moment for $\alpha_{\text{mean}} = 8^\circ$ for the blade section at $r/R = 95\%$ might be a result of some unexplained offset in the experimental data; the pitching moment coefficient $C_m \approx -0.05$ for all inboard sections, but suddenly jumps to $C_m \approx 0.0$. This event, however, does not happen for $\alpha_{\text{mean}} = 14^\circ$ (Fig. 4.40) or $\alpha_{\text{mean}} = 20^\circ$ (Fig. 4.42).

Figure 4.43 show the variation of C_n for a higher reduced mean frequency $k = 0.05$ and $\alpha_{\text{mean}} = 14^\circ$. Good agreement is obtained between the experimental data and the predictions. The inboard section at $r/R = 30\%$ is operating in the attached flow regime during the cycle, and the hysteresis in the ailoads is predicted well. The effective angle of attack exceeds the static stall angle for the section outboard of $r/R = 30\%$. It can be seen that the C_n values exceed the maximum static C_n because of the stall delay and the enhanced lift from the shed dynamic stall vortex. The presence of the dynamic stall in the flow is also shown by the moment stall for the outboard section, as shown in Fig. 4.44. Similar observation can be made for $\alpha_{\text{amp}} = 20^\circ$, where most of blade is operating in deep stall. The predictions of C_n and C_m show slight differences (see Figs. 4.45(e) and 4.46(e)) as compared to the measurements.

Similarly, for the higher angle of attack amplitude $\alpha_{\text{amp}} = 10^\circ$ and $\alpha_{\text{mean}} = 20^\circ$ at a reduced frequency of $k = 0.025$, the agreement between the predicted and the measured values for different mean angles of attack is reasonably good (see Figs. 4.47 and 4.48). The flow is attached at the inboard section of the blade at $r/R = 30\%$ for most of the cycle. The section at $r/R = 46\%$ operates in both attached and separated flow regime during the pitching cycle. Higher than static values are obtained for C_n (see Fig. 4.47(b)). A sudden increase in the nose-down pitching moment (see Fig. 4.48(b)) is also observed during the cycle. Outboard sections are operating in deep stall regime but the overall agreement is reasonably good. Similar predictions were obtained for the other forcing conditions, but only representative cases have been shown in this paper to demonstrate the validity of the model over the range of measured operating conditions.

Summary

This chapter has presented the development and validation of a modified Leishman–Beddoes (L–B) unsteady stall model for wind turbine applications. The unsteady airloads predictions on the S809 airfoil. The static stall model was modified to account for the separation point dynamics of the S809 airfoil in the post-stall region. The unsteady stall model was then integrated into a Weissinger-L type of 3D blade model. The numerical predictions of the aerodynamic force coefficients were compared against the NREL static and oscillating parked blade measurements.

The reconstruction of the aerodynamic force coefficients, expressed in terms of the effective trailing-edge flow separation point, was found to be in very good agreement with the 2D measurements for the S809 airfoil over a wide range of Reynolds numbers. Even in the deep stall regime, the predicted values of the normal force coefficient were found to be close to the experimental values. The leading-edge thrust coefficient was, however, underpredicted as compared to the experimental values. The discrepancy in the prediction of the leading-edge thrust coefficient

is probably an artifact of the errors introduced because of the sparse number of pressure taps used in the experiment. Good agreement was also obtained between the predictions and the experimental results for pitch oscillations at several mean angles of attack and reduced frequencies. The results showed encouraging agreement in predicting the onset and consequences of dynamic stall. The model was successful in predicting the dynamic stall characteristics of the S809 airfoil with almost same dynamic time constants as were used in the original L–B model.

A comparison between the predicted and measured aerodynamic force coefficients for both the static and oscillating NREL parked blade measurements showed a very encouraging agreement. The predicted force coefficients were also in agreement with the measured values for the attached flow and the post-stall regime, thus validating the effective integration of the 2D stall model into the 3D blade model. Three-dimensionality of the unsteady flow on the oscillating parked blade was represented well and the prediction of the aerodynamic coefficients over the blade span compared well with the experimental measurements.

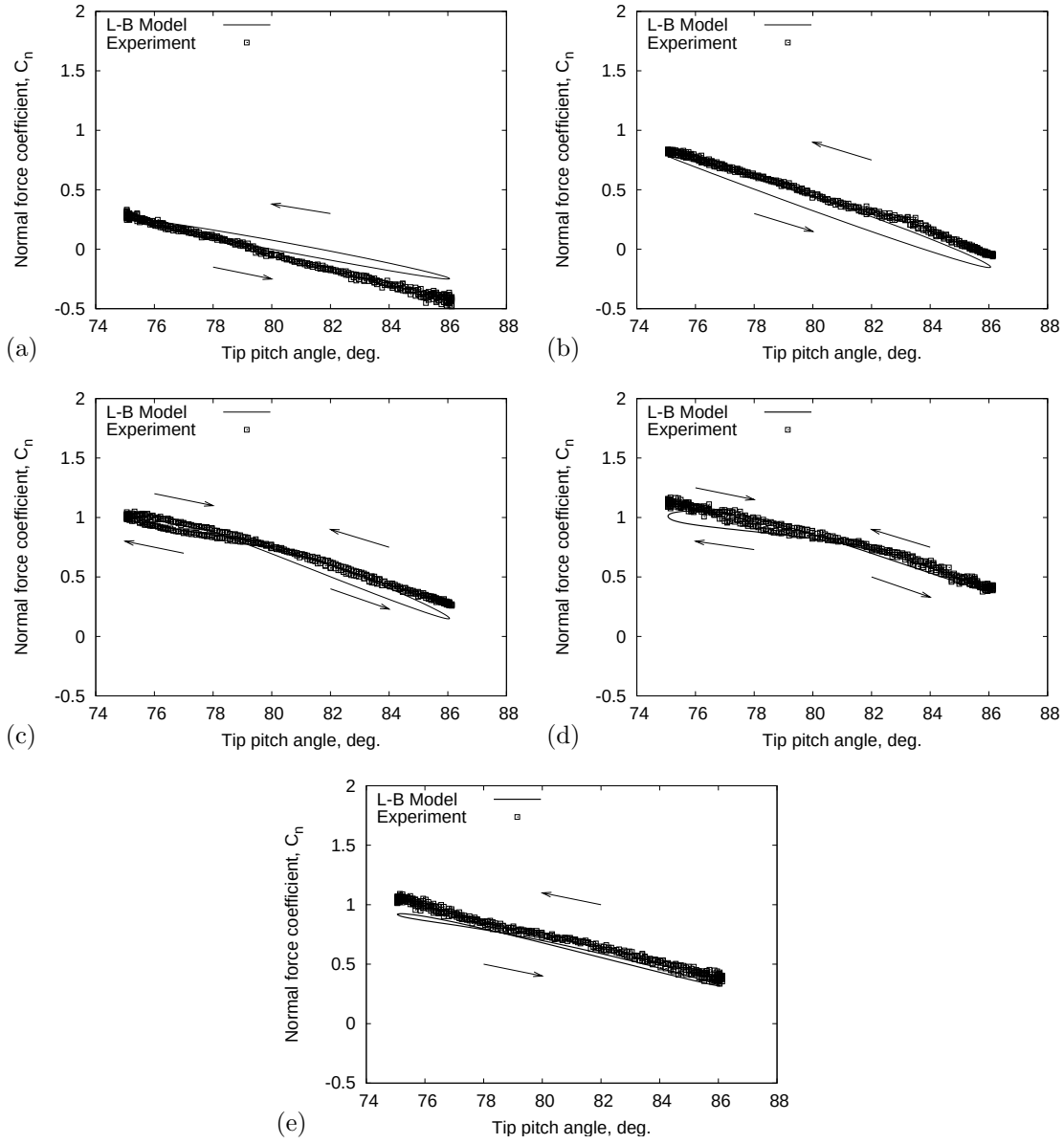

Figure 4.37: Variation of the normal force coefficient with tip pitch angle with spanwise station $r/R = 80\%$ subjected to a reduced frequency $k = 0.025$, angle of attack amplitude $\alpha_{\text{amp}} = 5.5°$ and $\alpha_{\text{mean}} = 8°$. (a) $r/R = 30\%$, (b) $r/R = 46\%$, (c) $r/R = 63\%$, (d) $r/R = 80\%$ and (e) $r/R = 95\%$.

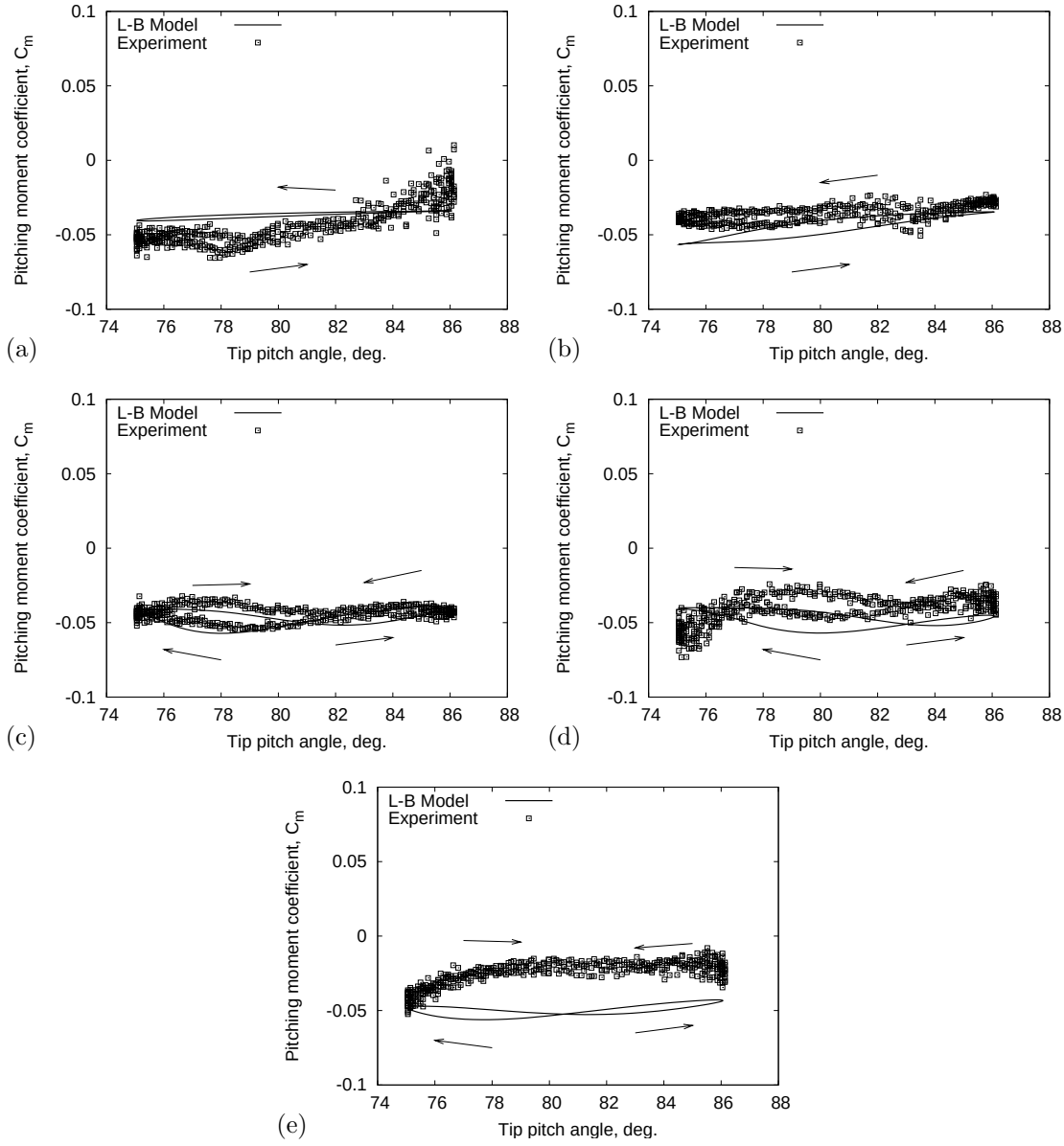

Figure 4.38: Variation of the pitching moment coefficient with tip pitch angle with spanwise station $r/R = 80\%$ subjected to a reduced frequency $k = 0.025$, angle of attack amplitude $\alpha_{\text{amp}} = 5.5°$ and $\alpha_{\text{mean}} = 8°$. (a) $r/R = 30\%$, (b) $r/R = 46\%$, (c) $r/R = 63\%$, (d) $r/R = 80\%$ and (e) $r/R = 95\%$.

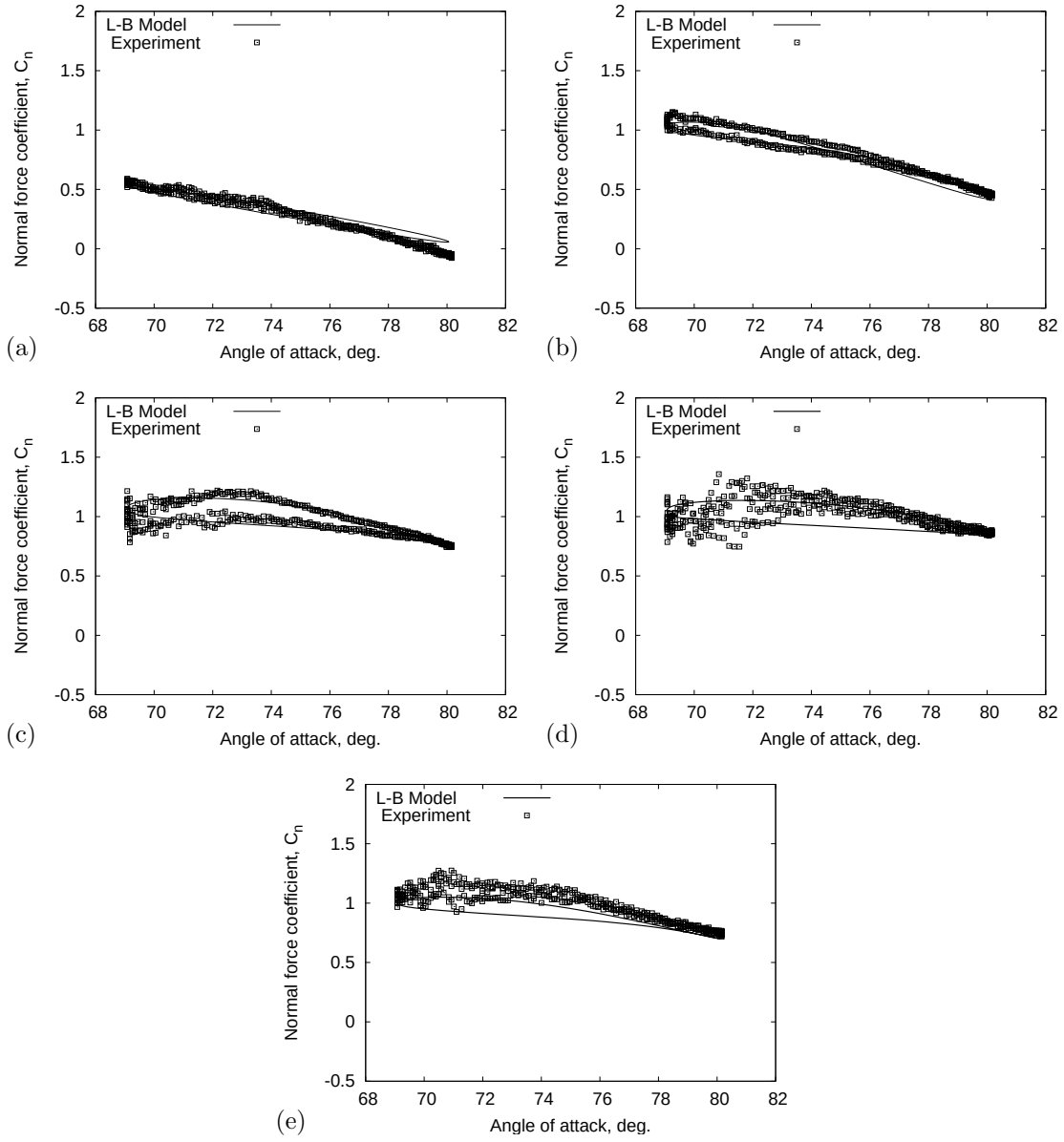

Figure 4.39: Variation of the normal force coefficient with tip pitch angle with spanwise station $r/R = 80\%$ subjected to a reduced frequency $k = 0.025$ and angle of attack amplitude $\alpha_{\text{amp}} = 5.5°$ and $\alpha_{\text{mean}} = 14°$. (a) $r/R = 30\%$, (b) $r/R = 46\%$, (c) $r/R = 63\%$, (d) $r/R = 80\%$ and (e) $r/R = 95\%$.

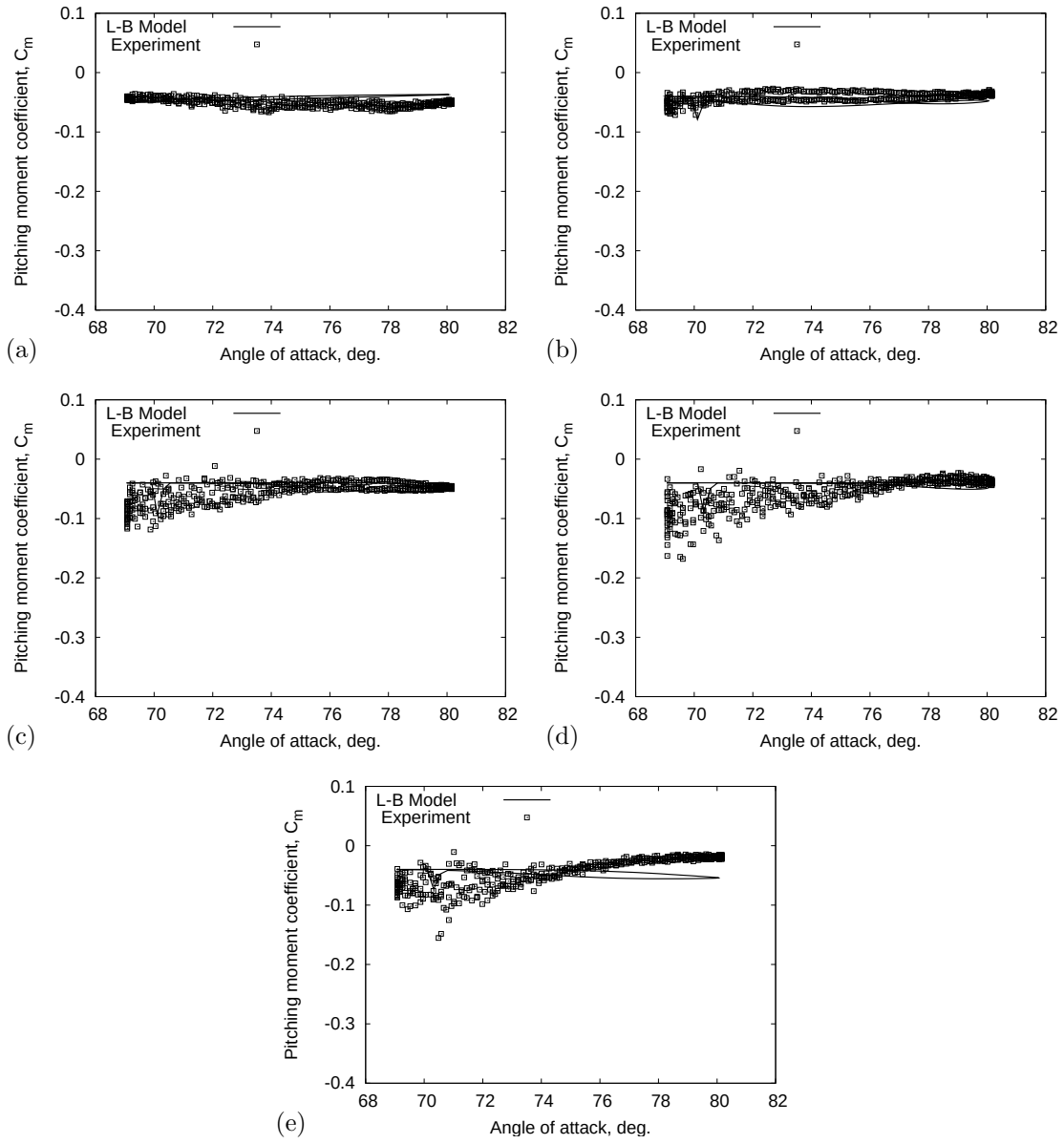

Figure 4.40: Variation of the pitching moment coefficient with tip pitch angle with spanwise station $r/R = 80\%$ subjected to a reduced frequency $k = 0.025$ and angle of attack amplitude $\alpha_{\text{amp}} = 5.5°$ and $\alpha_{\text{mean}} = 14°$. (a) $r/R = 30\%$, (b) $r/R = 46\%$, (c) $r/R = 63\%$, (d) $r/R = 80\%$ and (e) $r/R = 95\%$.

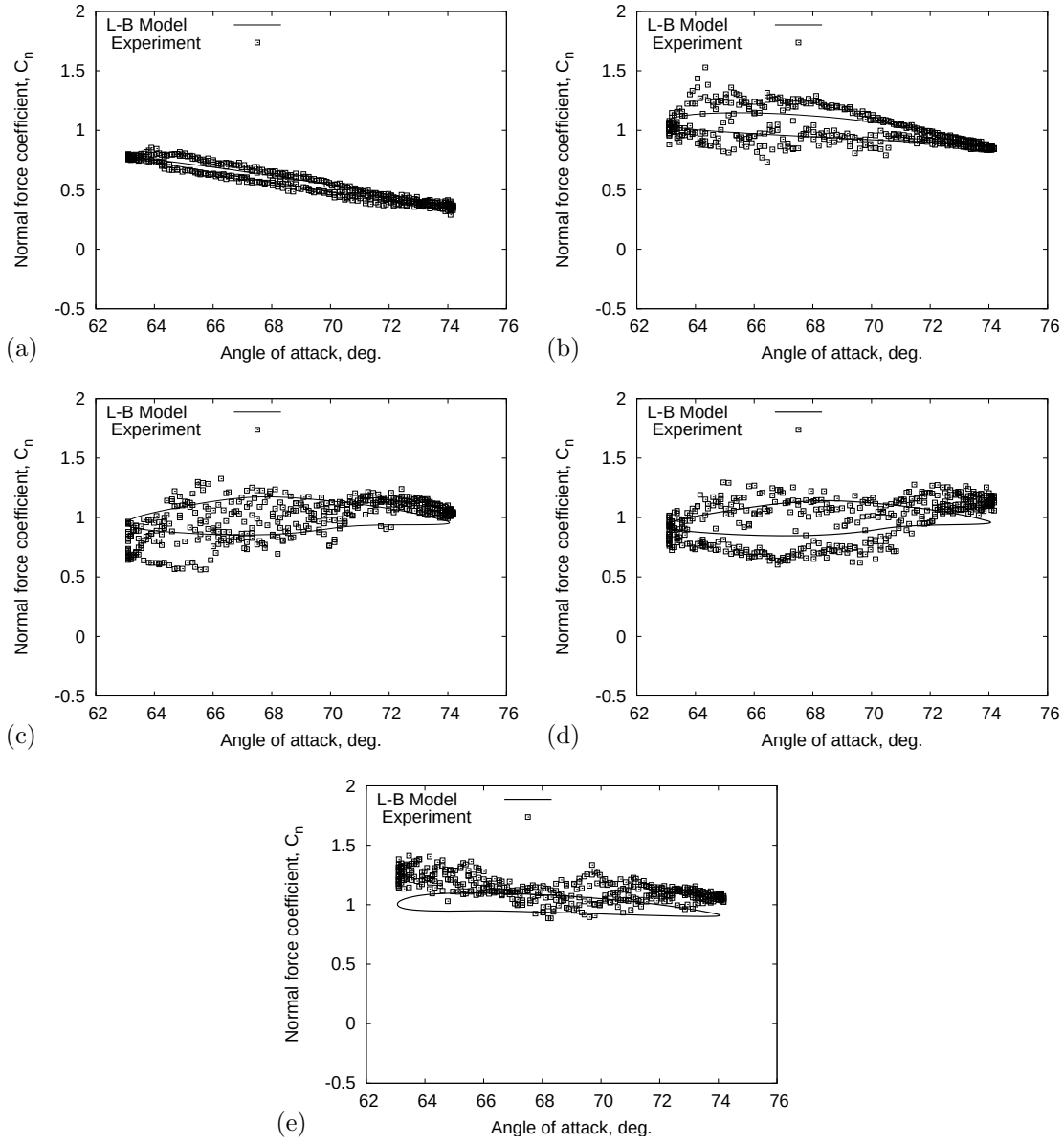

Figure 4.41: Variation of the normal force coefficient with tip pitch angle with spanwise station $r/R = 80\%$ subjected to a reduced frequency $k = 0.025$ and angle of attack amplitude $\alpha_{\text{amp}} = 5.5^\circ$ and $\alpha_{\text{mean}} = 20^\circ$. (a) $r/R = 30\%$, (b) $r/R = 46\%$, (c) $r/R = 63\%$, (d) $r/R = 80\%$ and (e) $r/R = 95\%$.

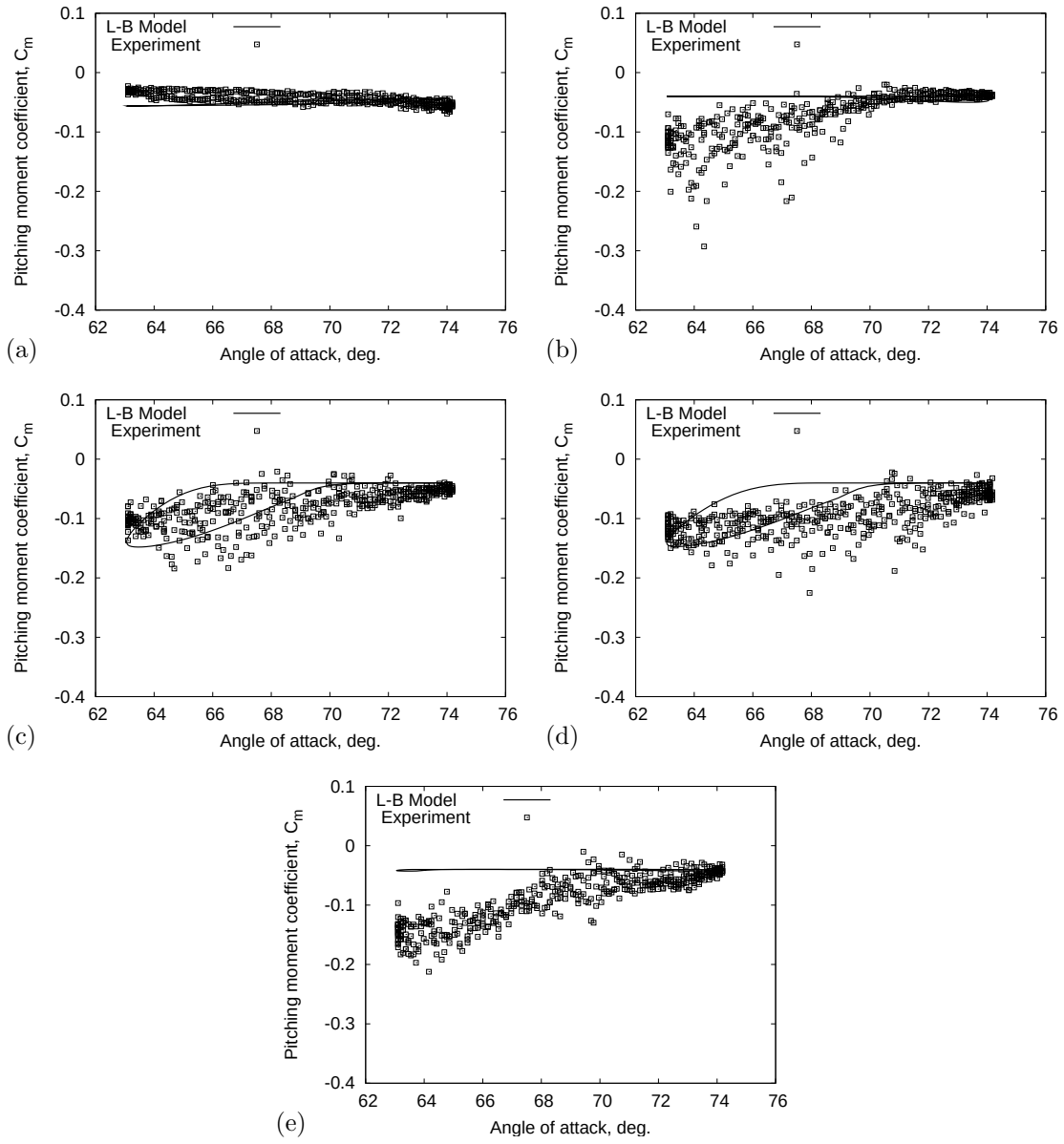

Figure 4.42: Variation of the pitching moment coefficient with tip pitch angle with spanwise station $r/R = 80\%$ subjected to a reduced frequency $k = 0.025$ and angle of attack amplitude $\alpha_{\text{amp}} = 5.5°$ and $\alpha_{\text{mean}} = 20°$. (a) $r/R = 30\%$, (b) $r/R = 46\%$, (c) $r/R = 63\%$, (d) $r/R = 80\%$ and (e) $r/R = 95\%$.

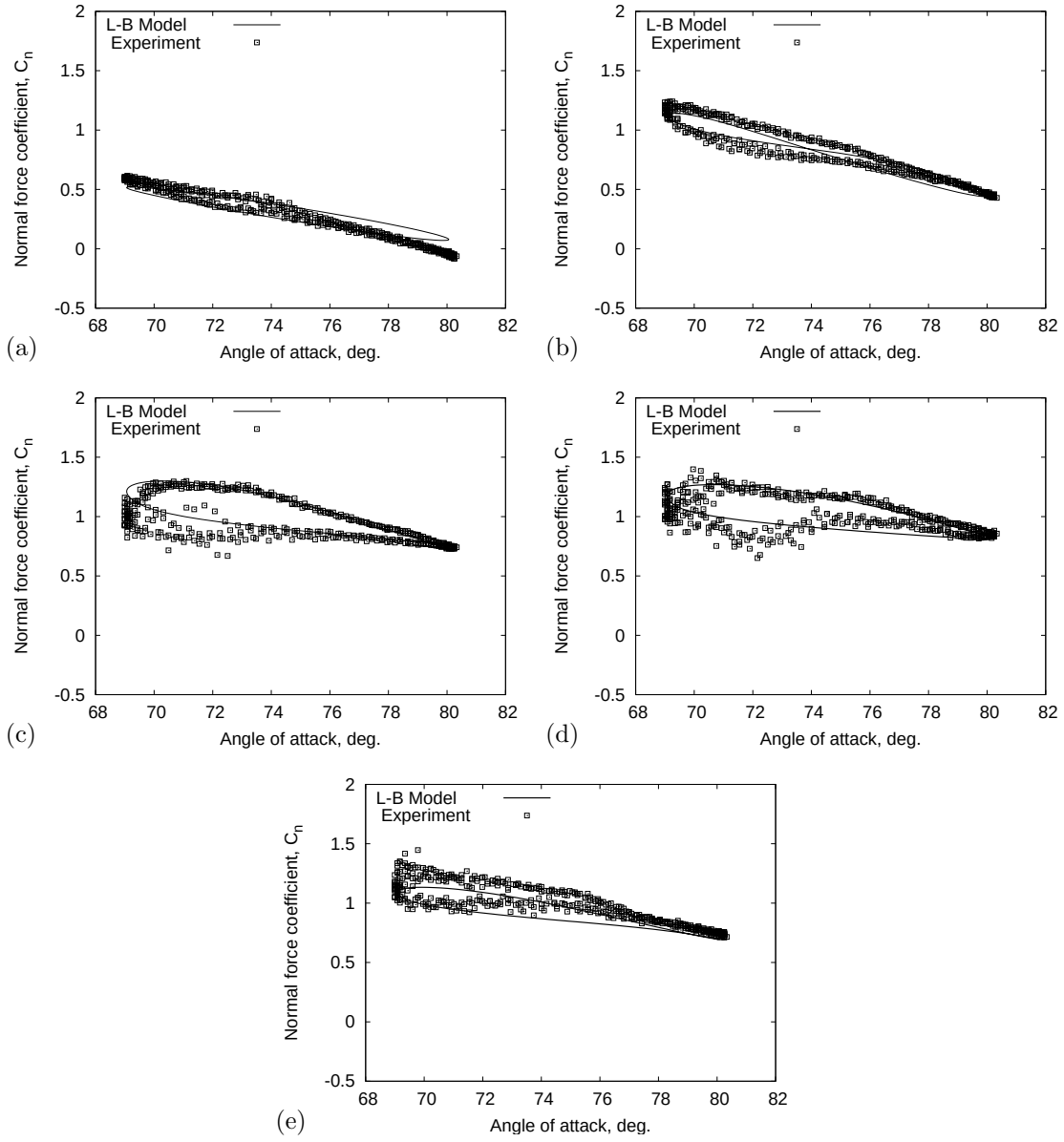

Figure 4.43: Variation of the normal force coefficient with tip pitch angle with spanwise station $r/R = 80\%$ subjected to a reduced frequency $k = 0.05$ and angle of attack amplitude $\alpha_{\text{amp}} = 5.5°$ and $\alpha_{\text{mean}} = 14°$. (a) $r/R = 30\%$, (b) $r/R = 46\%$, (c) $r/R = 63\%$, (d) $r/R = 80\%$ and (e) $r/R = 95\%$.

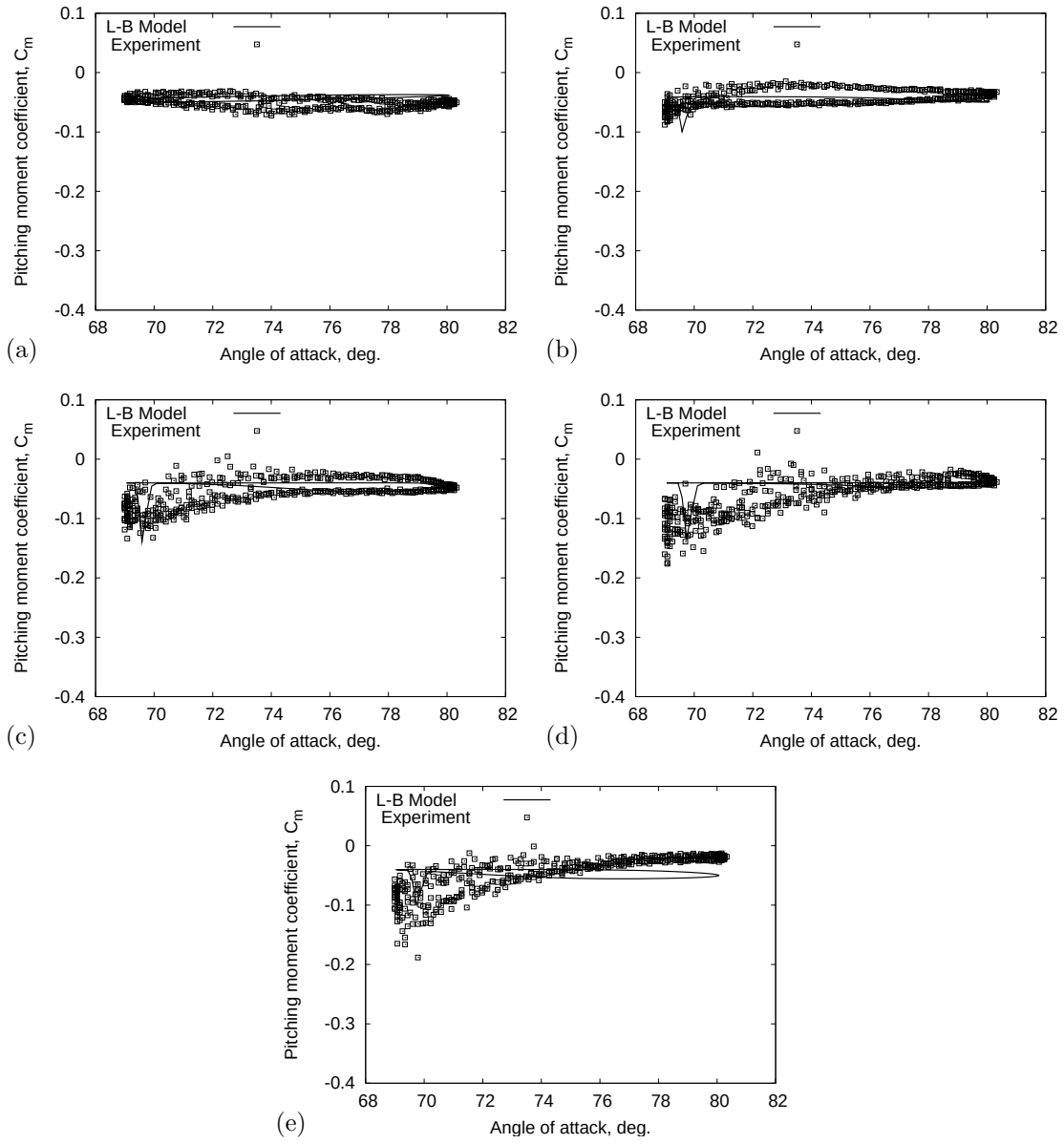

Figure 4.44: Variation of the pitching moment coefficient with tip pitch angle with spanwise station $r/R = 80\%$ subjected to a reduced frequency $k = 0.05$ and angle of attack amplitude $\alpha_{\text{amp}} = 5.5°$ and $\alpha_{\text{mean}} = 14°$. (a) $r/R = 30\%$, (b) $r/R = 46\%$, (c) $r/R = 63\%$, (d) $r/R = 80\%$ and (e) $r/R = 95\%$.

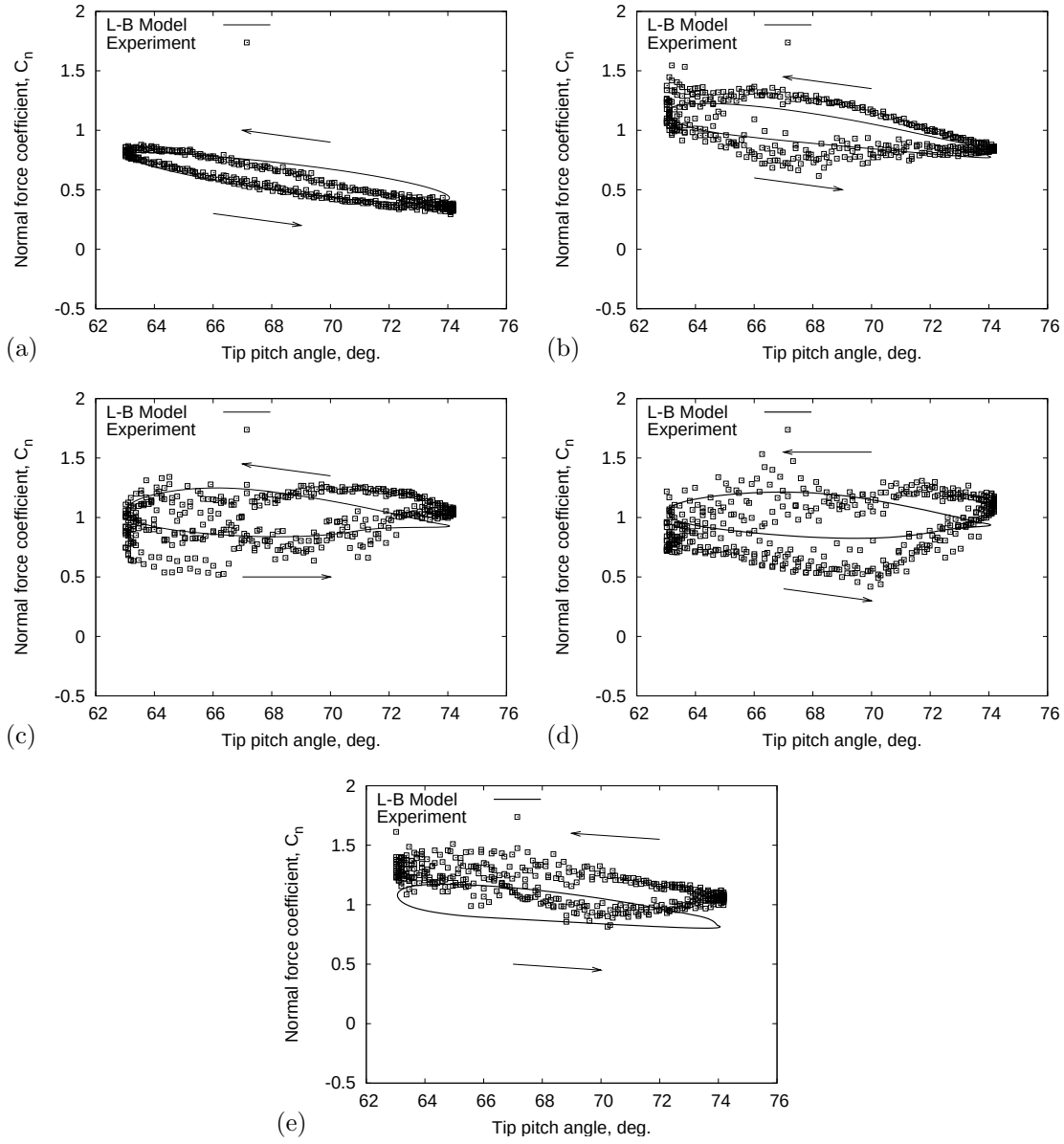

Figure 4.45: Variation of the normal force coefficient with tip pitch angle with spanwise station $r/R = 80\%$ subjected to a reduced frequency $k = 0.05$, angle of attack amplitude $\alpha_{\text{amp}} = 5.5^\circ$ and $\alpha_{\text{mean}} = 20^\circ$. (a) $r/R = 30\%$, (b) $r/R = 46\%$, (c) $r/R = 63\%$, (d) $r/R = 80\%$ and (e) $r/R = 95\%$.

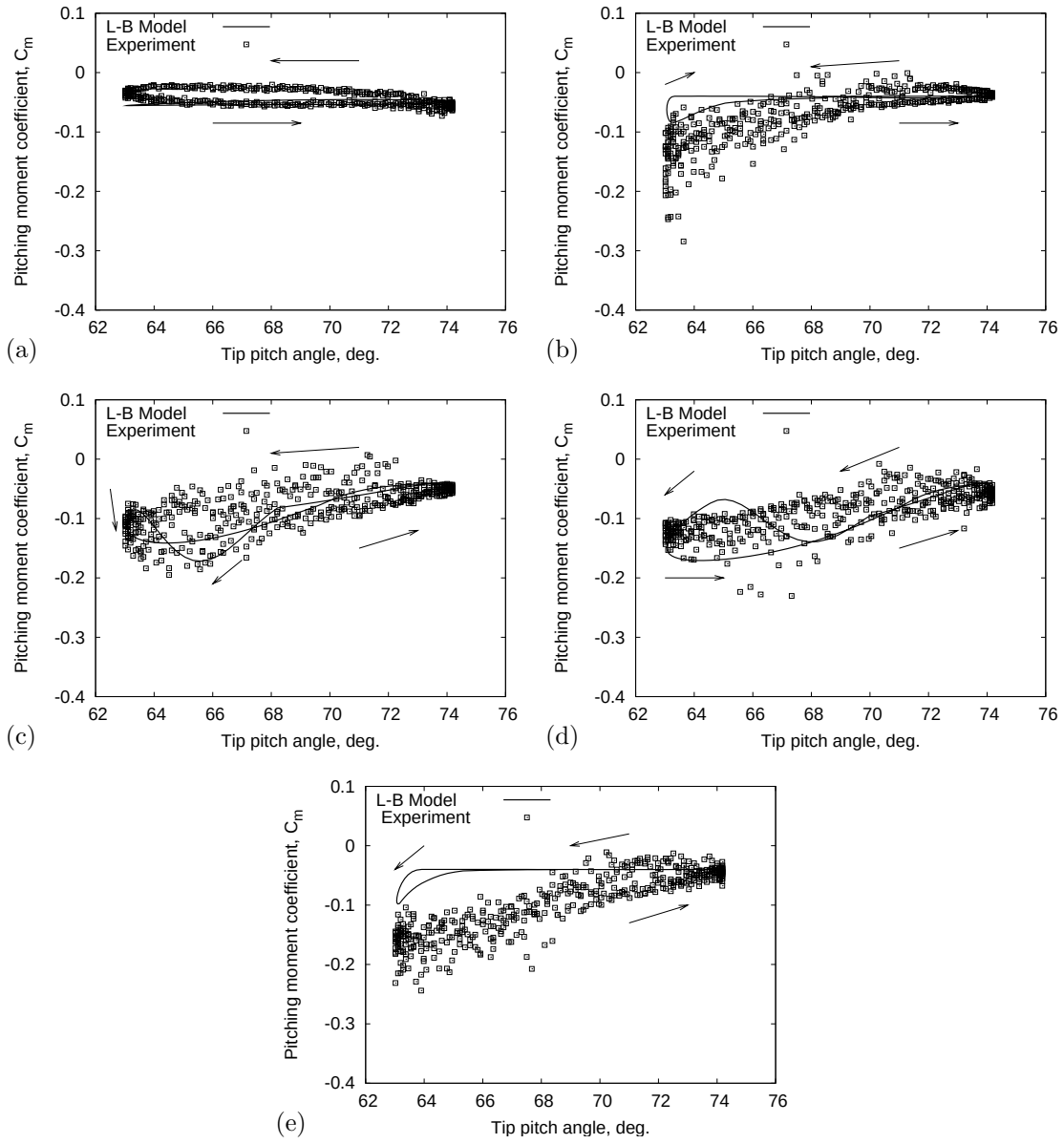

Figure 4.46: Variation of the pitching moment coefficient with tip pitch angle with spanwise station $r/R = 80\%$ subjected to a reduced frequency $k = 0.05$, angle of attack amplitude $\alpha_{\text{amp}} = 5.5°$ and $\alpha_{\text{mean}} = 20°$. (a) $r/R = 30\%$, (b) $r/R = 46\%$, (c) $r/R = 63\%$, (d) $r/R = 80\%$ and (e) $r/R = 95\%$.

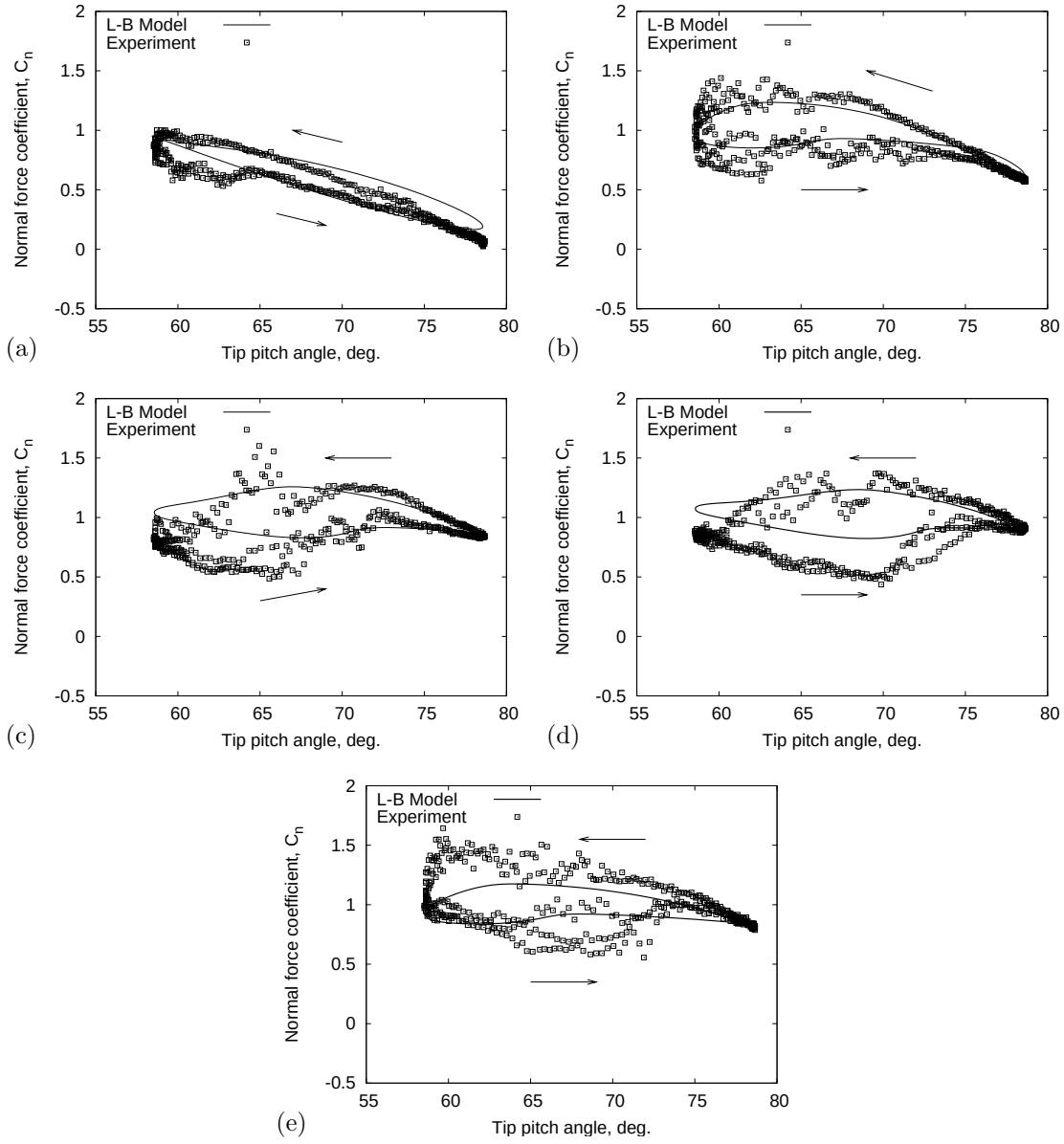

Figure 4.47: Variation of the normal force coefficient with tip pitch angle with spanwise station $r/R = 80\%$ subjected to a reduced frequency $k = 0.025$, angle of attack amplitude $\alpha_{\text{amp}} = 10^\circ$ and $\alpha_{\text{mean}} = 20^\circ$. (a) $r/R = 30\%$, (b) $r/R = 46\%$, (c) $r/R = 63\%$, (d) $r/R = 80\%$ and (e) $r/R = 95\%$.

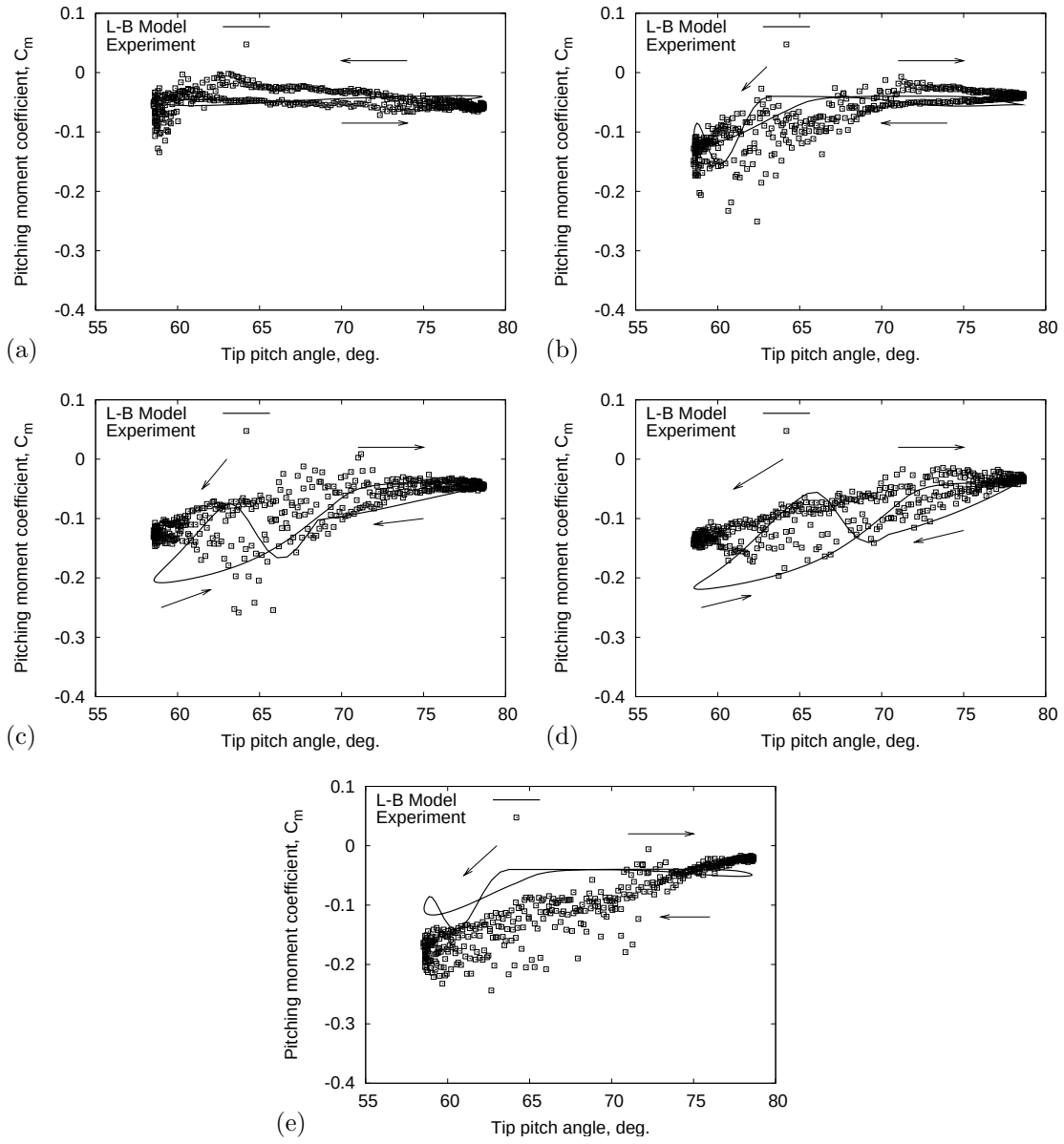

Figure 4.48: Variation of the pitching moment coefficient with tip pitch angle with spanwise station $r/R = 80\%$ subjected to a reduced frequency $k = 0.025$, angle of attack amplitude $\alpha_{\text{amp}} = 10^\circ$ and $\alpha_{\text{mean}} = 20^\circ$. (a) $r/R = 30\%$, (b) $r/R = 46\%$, (c) $r/R = 63\%$, (d) $r/R = 80\%$ and (e) $r/R = 95\%$.

Chapter 5

Comparison with Blade Element Momentum Methods

Blade element momentum (BEM) methods have been dominant in the wind turbine industry for the design of wind turbines, as was mentioned previously in Chapter 1. BEM methods are simple and fast, but are strictly valid only for a limited range of flow conditions, and breakdown in the turbulent wake state (TWS) and the vortex ring state (VRS). This chapter compares the results from the blade element momentum (BEM) theory and the free-vortex wake methods (FVM) for a 2-bladed rotor with ideal twist for a range of tip speed ratios. The various flow states of a wind turbine where BEM methods fail or are valid only with additional empirical approximations have also been identified.

FVM calculations were performed using a 2-bladed wind turbine to compare the results with BEM theory. The comparison was performed using tip losses alone, and also when both tip and viscous (profile) losses were accounted for. In the second case, a constant profile drag coefficient along the blade was assumed. However, no blade stall model was used in the calculation. The simulation was undertaken for a range of tip speed ratios (X_{TSR}) and the variation of the predicted power and thrust coefficients were then compared. The comparison was then extended to the prediction of the local axial induction factor, a, the turbine thrust coefficient, C_T, and the power coefficient, C_P. The turbine parameters that were used are given in Table 5.1.

A comparison is also made for a wind turbine yawing out of the wind. A

Table 5.1: Rotor geometry and operating parameters.

Number of blades	2
Solidity	0.05
Twist	Hyperbolic (θ_{tip}/r)
Radius	5 m
Chord	0.3926 m
Tip pitch	1° & 4°

simple inflow model has been used. Although more sophisticated inflow models have been developed for wind turbine applications in recent years, the comparison shown in this chapter shows the ability of the FVM to account for the nonlinearities involved in the turbulent wake state and yawed flow. This shows the flexibility and robustness of the FVM to capture the time-accurate aerodynamic response of a wind turbine.

5.1 Blade-Element Momentum Theory (BEM)

The BEM theory is a hybrid method [20, 139] that combines the principles of an equivalence between the circulation and momentum theories of lift. With certain assumptions, the BEM theory allows the induction factor (induced inflow) along the blade to be estimated. Thereafter, all of the airloads can be determined. The idea of this essentially analytical approach is to solve for the turbine inflow based on a combination of a momentum balance on successive annuli of the turbine disk and a blade element representation of the sectional aerodynamics. The underlying principle is that each section of the annulus behaves independently of each other, i.e. a 2D assumption. This approach generally gives acceptable approximations to the axisymmetric distribution of inflow and loads found under conditions where the wind is normal to the plane of rotation of the turbine (i.e., the turbine is unyawed

with respect to the oncoming wind).

On the basis of the simple momentum theory one may compute the incremental thrust on an annulus of the turbine disk. Neglecting the tangential induction factor (swirl) in the formulation, which is generally small, the mass flow rate over an annulus of the disk is given by

$$d\dot{m} = \rho dA(V_\infty - v_i) = 2\pi\rho(V_\infty - v_i)y\ dy \tag{5.1}$$

so that the incremental thrust on the annulus is

$$dT = 2\rho\left(V_\infty - v_i\right)v_i dA = 4\pi\rho\left(V_\infty - v_i\right)v_i y\ dy \tag{5.2}$$

In coefficient form this is simply

$$dC_T = \frac{dT}{\frac{1}{2}\rho A {V_\infty}^2} = 8\left(1 - \frac{v_i}{V_\infty}\right)\frac{v_i}{V_\infty}\left(\frac{y}{R}\right)d\left(\frac{y}{R}\right) \tag{5.3}$$

Writing in terms of the non-dimensional blade radius, $r = y/R$, then

$$dC_T = 8\left(1 - \frac{v_i}{V_\infty}\right)\frac{v_i}{V_\infty} r\ dr = 8(1-a)ar\ dr \tag{5.4}$$

where a is the induction factor. From the blade element approach, the thrust coefficient can be expressed as

$$dC_T = \sigma X_{\text{TSR}}^2 C_l r^2\ dr \tag{5.5}$$

where X_{TSR} is the tip speed ratio. Equating the results for the thrust from the momentum and blade element approaches gives

$$8(1-a)ar\ dr = \sigma X_{\text{TSR}}^2 C_l r^2\ dr \tag{5.6}$$

Assuming that C_l varies linearly with the angle of attack, then,

$$C_l = C_{l_\alpha}\left(\theta + \phi\right) \quad \text{with} \quad \phi = \left(\frac{1-a}{rX_{\text{TSR}}}\right) \tag{5.7}$$

Using this assumption gives

$$8(1-a)a = \sigma X_{\text{TSR}} C_l r = \sigma X_{\text{TSR}} C_{l_\alpha}(X_{\text{TSR}}\theta r + (1-a)) \tag{5.8}$$

and after further manipulation this later equation can be expressed in the form

$$a^2 - \left(\frac{\sigma X_{\text{TSR}} C_{l_\alpha}}{8} + 1\right) a + \frac{\sigma X_{\text{TSR}} C_{l_\alpha} (X_{\text{TSR}} \theta r + 1)}{8} = 0 \tag{5.9}$$

where the induction factor a is the unknown. This has the solution

$$a(r, X_{\text{TSR}}) = \left(\frac{\sigma X_{\text{TSR}} C_{l_\alpha}}{16} + \frac{1}{2}\right) - \sqrt{\left(\frac{\sigma X_{\text{TSR}} C_{l_\alpha}}{16} + \frac{1}{2}\right)^2 - \frac{\sigma X_{\text{TSR}} C_{l_\alpha} (X_{\text{TSR}} \theta r + 1)}{8}} \tag{5.10}$$

This is the fundamental equation in the BEM theory. However, it is valid only for the range $0 \leq a \leq 0.5$; the upper level of validity is because the turbine approaches the turbulent wake state and vortex ring state for which, $a > 0.5$ and so momentum theory affords no solution.

Equation 5.10 allows the induction factor a and the induced velocity v_i to be obtained as a function of radial position on the blade for any given blade pitch, blade twist, chord, and airfoil section distribution. Suitable design can be used to optimize the wind turbine rotor for the maximum performance (i.e. maximum power extraction). After the induction factor is obtained, the rotor thrust and power may then be found by integration across the rotor disk using

$$C_T = \sigma X_{\text{TSR}}^2 \int_0^1 C_l r^2 \, dr \tag{5.11}$$

and

$$C_P = \sigma X_{\text{TSR}}^3 \int_0^1 (\phi C_l - C_d) r^3 \, dr \tag{5.12}$$

Because the basis of the BEM theory is strictly a "two-dimensional" theory, 3D effects such as the physical roll-off in the lift as the blade tip is approached are treated using the Prandtl's tip loss function [95]. The Prandtl correction can approximately account for a finite number of blades, and also the effects of blade planform and twist distribution through the effect on the inflow angle. Prandtl's tip and root loss can be expressed in terms of a correction factor F to the change in momentum over the annulus of the disk given by Eq. 5.6 such that now

$$dC_T = 8F(1 - a) a r \, dr \tag{5.13}$$

where

$$F = F_{\text{tip}}\, F_{\text{root}} \tag{5.14}$$

where the tip loss is defined as

$$F_{\text{tip}} = \left(\frac{2}{\pi}\right) \cos^{-1} e^{-f_{\text{tip}}}, \tag{5.15}$$

The exponent f_{tip} is given in terms of the number of blades and the radial position of the blade element r by

$$f_{\text{tip}} = \frac{N_b}{2}\left(\frac{1-r}{r\phi}\right) = \frac{N_b}{2}\left(\frac{1-r}{1-a}\right) X_{\text{TSR}} \tag{5.16}$$

The root loss factor is defined in an analogous way to Eq. 5.15 but the exponent f_{root} is now given by

$$f_{\text{root}} = \frac{N_b}{2}\left(\frac{r-r_c}{r\phi}\right) = \frac{N_b}{2}\left(\frac{r-r_c}{1-a}\right) X_{\text{TSR}} \tag{5.17}$$

With the inclusion of the tip-loss factor, Eq. 5.10 can be written as

$$a(r, X_{\text{TSR}}, F) = \left(\frac{\sigma X_{\text{TSR}} C_{l_\alpha}}{16F} + \frac{1}{2}\right) - \sqrt{\left(\frac{\sigma X_{\text{TSR}} C_{l_\alpha}}{16F} + \frac{1}{2}\right)^2 - \frac{\sigma X_{\text{TSR}} C_{l_\alpha}(X_{\text{TSR}}\theta r + 1)}{8F}} \tag{5.18}$$

Because F is not known a priori, an iteration process is required to solve for a and F. This converges rapidly unless a becomes greater than 0.5, at which point BEM assumptions break down and the iteration process fails. To extend the application of BEM for average axial induction factors greater than 0.5, Glauert [27] suggested a correction in the thrust coefficient based on the experimental results by Lock [28]. Various curve fits have been used to fit the thrust coefficient curve suggested by Galuert. One of the representations of the curve fit is given by

$$dC_T = (8(a-1)a + 4)r\, dr \tag{5.19}$$

Using this latter result and equating the momentum and blade element results for dC_T gives

$$(8(a-1)a + 4)F = \sigma X_{\text{TSR}}^2 C_{l_\alpha} \left(X_{\text{TSR}}\theta r + (1-a)\right) \tag{5.20}$$

This gives a quadratic in a which has the solution

$$a(r, X_{\text{TSR}}, F) = - \left(\frac{\sigma X_{\text{TSR}} C_{l_\alpha}}{16F} - \frac{1}{2}\right) + \sqrt{\left(\frac{\sigma X_{\text{TSR}} C_{l_\alpha}}{16F} - \frac{1}{2}\right)^2 - \frac{\sigma X_{\text{TSR}} C_{l_\alpha} (X_{\text{TSR}} \theta r + 1)}{8F} - \frac{1}{2}} \tag{5.21}$$

This modified equation is valid for the range $0.5 < a < 1.0$, which extends the applicability of BEM to a wider range of operating conditions. However, the modified equation is based on empirical evidence and also breaks down for high tip speed ratios when the Prandtl tip-loss function is used. Notice that the effect of the wake rotation and the tangential induction factor (a') has not been accounted for in the above formulation. It will be shown later in this chapter that the effect of wake rotation is negligible in the predictions of the power output and aerodynamic loading on a wind turbine.

5.2 Unyawed Flow

The FVM wake structure and the corresponding particle streamtraces for various wind speeds (TSR) for $\theta_{\text{tip}} = 4^\circ$ is shown in Fig. 5.1. At 2 ms^{-1} [see Fig. 5.1(a)], the turbine operates in the vortex ring state. This is an operating state where the BEM theory breaks down. The wake interacts with the rotor and the flow direction is not unique, which is one of the assumptions made in the formulation of the BEM. The corresponding streamtraces for 2 ms^{-1} shows a significant flow recirculation region near the blades. At 2.5 ms^{-1} [see Fig. 5.1(b)], the rotor operates in the turbulent wake state. Here, the recirculation region moves downstream and a significant mixing region exists in the wake.

At 4 ms^{-1} ($X_{\text{TSR}} = 8.3333$) the wake is stable, but for the last turn the tip vortices interact to produce a form of pairing instability. The corresponding streamtraces show the wake expansion region and then a wake contraction near the last turn where the wake is unstable. At higher wind speeds (lower TSR), the wake structure is now stable [see Figs. 5.1(d) - 5.1(f)]. The streamtraces expand and pass

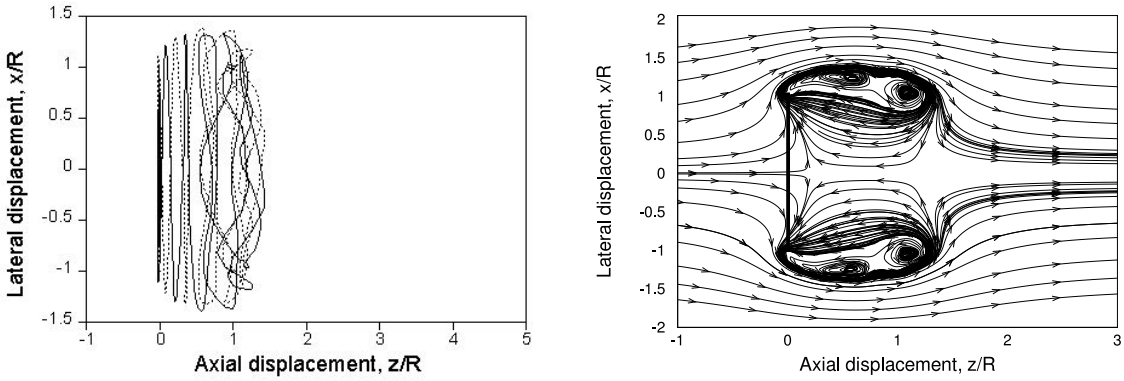

(a) $X_{\mathrm{TSR}} = 16.667, V_\infty = 2$ m/s

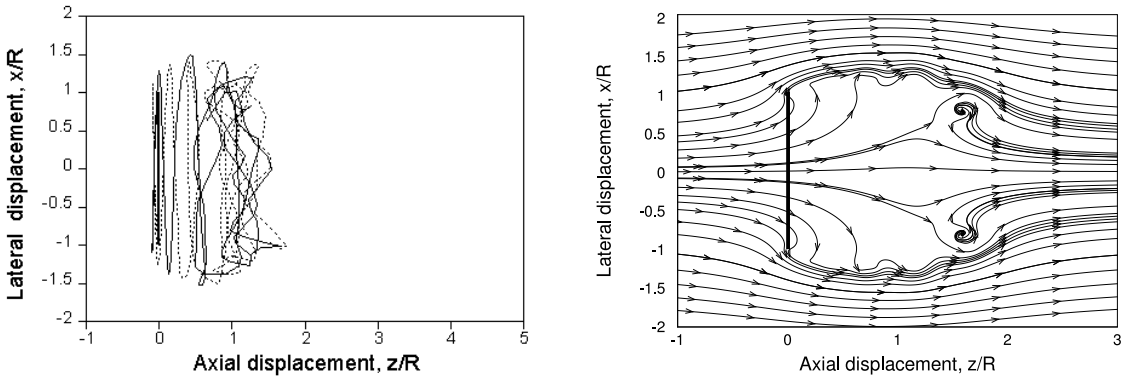

(b) $X_{\mathrm{TSR}} = 13.333, V_\infty = 2.5$ m/s

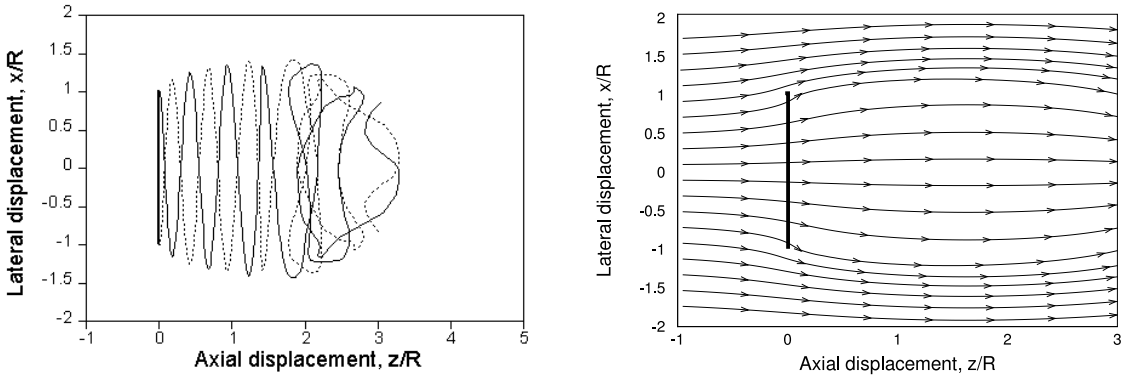

(c) $X_{\mathrm{TSR}} = 8.333, V_\infty = 4$ m/s

Figure 5.1: Top view of the wake geometry and the streamtraces behind the wind turbine for various tip speed ratios for a wind turbine rotor with ideal twist and $\theta_{\mathrm{tip}} = 4°$.

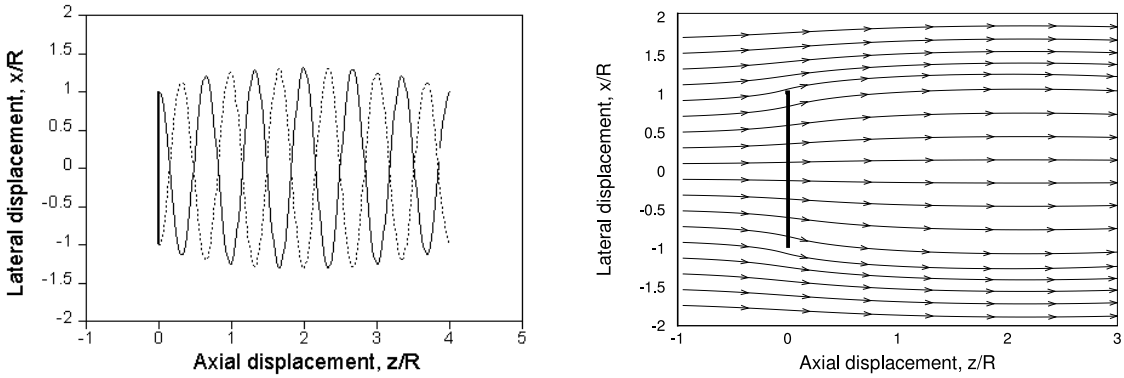

(d) $X_{\mathrm{TSR}} = 6.667, V_\infty = 5$ m/s

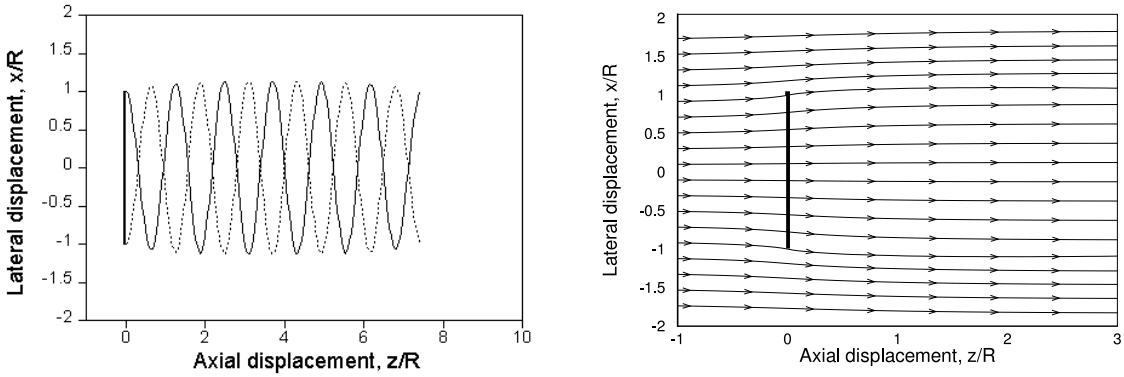

(e) $X_{\mathrm{TSR}} = 4.1667, V_\infty = 8$ m/s

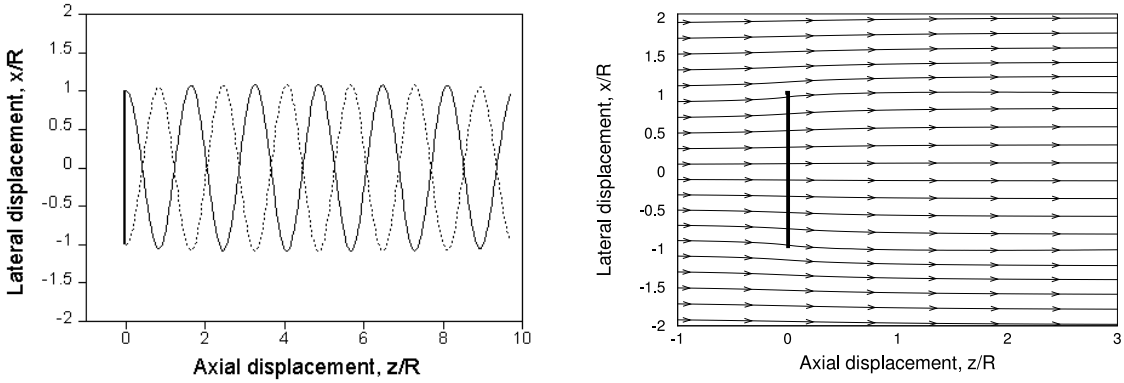

(f) $X_{\mathrm{TSR}} = 3.333, V_\infty = 10$ m/s

Figure 5.1: (Cont'd) Top view of the wake geometry and the streamtraces behind the wind turbine for various tip speed ratios for a wind turbine rotor with ideal twist and $\theta_{\mathrm{tip}} = 4°$.

smoothly through the rotor. The maximum expansion of the wake (corresponding to maximum power extraction) is obtained for $X_{\mathrm{TSR}} = 6.6667$ in this case. For higher wind speeds, the wake is stable but the wake expansion reduces and the power output from the turbine decreases.

Figure 5.2 shows the comparison of the predicted variation of power coefficient, C_P, versus TSR from the BEM analysis and the FVM calculations for a tip pitch of 4°. As the TSR is increased, an optimum tip speed ratio is reached where the power coefficient is maximum. For the BEM method with no losses, a maximum power coefficient of 0.593 corresponding to the Lanchester–Betz limit is obtained. When tip losses and profile losses are included into the calculation the maximum C_P is reduced, as would be expected. In this case, the maximum power coefficient is achieved for a TSR of around 5.75 from both the BEM theory and the FVM. From the BEM theory results, it is evident that the addition of the tip losses causes significant change in the predicted power output, whereas the addition of the viscous losses does not significantly alter the power output. For the low values of TSR, there is no significant difference in the predicted power output with and without viscous losses in the FVM calculations. The addition of viscous losses, however, reduces the power output at moderate to high values of TSR.

The agreement between the predicted power coefficient from the FVM and the BEM theory was noted to be very good for low values of TSR. As the TSR is increased further, however, the turbulent wake/vortex ring state is encountered. The BEM results shown here include the correction for $a > 0.5$ as given by Eq. 5.19. The variation of the thrust coefficient (see Fig. 5.3) with TSR is almost linear. Again, the BEM method and the FVM predictions are found to be in very good agreement up to a TSR of 6. For higher TSR, the modified BEM theory with the inclusion of tip losses also breaks down, and does not converge for blade section near the tip. BEM method with no tip or hub losses underpredicts the thrust coefficient.

Figure 5.4 shows the comparison of the power and thrust coefficient, respec-

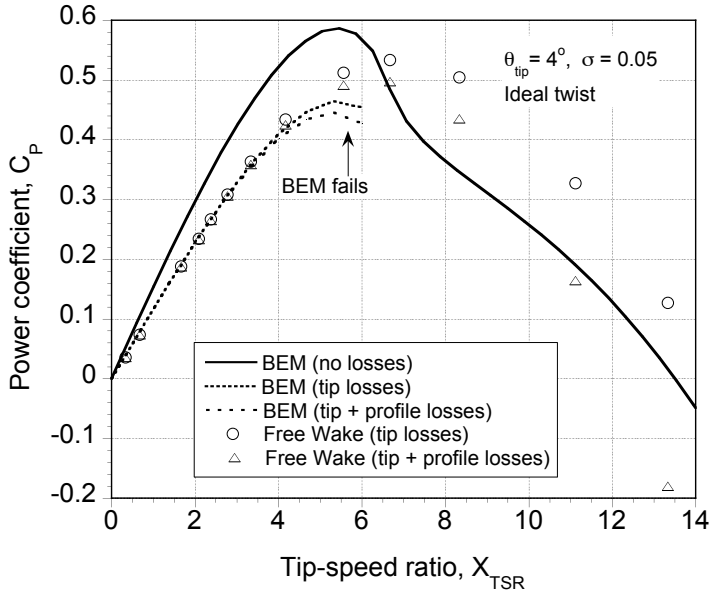

Figure 5.2: Comparison of the variation of the predicted power coefficient with tip speed ratio for $\theta_{\text{tip}} = 4°$.

tively, for $\theta_{\text{tip}} = 1°$ including both the tip losses and profile losses. Hereafter, a lower tip pitch angle ($\theta_{\text{tip}} = 1°$) is used because the modified BEM equations breakdown at higher values of TSR. The predicted power coefficient from the FVM and the BEM theory are in good agreement for $X_{\text{TSR}} < 5$. For higher values of TSR, the BEM calculation with the Glauert correction significantly underpredicts the power coefficient. Notice that the predicted thrust coefficient (Fig. 5.5) from the two methods are very similar until the BEM theory breaks down.

Figures 5.6(a) show the distribution of the axial and the tangential induction factor over the blade for various tip speed ratios, as obtained from the FVM calculation. For higher values of TSR, the average axial induction factor is larger. It can be seen that the value of the axial induction factor for moderate values of TSR is very large near the blade root and blade tip. The average value of the tangential induction factor [see Fig. 5.6(b)] decreases with increasing values of TSR. However, the tangential induction factor is noted to be very small compared to the axial in-

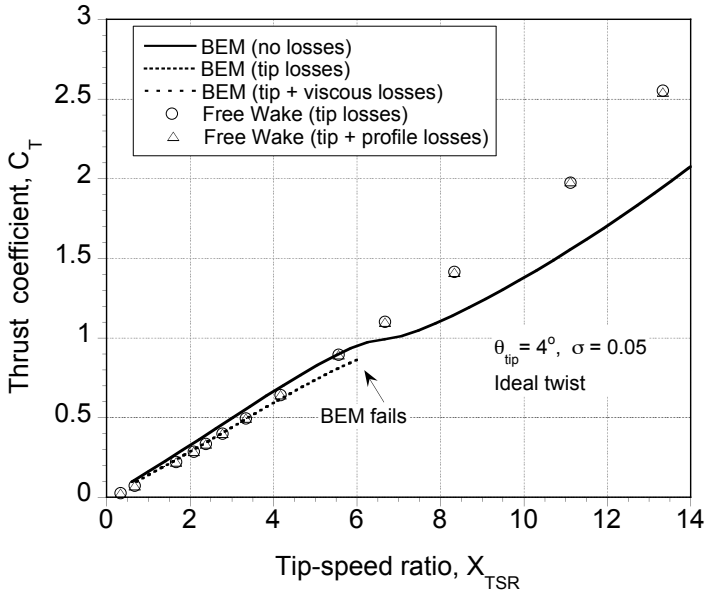

Figure 5.3: Comparison of the variation of the predicted thrust coefficient with tip speed ratio for $\theta_{\text{tip}} = 4°$.

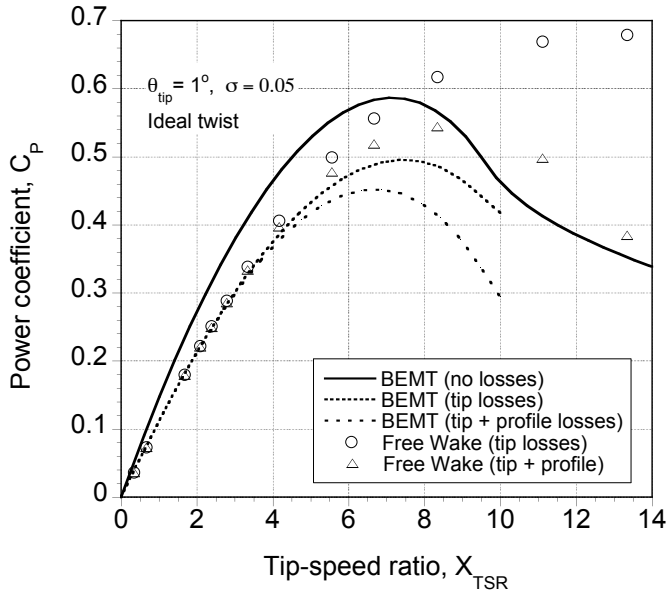

Figure 5.4: Comparison of the variation of the predicted power coefficient with tip speed ratio for $\theta_{\text{tip}} = 1°$.

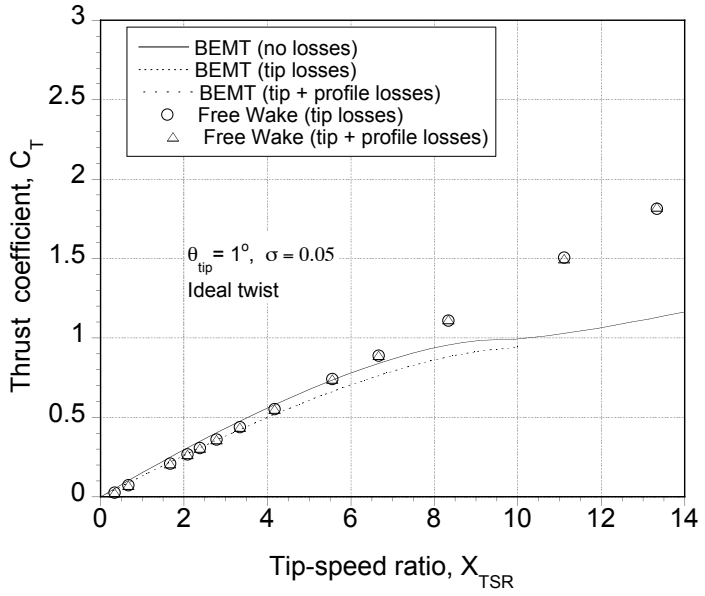

Figure 5.5: Comparison of the variation of the predicted thrust coefficient with tip speed ratio for $\theta_{\text{tip}} = 1°$.

duction factor except near the blade root. This justifies neglecting the effect of swirl in the BEM methodology, as assumed previously.

Although the above results show that the integrated thrust and power coefficients obtained from the BEM and FVM calculations are in good agreement for low values of TSR, predicting the local distribution of airloads accurately is very important for the reliable design of wind turbines. Figures 5.7 through 5.9 compare the local variation of the induction factor and the thrust and power coefficient for two different cases: (1) same tip pitch, and (2) same thrust coefficient. In the second case, the thrust coefficient obtained from the FVM is prescribed for the BEM calculation.

Figures 5.7(a) and (b) show the distribution of the induction factor over the blade for the two cases for a TSR of 6.0. The BEM result with no tip losses is also shown. It can be seen that the tip losses cause an increase in the axial induction factor near the blade tip and root, which is captured very well in the BEM method

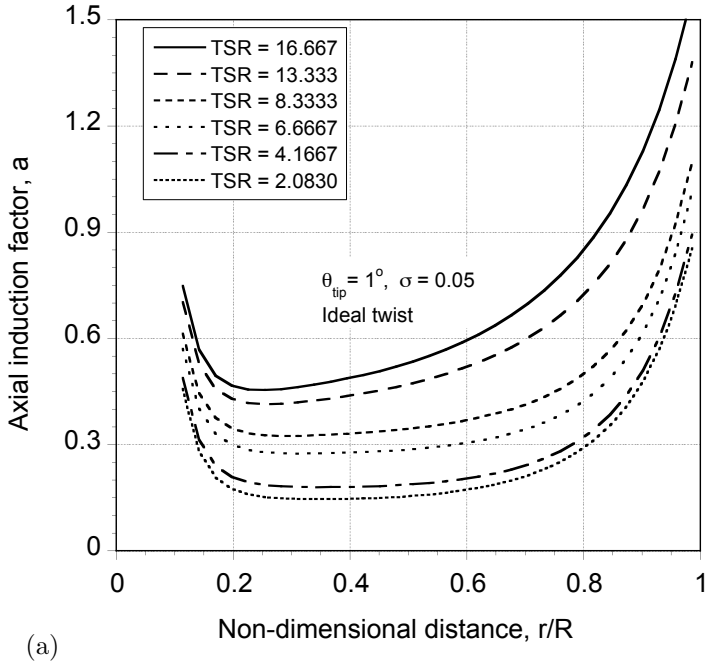

(a)

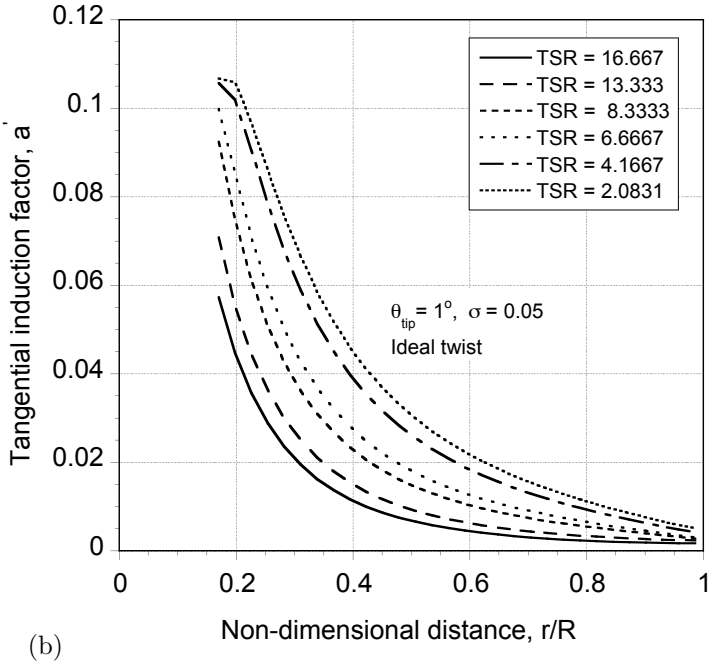

(b)

Figure 5.6: FVM wake prediction of the distribution of the induction factors for various tip speed ratios: (a) axial induction factor, (b) tangential induction factor.

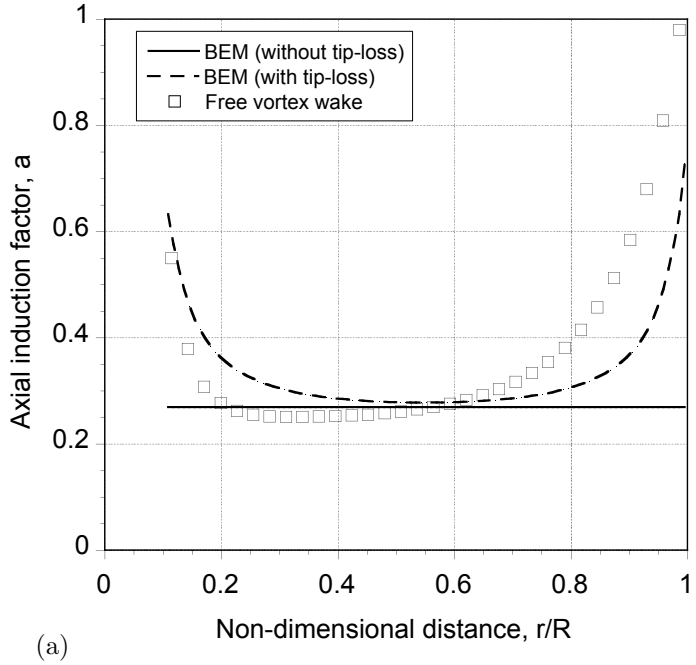

(a)

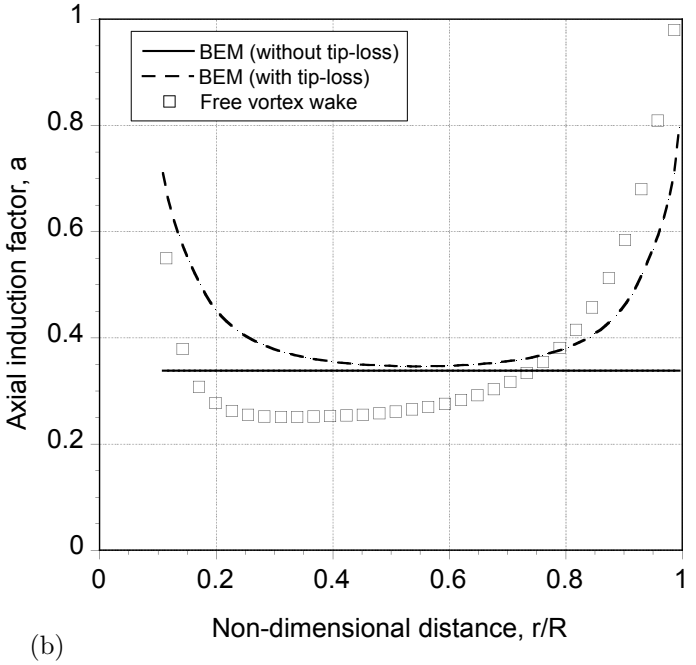

(b)

Figure 5.7: Distribution of the induction factor along the blade for a tip speed ratio of $X_{\mathrm{TSR}} = 6.0$ and $\theta_{\mathrm{tip}} = 1°$: (a) same value of θ_{tip}, (b) same value of C_T.

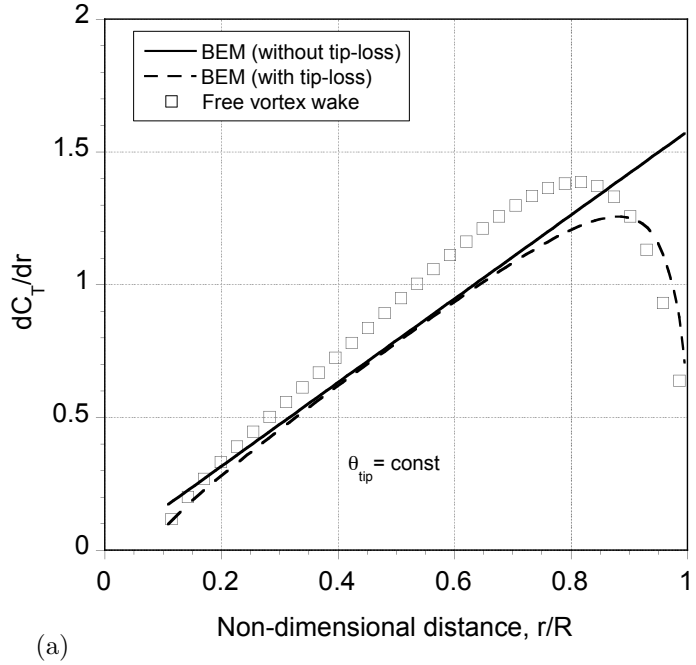

(a)

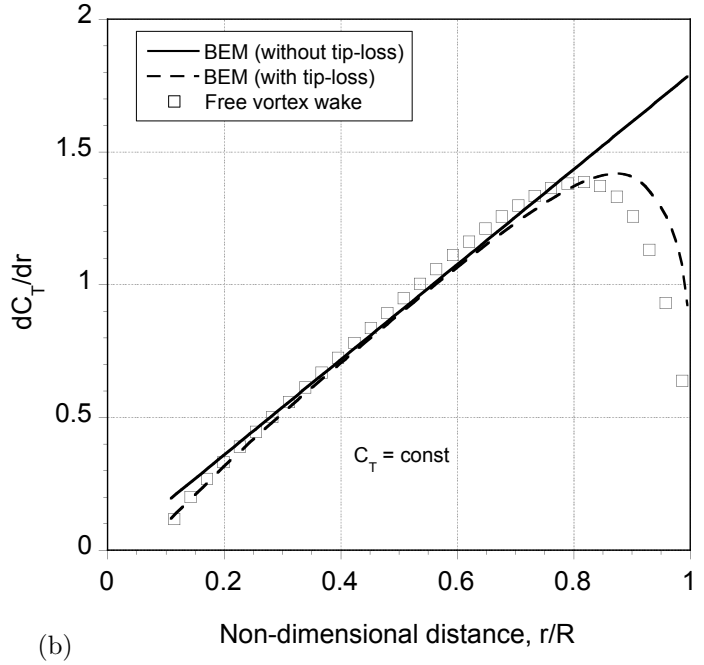

(b)

Figure 5.8: Distribution of the thrust coefficient along the blade for a tip speed ratio of $X_{\mathrm{TSR}} = 6.0$ and $\theta_{\mathrm{tip}} = 1°$: (a) same value of θ_{tip}, (b) same value of C_T.

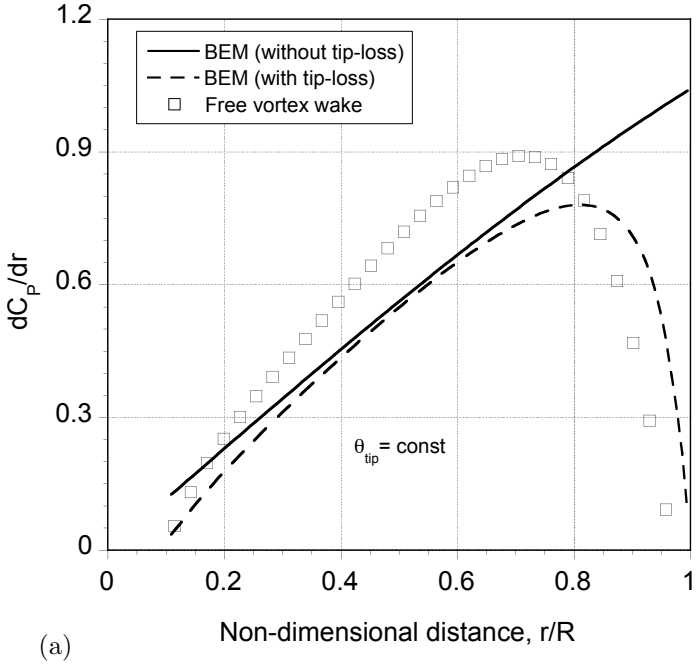

(a)

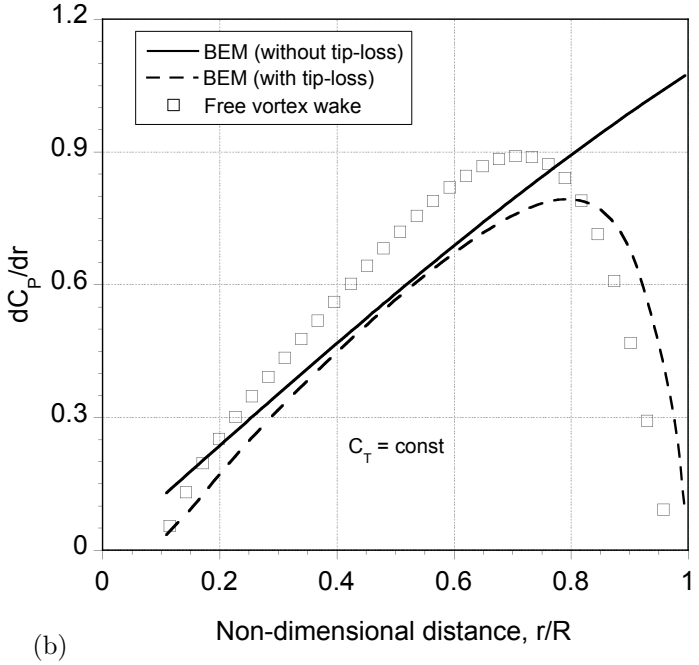

(b)

Figure 5.9: Distribution of the power coefficient along the blade for a tip speed ratio of $X_{\mathrm{TSR}} = 6.0$ and $\theta_{\mathrm{tip}} = 1°$: (a) same value of θ_{tip}, (b) same value of C_T.

using the Prandtl tip-loss function. The overall agreement in the local induction factors obtained with the FVM and BEM theory is good when the tip pitch is the same for the two calculations, but is not as good when the thrust coefficient obtained from the BEM is trimmed to match the thrust from the FVM.

Figures 5.8 and 5.9 show the thrust and the power coefficient distributions for the two cases. The thrust coefficient distribution agrees very well for the second method, whereas the local C_T is overpredicted when the tip pitch is kept the same in the two calculations. In both cases, the FVM gives a slightly higher local power coefficient as compared to the BEM theory. These results shows that the integrated power and thrust predicted by the two methods are in good agreement. However, the predictions of the local induction factor, the thrust coefficient and the power coefficient are not so similar for the two methods, even for moderate tip speed ratios.

5.3 Wind Turbine in Yawed Flow

Because of the variability of wind direction and the need to yaw the rotor out of the wind to limit power at high wind speeds, wind turbines work in yawed flow for a significant amount of their operational time. BEM methods are fundamentally incapable of handling this problem without the prescription of a modified inflow at the rotor disk.

A FVM calculation has been performed where a turbine yaws 30° out of the wind during the period of 5 revolutions. Figure 5.10 shows the top view of the evolving wake at different times. Just after the yaw starts, the turbine moves into its own wake, which can cause highly unsteady loads on the rotor blades. After 5 revolutions, the wake reorganizes and shows disturbances only along the filaments for the last 2 to 3 wake turns. After about 10 revolutions, the wake becomes essentially periodic.

The corresponding time-history of the power output is shown in Fig. 5.11. Notice that the power output drops rapidly with yaw; this drop is proportional

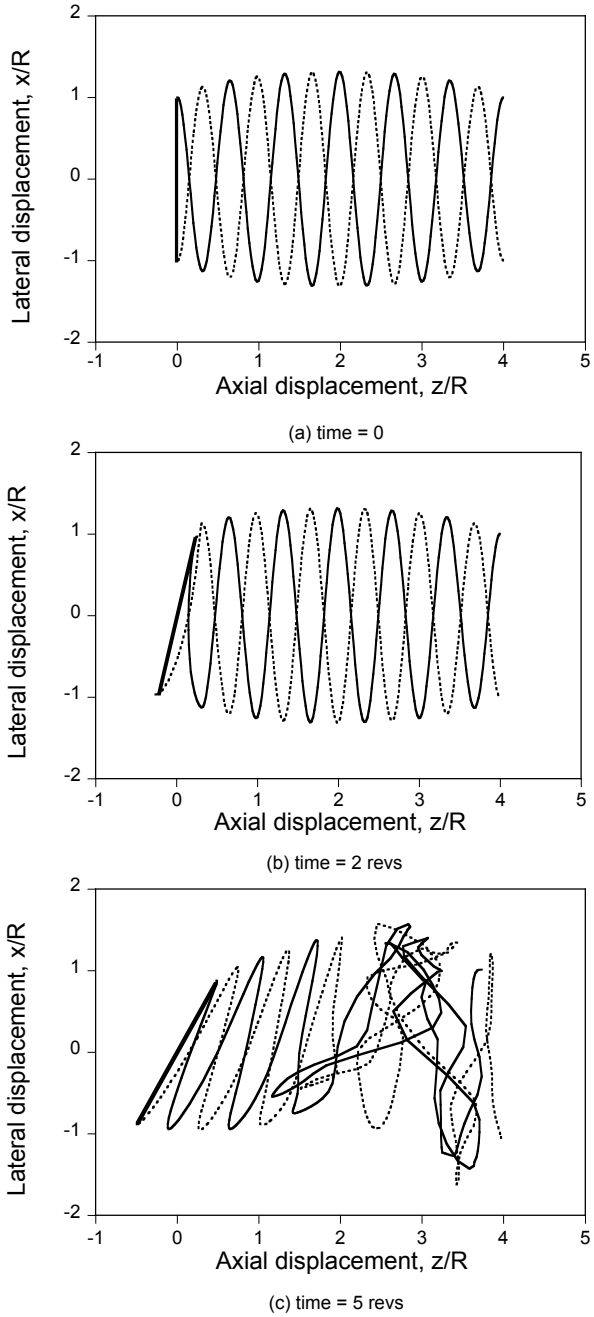

Figure 5.10: Top view of the evolving wake geometry behind the wind turbine yawing 30° out of the wind: (a) time = 0, (b) time = 2 revs., (c) time = 5 revs.

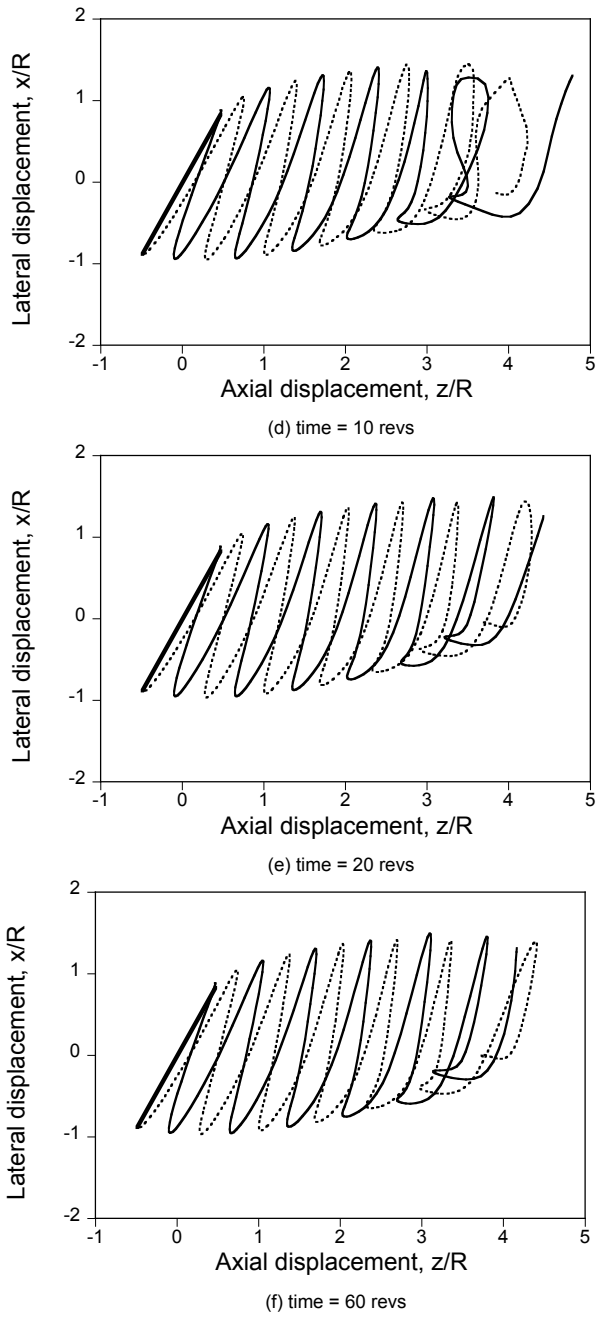

Figure 5.10: (Cont'd) Top view of the evolving wake geometry behind the wind turbine yawing 30° out of the wind: (d) time = 10 revs., (e) time = 20 revs. and (f) time = 60 revs.

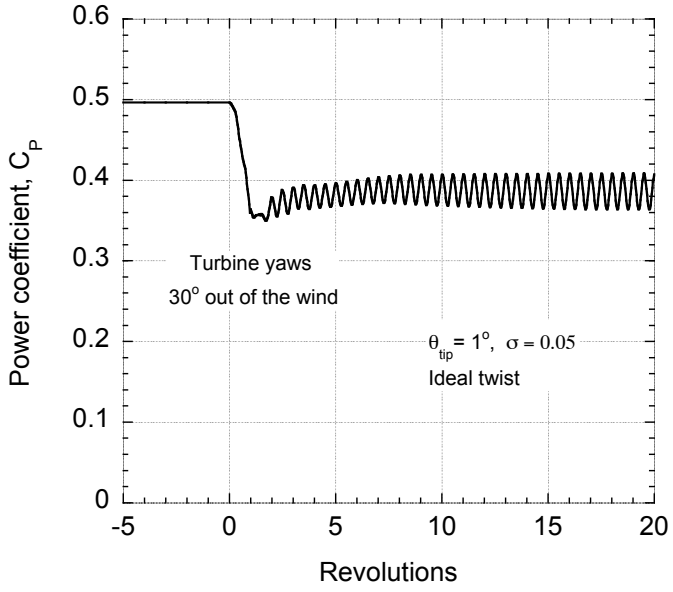

Figure 5.11: Power coefficient as a function of time for when the turbine is yawed 30° out of the wind.

to the cube of the yaw angle. After the wake starts reorganizing, there is some recovery in the power output. After 10 revolutions, the power output becomes essentially periodic with a strong 2/rev output variation.

To apply the BEM method to a wind turbine in yawed flow, an additional approximation to the inflow through the wind turbine rotor is required. Usually the axial induction factor for the unyawed case is calculated first and a correction for the yawed flow effects [140] based on linear inflow models [22–24] is then applied. For a wind turbine operating in yawed flow at an angle γ, the inflow can be represented by

$$a(r, \gamma) = a(r, \gamma = 0) + a_0(k_x r \cos\psi + k_y r \sin\psi) \tag{5.22}$$

where a_0 is the mean axial induction factor given by the momentum theory. The coefficients k_x and k_y are the longitudinal and lateral inflow weighting factors, respectively, which vary with the linear inflow model being used. In this study, a

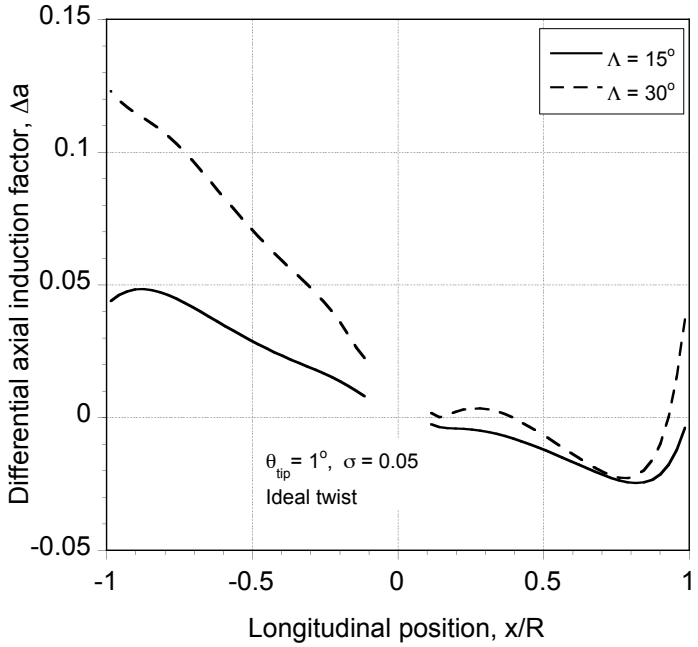

Figure 5.12: Distribution of the differential axial induction factor along the longitudinal axis in yawed flow with respect to the unyawed flow.

simple Coleman model [22] is considered for the comparison with the FVM, which seems to be a common model used in wind turbine applications. In the Coleman model, the weighting factors are given by

$$k_x = \tan(\chi/2) \quad \text{and} \quad k_y = 0.0 \tag{5.23}$$

where χ is the wake skew angle obtained using the momentum theory and is given by

$$\chi = \tan^{-1}\left(\frac{V_\infty \sin\gamma}{V_\infty \cos\gamma - v_i}\right) \tag{5.24}$$

Figure 5.12(a) shows the distribution of the axial induction factor along the longitudinal axis in the rotor disk plane for different yaw angles as obtained using the FVM method and from the BEM theory with a Coleman inflow correction. The comparison shows that the BEM method with a yawed flow correction gives good agreement with the FVM for smaller yaw angles, whereas the agreement is not as good for the larger yaw angles. The asymmetry in the axial induction factor across

the disk is also not in agreement with the FVM. The distribution of axial induction factors along the lateral axis of the rotor is shown in Fig. 5.12(b). It can be seen that the distribution of a is symmetric over the rotor for smaller yaw angles. However, for $\gamma = 30^\circ$ some asymmetry can be observed in the FVM calculation. The BEM predictions with the Coleman correction overlap for different yaw angles because $k_y = 0$, which holds for smaller yaw angles but is obviously not valid for larger yaw angles.

The above results show that the BEM theory with linear inflow assumption seems to give acceptable agreement with the FVM calculation, but only for small yaw angles. For larger yaw angles, the agreement between the predicted induction factor distribution along the longitudinal and lateral axis of the turbine disk from the BEM theory and the FVM is not as good.

5.4 Universal Thrust and Power Coefficient Curve

To understand various flow states of a rotor over which the BEM theory can be applied, it is instructive to construct a universal power and thrust coefficient curve. In helicopter theory, the universal induced velocity curve gives the relation between the axial velocity and the induced velocity at a constant thrust. This relation can be expressed in terms of the variation of thrust coefficient with the axial induction factor.

The axial induction factor for a wind turbine, a, is defined as the ratio of induced velocity at the rotor disk to the free stream velocity (i.e., $a = v_i/V_\infty$). This can be expressed in terms of the ratio of induced velocity and induced velocity of a powered rotor in hovering flight using

$$a = \frac{v_i}{V_\infty} = \frac{v_i}{v_h}\Big(\frac{v_h}{V_\infty}\Big) \tag{5.25}$$

where v_i/v_h is a function of the axial free-stream velocity, V_∞. The exact solution

for v_i/v_h in the normal working state ($V_\infty/v_h > 0$) is given by

$$\frac{v_i}{v_h} = -\frac{V_\infty}{2v_h} + \sqrt{\Big(\frac{V_\infty}{2v_h}\Big)^2 + 1} \tag{5.26}$$

In the windmill brake state ($V_\infty/v_h < -2$), the solution is given by

$$\frac{v_i}{v_h} = -\frac{V_\infty}{2v_h} - \sqrt{\Big(\frac{V_\infty}{2v_h}\Big)^2 - 1} \tag{5.27}$$

For the turbulent wake state/vortex ring state, no exact solution is available from the momentum theory. The relation for the induced velocity in the range $-2 < V_\infty/v_h < 0$ has been expressed as a quartic fit by Leishman [95] based on experimental measurements for helicopter rotors as given by Gessow in Ref. 141. This relation can be used to express the axial induction factor in terms of V_∞/v_h using Eq. 5.25, i.e.,

$$\frac{v_i}{v_h} = A + B\frac{V_\infty}{v_h} + C\Big(\frac{V_\infty}{v_h}\Big)^2 + D\Big(\frac{V_\infty}{v_h}\Big)^3 + E\Big(\frac{V_\infty}{v_h}\Big)^4 \tag{5.28}$$

where $A = 1.15$, $B = -1.125$, $C = -1.372$, $D = -1.718$ and $E = -0.665$. The thrust coefficient for a helicopter is defined as

$$C_{T_{\text{hel}}} = \frac{T}{\rho A(\Omega R)^2} \tag{5.29}$$

This form of the thrust coefficient can be expressed in terms of the mean inflow as

$$C_{T_{\text{hel}}} = 2\lambda_h^2 \tag{5.30}$$

where $\lambda_h = v_h/\Omega R$. Here v_h is the induced velocity at the rotor disk in hover. The thrust coefficient for a wind turbine is defined as

$$C_{T_{\text{wt}}} = \frac{T}{\frac{1}{2}\rho A V_\infty^2} \tag{5.31}$$

which can be re-expressed in terms of the helicopter thrust coefficient as

$$C_{T_{\text{wt}}} = 2C_{T_{\text{hel}}}\Big(\frac{\Omega R}{V_\infty}\Big)^2 = 4\Big(\frac{V_\infty}{v_h}\Big)^{-2} \tag{5.32}$$

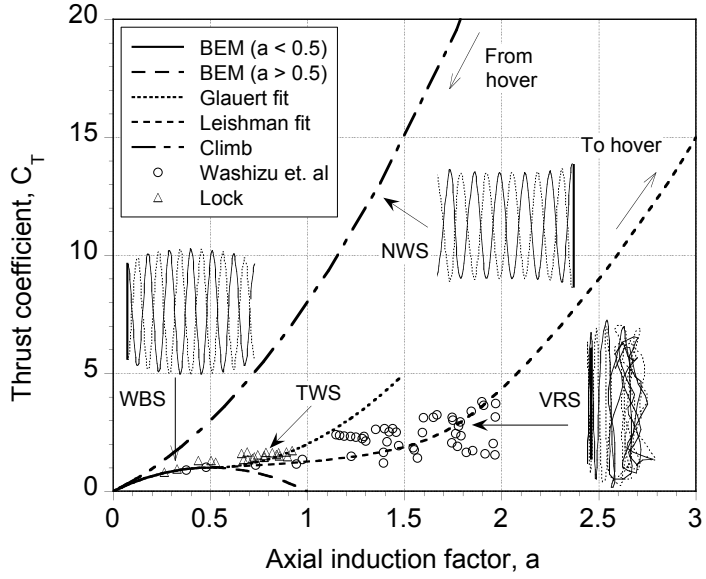

(a)

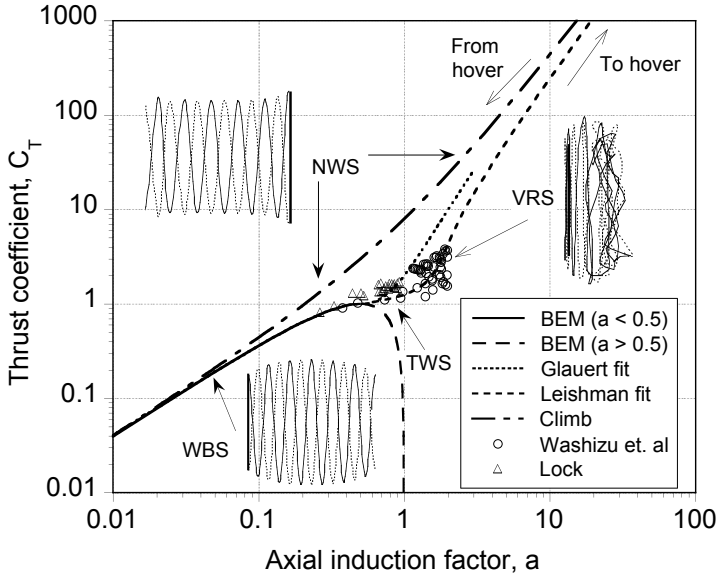

(b)

Figure 5.13: Variation of the thrust coefficient with the axial induction factor for normal working state (NWS), turbulent wake state (TWS), vortex ring state (VRS) and windmill brake state (WBS): (a) linear scale and (b) log scale to show the asymptotic values.

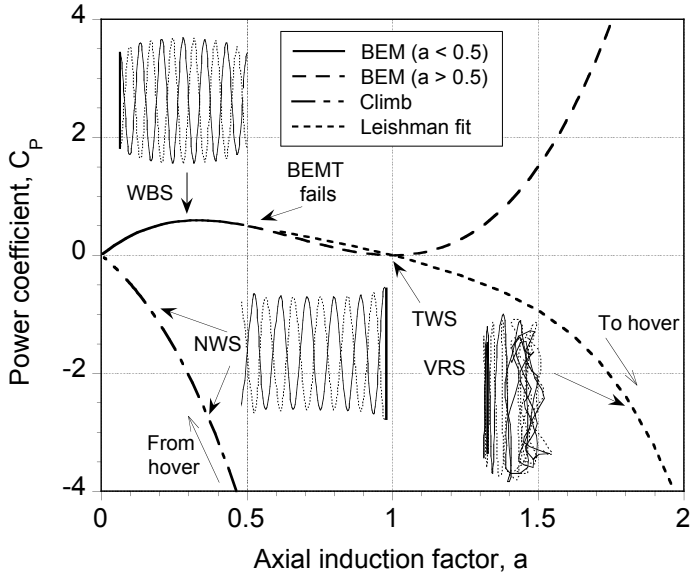

(a)

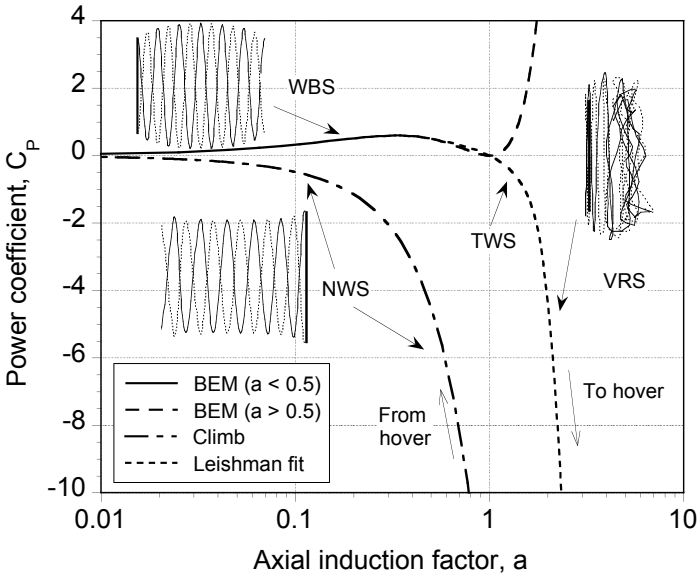

(b)

Figure 5.14: Variation of the power coefficient with the axial induction factor for normal working state (NWS), turbulent wake state (TWS), vortex ring state (VRS) and windmill brake state (WBS): (a) linear scale and (b) log scale to show the asymptotic values.

In a similar manner, the power coefficient for wind turbine is defined as

$$C_{P_{\text{wt}}} = \frac{P}{\frac{1}{2}\rho A V_\infty^3} = C_{T_{\text{wt}}}(1-a) \tag{5.33}$$

The value of $C_{P_{\text{wt}}}$ can now be expressed in terms of the ratio V_∞/v_h using the expressions for $C_{T_{\text{wt}}}$ and a in terms of V_∞/v_h.

For a given V_∞/v_h, the thrust coefficient and the axial induction factor can be obtained and these are plotted in Fig. 5.13. The solid line shows the momentum theory predictions in the windmill brake state. The momentum theory fails when the axial induction factor is greater than 0.5. Various empirical corrections have been suggested for this range some of which are shown in Fig. 5.13(a). Experimental measurements in this flow state from Lock [28] and Washizu et al. [142] are also shown. As the descent velocity through the rotor decreases and the hovering state is approached, the thrust coefficient and the axial induction factor approach infinity, which indicates the asymptotic limits shown in Fig. 5.13(b). This corresponds to the VRS where the vortex filaments are bundled up near the rotor disk. In the second branch, the climb velocity is increased from hover and the variation of the thrust coefficient with the axial induction factor is shown. As the climb velocity is increased, the thrust coefficient approaches zero.

The variation of the power coefficient with the axial induction factor for the various flow states is shown in Fig. 5.14(a). The power coefficient, C_P is defined as positive when the rotor is extracting power from the wind. The momentum theory is valid until $a = 0.5$. An approximate fit for the C_P variation (Leishman fit) is also shown in this figure. Again, when powered hovering flight is approached the value of the power coefficient and the axial induction factor approaches infinity, as shown in Fig. 5.14(b). The above results show that the Glauert correction was really obtained only for a limited set of experimental values. The agreement between the extended set of experimental results and Glauert correction in the vortex ring state is not as good, whereas the Leishman fit shows a good agreement for the whole range of axial induction factors.

5.5 Summary

A comparison of the power output and thrust based on blade-element momentum theory (BEM) and free-vortex model (FVM) has been performed. Good agreement in the power and thrust prediction is observed between the FVM and BEM methods for low tip speed ratios ($X_{\mathrm{TSR}} < 6$). For higher tip speed ratios, the wake induction factor is very high near the tip region and the BEM model fails. It is also shown that the corrections for C_T at higher axial induction factors may break down. On the other hand, the FVM shows the flexibility for the aerodynamic analysis of wind turbines in all working states including the vortex ring state (high TSR).

The FVM can also be used for the aerodynamic analysis of wind turbines in yawed flow for which BEM method is less applicable without resorting to various types of approximations. It is also shown that the linear inflow models often used with the BEM theory are probably not applicable for large yaw angles. The ability of the FVM to capture the time-accurate behavior of the aerodynamic response of wind turbines (in yawed flow) has also been shown. A universal thrust and power coefficient curve has been derived to understand various flow states of a wind turbine (i.e., normal working state, turbulent wake state and the windmill brake state). In the vortex ring state, the Glauert correction is shown to be adequate only when the axial induction factor is between 0.5 and 1.

Chapter 6

Comparison with Experiments

In Chapter 4, the nonlinear unsteady airfoil model was coupled with the Weissinger-L blade model, and was validated against the experimental measurements from the NREL parked blade test. In Chapter 5, the coupling between the blade model and the vortex wake model was analyzed, and validated for attached flow conditions. The next step is to couple the airfoil and blade model with the vortex wake model. Before the resulting model can be used in the design phase for the calculation of loads and power output for a wind turbine, the effectiveness and robustness of the free-vortex wake model needs to be established properly. In this chapter, the numerical predictions obtained from the the free-vortex wake method (FVM) are validated against the experimental measurements obtained for a wind turbine that was operated under controlled conditions.

The emphasis of the first part of this chapter will be on the validation of the wake geometry behind a horizontal axis wind turbine that is predicted by the FVM. Defining accurately the aerodynamic angle of attack at the blades is obviously key to predicting the airloads and the power produced by the wind turbine. An important part of this problem is to consider the effects of the self-generated vortical wake downstream of the turbine disk, which is a source of a non-uniform velocity field and three-dimensional angle of attack distribution over the disk. Wind turbines also operate in yawed flow for a significant part of their operational time. The wake behind a wind turbine in yawed flow is skewed (epicycloidal), and contributes further to the non-uniformity of the inflow. This results in a time-varying aerodynamic loading on the blades and, hence, a fluctuating power output. Therefore,

proper modeling and an accurate treatment of the wake becomes fundamental to the problem of predicting the loads and operational performance of a wind turbine.

Over the past decade, free-vortex wake methods (FVM) have emerged as very flexible numerical tools for modeling helicopter rotor wakes [83]. The progress in improving the free-vortex wake modeling of helicopter rotors has been accelerated by detailed flow experiments that have been used to validate the FVM and to develop viscous-corrected models of the concentrated tip vortices [82, 143, 144]. These experimental data have been used to validate the FVM over a wide range of operating conditions. However, for wind turbines, despite similarities to the helicopter problem, only a very few experimental studies have been undertaken to investigate its detailed structure and evolution. Notable work includes Vermeer et al. [72], who conducted experiments with a two-bladed turbine in axial flow. Also, Grant et al. [145, 146] performed flow visualization experiments and particle image velocimetry (PIV) studies on a wind turbine in an open-jet facility.

More recently, a quantitative flow visualization of the wake geometry behind a two-bladed model turbine has been performed by Haans et al. [73] in an open-jet tunnel at Delft University of Technology (DUT), and in both axial and yawed flow operating conditions. In the present study, the wake geometry measurements obtained by Haans et al. will be used. This comparison is valuable because it provides confidence in the FVM to accurately capture the wake geometry behind a wind turbine. This is fundamental to predict the induced velocity on the rotor disk, and subsequently the angle of attack and airloads on the blade.

In the second part of this chapter, the validation of the FVM is extended to measurements from the NREL Phase VI wind turbine [91, 92]. In this experiment, a two-bladed wind turbine with twisted and tapered blades was tested over a wide range of operating conditions in the full-scale NASA Ames 80×120 ft wind tunnel. This experiment provides a comprehensive set of airloads and performance measurements. NREL blind comparison study based on the Phase VI tests underlined the

inadequacies of the current predictive tools [94] used to model the aerodynamic loads and performance of a wind turbine. Even for unyawed and unstalled conditions flow, predictions of blade loads and power output using various numerical methodologies were found to be significantly different from the experimental measurements. It was also found that numerical models with essentially the same set of sub-models gave different results. This is the motivation behind the crawl-walk-run approach followed in this study. In this part, the validation of the free-vortex wake model will be extended to the azimuthal and spanwise variations of the airloads, in addition to the integrated thrust and power output. The ability of the FVM to predict the unsteady aerodynamic response of a wind turbine in a time-accurate manner will also be shown.

6.1 Wake Geometry Validation

The validation of the free-vortex wake method for a wind turbine in axial and yawed flow was performed against the wake geometry measurements obtained by Haans et al. [73]. A two-bladed rotor model was placed in the Open Jet Facility of the Delft University of Technology (DUT). The open jet tunnel has a maximum attainable wind speed of 14.5 ms^{-1} and free-stream turbulence intensities of $1.2 \pm 0.2\%$ at 5.5 ms^{-1}, the wind tunnel speed at which the measurements were taken. The readings from three inter-connected Pitot-static tubes, mounted in the jet exit plane, together with ambient pressure and jet temperature recordings, were used to derive the wind tunnel speed. The rotor hub is located 1 m downstream of the jet exit plane. This tunnel was not equipped with a separate return channel; the tunnel hall was used for recirculation instead. The distance from the rotor hub to the downstream tunnel wall is 11 m. For the setup and coordinate systems, see Figure 6.1.

The geometric properties of the wind turbine rotor blade used in the experiment are given in Table 6.1. The blade pitch was varied by altering the tip pitch

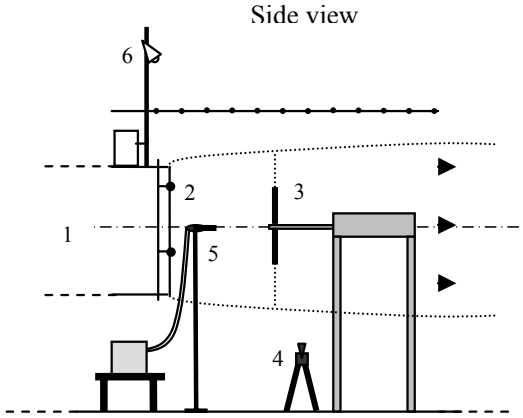

(a)

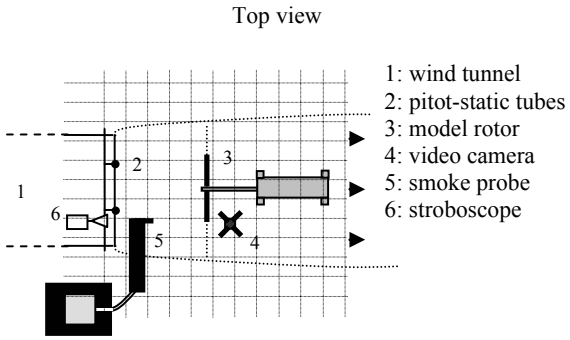

(b)

Figure 6.1: Schematic of the experimental test setup. (Taken from Ref. 73): (a) side view (b) top view.

Number of blades	2
Airfoil Section	NACA 0012
Rotor radius (m)	0.6
Root cut-out	30%
Chord (m)	0.08
Blade twist (deg.)	$6 - 6.67r/R$ for $r/R \leq 0.9$
	0 for $r/R \geq 0.9$

Table 6.1: Geometric properties of the model scale wind turbine used by Haans et al. in Ref. 73.

angle θ_{tip}. Yaw angle ψ was defined as the angle between the normal to the rotor plane and the undisturbed wind speed. Experimental data were obtained for three tip speed ratios of $\lambda = 6$, 8 and 10. The tunnel wind velocity was kept constant at $V_\infty = 5.5$ ms^{-1}, and the tip speed ratio was changed by changing the rotational speed of the turbine.

A strain gauge attached on the rotor shaft enabled measurement of axial force on the rotor. The second strain gauge on the root of one blade was used to quantify the flapping moment, and another for the lead-lag moment on the instrumented blade. The axial force is the force on the rotor in the direction of the rotor axis. Hence, for yawed conditions, the axial force vector is directed at an angle to the free-stream flow velocity. The side force on the rotor was not recorded. Details of the experimental setup and the procedure to quantify the wake positions can be found in Ref. 73.

A representative result from the flow visualization is shown in Fig. 6.2, which uses a form of smoke to seed the flow. It can be seen that the wake behind the turbine expands because it is extracting energy from the flow. The concentrated tip vortices can be clearly identified by the swirling smoke patterns and the dark "seed" voids at the center of the vortex cores. Notice that the smoke becomes quite

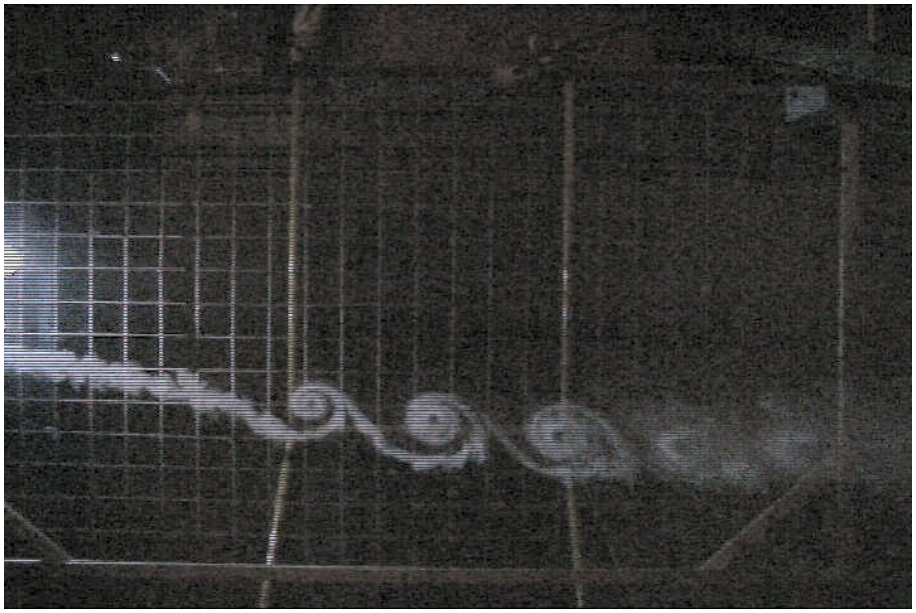

Figure 6.2: Typical flow visualization showing the tip vortex and the blade for $\Lambda = 0°,\ \lambda = 8$ and $\theta_{\text{tip}} = 2$. (Image courtesy of Wouter Haans from DUT.)

diffused at older wake ages, and the vortex cores are more difficult to discern. It is clear that the core radii of the vortices increases. By $\zeta = 720°$ the vortex core is filled with smoke and the vorticity near the vortex cores is now relatively well diffused.

6.1.1 Wind Turbine in Axial Flow

Numerical simulations were performed using the FVM for the given turbine geometry at various tip-speed ratios and tip pitch angles in both axial and yawed flow conditions. A numerical discretization of $\Delta\psi = \Delta\zeta = 10°$ was used in the simulations. This level of discretization gives only a small error in the reconstruction of the tip vortex induced velocity field (as concluded in Chap. 3) in and is a relatively inexpensive solution to run on a high-end computer workstation.

Figure 6.3(a) shows a comparison of the tip vortex positions obtained from the experiment versus results from the FVM for axial (unyawed) flow conditions for $\lambda = 8$, $\theta_{\text{tip}} = 0°$, and $\Lambda = 0°$. The wake expands behind the turbine, and the FVM

captures the tip vortex locations well for younger wake ages. Some differences can be seen in the positions of the tip vortices for older wake ages. The increased uncertainty in defining the tip vortex core positions is because of the diffusion of smoke particles. In addition, some aperiodicity of the flow may account for the differences in the locations for older wake ages. However, the predicted tip vortex locations are still within the experimental uncertainty bounds in marking the position of the tip vortices as the center of the dark seed void or "core" regions free of smoke.

As the blade tip pitch angle increases, the thrust on the turbine decreases. (Note that blade pitch angle convention is positive towards nose down). The wake expansion is found to be reduced as compared to the wake at lower tip pitch angle. With decreased induced velocity at the disk, the effective velocity behind the turbine disk increases. Hence, the helical pitch of the vortical wake also increases, which is represented well by the FVM. The predicted tip vortex positions were found to be in good agreement with the experimental measurements for $\theta_{\text{tip}} = 2^\circ$, as shown in Fig. 6.3(b). For $\theta_{\text{tip}} = 4^\circ$ - see Fig. 6.3(c), the tip vortex positions were slightly overpredicted by the FVM for older wake ages.

A comparison of the predicted and experimental turbine thrust coefficient for the unyawed case is shown in Fig. 6.4. In the experiment, turbine thrust was measured using a strain gauge, which provides an azimuthally averaged measurement. The predicted C_T was found to be in good agreement with the experimental values. The underpredicted thrust for $\lambda = 8$ and $\theta_{\text{tip}} = 4^\circ$ correlated well with the corresponding overprediction of the tip vortex positions, as shown in Fig. 6.3(c). The induced inflow at the disk as predicted by the FVM for this case is lower than compared to experiment. Thrust coefficient C_T is, therefore, lower than in experiments and the helical pitch of the wake is higher.

The corresponding values of the predicted power coefficient is shown in Fig. 6.5. The power output from the turbine was not measured in the experiment, so a comparison could not be made. It can be seen, however, that the power decreases with

increasing tip speed ratio for a given tip pitch angle. A tip speed ratio $\lambda = 6$ gives the maximum power coefficient.

6.1.2 Wind Turbine in Yawed Flow

Figure 6.6 shows the wake geometry behind the turbine for a yaw angle of $\Lambda = -30^\circ$ and $\lambda = 8$. The wake expands and now develops a significant asymmetry on the upstream and downstream sides (it becomes more epicycloidal in form). This asymmetric development of the wake results in a non-uniform induced velocity over the turbine disk, which leads to cyclic loading on the blades. The FVM better represents this asymmetric wake geometry, and hence the cyclic loading will be predicted without any additional modeling requirements such as would be required with BEM methods.

Figure 6.6(a) compares the predicted and measured tip vortex locations for $\theta_{\text{tip}} = 0^\circ$. The vortex positions on the downstream side agree very well with the experimental measurements. However, the tip vortex locations show slight differences on the upstream side of the wake at older wake ages. For the higher tip pitch angles, a similar trend is seen – see Figs. 6.6(b) and 6.6(c).

A time history of the thrust and power coefficient for $\lambda = 8$ and $\theta_{\text{tip}} = 2^\circ$ for two yaw angles is shown in Figs. 6.7 and 6.8, respectively. For axial flow case ($\Lambda = 0^\circ$), C_T and C_P are steady and do not vary with time. In the FVM, to model the behavior of a wind turbine in yawed flow, the wake geometry for the unyawed case was used as the initial condition. After the fourth revolution, the wind turbine rotor is yawed out of the wind to the desired yaw angle over four revolutions. As the yaw angle is increased, the wake behind the turbine reorganizes itself and the FVM predicts the transient behavior of the wake in a time-accurate manner.

Even after the desired yaw angle has been achieved, there is a slight lag until the wake becomes periodic. Once all the vortex filaments have the correct circulation, the numerical solution becomes periodic. Both the thrust and power decrease

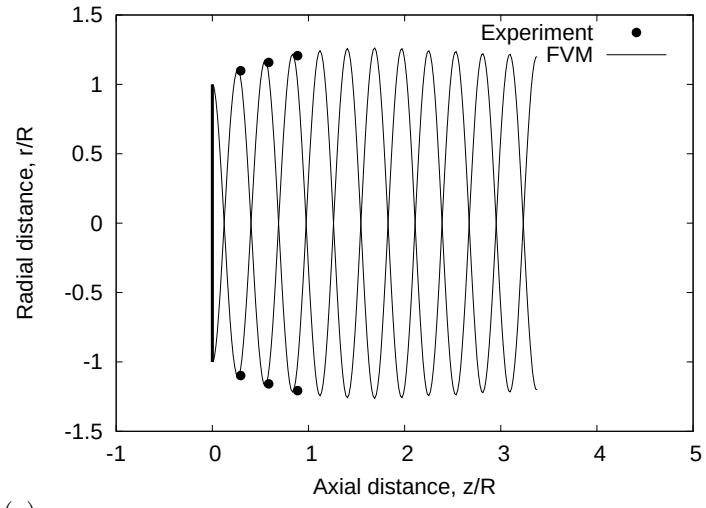

(a)

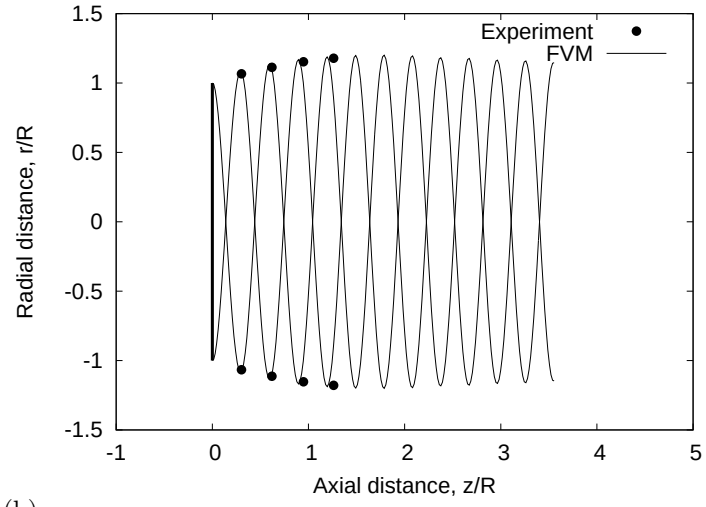

(b)

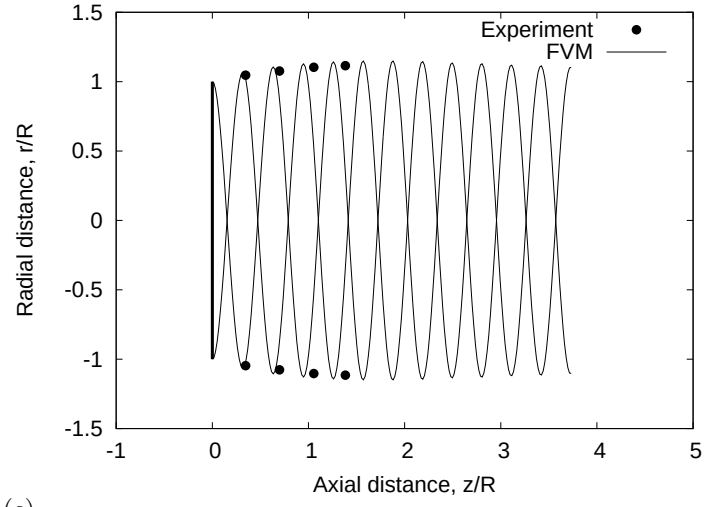

(c)

Figure 6.3: Comparison of the tip vortex geometry for $\Lambda = 0°$ and $\lambda = 8$; (a) $\theta_{\text{tip}} = 0°$, (b) $\theta_{\text{tip}} = 2°$, and (c) $\theta_{\text{tip}} = 4°$.

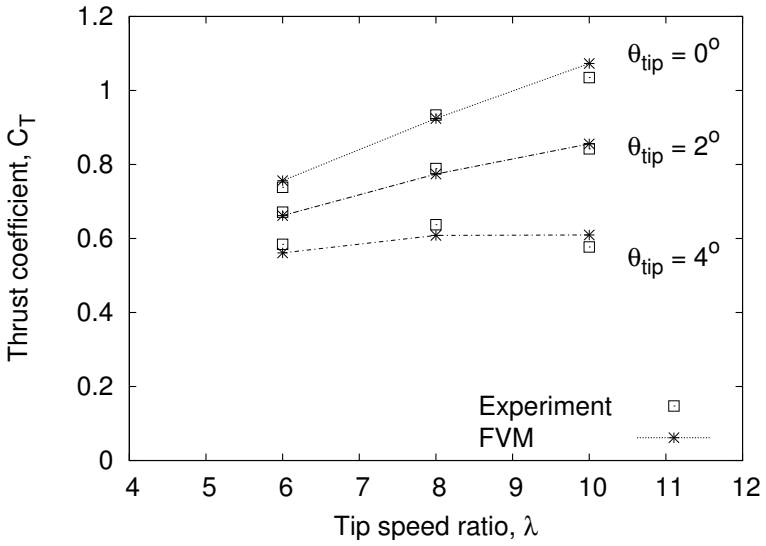

Figure 6.4: Comparison of the measured and predicted average thrust coefficient for unyawed flow as a function of the tip speed ratio for $\theta_{\text{tip}} = 0°$, $2°$ and $4°$.

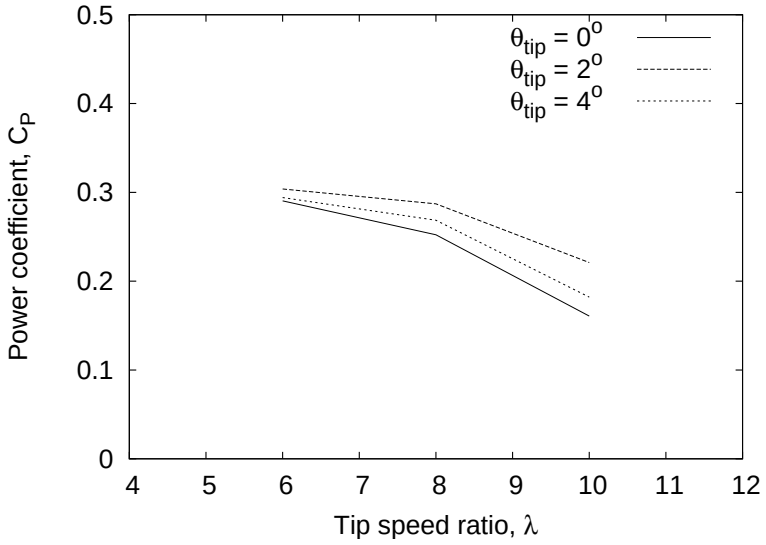

Figure 6.5: Variation of the predicted average power coefficient for unyawed flow as a function of the tip speed ratio for $\theta_{\text{tip}} = 0°$, $2°$ and $4°$.

with increasing yaw angle. According to the momentum theory (as shown in Chapter 1), the power output is proportional to the cube of the wind speed normal to the rotor disk; it can be seen that C_p is reduced by an amount proportional to $\cos^3 \Lambda$. However, as the wake reorganizes, there is a slight recovery in the power coefficient.

Figure 6.9 shows a comparison of the predicted and measured tip vortex locations for $\lambda = 6$ for the unyawed and yawed cases at a tip pitch angle of $\theta_{\text{tip}} = 0°$. It can be seen that the helical pitch of the tip vortex is higher for $\lambda = 6$ as compared to the $\lambda = 8$ case. For $\Lambda = 0°$, the predicted wake is in good agreement with the measured wake geometry. As the yaw angle is increased to $-30°$, the wake develops asymmetrically, and as seen for $\lambda = 8$, the upstream wake positions are slightly overpredicted. For $\Lambda = -45°$ (see Fig. 6.9(c)), the wake starts to roll up along its edges, but this effect is limited to last few turns of the wake. A considerable amount of asymmetry can now be seen in the wake. The comparison between the predicted and measured tip vortex positions is not quite as good as the $\Lambda = -30°$ case.

For a higher tip speed ratio of $\lambda = 10$, the predicted and measured wake positions are shown in Fig. 6.10. In this condition, the wake behind the turbine is much more compact with a smaller helical pitch of the tip vortices. The agreement between measurements and predictions is good, except for the highest yaw angle of $\Lambda = -45°$. For this case (see Fig. 6.10(c)), the radial displacement of the tip vortex on the downstream side is overestimated at all wake ages.

The variation of the azimuthally averaged turbine thrust coefficient with yaw angle and tip pitch angle is shown in Fig. 6.11 for a tip speed ratio of 6. It can be see that the FVM predicts the thrust coefficient very well for all operating conditions. As the magnitude of the yaw angle is increased, the thrust coefficient decreases. For both negative and positive yaw angles, it was found that the turbine thrust was almost the same, which was well predicted by the FVM.

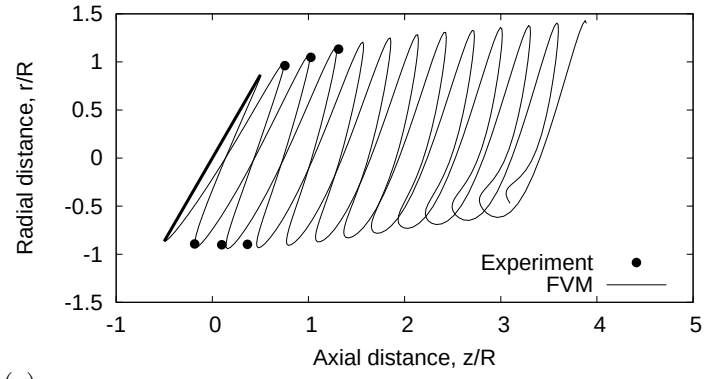

(a)

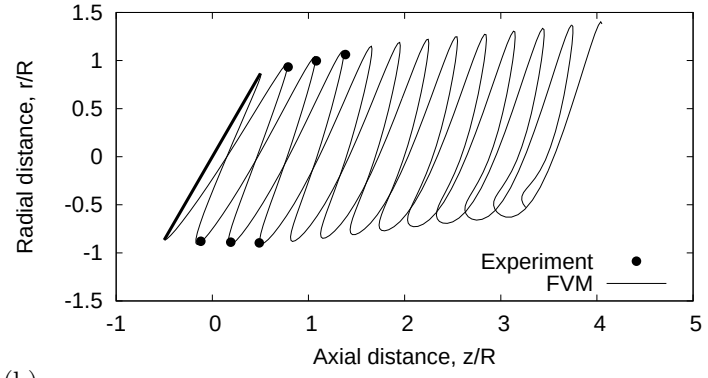

(b)

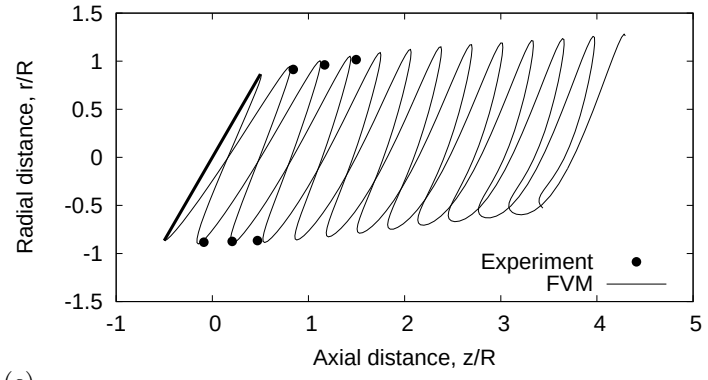

(c)

Figure 6.6: Comparison of the tip vortex geometry for $\Lambda = -30^\circ$ and $\lambda = 8$: (a) $\theta_{\text{tip}} = 0^\circ$, (b) $\theta_{\text{tip}} = 2^\circ$, and (c) $\theta_{\text{tip}} = 4^\circ$.

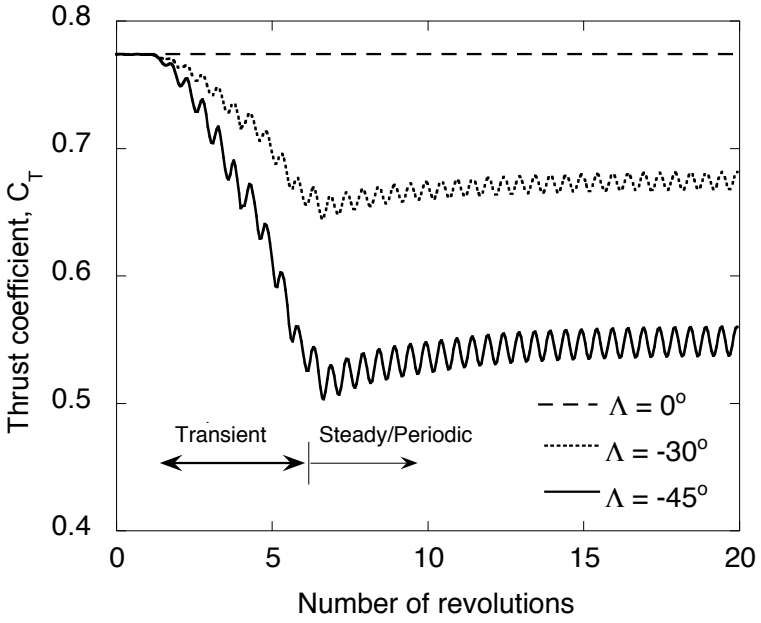

Figure 6.7: Time history of the thrust coefficient for unyawed and yawed flow; $\lambda = 8$ and $\theta_{\text{tip}} = 2°$.

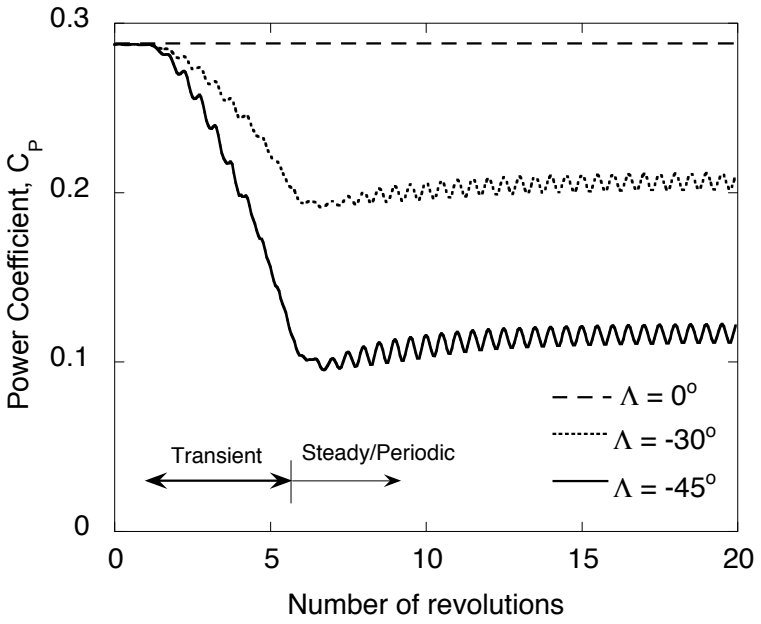

Figure 6.8: Time history of the power coefficient for unyawed and yawed flow; $\lambda = 8$ and $\theta_{\text{tip}} = 2°$.

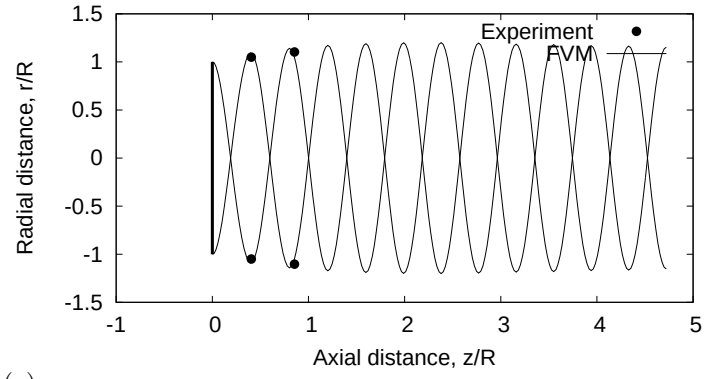

(a)

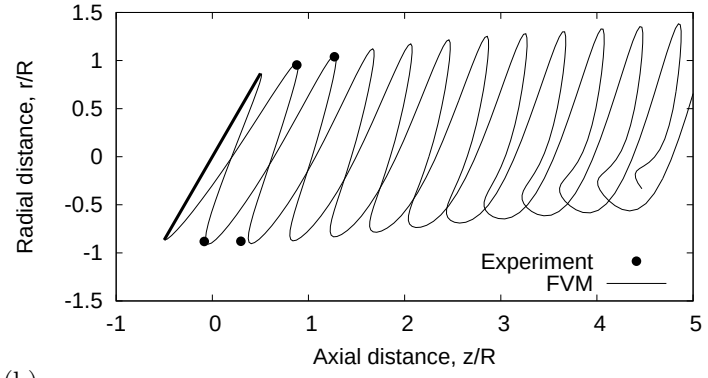

(b)

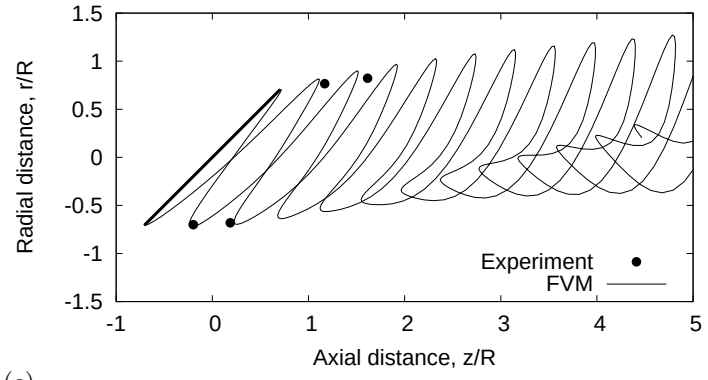

(c)

Figure 6.9: Comparison of the tip vortex geometry for a tip speed ratio $\lambda = 6$ and $\theta_{\text{tip}} = 0°$; (a) $\Lambda = 0°$, (b) $\Lambda = -30°$, and (c) $\Lambda = -45°$.

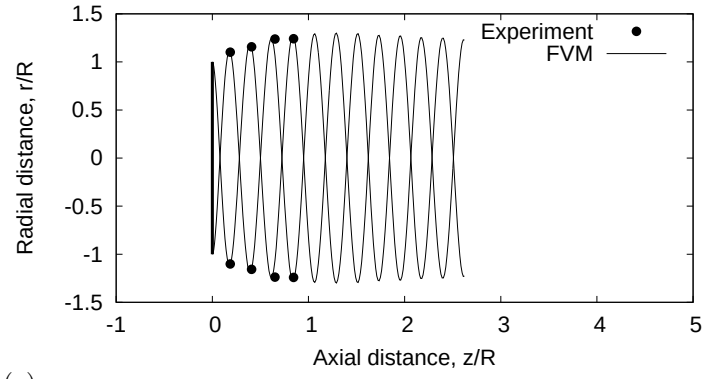

(a)

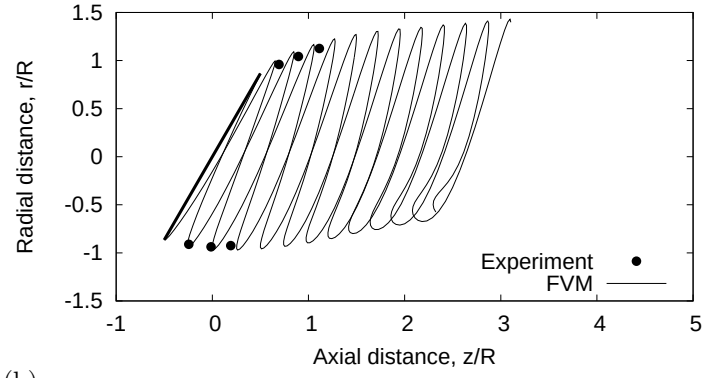

(b)

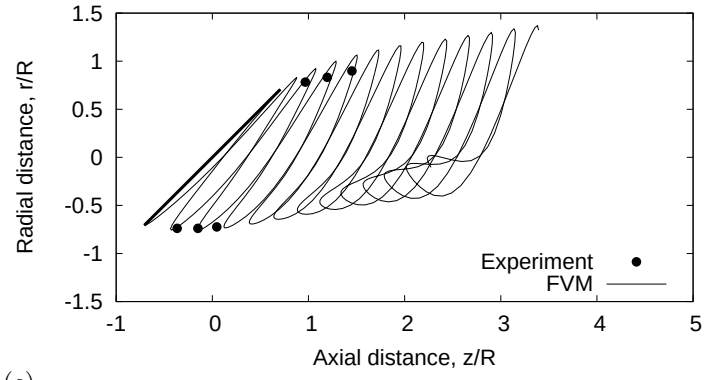

(c)

Figure 6.10: Comparison of the tip vortex geometry for a tip speed ratio $\lambda = 10$ and $\theta_{\text{tip}} = 0°$; (a) $\Lambda = 0°$, (b) $\Lambda = -30°$, and (c) $\Lambda = -45°$.

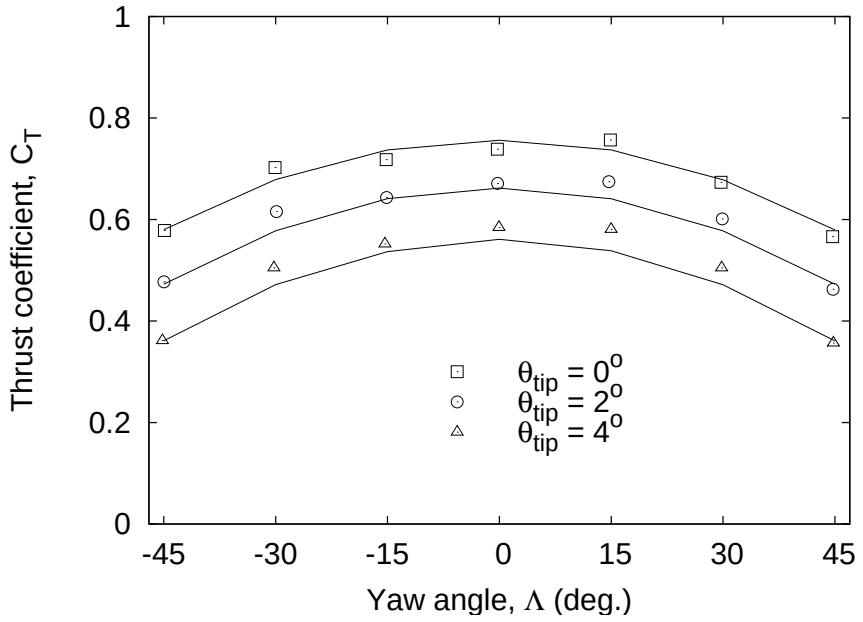

Figure 6.11: Comparison of the measured and predicted average thrust coefficient for various yaw angles for $\theta_{\text{tip}} = 0°$, $2°$ and $4°$ at a tip speed ratio of $\lambda = 6$. The solid lines are FVM predictions and the symbols are the measured values.

6.2 NREL Phase VI Validation

The validation of the wake geometry and thrust coefficients in attached flow, as discussed in the previous section, provides confidence in the ability of the free-vortex wake method to predict the unsteady aerodynamic loads on a wind turbine. In this section, the validation of FVM will be extended to the prediction of the aerodynamic loads and performance of a wind turbine over a wider range of operating conditions. Numerical simulations were performed for the NREL Phase VI turbine. The comparison was mainly performed for the wind turbine in the upwind configuration, i.e., sequence S in Ref. 91. This test sequence used an upwind rigid turbine with 0° blade cone angle, and with a tip blade pitch angle of 3°. The wind turbine was maintained at a rotational speed of 72 rpm, and the five-hole probes were removed to reduce any interference effects. Calculations were performed for wind turbine operating in unyawed and yawed flow. Table 6.2 gives the main geometric and operational parameters of the turbine.

Table 6.2: Geometric properties of the NREL Phase VI wind turbine.

Number of blades	2
Airfoil section	S809
Rotor radius	5.029 m
Blade taper	2:1
Blade twist	Hyperbolic
Rotational speed	72 rpm

In this section, the predicted results obtained for three yaw angles ($\Lambda = 0°$, 30° and 60°) will be shown. A comparison of the net aerodynamic power and turbine thrust is presented first. The comparison is then extended to the azimuthal variation of the integrated quantities such as turbine torque, root flapwise and edgewise bending moments. To show the robustness and capability of the free-vortex

wake method, azimuthal and spanwise variation of the aerodynamic coefficients (i.e., normal force coefficient C_n, leading-edge thrust coefficient C_t and pitching moment coefficient C_m) are compared against the experimental measurements. Spanwise and azimuthal variation of the aerodynamic coefficients will be shown for three wind speeds of $V_\infty = 5$ ms^{-1}, 10 ms^{-1} and 15 ms^{-1}.

6.2.1 Wind Turbine in Unyawed Flow

In unyawed flow, the wind direction is aligned with the rotational axis of the turbine and there is no yaw error. This is the simplest case, mainly because there are no cyclic variations in the airloads and power output. Figure 6.12 shows the variation of the predicted and measured azimuthally averaged thrust with wind speed for the unyawed case. Notice that there is good agreement between the predicted and measured thrust at low wind speeds. As the wind speed increases, however, the difference between the predicted and measured thrust increases, significantly underpredicting thrust at wind speeds above 12 ms^{-1}. This difference can be attributed to rotational boundary layer augmentation and 3D effects. Because of these effects, the inboard regions of the wind turbine blade experience a delay in stall and enhanced values of the normal force coefficient. Various stall delay models [36–38] have been developed to account for the enhanced values of C_n in the post-stall regime. In this study, the model developed by Raj and Selig [38] will be used. This model is representative of the general formulation of the stall delay models used in the wind turbine community.

The Raj–Selig model models the rotational augmentation effects by assuming that the 3D airfoil are approximately equal to that obtained in 2D wind tunnel data plus an increment in lift and drag, i.e.,

$$C_{l_{3D}} = C_{l_{2D}} + \Delta C_l \tag{6.1}$$

$$C_{d_{3D}} = C_{d_{2D}} + \Delta C_d \tag{6.2}$$

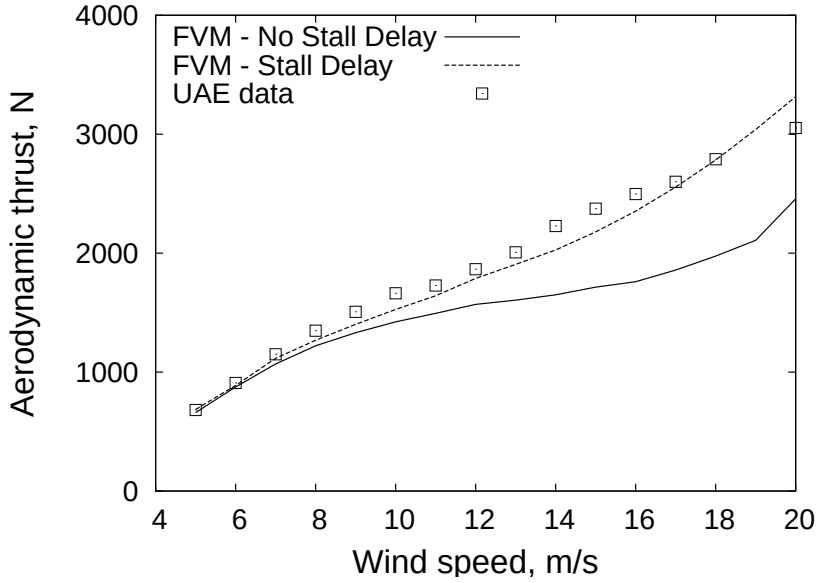

Figure 6.12: Comparison of the predicted and measured aerodynamic thrust for Phase VI turbine in unyawed flow.

where ΔC_l and ΔC_d are increments in the lift and drag. These increments are given by

$$\Delta C_l = f_l(C_{l,pot} - C_{l_{2D}}) \tag{6.3}$$

$$\Delta C_d = f_d(C_{d,pot} - C_{d_0}) \tag{6.4}$$

where $C_{l,pot} = 2\pi(\alpha - \alpha_0)$ and $C_{d_0} = C_{d_{2D}}$ for $\alpha = 0$. The factors f_l and f_d are a function of the radial location and are given by

$$f_l = \frac{1}{2\pi}\left[\frac{1.6(c/r)}{0.1267}\frac{a-(c/r)^{\frac{d}{\lambda}\frac{R}{r}}}{b+(c/r)^{\frac{d}{\lambda}\frac{R}{r}}}\right]\left(1-\frac{r}{R}\right) \tag{6.5}$$

$$f_d = \frac{1}{2\pi}\left[\frac{1.6(c/r)}{0.1267}\frac{a-(c/r)^{\frac{d}{2\lambda}\frac{R}{r}}}{b+(c/r)^{\frac{d}{2\lambda}\frac{R}{r}}}\right]\left(2-\frac{r}{R}\right) \tag{6.6}$$

where a, b and d are empirical correction factors. These factors have been modified to provide a better fit to the experimental data. The variation of thrust with wind speed in the presence of the Raj–Selig stall delay is also shown in Fig. 6.12. It can be seen that the predicted thrust coefficients are in very good agreement with the measurements from the NREL tests for all wind speeds. Even in the post-stall

region, there is a very small error in the predicted thrust unlike, that found in the absence of stall delay model.

The predicted power output is shown see Fig. 6.13. The aerodynamic power output without the stall delay model is found to be in very good agreement with the experimental measurements. Aerodynamic power agrees well with the measurements in the attached flow region. However, the peak power and the corresponding wind speed is slightly overpredicted. As the wind speed increases and most of the blade is operating in the stalled flow, the aerodynamic power output matches the experimental measurements. It should be noted that the discrepancy in predicted and measured power is not as significant as was found in the prediction of thrust. The reason for this is that stall delay is dominant mainly on the inboard sections of the blade. Torque and hence the power output are proportional to the contribution of lift multiplied by the radius of the blade sections. This reduces the net effects of the enhanced lift on power production. Moreover, inplane forces are more dominant in determining the torque (power) generated by a wind turbine blade.

On the other hand, with the Raj–Selig stall delay model, the maximum power output is grossly overpredicted. Again, the wind speed corresponding to the peak power output is 11 ms^{-1}, which is higher than the experimental value (9 ms^{-1}). However, the aerodynamic power is grossly underpredicted in the post-stall region. As mentioned previously, the effect of the enhanced lift on power output is not very significant. In addition, the profile drag is also enhanced according to the Raj–Selig model, which reduces the net power output. It was also noted by Laino and Hansen [147] that the empirical correction factors need to be adjusted for the Raj–Selig stall delay model to achieve a better agreement with the measured power. A similar conclusion can be drawn for all of the other stall delay model used in the wind turbine community, which are essentially postdictive. There is clearly a need to formulate a stall delay model, which models the physics of the flow irrespective of the blade geometry. Moreover, it will be shown in the next section that the stall

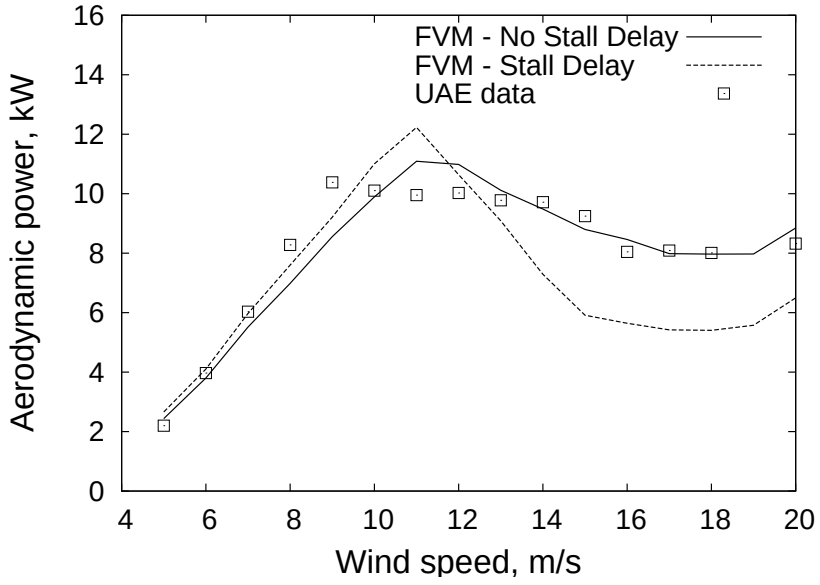

Figure 6.13: Comparison of the predicted and measured aerodynamic power for Phase VI turbine in unyawed flow.

delay models are not directly applicable to the prediction of the aerodynamic loads on a wind turbine operating in yawed flow condition.

Figure 6.14 shows the predicted and measured azimuthal variation of the root flap bending moment for three wind speeds. Both the strain gauge flap bending moment (B3RFB) and an estimated aerodynamic flap bending moment (EAEROFB) as derived from pressure measurements are shown. There is an offset between the two values, with the estimated value being larger than the strain gauge measurement. The decrease in the estimated flap bending moment at $\psi = 180°$ is caused by the tower shadow effect. As the blade passes in front of the tower, the effective velocity at each blade sections decreases. This leads to a reduction in the net lift and torque produced by the blade. In the FVM, the effect of the tower shadow is modeled as a velocity deficit centered around the azimuth angle of $\psi = 180°$ as described in Section 2.2.5. The net decrease in velocity and the azimuthal span of the velocity deficit are determined empirically.

The predicted flap bending moment from the aerodynamic loads was found

to be in good comparison with the estimated flap bending moment EAEROFB for $V_\infty = 5$ ms^{-1}. For higher wind speeds ($V_\infty = 10$ ms^{-1} and 15 ms^{-1}), the flap bending moment was underpredicted. This was found to be consistent with the underpredicted net thrust for higher wind speeds, and may be because of the absence of a stall delay model (see later). However, the strain gauge flap bending value shows a sinusoidal variation because of the elastic deformations of the blade. These deformations are not modeled in this version of the FVM. The in-plane moment or the edgewise bending moment is dominated mainly by 1/rev variation because of the gravitational loads. No estimated values of the in-plane moment were available from the pressure measurements, so only the strain gauge values are shown. The predictions and measurements showed good comparisons for the azimuthal variation of the in-plane moment (Fig. 6.15) at all three wind speeds.

The average value of the aerodynamic torque was predicted accurately (Fig. 6.15). Again, the decrease in the aerodynamic torque near $\psi = 180°$ is caused by the tower shadow effect. It can be seen that the torque predictions and measurements are also in agreement at higher wind speeds. This is consistent with the predictions of the aerodynamic power, as shown previously in Fig. 6.13. The torque measurements made using a strain gauge on the low speed shaft shows a sinusoidal variation, which is introduced because of the drive-train shaft degree of freedom. Again, the structural deformations have not been modeled in this version of FVM, but in principle these can be modeled by interfacing FVM with a dynamics code like YawDyn [32], FAST [148, 149], or ADAMS [150].

A comparison of the radial variation of C_n and C_t is shown in Figs. 6.17 and 6.18, respectively. The stall delay effect in the inboard regions of the blade can be clearly seen for higher wind speeds in the measured C_n. There is a considerable difference between the predictions and the measurements of C_n for ($V_\infty = 10$ ms^{-1} and 15 ms^{-1}). For $V_\infty = 5$ ms^{-1}, where the turbine is operating in essentially attached flow conditions, the predicted C_n values are found to be in good agreement

with the measurements.

The C_t values also compared very well with the experimental measurements for all wind speeds. For $V_\infty = 10$ ms^{-1}, the loss in the C_t at $0.47R$ is, however, not predicted. This sudden loss in suction could be because of the rapid movement of the flow separation point from the trailing edge to the leading edge of the blade. It was found that the effect of the rotational stall delay on the leading-edge thrust coefficient is not very clear. One of the reasons for this, is the difficulty associated with measuring C_t in the experiment when the flow is stalled. Flow in the post-stall regime is very unsteady and the number of pressure taps used in the experiment are limited by physical considerations.

The spanwise variation of the predicted and measured pitching moment coefficient C_m is shown in Fig. 6.19. A similar decrease in C_m is observed for $V_\infty = 10$ ms^{-1} at the same point where C_t decreases. The presence of laminar flow separation and turbulent reattachment downstream has been cited as one of the possible explanations for this behavior [151]. The reconstructed C_m from FVM agree well with the measurements at low wind speeds. However, there is a considerable difference in the predicted pitching moment coefficients at 15 ms^{-1}.

6.2.2 Wind Turbine in Yawed Flow

Wind gusts and turning the turbine out of the wind to control power in small wind turbines causes them to operate under yawed flow conditions. The larger wind turbines usually have yaw control capabilities, but the response time to sudden changes in wind direction or gusts can lead to at least some time of operation in yawed flow. The turbine disk yaws with respect to the wind, and the skewed wake behind the wind turbine causes a non-uniform inflow and unsteady airloads to be produced on the turbine blades. The power output from the wind turbine also varies in a periodic manner. Accurately modeling the aerodynamic behavior of wind turbines in yawed flow is known to be very important to predict their fatigue

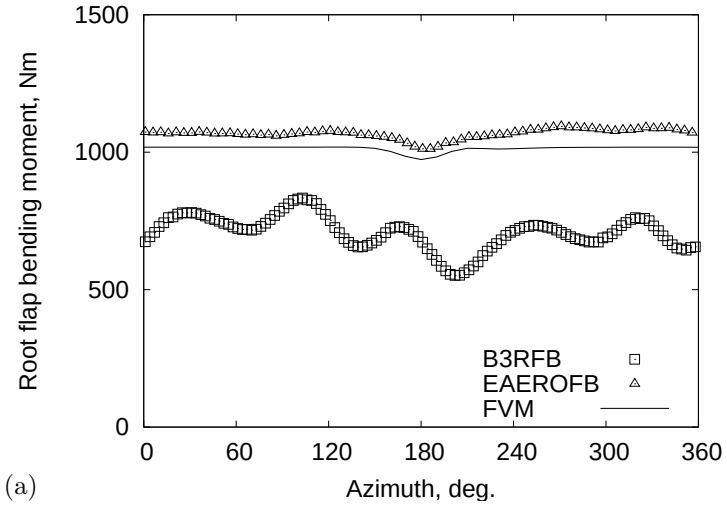

(a)

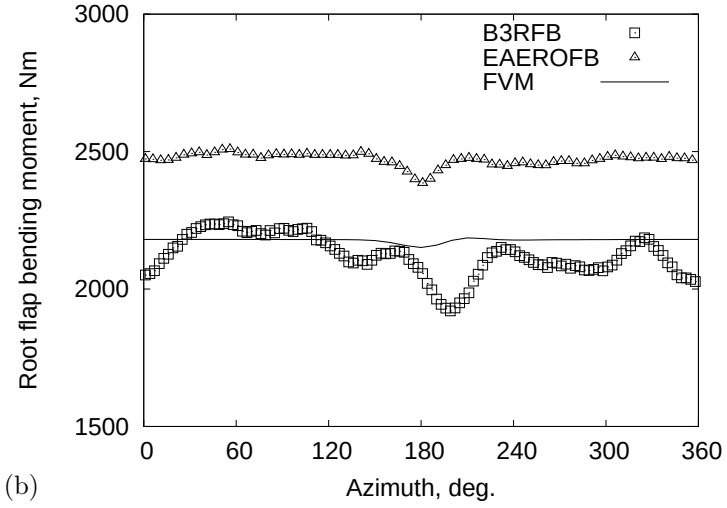

(b)

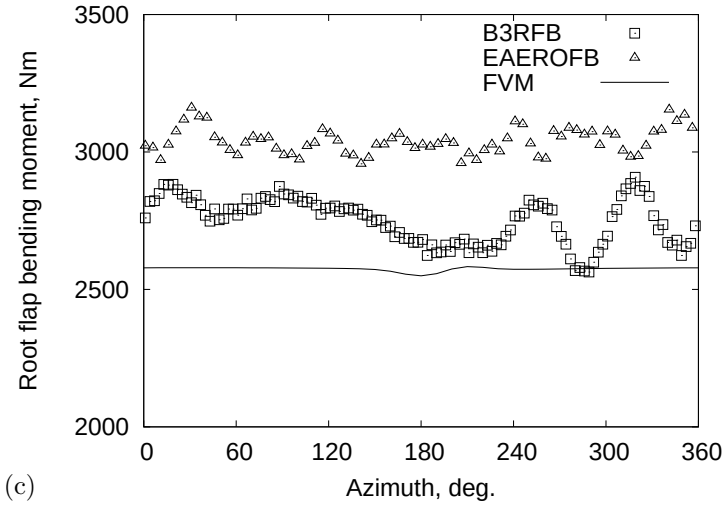

(c)

Figure 6.14: Comparison of the measurement and predictions of the azimuthal variation of the root flap bending moment in unyawed flow for a wind speed of (a) 5 ms^{-1}, (b) 10 ms^{-1}, and (c) 15 ms^{-1} .

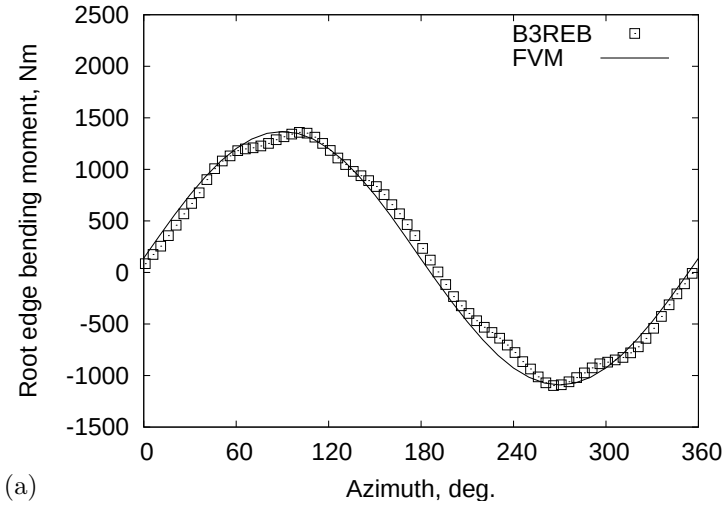

(a)

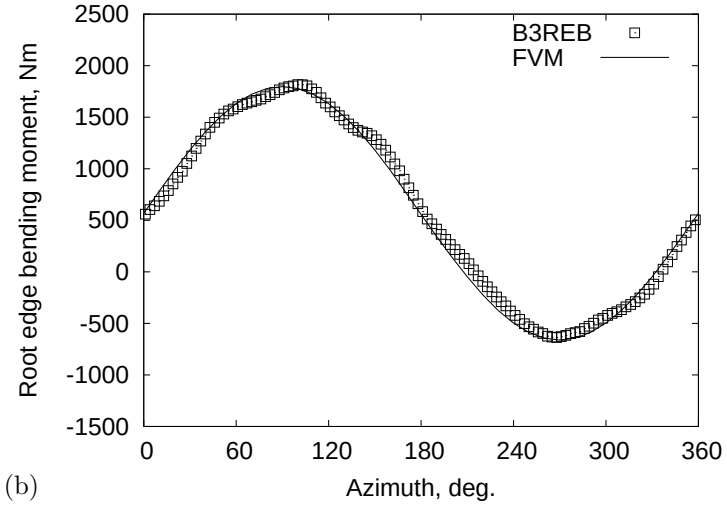

(b)

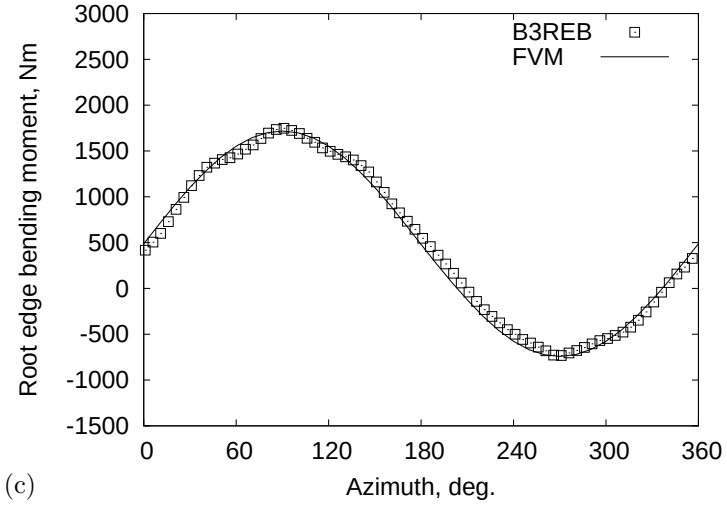

(c)

Figure 6.15: Comparison of the measurement and predictions of the azimuthal variation of the root edge bending moment in unyawed flow for a wind speed of (a) 5 ms^{-1}, (b) 10 ms^{-1}, and (c) 15 ms^{-1} .

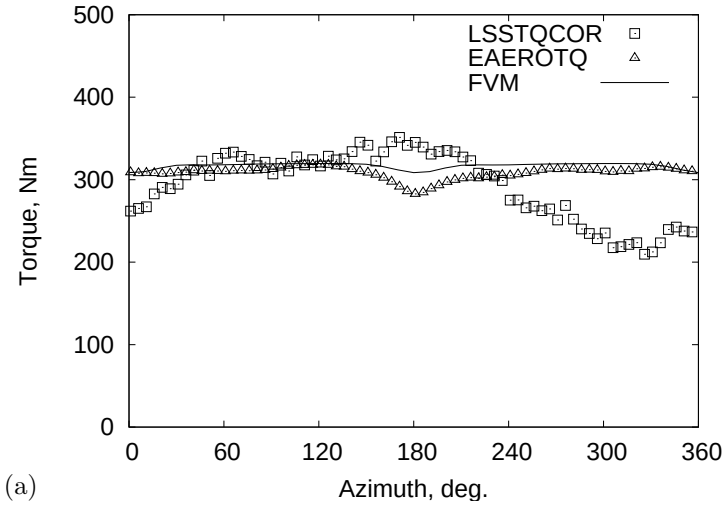

(a)

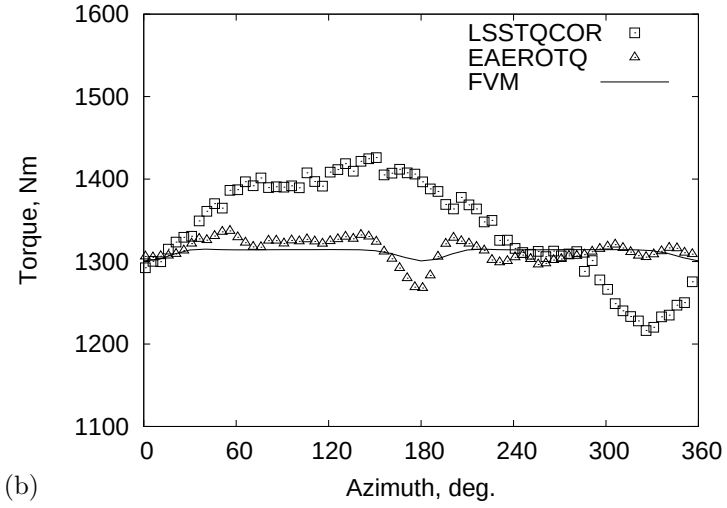

(b)

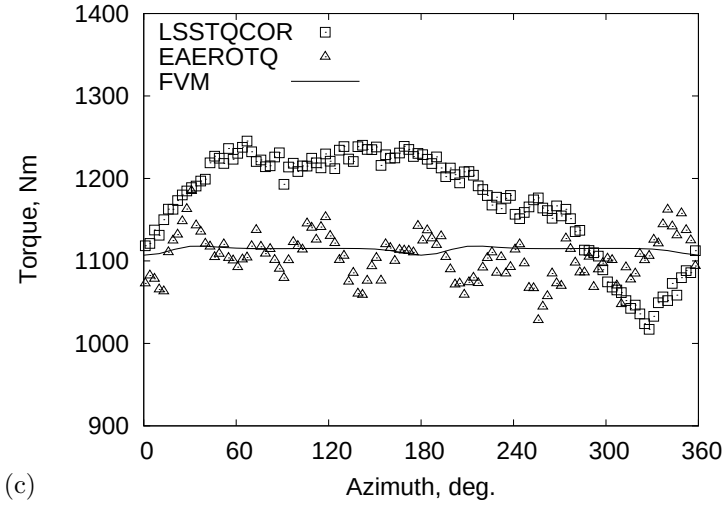

(c)

Figure 6.16: Comparison of the measurement and predictions of the azimuthal variation of the LSS torque in unyawed flow for a wind speed of (a) 5 ms^{-1}, (b) 10 ms^{-1}, and (c) 15 ms^{-1} .

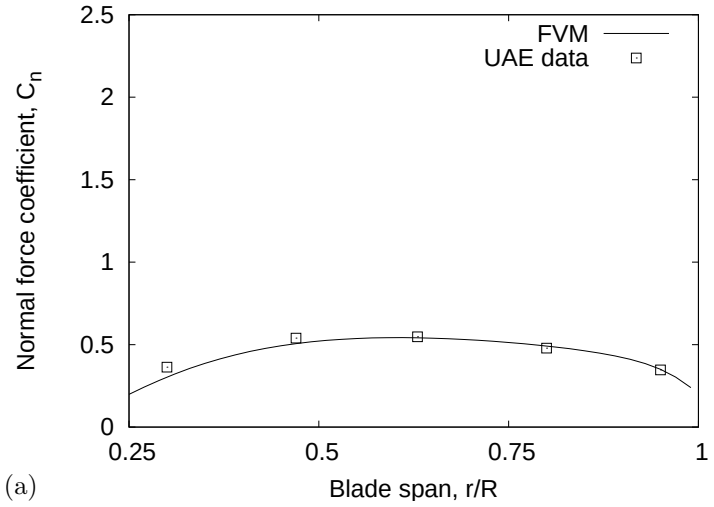

(a)

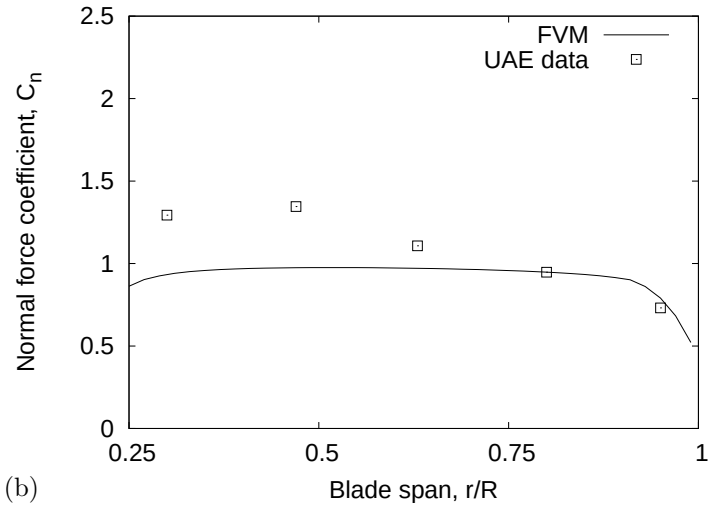

(b)

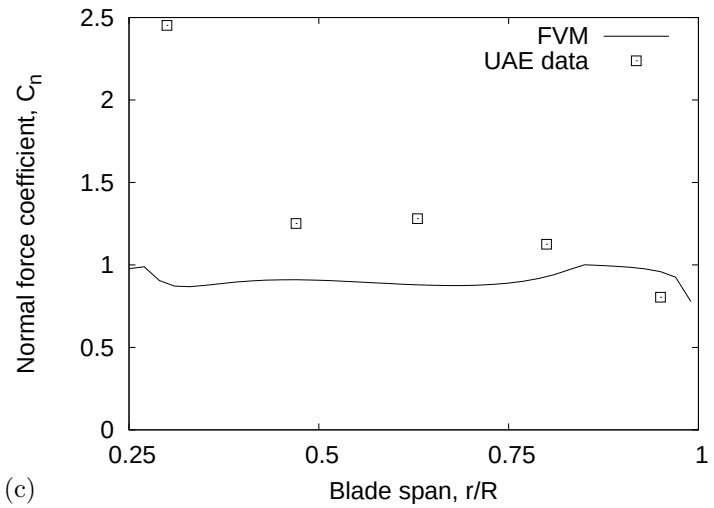

(c)

Figure 6.17: Comparison of the measurement and predictions of the normal force coefficient along the span of the blade in unyawed flow for a wind speed of (a) 5 ms^{-1}, (b) 10 ms^{-1}, and (c) 15 ms^{-1}.

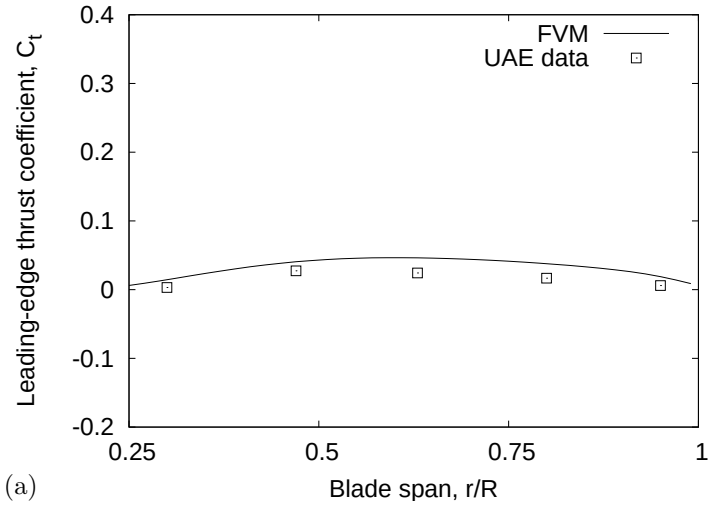

(a)

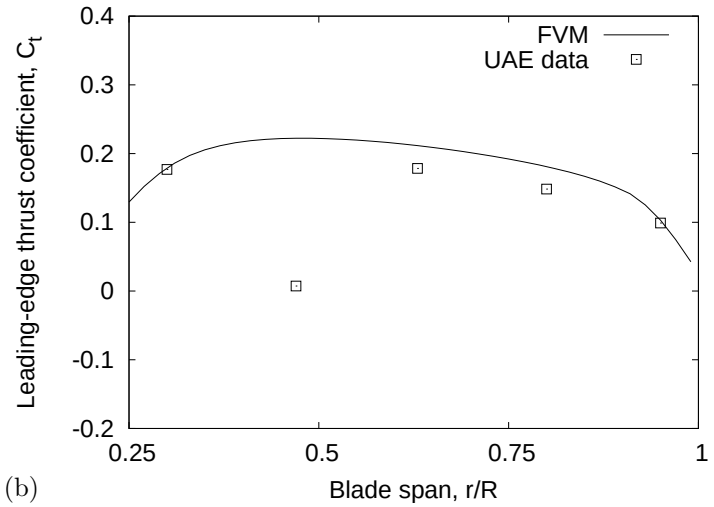

(b)

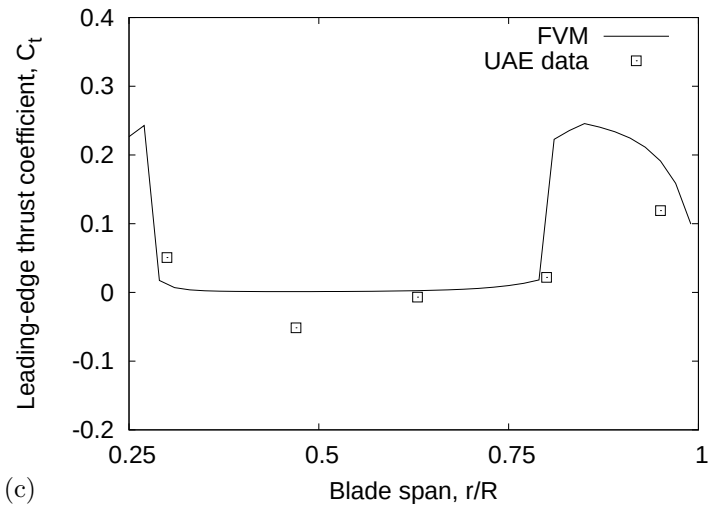

(c)

Figure 6.18: Comparison of the measurement and predictions of the leading-edge thrust coefficient along the span of the blade in unyawed flow for a wind speed of (a) 5 ms^{-1}, (b) 10 ms^{-1}, and (c) 15 ms^{-1}.

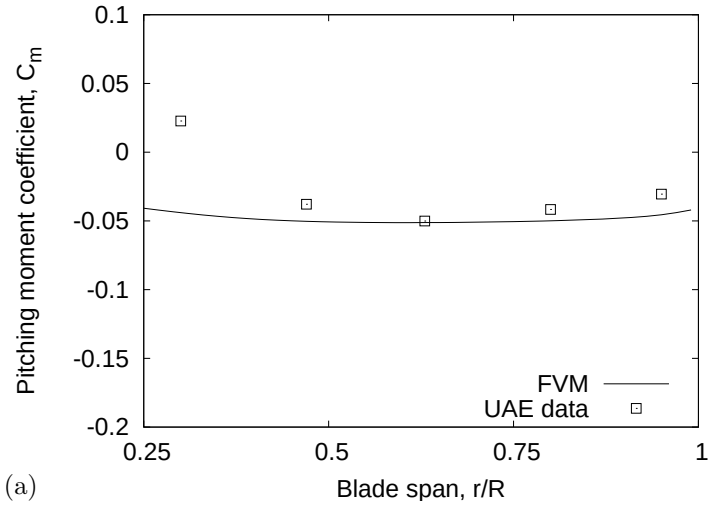

(a)

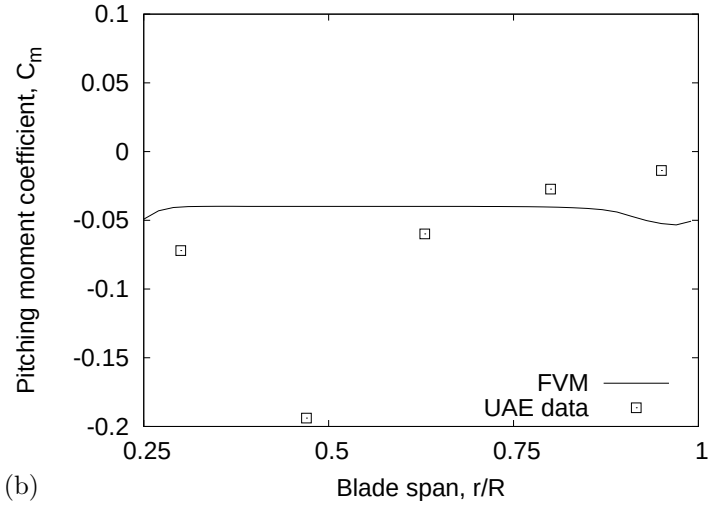

(b)

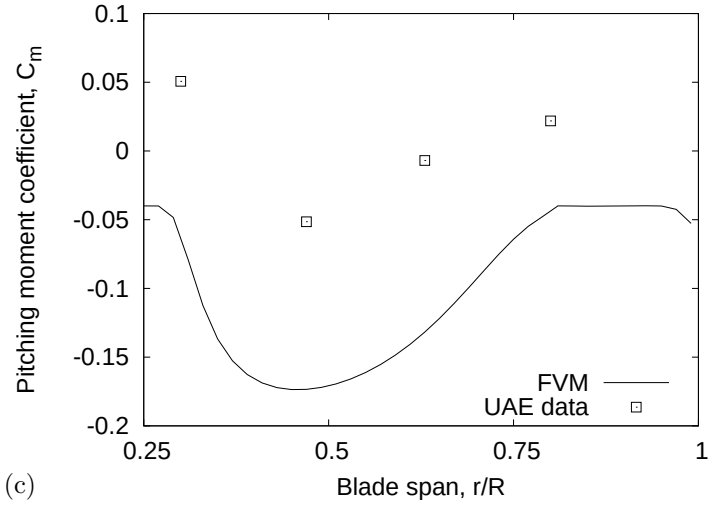

(c)

Figure 6.19: Comparison of the measurement and predictions of the pitching moment coefficient along the span of the blade in unyawed flow for a wind speed of (a) 5 ms^{-1}, (b) 10 ms^{-1}, and (c) 15 ms^{-1}.

loads and power output quality.

Performance methods based on the blade-element momentum theory generally use dynamic inflow models to account for the azimuthal variation in inflow [23,24] as was mentioned previously in Section 5.3. The dynamic inflow models are based on the idea of representing the unsteady aerodynamic lag associated with the changes in turbine thrust or blade pitch. However, some of these inflow models have been shown to have numerical convergence issues when coupled with the BEM method [152], and are not universally applicable. On the other hand, the skewed and freely deforming wake in the FVM inherently accounts for the asymmetry in inflow over the turbine disk without any additional approximations.

Figure 6.20 shows the variation of the azimuthally averaged aerodynamic thrust with wind speed for the NREL unsteady aerodynamic experiment and the FVM predictions for three yaw angles ($\Lambda = 10^\circ,\ 30^\circ$ and $, 60^\circ$). The agreement between the predictions and the measurement is very good for low wind speeds. As the wind speed increases, aerodynamic thrust is slightly underpredicted because of 3D stall delay effects near the inboard regions of the blade. However, notice that the stall delay effects are not as significant as for the unyawed case. Because of the unsteady variation of the local blade section angle of attack beyond stall, the sections undergo dynamic stall, which dominates the flow field under yawed flow conditions. This can also be seen from the fact that the error in predicting the turbine thrust decreases with increasing yaw angle. For $\Lambda = 60^\circ$, the difference between the measured and predicted thrust is almost negligible.

The aerodynamic power prediction was compared against the experimental measurements, as shown in Fig. 6.21. For the low and moderate yaw angles, the extracted power is predicted very well for wind speeds up to 8 ms^{-1}. However, as the wind speed further increases, the aerodynamic power is slightly underpredicted. The predicted power matches well with the measured power for $\Lambda = 60^\circ$. For higher wind speeds, the predicted power was found to be in good agreement with

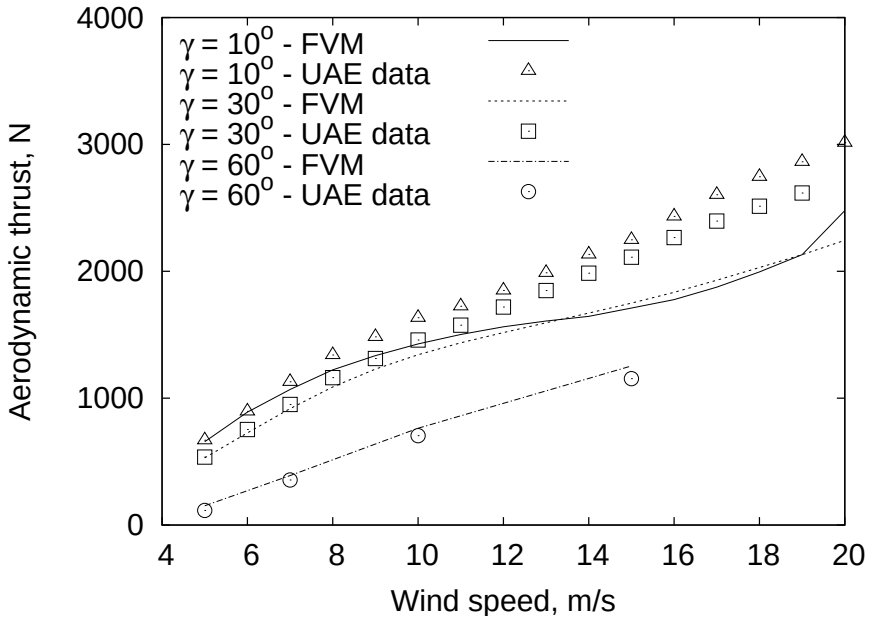

Figure 6.20: Variation of the aerodynamic thrust with wind speed for the Phase VI turbine for yawed flow.

the measured power for all yaw angles. The peak power was, however, slightly underpredicted. Notice that the FVM predicts well the the performance of a wind turbine in yawed flow, especially for higher yaw angles. This is where the BEM based methods generally fail or show otherwise poor predictions. BEM methods are strictly valid only under unyawed flow conditions, and are extended to yawed flow conditions with some form of dynamic inflow models to account for the asymmetric loading over the turbine disk. Although there has been some progress in developing dynamic inflow models for wind turbines [24], these methods need to be refined further, mainly because they do not apply to the windmill flow state and so their validity is not guaranteed for all turbine operating conditions [147].

Figure 6.22 shows a comparison of the aerodynamic power prediction with and without the Raj–Selig stall delay model at a yaw angle of 30°. It can be seen that the presence of a stall delay model does not affect the net power output. On the other hand, the increased drag in the Raj-Selig delay model leads to slight underprediction

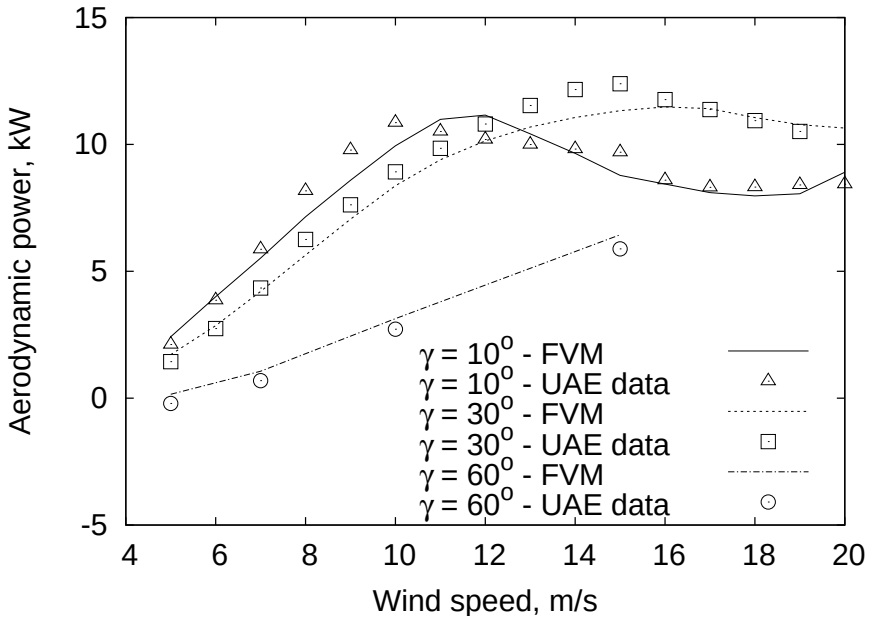

Figure 6.21: Variation of the aerodynamic power with wind speed for the Phase VI turbine for yawed flow.

of the power output at very high wind speeds. This discrepancy can be improved by adjusting the empirical factors in the stall delay model. However, these values are not unique and so need to be adjusted for different turbine configurations and geometry.

Figure 6.23 shows the comparison of the predicted and measured flap bending moment for three wind speeds at a yaw angle of 30°. It can be seen that the strain gauge root flap moment (B3RFB) shows a mean offset, which is significant for $V_\infty = 5$ ms^{-1}. However, the predicted values of flap bending moment are in good comparison with the estimated flap bending (EAEROFB). For higher wind speeds ($V_\infty = 10$ ms^{-1} and 15 ms^{-1}), the strong 1/rev found in the flap bending moment variation is predicted well by the FVM. Strain gauge measurements (B3RFB) contain a 5/rev frequency signal. However, it is not clear where this variation arises from, because the first flapwise bending frequency of the blade is around 6/rev. Notice that the flap bending moment is not significantly underpredicted at higher

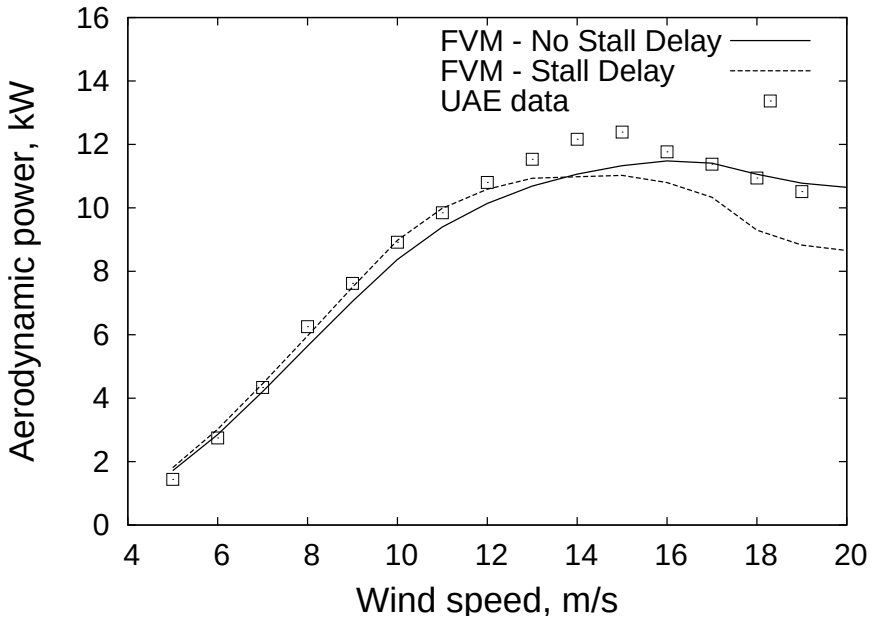

Figure 6.22: Comparison of the predicted aerodynamic power with and without the stall delay model for a yaw angle of $\Lambda = 30°$ for the Phase VI turbine.

wind speeds as was observed in the unyawed case. This is consistent with a small underprediction of the predicted turbine thrust for $\Lambda = 30°$ for higher wind speeds. More importantly, it reinforces the fact that dynamic stall is more dominant than stall delay phenomenon when a wind turbine operates in yawed flow. One of the major weakness of the present empirical stall delay models is that they do not apply for unsteady flows, which would always lead to an overprediction of the aerodynamic forces.

The azimuthal variation of the edgewise bending moment (see Fig. 6.24) shows a very high frequency (7/rev) signal superimposed on the 1/rev gravity loading, which is probably because of the first edgewise bending frequency. The magnitude of the 7/rev load increases with increasing wind speed. However, the mean edgewise bending moment is still predicted well by the FVM.

Figure 6.25 shows a weak 1/rev variation in the torque measurement LSSTQ-COR (measured with a strain gauge) at the lower wind speeds, which increases in

magnitude with increasing wind speed. Again, this 1/rev variation in strain gauge torque is probably a result of the drive-train dynamics. A sinusoidal variation is also observed in the EAEROTQ, which is a result of the tower shadow effect. The FVM predicts the mean value of the torque very well, but does not predict the cyclic variation.

The spanwise distribution of the aerodynamic coefficients (C_n, C_t and C_m) as predicted by the FVM is compared with the experimental measurements at an azimuth angle of $\psi = 0°$. The predicted aerodynamic coefficients show reasonable agreement with the experimental data. C_n is predicted well over the span of the blade (see Fig. 6.26) except at the $30\%R$ station for 10 ms^{-1}. Similar observations can be made for C_t and C_m here. The FVM model does not predict incipient dynamic stall for $V_\infty = 10$ ms^{-1}, and hence underpredicts C_n and C_m.

The azimuthal variation of the aerodynamic coefficients for different wind speeds also shows close agreement with UAE data for 5 ms^{-1} (see Figs. 6.29 through 6.31). However, for the intermediate wind speed of 10 ms^{-1}, the absence of contributions from dynamic stall leads to an underprediction of C_n and C_m (see Figs. 6.32 through 6.34). For higher wind speeds (see Figs. 6.35 through 6.37), the critical condition for the onset of dynamic stall is satisfied over most of the azimuth range, and excellent agreement is achieved for the C_t and C_m components, while C_n is underpredicted at the inboard section. Similar level of agreement was achieved for the larger yaw angles.

6.3 Summary

This chapter has been directed towards demonstrating the capability of the free-vortex wake model to model the aerodynamics of a horizontal axis wind turbine in a time-accurate manner. Performance and airloads prediction of FVM were validated against experimental measurements. The emphasis of the first part of this chapter was to validate the prediction of the wake geometry from FVM. This was

achieved by comparing wake positions obtained from the wake visualization conducted in DUT on a two-bladed rotor. The wake geometry was predicted well for all the measured tip speed ratios and tip pitch angles under both axial and the yawed flow conditions. However, there were slight differences in the predictions at higher yaw angles. This is in part because of the uncertainty in defining the center of tip vortices in the measurements because of the diffusion of the smoke with increasing wake age.

The second part of this chapter was focussed on the validation of FVM against comprehensive loads and performance measurements that were available from the NREL Phase VI turbine tests. The numerical predictions of thrust and aerodynamic power output showed good agreement against the experimental data for attached and deep stall conditions. During incipient (moderate stall) conditions, the absence of a 3D stall delay model leads to a slight underprediction of the aerodynamic power and thrust. The spanwise variation of loads is predicted well at all spanwise sections except for the inboard sections, where stall delay effects are more dominant. However, dynamic stall effects dominate the flow field in the yawed flow conditions, and good agreement was obtained between measurements and predictions. The unsteady loads on the blade and dynamic stall hysteresis was predicted well for attached flow and deep stall conditions, respectively. The onset of dynamic stall under incipient separation conditions was, however, not predicted very well. This leads to slight underprediction in the azimuthal variation of the normal force and pitching moment coefficients.

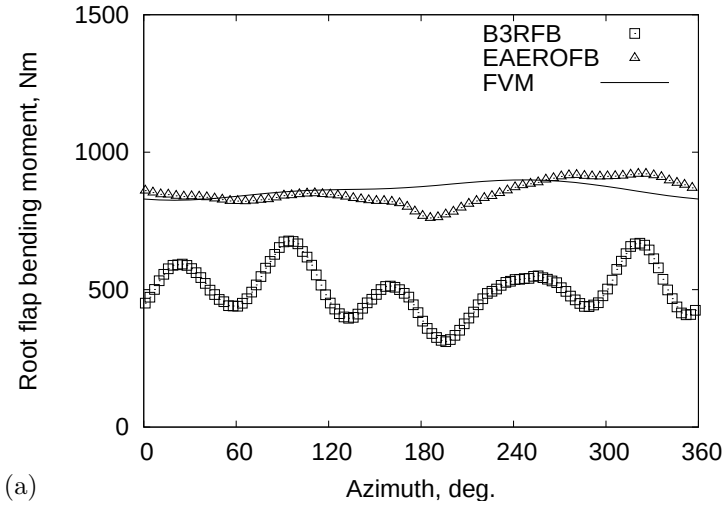

(a)

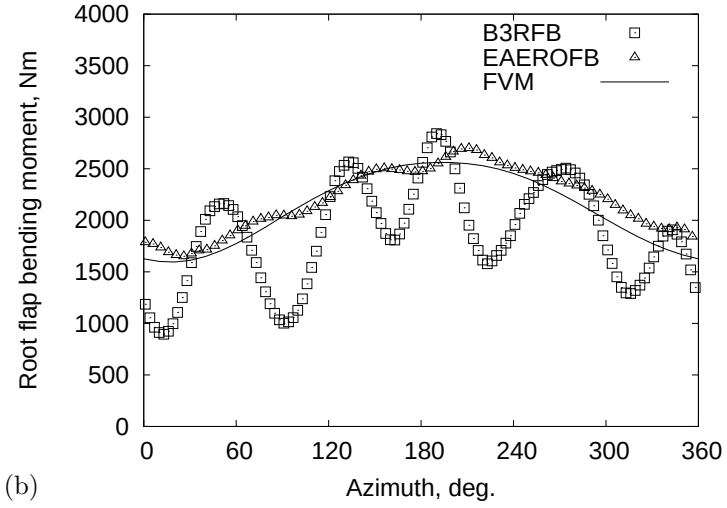

(b)

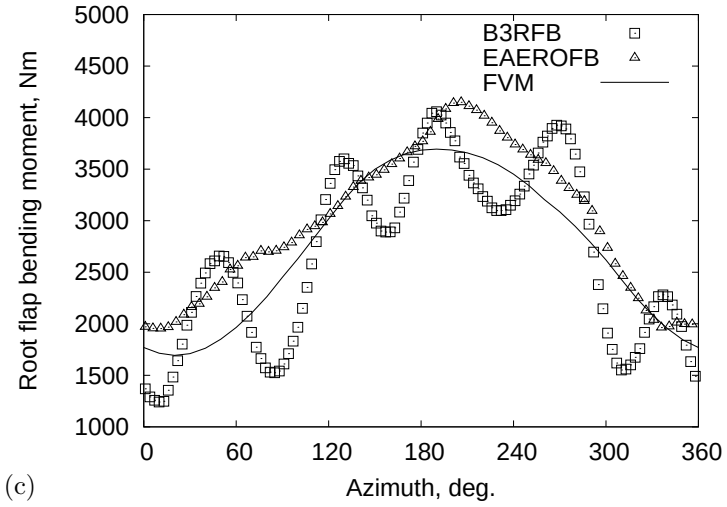

(c)

Figure 6.23: Comparison of the measurement and predictions of the azimuthal variation of the root flap bending moment for a yaw angle of 30° and a wind speed of (a) 5 ms^{-1}, (b) 10 ms^{-1}, and (c) 15 ms^{-1}.

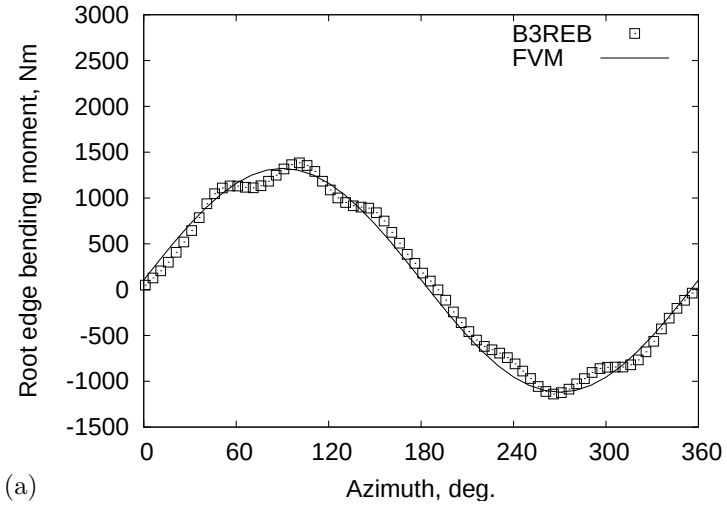

(a)

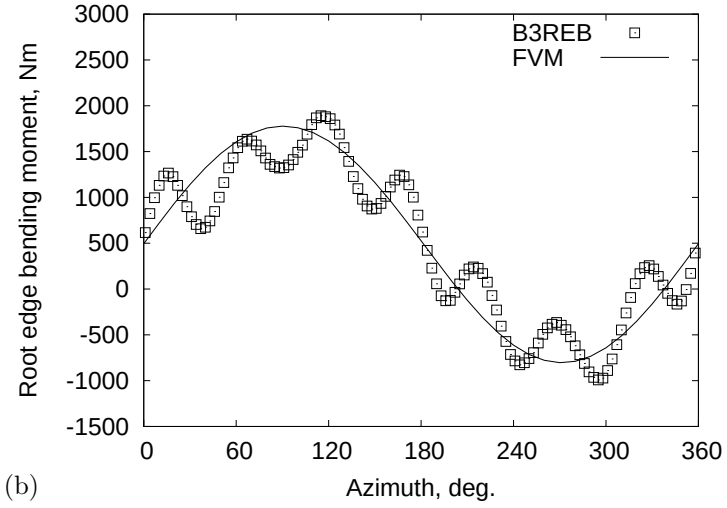

(b)

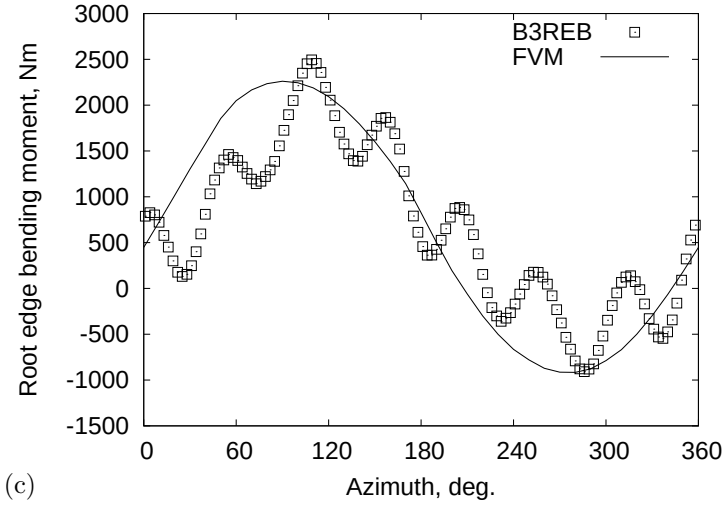

(c)

Figure 6.24: Comparison of the measurement and predictions of the azimuthal variation of the root edge bending moment for a yaw angle of 30° and a wind speed of (a) 5 ms^{-1}, (b) 10 ms^{-1}, and (c) 15 ms^{-1}.

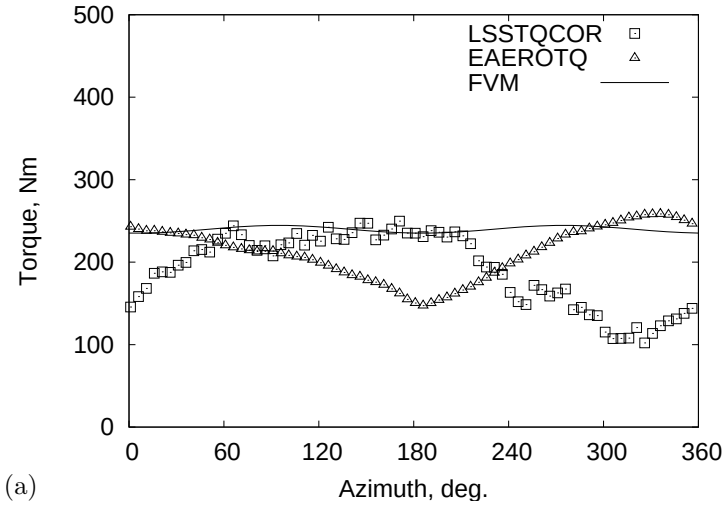

(a)

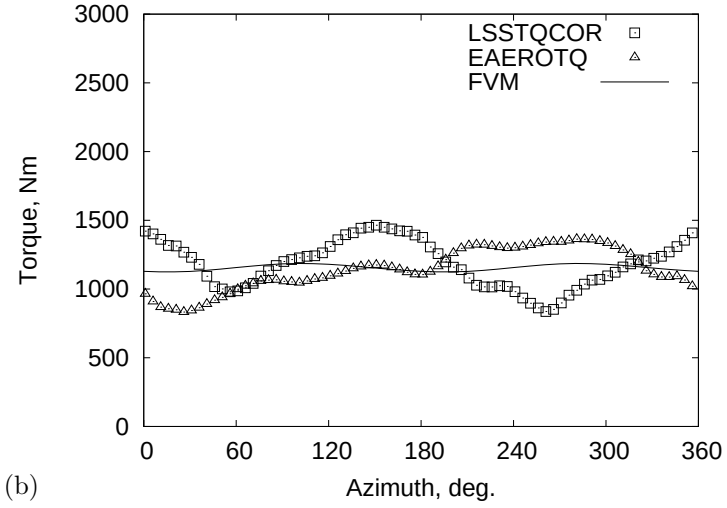

(b)

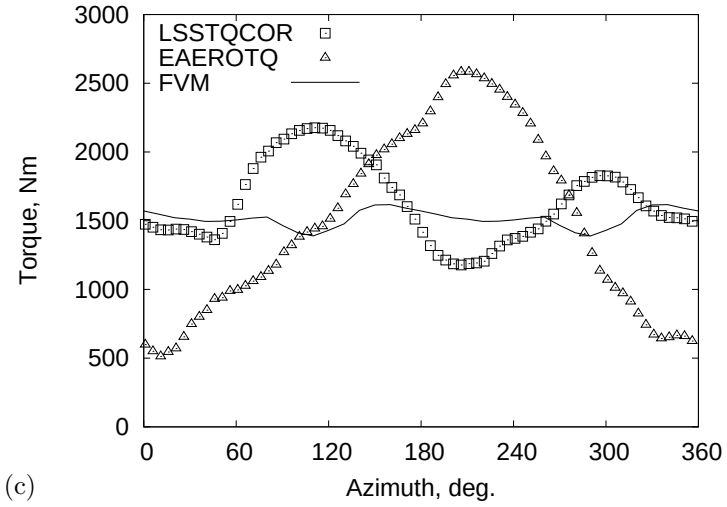

(c)

Figure 6.25: Comparison of the measurement and predictions of the azimuthal variation of the LSS torque for a yaw angle of 30° and a wind speed of (a) 5 ms^{-1}, (b) 10 ms^{-1}, and (c) 15 ms^{-1}.

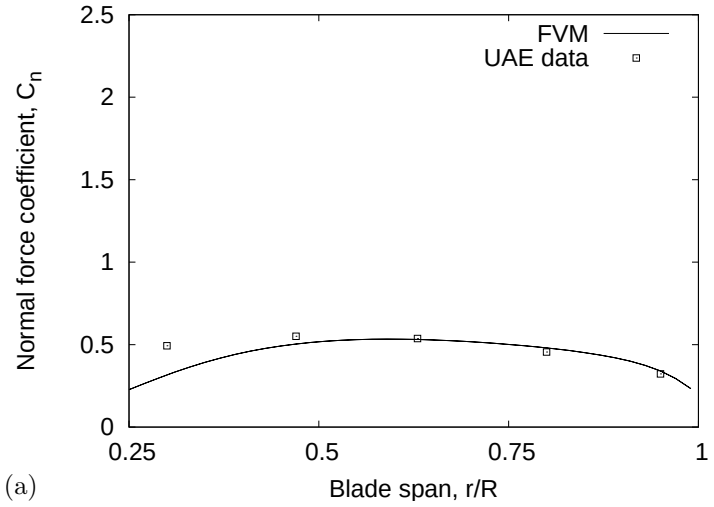

(a)

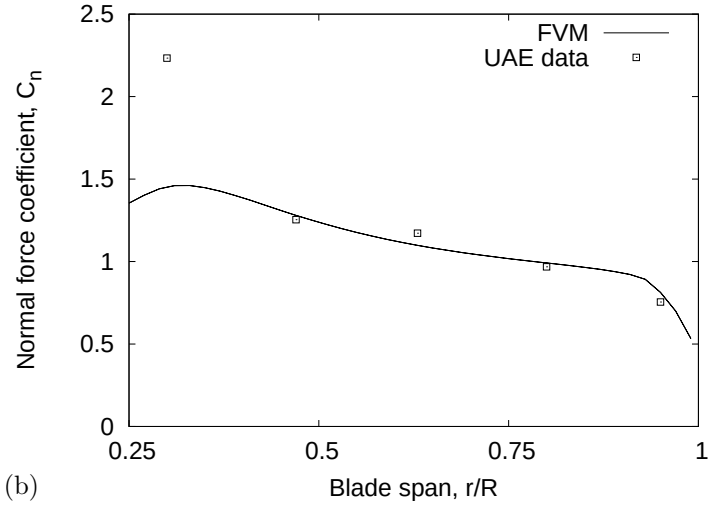

(b)

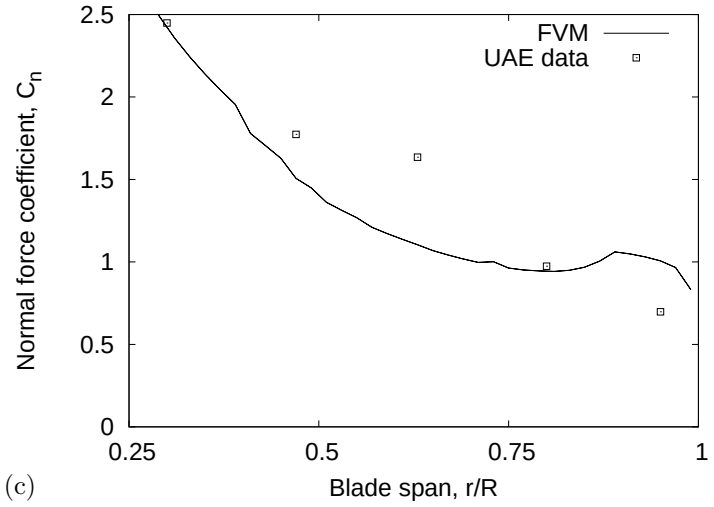

(c)

Figure 6.26: Comparison of the measurement and predictions of the normal force coefficient along the span of the blade for a yaw angle of 30° and a wind speed of (a) 5 ms^{-1}, (b) 10 ms^{-1}, and (c) 15 ms^{-1}.

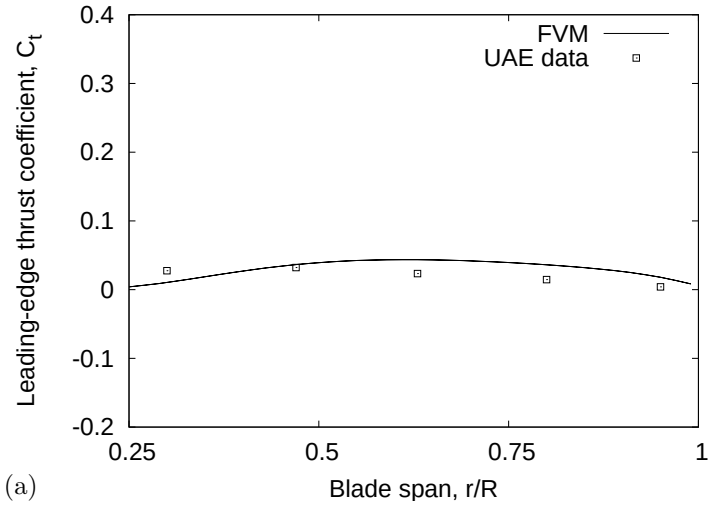

(a)

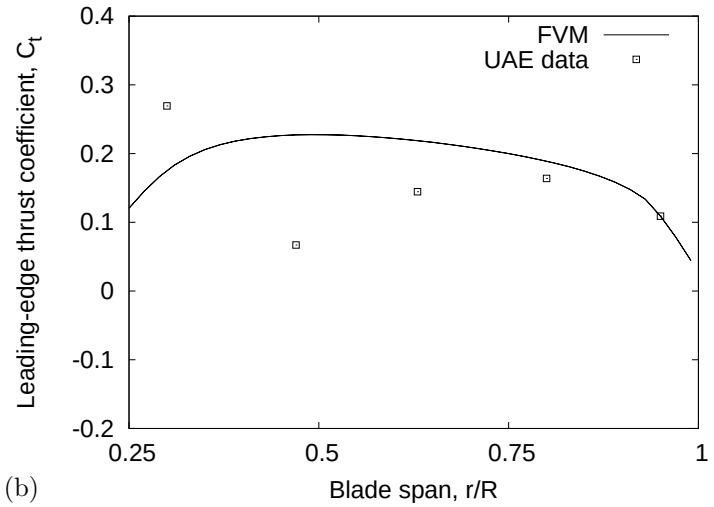

(b)

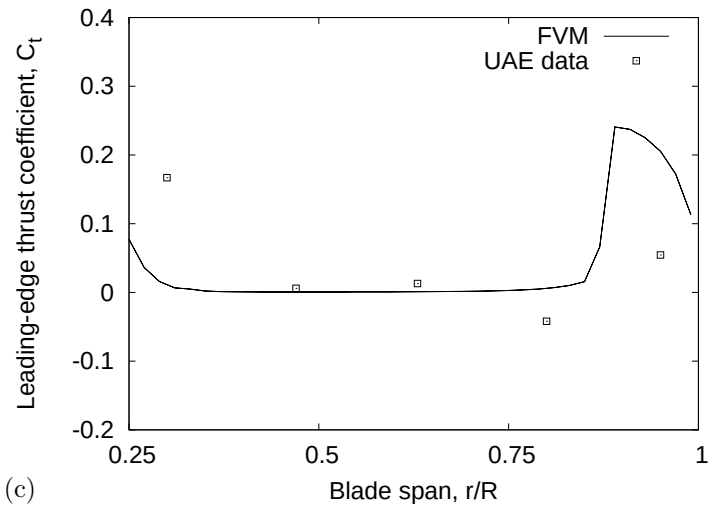

(c)

Figure 6.27: Comparison of the measurement and predictions of the leading-edge thrust coefficient for $\psi = 0$ along the span of the blade for a yaw angle of 30° and a wind speed of (a) 5 ms^{-1}, (b) 10 ms^{-1}, and (c) 15 ms^{-1}.

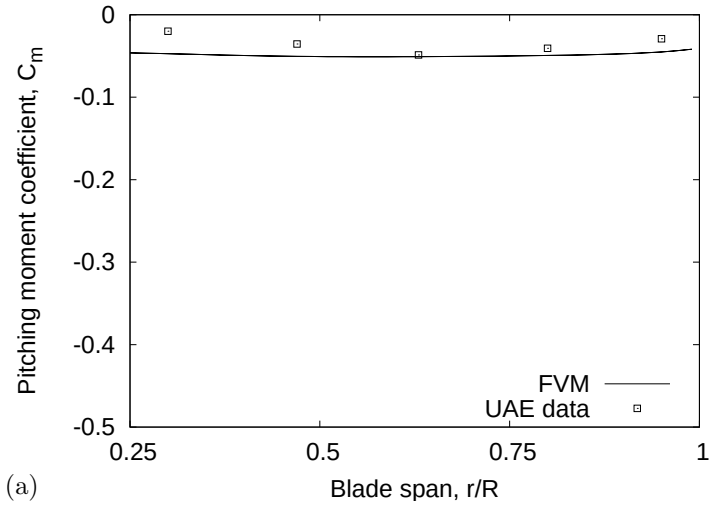

(a)

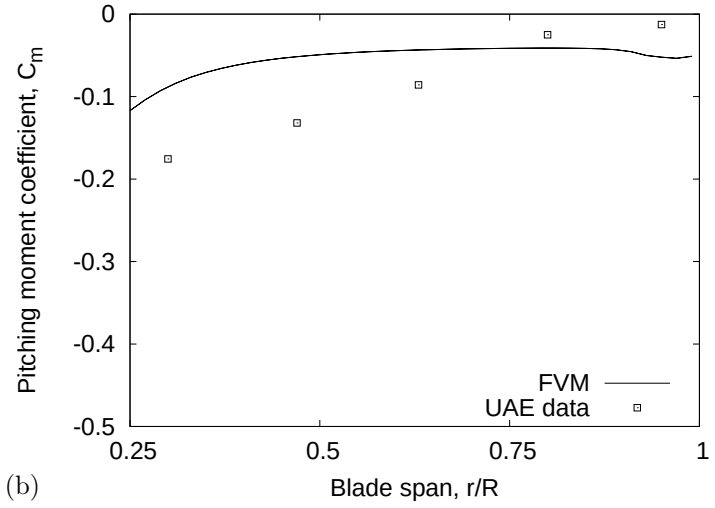

(b)

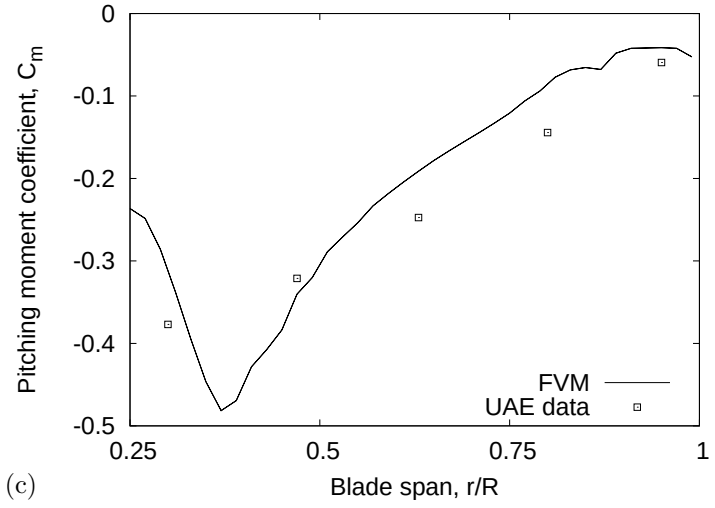

(c)

Figure 6.28: Comparison of the measurement and predictions of the the pitching moment coefficient for $\psi = 0$ along the span of the blade for a yaw angle of 30° and a wind speed of (a) 5 ms^{-1}, (b) 10 ms^{-1}, and (c) 15 ms^{-1}.

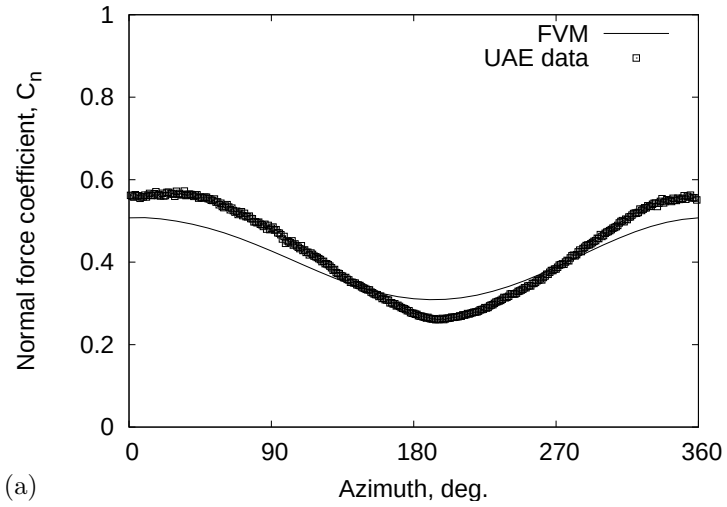

(a)

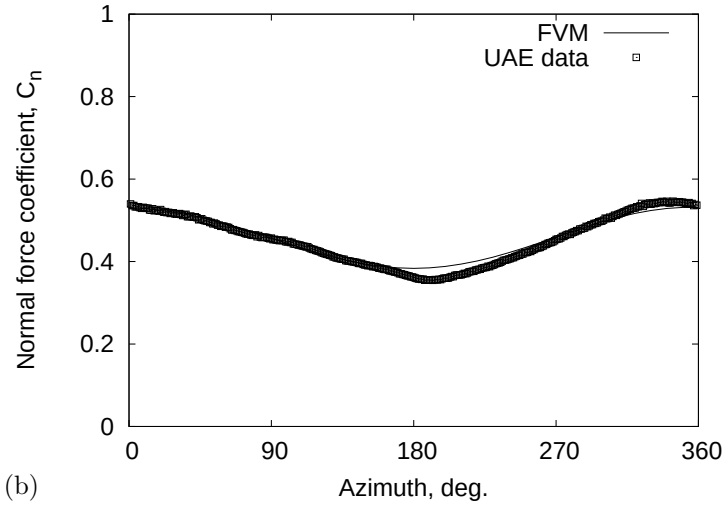

(b)

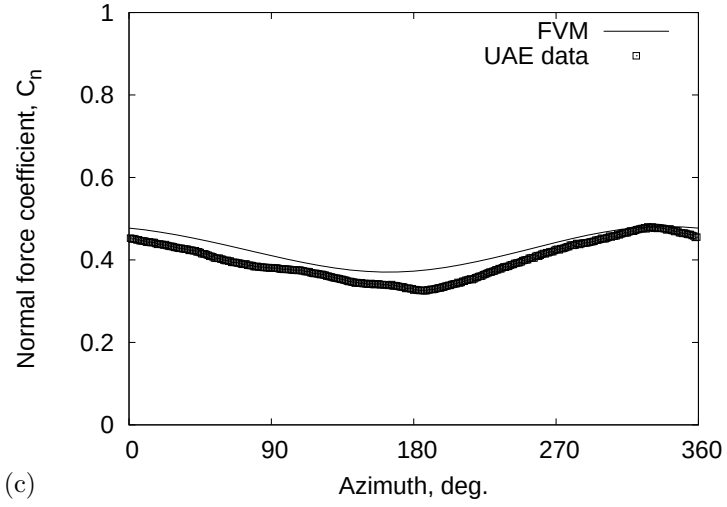

(c)

Figure 6.29: Comparison of the measurement and predictions of the azimuthal variation of normal force coefficient for (a) 47%R, (b) 63%R, and (c) 80%R at 5 ms^{-1} and a yaw angle of 30°.

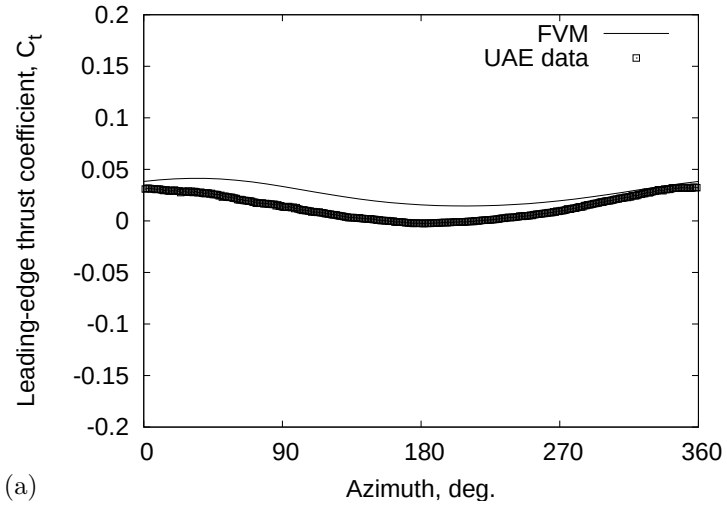

(a)

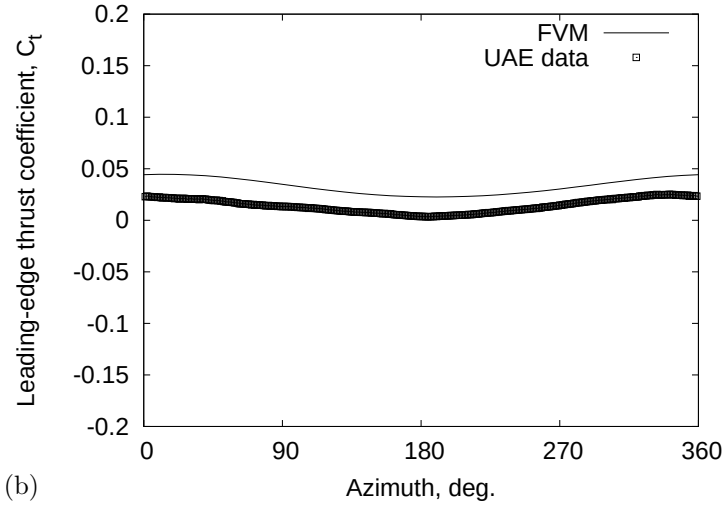

(b)

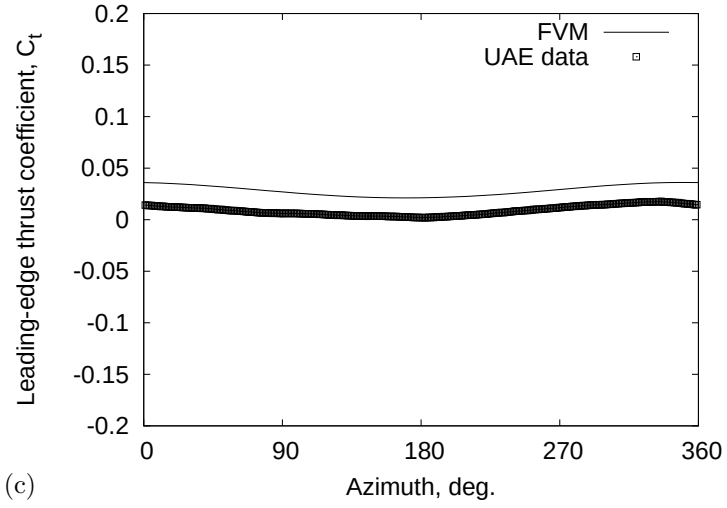

(c)

Figure 6.30: Comparison of the measurement and predictions of the azimuthal variation of the leading-edge thrust coefficient for (a) 47%R, (b) 63%R, and (c) 80%R at 5 ms^{-1} and a yaw angle of 30°.

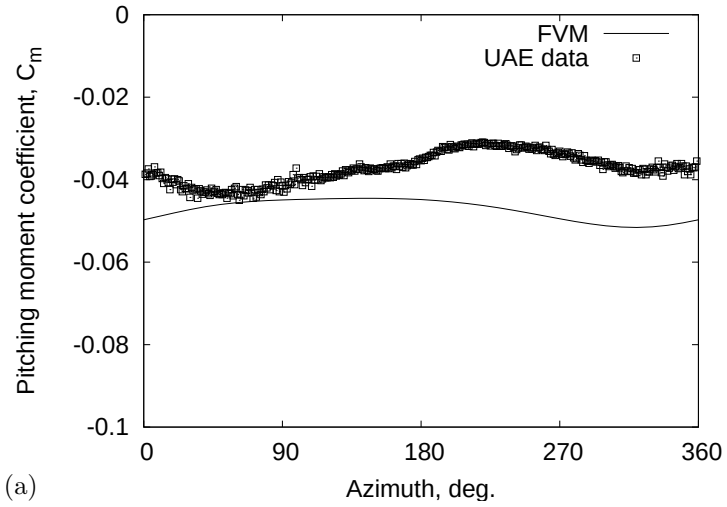

(a)

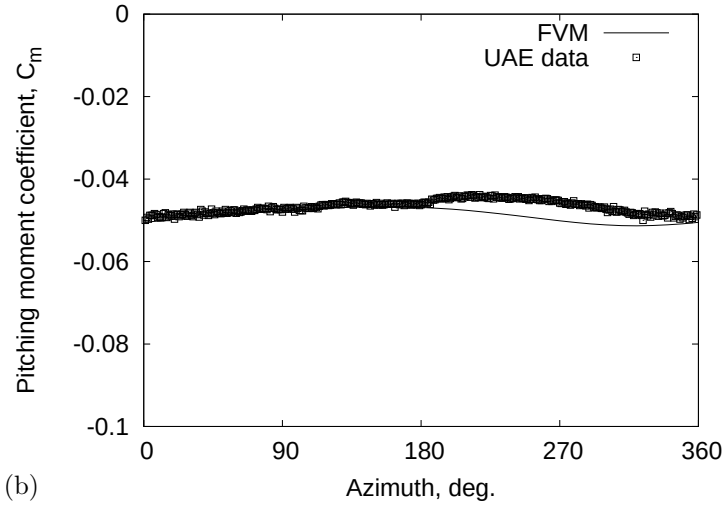

(b)

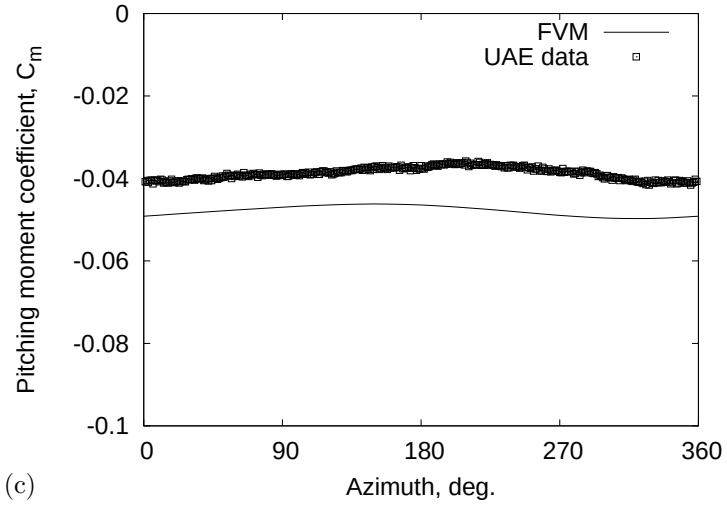

(c)

Figure 6.31: Comparison of the measurement and predictions of the azimuthal variation of the pitching moment coefficient for (a) 47%R, (b) 63%R, and (c) 80%R at 5 ms^{-1} and a yaw angle of 30°.

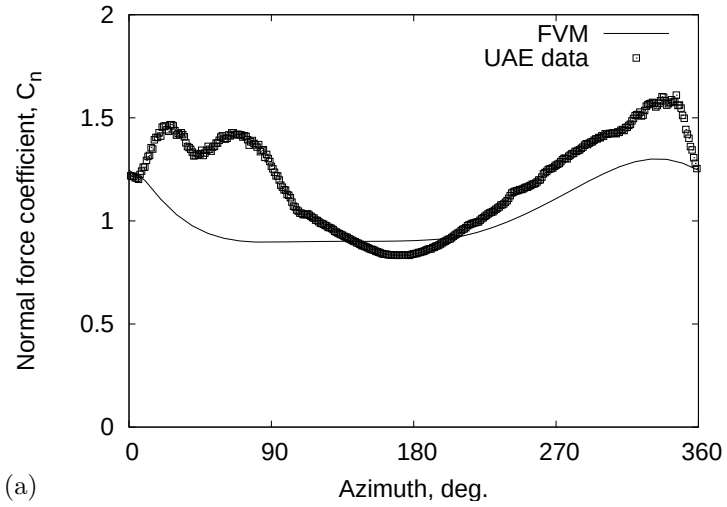

(a)

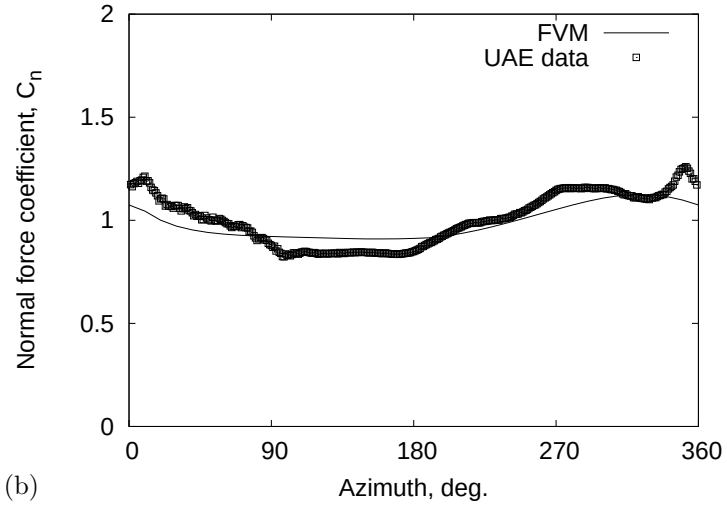

(b)

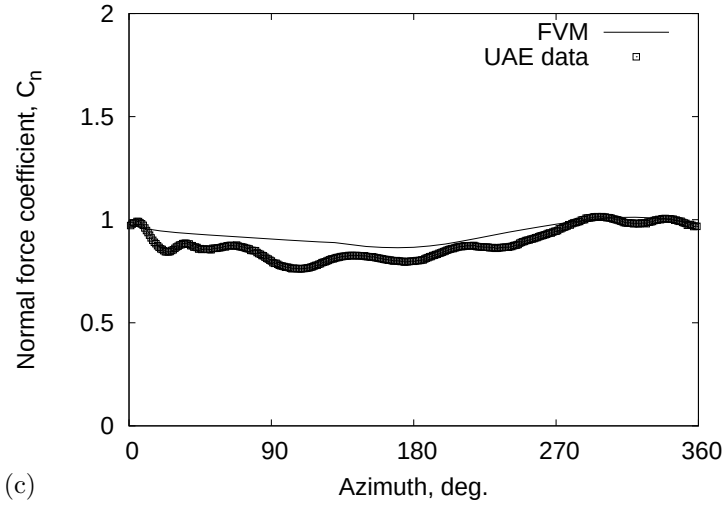

(c)

Figure 6.32: Comparison of the measurement and predictions of the azimuthal variation of normal force coefficient for (a) 47%R, (b) 63%R, and (c) 80%R at 10 ms^{-1} and a yaw angle of 30°.

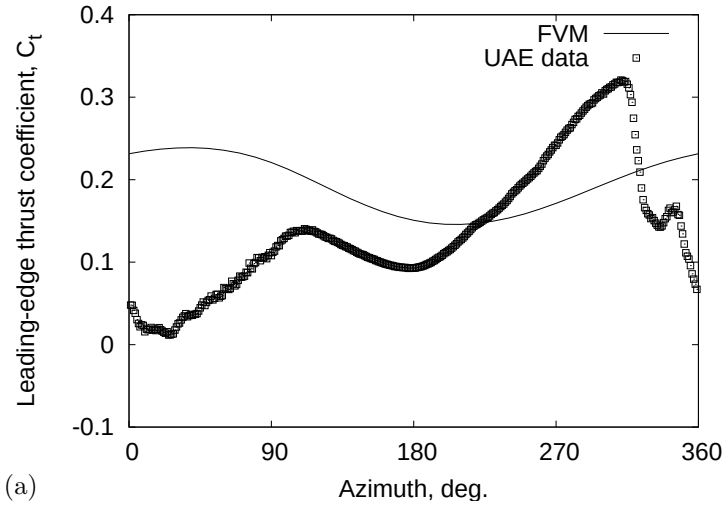

(a)

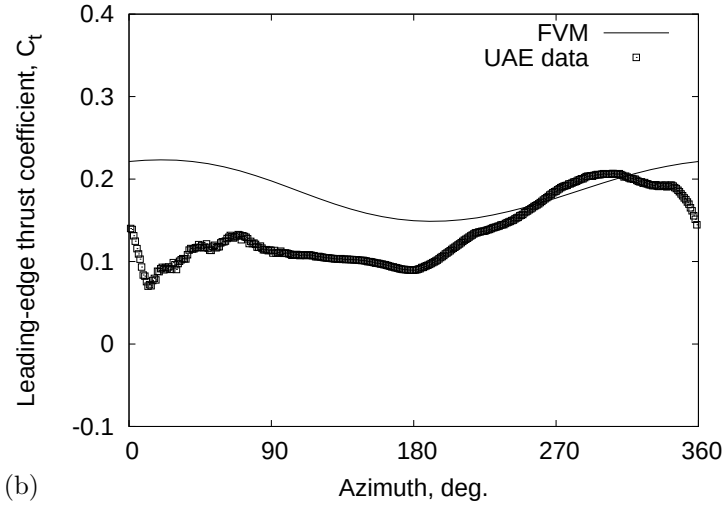

(b)

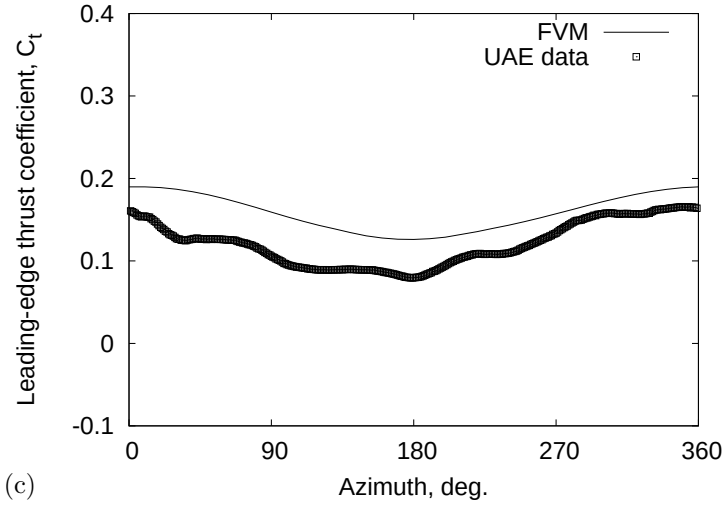

(c)

Figure 6.33: Comparison of the measurement and predictions of the azimuthal variation of leading-edge thrust coefficient for (a) 47%R, (b) 63%R, and (c) 80%R at 10 ms^{-1} and a yaw angle of 30°.

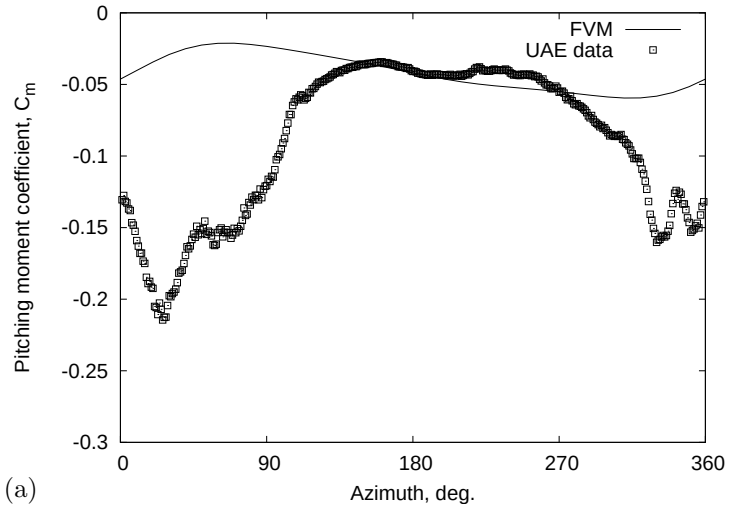

(a)

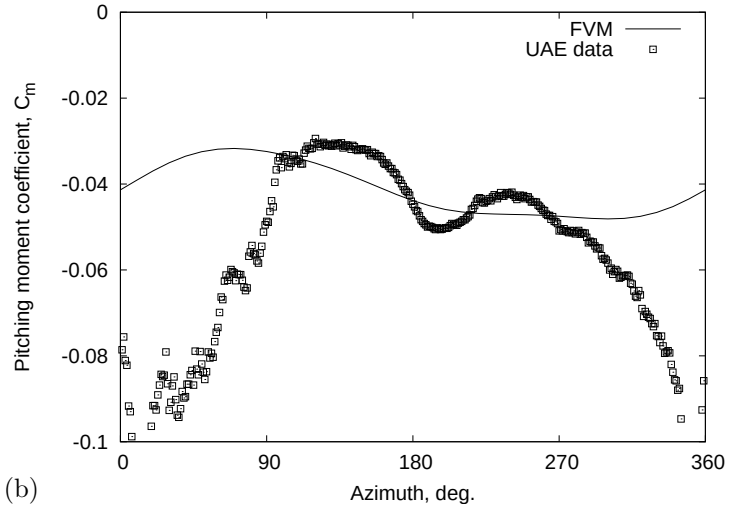

(b)

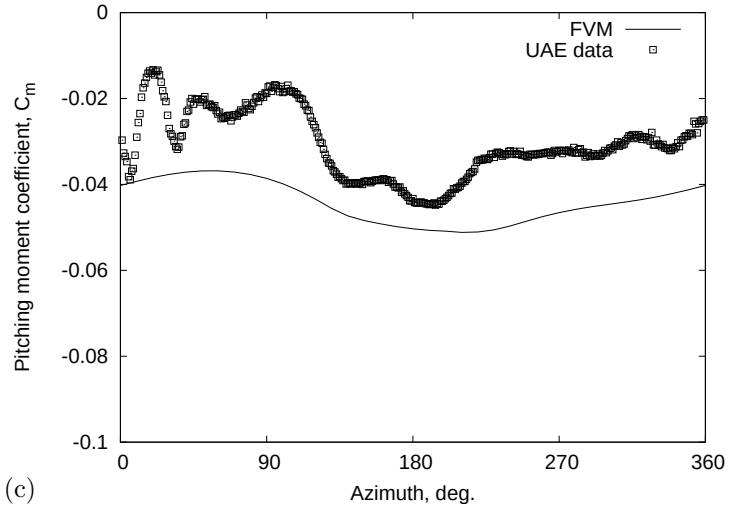

(c)

Figure 6.34: Comparison of the measurement and predictions of the azimuthal variation of the pitching moment coefficient for (a) 47%R, (b) 63%R, and (c) 80%R at 10 ms^{-1} and a yaw angle of 30°.

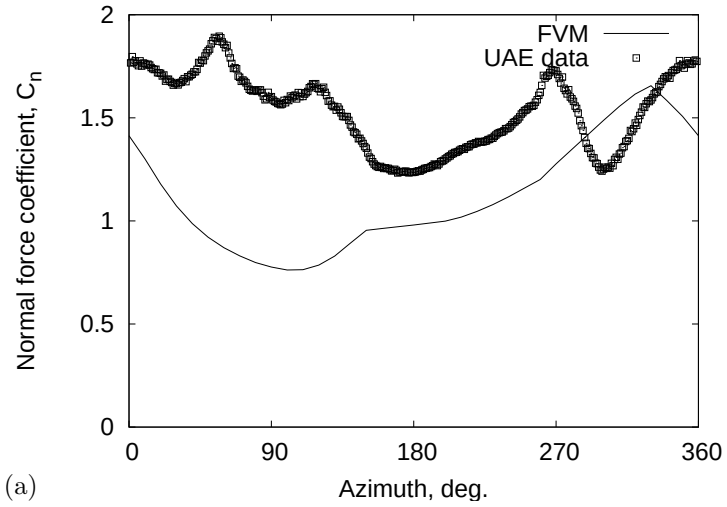

(a)

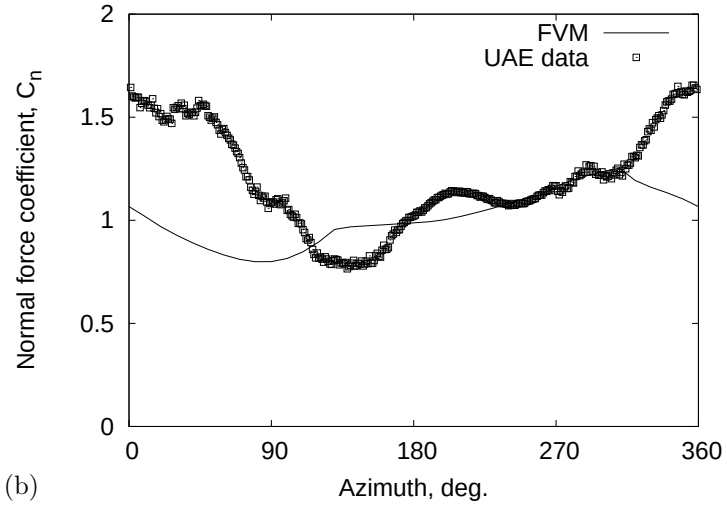

(b)

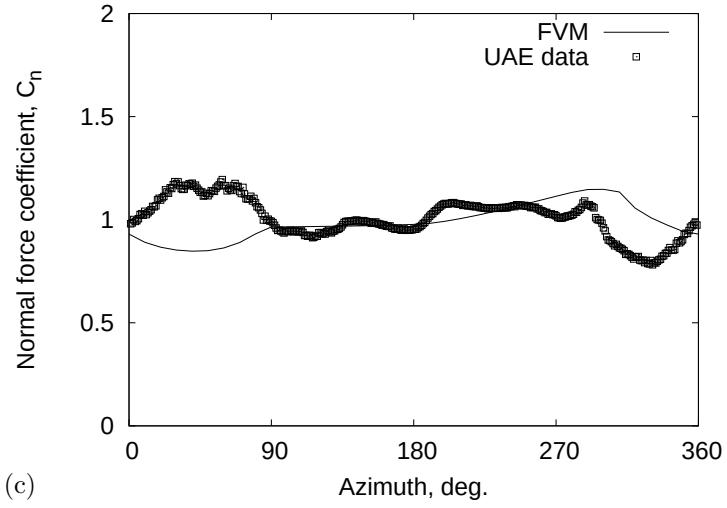

(c)

Figure 6.35: Comparison of the measurement and predictions of the azimuthal variation of normal force coefficient for (a) 47%R, (b) 63%R, and (c) 80%R at 15 ms^{-1} and a yaw angle of 30°.

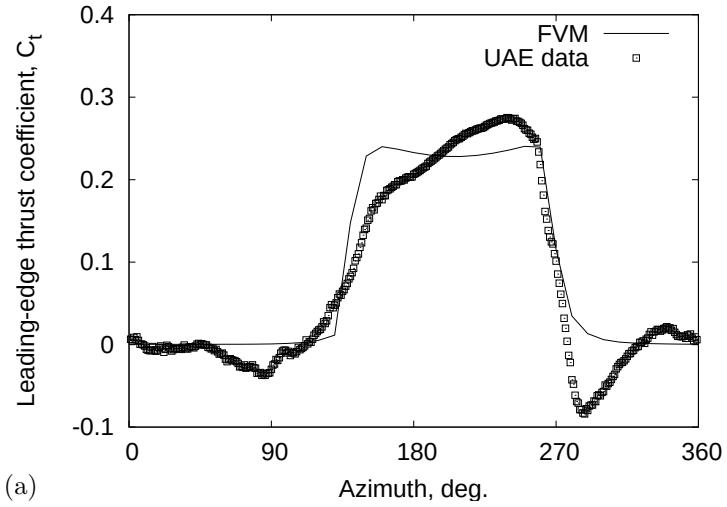

(a)

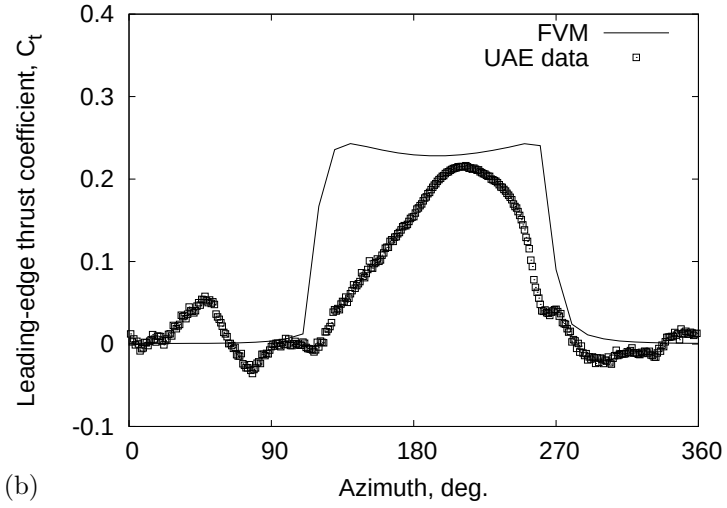

(b)

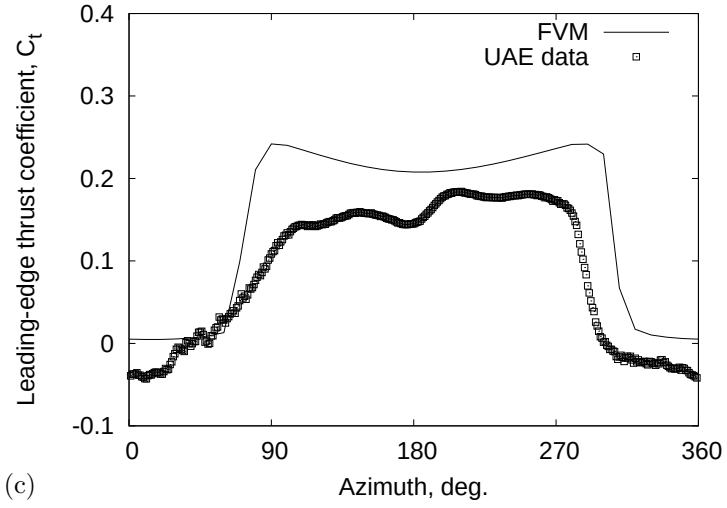

(c)

Figure 6.36: Comparison of the measurement and predictions of the azimuthal variation of leading-edge thrust coefficient for (a) 47%R, (b) 63%R, and (c) 80%R at 15 ms^{-1} and a yaw angle of 30°.

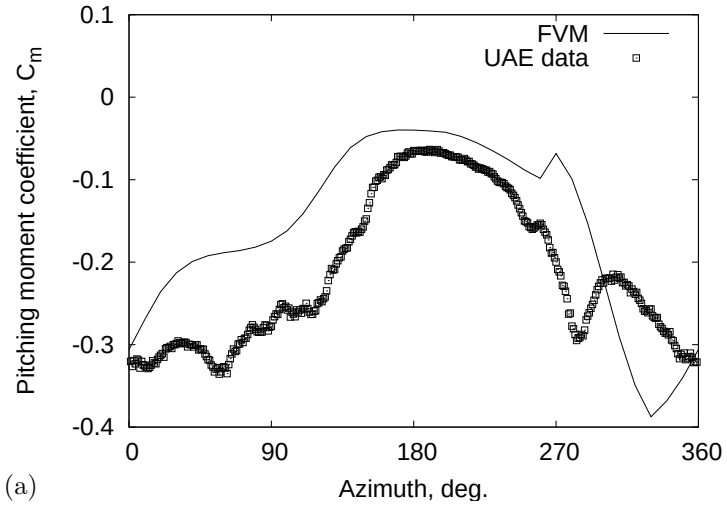

(a)

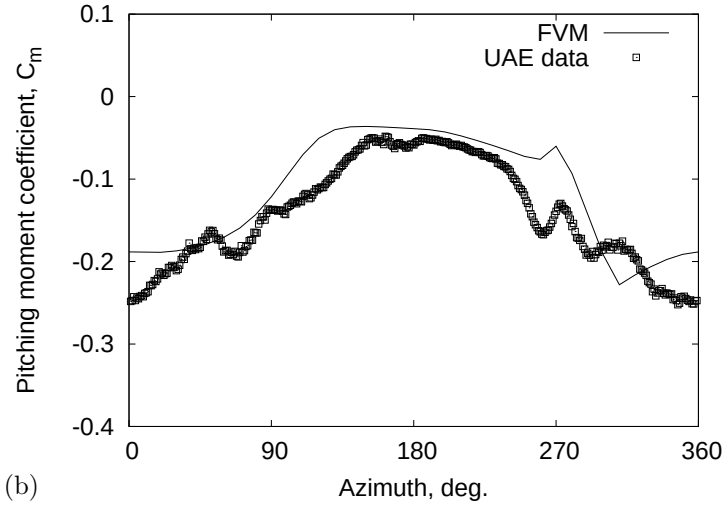

(b)

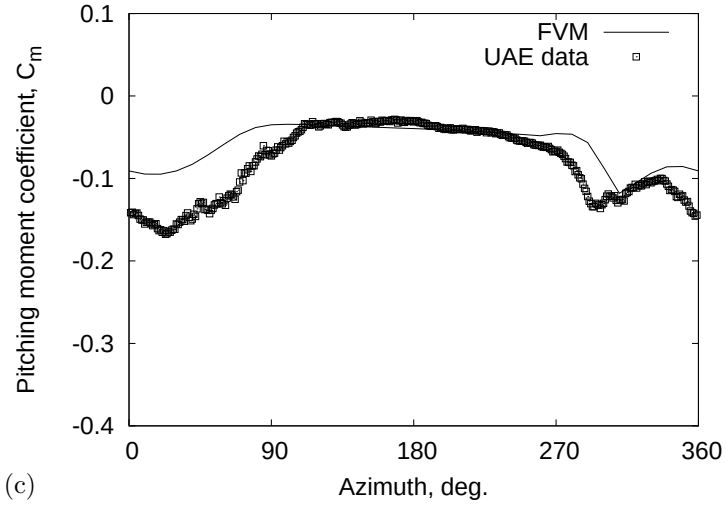

(c)

Figure 6.37: Comparison of the measurement and predictions of the azimuthal variation of the pitching moment coefficient for (a) 47%R, (b) 63%R, and (c) 80%R at 15 ms^{-1} and a yaw angle of 30°.

Chapter 7

Summary and Conclusions

Reducing the cost of the wind energy per unit of power produced mandates an improved and reliable design of wind turbines. This requires the capability to accurately predict the aerodynamic loads on different components of the wind turbine. To this end, the present work provides a robust and accurate numerical method to understand and predict the complex unsteady aerodynamics of a wind turbine. This chapter presents a summary of the present work and conclusions drawn from this dissertation.

A time-accurate Lagrangian vortex wake model has been developed for wind turbine applications. The complex aerodynamic environment of the wind turbines is described in Chapter 1 with an emphasis on the unsteady nature of the rotor wake behind a wind turbine. A survey of the existing methodologies available for predicting the aerodynamic loads on a wind turbine showed several shortcomings.

7.1 Conclusions

A time-accurate Lagrangian vortex wake model was developed and validated for the modeling the unsteady aerodynamic of horizontal axis wind turbines. Following conclusion have been drawn from this work. The conclusions are divided into four separate subsection dealing with the different aspects of this work. The first part focuses on the accuracy and stability of the time-marching numerical method. The second part deals with the development of the unsteady nonlinear airfoil model and its coupling with the blade model. Third part focusses on the comparison of

the blade element momentum (BEM) results against the free-vortex wake method (FVM) , and the fourth on validating the predictions against experimental measurements.

7.1.1 Numerical Issues: Stability and Convergence

The overall order of accuracy of the numerical solution is governed by the order of accuracy of the lowest order accurate term. Hence, it is important to analyze the order of accuracy of both sides of the governing equation to ensure a consistent order of accuracy. A numerical solution with a higher order of accuracy is also computationally expensive. For the engineering analysis of wind turbines, there is a need to carefully evaluate the accuracy of the numerical solution, and to establish thresholds of discretization that will provide acceptable levels of accuracy while still containing computational costs. The stability and accuracy of the time-marching wake algorithm was examined first using a linearized analysis. It has been shown that because the governing equations are highly nonlinear, a classic linear stability analysis is insufficient to guarantee a stable algorithm and a convergent solution. Numerical stability was also analyzed using modified equations and the solution convergence was then verified through numerical experimentation.

1. A systematic study of the accuracy of the reconstruction of the induced velocity from helical vortices was performed for a range of values of helical pitch, number of turns and wake skew angles. The accuracy of the straight-line segmentation approach of discretizing a helical vortex is second-order for different combinations of pitch, skew and number of turns. A minimum discretization of $\Delta\theta = 10^\circ$ is required to keep the maximum error in the induced velocity field less than 10%. To keep the maximum error less than 1%, a discretization of $\Delta\theta < 2.5^\circ$ is required, which may be less practical for routine engineering use of vortex wake models.

2. A vortex ring can be viewed as a special case of helical vortex with its helical pitch tending to zero. The induced velocity from helical vortices with a helical pitch $p \to 0$ and scaled by number of turns was shown to reduce to that of a vortex ring. A vortex ring was found to be a more challenging case to model accurately using the straight-line segmentation approach than for the helical vortex. In the case of a vortex ring, the magnitude of the errors in the induced velocity for a particular level of discretization has been found to be larger than the corresponding helical vortex. The reconstruction of induced velocity by straight-line approximation of a skewed helical vortex was also found to be second-order accurate, and the magnitude of the errors were found to be comparable to those of the unskewed case.

3. The linear and nonlinear stability of various time-marching methods used in free-vortex wake methods has been analyzed. The linear stability analysis has shown that the PCC and PC2B schemes are stable for all values of time discretization. The Euler explicit and second-order Adams–Bashforth schemes are unstable for all values of discretization. The fourth-order Adams–Moulton scheme is stable for values of $\omega h < 0.7$. The fourth-order AM4 scheme produces the lowest phase error and the Euler explicit scheme has the largest error. From a linear stability point of view, the AM4 scheme seems to be the best scheme. However the Adams–Moulton scheme is implicit and computationally very expensive especially for a free-vortex wake analysis. Any linearization or approximation to make this scheme explicit or semi-implicit will change the stability and dispersion characteristics of the scheme.

4. Considering the stability and dispersion characteristics as well as the computational cost, the PC2B algorithm seems to be the ideal scheme. The modified equation approach showed that the PC2B scheme introduces extra implicit dissipation that is independent of the velocity gradients. The dissipation term

in all other schemes (Euler explicit, PCC and Adams–Bashforth) is affected by the induced velocity field gradients. The presence of the negative velocity gradients then introduces an anti-dissipation, which has a destabilizing effect on the developing wake geometry.

5. Numerical experiments were performed for a three-bladed Grumman wind turbine in the zero yaw condition and 30° yawed out of the wind. The Euler explicit method produces and non-physical unstable wake system. The PCC scheme showed a modest growth of numerical errors with time, albeit bounded. The PC2B scheme was found to produce a stable and convergent wake system free of any types of disturbances.

7.1.2 Nonlinear Airfoil Model

The numerical analysis of the free-vortex wake solution algorithms ensured that the discretized solution of the rotor wake is an accurate and consistent representation of the physical solution. The next step was development and validation of a modified Leishman–Beddoes (L–B) unsteady stall model for unsteady airloads predictions on the S809 airfoil. The unsteady stall model was then integrated into a Weissinger-L type of 3D blade model and comparisons were made against the NREL parked blade measurements.

1. The reconstruction of the aerodynamic force coefficients, expressed in terms of the effective trailing-edge flow separation point, was found to be in very good agreement with the 2D measurements for the S809 airfoil over a wide range of Reynolds numbers. Even in the deep stall regime, the predicted values of the normal force coefficient were found to be close to the experimental values. The leading-edge thrust coefficient is, however, underpredicted as compared to the experimental values. The discrepancy in the prediction of the leading-edge thrust coefficient is probably an artifact of the errors introduced because of

the sparse number of pressure taps used in the experiment.

2. Good agreement was also obtained between the predictions and the experimental results for pitch oscillations at several mean angles of attack and reduced frequencies. The results showed encouraging agreement in predicting the onset and consequences of dynamic stall. The model showed slight differences in the reattachment phase during downstroke, which could be improved. The model was successful in predicting the dynamic stall characteristics of the S809 airfoil with almost same dynamic time constants as were used in the original L–B model. It has been shown that with a proper representation of the static stall characteristics, this model can be used to predict dynamic stall for airfoil sections typical of those used for wind turbines applications.

3. A comparison between the predicted and measured aerodynamic force coefficients for both the static and oscillating NREL parked blade measurements showed a very encouraging agreement. The predicted force coefficients were also in agreement with the measured values for the attached flow and the post-stall regime, thus validating the effective integration of the 2D stall model into the 3D blade model. Three-dimensionality of the unsteady flow on the oscillating parked blade was represented well and the prediction of the aerodynamic coefficients over the blade span compared well with the experimental measurements.

7.1.3 Comparison with Blade Element Momentum Methods

Blade element momentum (BEM) methods have been dominant in the wind turbine industry for the design of wind turbines. Although BEM methods are simple and fast, they are strictly valid only for a limited range of flow conditions. Their validity can be extended with additional approximations, which are usually based on empirical measurements and observations. A comparison of the power output

and thrust based on BEM and free-vortex model (FVM) has been performed.

1. Good agreement in the power and thrust prediction was observed between the FVM and BEM methods for low tip-speed ratios ($X_{\mathrm{T}SR} < 6$). For higher tip-speed ratios, the wake induction factor was found to be very high near the tip region, where the BEM model failed.

2. It was shown that the corrections for C_T at higher axial induction factors may break down. On the other hand, the FVM showed flexibility for the aerodynamic analysis of wind turbines in all working states including the turbulent wake state and the vortex ring state (high TSR).

3. The FVM was shown to be applicable for the aerodynamic analysis of wind turbines in yawed flow for which BEM method is less applicable without resorting to various types of approximations. It was also shown that the linear inflow models often used with the BEM theory are probably not applicable for large yaw angles. The ability of the FVM to capture the time-accurate behavior of the aerodynamic response of wind turbines (in yawed flow) was also shown.

4. A universal thrust and power coefficient curve was derived to understand various flow states of a wind turbine (i.e., normal working state, turbulent wake state and the windmill brake state). In the vortex ring state, the Glauert correction was shown to be adequate only when the axial induction factor is between 0.5 and 1.

7.1.4 Comparison with Experiments

The free-vortex wake method was comprehensively validated against experimental measurements of rotor wakes behind a wind turbines to validate the physics modeling of the present analysis. Comparisons were made of wake geometry measurements made using flow visualization techniques. Comparisons were also made

with performance and airloads measurements for the NREL Phase VI wind turbine to test the predictive capability of the numerical method.

1. The predicted wake geometry was compared against the wake positions obtained from the flow visualization conducted on a two-bladed wind turbine. The wake geometry was predicted well for all the measured tip speed ratios and tip pitch angles under both the axial and the yawed flow conditions except for very high yaw angles.

2. The numerical predictions of thrust and aerodynamic power output showed good agreement against the experimental data for attached and deep stall conditions. However, during incipient (moderate stall) conditions, the absence of a 3D stall delay model leads to an underprediction of the aerodynamic thrust. But the power output compares well with the measurements.

3. he spanwise variation of loads is predicted well at all spanwise sections except for the inboard sections, where stall delay effects are more dominant. However, dynamic stall effects dominate the flow field in the yawed flow conditions, and good agreement is obtained between measurements and predictions.

4. The unsteady loads on the blade and dynamic stall hysteresis is predicted well for attached flow and deep stall conditions, respectively. The onset of dynamic stall under incipient separation conditions is, however, not predicted very well.

5. It was also shown that the stall delay models used in the wind turbine community are not applicable in all flow conditions and are essentially post-dictive.

7.2 Recommendation for Future Work

The work done in this dissertation has demonstrated the viability and robustness of the free-vortex wake method for wind turbine applications. Good comparison

of the performance and airloads was obtained against the experimental measurements for wind turbines tested under controlled conditions. However, this is the first step in the development of FVM as a tool for the design and analysis of wind turbines. Following are the recommendations for future work to make this method more viable for wind turbine design.

1. The free-vortex wake methodology needs to be coupled with a comprehensive dynamics code like FAST or ADAMS to account for the effects of aeroelastic coupling. It was seen that the measured azimuthal variation of airloads included the effect of the blade and tower vibrations modes. However, in the present analysis, such deformations are not modeled. A coupled dynamics and aerodynamics model can remove the deficiencies in the present approach, which will allow for a comprehensive validation of the airloads predictions from free-vortex wake model with measured data from NREL Phase VI and similar experiments.

2. The computation of induced velocity using the Biot–Savart law at each time step, makes FVM computationally expensive. In this study a discretization of $\Delta\zeta = \Delta\psi = 10^\circ$ has been used. However, to better resolve the azimuthal variation of the airloads because of unsteady effects such as turbulence and tower shadow, finer discretization needs to be used. This will significantly increase the computational expense. The computational complexity of the FVM can be improved by using acceleration techniques such as a Fast Multipole (FMM) algorithm. The use of FMM techniques can reduce the order of complexity of a N body problem from N^2 to $N \log N$. In addition, modifying the numerical method to use the capabilities of multiple processors at the same time (parallel processing), will reduce the computational time.

3. Representation of the rotational stall delay using the present stall delay models has been shown to be inadequate. The present models are essentially post-

dictive, and require a priori knowledge of the power and thrust output. There is clearly a need to develop a stall delay model, which can take into account the effect of the change of geometry and is valid for all operating conditions.

4. Recent experiments to obtain measurements of wake geometry, airloads and power output have helped increase the understanding of the wind turbine aerodynamics. Although, the availability of the high fidelity performance and airloads measurements have helped validate existing models, much more needs to be done. Measurements of tip vortex velocity profiles behind the turbine using LDV or PIV will help in developing and validating more accurate viscous diffusion and stretching models for wind turbines. Flow visualization on the blade surface will help in unravelling the physics behind the stall delay phenomenon.

Appendix A

User Guide

MFW (Maryland Free Wake) uses a time-accurate free-vortex wake method for predicting the aerodynamics and performance of wind turbines. This code was originally developed for helicopter applications but has been substantially modified for its use in modeling wind turbine aerodynamics. This user guide gives a very brief description on the use of MFW.

A.1 Usage in Unix System

The archive MFW.zip contains the configuration files, which detect the system configuration and sets up the environmental variables accordingly. To use this in a unix system read the INSTALL file. To run the code for the first time, do the following steps:

sh ./configure

sh ./runscript

Once the code is setup for the first time, only sh ./runscript is necessary afterwards to run the code. There are two executable files in the archive: MFW and PREWAKE. PREWAKE sets up the correct array dimensions after reading .input files and MFW is the final executable file necessary for running MFW. Various executable scripts are also provided in the archive.

- *runscript* - runs the freewake code after necessary recompilations
- *savedata* - move all data files to another directory (easy saving)

- *bindir* - compiles the code and then copies it (along with necessary input files) to another directory

A.2 Input Files

Various input files required to run a MFW calculation.

1. user.input - Grid resolutions, method, trim option etc.
2. flight.input - Flight conditions
3. geometry.input - Rotor parameters
4. rotprop.input - Rotor blade properties
5. lbcoeff.input - Parameters for the Leishman-Beddoes dynamic stall model
6. freq.input - Control input perturbations (yaw control etc.)
7. usa.input - Unsteady aerodynamics parameters
8. nwakeopt.input - Near wake parameters

The most frequently used input files are user.input and flight.input. Two other input files, geometry.input and rotprop.input need to be changed only if computing for different rotors. The other input files can be left at their default states. A description of the main input parameters in user.input files and flight.input is given below. If we need to continue computations from a particular initial solution, three input files IWGEOM.data, IWG_b.data, flap.data are required to start the computation. This feature can be used to run the simulation for some time, and then restart it instead of starting from the beginning.

A.3 Setting up the Analysis

The parameters required to setup the analysis are specified in user.input file. **nw** is the number of the trailers used to model the far-wake in the free-vortex method. The free-vortex wake can be used with multiple trailers to better represent the aerodynamics of the wind turbine rotor. It has to be kept in mind that the cost of computation increases with increasing number of trailers. Usually **nw** =1 or 2 is usually used.

nfw is the number of iterations. The number of iterations can be obtained by multiplying required number of revolutions multiplied by the number of blades. **ft** is the number of free turns used in the calculation. Because of the truncation of the wake behind a turbine to a finite number of turns, the wake contracts in the last few turns. Therefore, periodic boundary conditions are used for last few turns and **bct** is the number of boundary turns in the calculation. **dp** and **dz** are the values of azimuthal and wake discretization, respectively.

vn is the exponent used in the Vatistas model as described in Section 2.1.2. **rcb** is the initial viscous core radius. **dcy** is the turbulent eddy coefficient in the viscous core diffusion model. **method** specifies the type of analysis used for free-vortex calculation. A value of **method = 't'** is used for time-accurate simulation and **method = 'r'** represents relaxation wake analysis.

A.4 Operational Input Parameters

The operations parameters for the simulation are specified in flight.input. **vinf** is the mean wind speed at hub-height. **gamma** is the prescribed yaw angle. ct_0 is the initial guess for the thrust coefficient. This thrust coefficient is expressed in helicopter terminology as thrust normalized by $\rho A(\Omega R)^2$. Tolerance parameters are specified by **cttol** , **fltol** and **cqtol**. **dsigma** is used to account for the change in density with height.

A.5 Rotor Geometry

Rotor geometry properties are listed in geometry.input file. **nr** is the number of rotors. **nb** specifies the number of blades in the rotor. **ns** is the number of spanwise segments used to represent the lifting surface model. **asr0** is the shaft tilt angle. **rad** is the radius of the blade. **flph** is the location of the flap hinge normalized by the rotor radius. For teeter case, the location of the flap hinge is negative. **rcout** is the root cut-out radius. **om** is the rotation speed of the rotor in rad/sec. Other parameters such as chord and taper in this file can be neglected. **rotgeo** is is logical flag, which is used by the subroutine rotor.f for specifying the blade chord and taper distribution.

A.6 Output Files

MFW output a lot of results, which are stored in different output files. A brief description of the output files is given below.

1. **FWGEOM.dat** - MFW outputs the wake geometry data for all azimuth positions in this file. The columns in this file are rotor number, azimuth position, coordinates of vortex filaments (x, y, z), circulation of each vortex filaments and core radius.

2. **FW[R,S,T].dat** - Three views of wake geometry are stored in these files. These files only have the position data of the wake elements (x, y, z).

3. **timectcq.dat** - Thrust and power time histories for the rotor. The columns in this file are rotor number, azimuthal time, thrust coefficient C_t, power coefficient C_p, inflow and inertial load.

4. **timeflap.dat** - This file stores the flapping time histories for each blade. Again, the columns in this file are rotor number, azimuthal time, flap angle (blade 1-4), and flapping moment (blade 1-4).

5. **clhist.dat** - Lift coefficient C_l time histories at all blade segments. Columns in this file are rotor number, blade number, azimuthal time, C_l at each segment.

6. **lifthist.dat** - ClM^2 time histories at all blade segments is output in this file. Rotor number, Blade number, azimuthal time, ClM^2 at each segment.

7. **VBZ.dat** - Inflow through the rotor disk is output to this file.

BIBLIOGRAPHY

[1] Hau, E., *Wind Turbines: Fundamentals, Technologies, Application, Economics* Springer, 2000, Ch. 1.

[2] Spera, D. A., "The Brush Wind Turbine Generator as Described in Scientific American of Dec. 20, 1890," Proceedings of the Workshop on Wind Turbine Structural Dynamics, Cleveland, OH, 1977.

[3] Kulkarni, P., Rohy, D. A., Laurie, R. A., and Smith, M., "Energy Technology Status Report," California Wind Energy Commission 500-96-006, 1996.

[4] Mays, I. D., "The Development Programme for the Musgrove wind Turbine," Proceedings of the Fourth International Conference on Energy Options, London, England, April 3–6 1984.

[5] Froude, R. E., "On the Part Played in Propulsion by Differences of Fluid Pressure," *Transacations of Institute of Naval Architecture*, Vol. 30, 1889.

[6] Betz, A., "Das Maximum der theoretisch möglichen Ausnützung des Windes durch Windmotoren," *Z. Gesamte Turbinewesen*, Vol. 26, 1920.

[7] Lanchester, F. W., "A Contribution to the Theory of Propulsion and the Screw Propeller," *Transacations of Institute of Naval Architecture*, Vol. 57, 1915.

[8] van Kuik, G. A. M., *On the limitations of Froude's actuator disc* PhD thesis, University of Eindhoven, 1991.

[9] Igra, O., "Research and Development for Shrouded Wind Turbines," Proceedings of the European Wind Energy Conference, Hamburg, Germany, 1984.

[10] van Holten, T., "Windmills with Diffuser Effect by Small Tip Vanes," Proceedings of the International Symposium on Wind Energy Systems, Cambridge, MA, USA, 1976.

[11] Leishman, J. G., "Challenges in Modeling the Unsteady Aerodynamics of Wind Turbines," *Wind Energy*, Vol. 5, 2002, pp. 86–132.

[12] Hansen, A. C., and Butterfield, C. P., "Aerodynamics of Horizontal-Axis Wind Turbines," *Annual Review of Fluid Mechanics*, Vol. 25, 1993, pp. 115–149.

[13] Rasmussen, R., Peterson, J. T., and Madsen, H. A., "Dynamic Stall and Aerodynamic Damping," *ASME Journal of Solar Energy Engineering*, Vol. 121, 1999, pp. 150–155.

[14] Garrad, A. D., and Hassan, U., "Taking the Guesswork Out of Wind Turbine Design," Proceedings of the AWEA National Conference, Cambridge, MA, 1986.

[15] Frost, W., Long, B. H., and Turner, R. E., "Engineering Handbook on the Atmospheric environment Guidelines for Use in Wind Turbine Generator Development," NASA TP-1359, 1978.

[16] Spera, D. A., *Wind Turbine Technology: Fundamental Concepts of Wind Turbine Engineering* ASME Press, New York, 1994, p. 391.

[17] Lissaman, P. B. S., Zalay, A., and Gyatt, G. W., "Critical Issues in the Design and Assessment of Wind Turbine Arrays," Proceedings of the 4th International Symposium on Wind Energy Systems, Stockholm, Sweden, 1982.

[18] Kelley, N. D., "An Initial Look at the Dynamics of the Microscale Flow Field within a Large Wind Farm in Response to Variations in the Natural Flow," NREL SERI/TP-257-3591, 1989.

[19] Bergey, K. H., "The Lanchester-Betz Limit," *Journal of Energy*, Vol. 3, No. 6, 1979, pp. 382–384.

[20] Glauert, H., *Aerodynamic Theory*, Vol. IV Julius Springer, 1935, Ch. III, pp. 191–200.

[21] E.Wilson, R., and Lissaman, P. B. S., "Applied Aerodynamics of Wind Power Machines," Oregon State University NSF/RA/N-74113, 1974.

[22] Coleman, R. P., Fiengold, A. M., and Stempin, C. W., "Evaluation of the Induced Velocity Fields of an Idealized Helicopter Rotor," NACA ARR L5E10, 1945.

[23] Pitt, D. M., and Peters, D., "Theoretical Predictions of Dynamic Inflow Derivatives," *Vertica*, Vol. 5, 1981, pp. 21–34.

[24] Schepers, J. G., "An Engineering Model for Yawed Conditions Developed on the Basis of Wind Tunnel Measurements," Proceedings of 18th Wind Energy Symposium and the 37th AIAA Aerospace Sciences Meeting, Reno, NV, Jan. 11–14 1999, pp. 164–174.

[25] Snel, H., "Survey of Induction Dynamics Modelling Within BEM Like Codes: Dynamic Inflow and Yawed Flow Modelling Revisited," Proceedings of 20th Wind Energy Symposium and the 39th AIAA Aerospace Sciences Meeting, Reno, NV, Jan. 8–11 2001.

[26] Snel, H., and Schepers, J. G., "JOULE1: Joint Investigation of Dynamic Inflow effects and Implementation in Engineering Methods," ECN C-94-107, Petten, Holland, 1994.

[27] Glauert, H., "The Analysis of Experimental Results in the Windmill Brake and Vortex Ring States of an Airscrew," ARC R & M No. 1026, 1926.

[28] Lock, C. N. H., Bateman, H., and Townsend, H., "An Extension of the Vortex Theory of Airscrews with Applications to Airscrews of Small Pitch Including Experimental Results," ARC R & M No. 1026, 1926.

[29] Sorenson, J. N., and Mikkelsen, R., "On the Validity of the Blade Element Momentum Method," Proceedings of the European Wind Energy Conference, Copenhagen, Denmark, July 2–6 2001.

[30] Sorenson, J. N., Shen, W. Z., and Munduate, X., "Analysis of Wake States by a Full-Field Actuator Disc Model," *Wind Energy*, Vol. 1, 1998, pp. 73–88.

[31] Snel, H., "Review of the Present Status of Rotor Aerodynamics," *Wind Energy*, Vol. 1, 1998, pp. 46–69.

[32] Hansen, A. C., and Laino, D. J., "Validation Study for AeroDyn and YawDyn Using Phase II Combined Experiment Data," Proceedings of the 16th ASME Wind Energy Symposium and the 35th AIAA Aerospace Sciences Meeting, Reno, NV, Jan. 6–9 1997.

[33] Bossanyi, E. A., "GH Bladed Version 3.6 User Manual," Garrad Hassan and Partners Limited Document 2.82/BR/010 Issue 12, 2003.

[34] McCoy, T., "Wind Turbine ADAMS Model Linearization Including Rotational and Aerodynamic Effects," Proceedings of 23rd Wind Energy Symposium and the 42nd AIAA Aerospace Sciences Meeting, Reno, NV, Jan. 5–8 2004.

[35] Robinson, M. C., Hand, M. M., Simms, D. A., and Schreck, S. J., "Horizontal Axis Wind Turbine Aerodynamics: Three–Dimensional, Unsteady, and Separated Flow Influences," NREL CP-500-26337, April 1999.

[36] Corrigan, J. J., and Schillings, J. J., "Empirical Model for Stall Delay Due to Rotation," Proceedings of the American Helicopter Society Aeromechanics Specialists Conference, San Francisco, CA, January 1994.

[37] Du, Z., and Selig, M., "A 3-D Stall Delay Model for Horizontal Axis Wind Turbine Performance Prediction," Proceedings of the 17th ASME Wind En-

ergy Symposium and the 36th AIAA Aerospace Sciences Meeting, Reno, NV, January 12–15 1998, pp. 9–19.

[38] Raj, N. V., "An Improved Semi-Empirical Model for 3-D Post-Stall Effects in Horizontal Axis wind Turbines," Master's thesis, University of Illinois at Urbana Champaign, 2000.

[39] McCroskey, W., Carr, L. W., and McAlister, K. W., "Dynamic Stall Experiments on Oscillating Airfoils," *AIAA Journal*, Vol. 14, No. 1, 1967, pp. 57–63.

[40] Leishman, J. G., and Beddoes, T. S., "A Semi-Empirical Model for Dynamic Stall," *Journal of the American Helicopter Society*, Vol. 34, No. 3, 1989, pp. 3–17.

[41] Tran, C. T., and Pitot, D., "Semi-Empirical Model for the Dynamic Stall of Airfoils in View of the Application to the Calculation of the Responses of a Helicopter Blade in Forward Flight," *Vertica*, Vol. 5, No. 1, 1981, pp. 35–53.

[42] Madsen, H. A., "Application of Actuator Surface Theory on Wind Turbines," Proceedings of the 2nd IEA Symposium on Aerodynamics of Wind Turbines, Lyngby, Denmark, 1988.

[43] van Holten, T., "On the Validity of the Lifting Line Concepts in Rotor Analysis," *Vertica*, Vol. 1, 1977.

[44] van Bussel, G. J. W., *The Aerodynamics of Horizontal Axis Wind Turbine Rotors Explored with Asymptotic Expansion Methods* PhD thesis, Delft University, February 1995.

[45] Spalart, P. R., and Allamaras, S. R., "A One-Equations Turbulence Model for Aerodynamic Flows," *AIAA Paper 92-0439*, 1992.

[46] Baldwin, B. S., and Lomax, H., "Thin Layer Approximation and Algebraic Model for Separated Turbulent Flows," *AIAA Paper 78-257*, 1978.

[47] Baldwin, B. S., and Barth, T. J., "A One-Equation Turbulence Transport Model for High Reynolds Number Wall-Bounded Flows," NASA TM 102847, 1990.

[48] Jones, W. P., and Launder, B. L., "The Prediction of Laminarization With a Two-Equation Model for Turbulence," *International Journal of Mass and Heat Transfer*, Vol. 16, 1973, pp. 1119–1130.

[49] Ekaterinaris, J. A., "Numerical Simulation of Incompressible Two-Bladed Rotor Flow Field," Proceedings of 16th ASME Wind Energy Symposium and the 35th AIAA Aerospace Sciences Meeting, Reno, NV, Jan. 1997.

[50] Duque, E. P. N., van Dam, C. P., and Hughes, S. C., "Navier–Stokes Simulations of the NREL Combined Experiment Phase II Rotor," Proceedings of 18th ASME Wind Energy Symposium and the 37th AIAA Aerospace Sciences Meeting, Reno, NV, Jan. 11–14 1999.

[51] Sorenson, N. N., and Michelsen, J. A., "Aerodynamic Predictions for the Unsteady Aerodynamics Experiment Phase-II at the National Renewable Energy Laboratory," Proceedings of 19th ASME Wind Energy Symposium and the 38th AIAA Aerospace Sciences Meeting, Reno, NV, Jan. 10–13 2000.

[52] Wolfe, W. P., and Ochs, S. S., "Predicting Aerodynamic Characteristics of Typical Wind Turbine Airfoils Using CFD," Sandia National Laboratories SAND96-2345, 1997.

[53] Chaviaropolous, P. K., "Investigating Dynamic Stall, 3-D and Rotational Effects on Wind Turbine Blades by Means on an Unsteady Quasi-3D Navier Stokes Solver," Proceedings of 10th IEA Symposium on Aerodynamics of Wind Turbines, Edinburgh, 1996, pp. 175–182.

[54] Langtry, R., Gola, J., and Menter, F., "Predicting 2D Airfoil and 3D Wind Turbine Rotor Performance using a Transition Model for General CFD

Codes," Proceedings of 25th Wind Energy Symposium and the 44th AIAA Aerospace Sciences Meeting, Reno, NV, Jan. 9–12 2006.

[55] Benjanirat, S., Sankar, L., and Xu, G., "Evaluation of Turbulence Models for the Prediction of Wind Turbine Aerodynamics," Proceedings of 22nd ASME Wind Energy Symposium and the 41st AIAA Aerospace Sciences Meeting, Reno, NV, January 6–9 2003.

[56] Hansen, M. O. L., Sørenson, N. N., Sørenson, J. N., and Michelsen, J. A., "A Global Navier Stokes Rotor Prediction Model," *AIAA Paper 97-0970*, 1997.

[57] Menter, F. R., "Zonal Two Equation $k - -\omega$ Model for Aerodynamic Flows," *AIAA Paper 93-2906*, 1993.

[58] Xu, G., *Computational Studies of Horizontal Axis Wind Turbines* PhD thesis, Georgia Institute of Technology, May 2001.

[59] Benjanirat, S., and Sankar, L., "Recent Improvements to a Combined Navier-Stokes Full Potential Methodology for Modeling Horizontal Axis Wind Turbines," Proceedings of 23rd ASME Wind Energy Symposium and the 42nd AIAA Aerospace Sciences Meeting, Reno, NV, January 5–8 2004, pp. 378–385.

[60] Tongchitpakdee, C., Benjanirat, S., and Sankar, L., "Numerical Simulation of the Aerodynamics of Horizontal Axis Wind Turbines Under Yawed Flow Conditions," Proceedings of 24th ASME Wind Energy Symposium and the 43rd AIAA Aerospace Sciences Meeting, Reno, NV, January 10–13 2005.

[61] Truesdell, C., *The Kinematics of Vorticity* Indiana University Press, Bloomington, 1954, Ch. 2, pp. 82–88.

[62] Scully, M. P., "A Method of Computing Helicopter Vortex Wake Distortion," Massachusetts Institute of Technology ASRL TR 138-1, June 1967.

[63] Landgrebe, A. J., "An Analytical Method for Predicting Rotor Wake Geometry," Proceedings of the AIAA/AHS VTOL Research, Design & Operations Meeting, Atlanta, GA, 1969.

[64] Landgrebe, A. J., "The Wake Geometry of a Hovering Rotor and its Influence on Rotor Performance," *Journal of the American Helicopter Society*, Vol. 17, No. 4, October 1972, pp. 2–15.

[65] Kocurek, J. D., and Tangler, J. L., "A Prescribed Wake Lifting Surface Hover Performance Analysis," *Journal of the American Helicopter Society*, Vol. 22, No. 1, January 1977, pp. 24–35.

[66] Egolf, T. A., and Landgrebe, A. J., "Helicopter Rotor Wake Geometry and its Influence in Forward Flight, Vol. 1 Generalized Wake Geometry and Wake Effects in Rotor Airloads and Performance," NASA CR-3726, October 1983.

[67] Kocurek, D., "Lifting Surface Performance Analysis for Horizontal Axis Wind Turbines," *SER/STR-217-3163*, 1987.

[68] Coton, F. N., and Wang, T., "The Prediction of Horizontal Axis Wind Turbine Performance in Yawed Flow Using an Unsteady Prescribed Wake Model," *Journal of Power and Energy*, Vol. 213, 1999, pp. 33–43.

[69] Wang, T., and Coton, F. N., "A High Resolution Tower Shadow Model for Downwind Turbines," *Journal of Wind Engineering and Industrial Aerodynamics*, Vol. 89, 2001, pp. 873–892.

[70] Dumitrescu, H., and Cardos, V., "Wind Turbine Aerodynamic Performance by Lifting Line Method," *International Journal of Rotating Machinery*, Vol. 4, No. 3, 1999, pp. 141–149.

[71] Grant, I., Mo, M., Parkin, P., Pan, X., Powell, J., Reinecke, H., Shuang, K., Coton, F., and Lee, D., "An Experimental and Numerical Study of the

Vortex Filaments in the Wake of an Operational, Horizontal-Axis, Wind Turbine," *Journal of Wind Engineering and Industrial Aerodynamics*, Vol. 85, April 2000, pp. 177–189.

[72] Vermeer, L. J., Sorenson, J. N., and Crespo, A., "Wind Turbine Wake Aerodynamics," *Progress in Aerospace Sciences*, Vol. 39, 2003, pp. 467–510.

[73] Haans, W., Sant, T., van Kuik, G., and van Bussel, G., "Measurement and Modeling of Tip Vortex Paths in the Wake of a HAWT under Yawed Flow Conditions," Proceedings of 24th Wind Energy Symposium and the 43rd AIAA Aerospace Sciences Meeting, Reno, NV, Jan. 10–13 2005, pp. 136–145.

[74] Clark, D. R., and Leiper, A. C., "The Free Wake Analysis A Method for Prediction of Helicopter Rotor Hovering Performance,," *Journal of the American Helicopter Society*, Vol. 15, No. 1, January 1970, pp. 3–11.

[75] Scully, M. P., "Computation of Helicopter Rotor Wake Geometry and Its Influence on Rotor Harmonic Airloads," Massachusetts Institute of Technology ASRL TR 178-1, March 1975.

[76] Miller, R. H., "A Simplified Approach to the Free Wake Analysis of a Hovering Rotor," *Vertica*, Vol. 6, 1982, pp. 89–95.

[77] Bliss, D. B., Quackenbush, T. R., and Bilanin, A. J., "A New Methodology for Helicopter Free-Wake Analyses," Proceedings of the 39th Annual National Forum of the American Helicopter Society, St. Louis, MO, May 9–11 1983.

[78] Bagai, A., and Leishman, J. G., "Rotor Free-Wake Modeling Using a Relaxation Technique - Including Comparisons with Experimental Data," *Journal of the American Helicopter Society*, Vol. 40, No. 3, July 1995, pp. 29–41.

[79] Johnson, W., "A Comprehensive Analytical Model of Rotorcraft Aerodynamics and Dynamics, Part I: Analytical Development," NASA TM 81182, 1980.

[80] Datta, A., Sitaraman, J., Chopra, I., and Baeder, J., "Analysis Refinements for Prediction of Rotor Vibratory Loads in High-Speed Forward Flight," Proceedings of the 60th Annual National Forum of the American Helicopter Society, Baltimore, MD, June 7–10 2004.

[81] Kini, S., and Conlisk, A. T., "Nature of Locally Steady Rotor Wakes," *Journal of Aircraft*, Vol. 39, No. 5, 2002, pp. 750–758.

[82] Bhagwat, M. J., and Leishman, J. G., "Correlation of Helicopter Tip Vortex Measurements," *AIAA Journal*, Vol. 38, No. 2, Feb. 2000, pp. 301–308.

[83] Leishman, J. G., Bhagwat, M. J., and Bagai, A., "Free Vortex Methods for Helicopter Rotor Wake Analyses," *Journal of Aircraft*, Vol. 39, No. 5, 2003, pp. 759–775.

[84] Simoes, F. J., and Graham, J. M. R., "Application of a Free Vortex Wake Model to a Horizontal Axis Wind Turbine," *Journal of Wind Engineering and Industrial Aerodynamicst*, Vol. 39, 1992, pp. 129–138.

[85] Bareiss, R., and Wagner, S., "The Free Wake/Hybrid Wake Code RVOLM-A Tool for Aerodynamic Analysis of Wind Turbines," Proceedings of the European Community Wind Energy Conference, Lübeck-Travemünde, Germany, March 8–12 1993, pp. 424–427.

[86] Voutsinas, S. G., Belessis, M., and Huberson, S., "Dynamic Inflow Effects and Vortex Particle Methods," Proceedings of the European Community Wind Energy Conference, Lübeck-Travemünde, Germany, March 8–12 1993, pp. 428–431.

[87] Voutsinas, S. G., Belessis, M., and Rados, K. G., "Investigation of the Yawed Operation of Wind Turbines by Means of a Vortex Particle Method," Proceedings of the AGARD Conference, 1995, Vol. 552, pp. 11–12.

[88] Oye, S., "Tjaereborg wind turbine, First Dynamic InflowMeasurements," AFM Notak Vk-189, April 1991.

[89] Duque, E. P. N., van Dam, C. P., and Hughes, S. C., "Numerical Predictions of Wind Turbine Power and Aerodynamic Loads for the NREL Phase II Combined Experiment Phase II Rotor," Proceedings of 19th ASME Wind Energy Symposium and the 38th AIAA Aerospace Sciences Meeting, Reno, NV, Jan. 10–13 1999.

[90] Johnson, W., "Rotocraft Aerodynamics Models for a Comprehensive Analysis," Proceedings of the 54th Annual National Forum of the American Helicopter Society, Washington, DC, May 1998.

[91] Hand, M. M., Simms, D. A., Fingersh, L. J., Jager, D. W., Cortell, J. R., Schreck, S., and Larwood, S. M., "Unsteady Aerodynamics Experiment Phase VI: Wind Tunnel Test Configurations and Available Data Campaigns," NREL TP-500-29955, December 2001.

[92] Fingersh, L. J., Simms, D., Hand, M., Jager, D., Cotrell, J., Robinson, M., Schreck, S., and Larwood, S., "Wind Tunnel Testing of NREL's Unsteady Aerodynamics Experiment," *Proceedings of the 20th ASME Wind Energy Symposium and the 39th AIAA Aerospace Sciences Meeting*, Jan. 8–11 2001.

[93] Simms, D. A., Hand, M. M., Schreck, S., and Fingersh, L. J., "NREL Unsteady Aerodynamics Experiment in the NASA-Ames Wind Tunnel: A Comparison of Predictions to Measurements," NREL TP-500-29494, June 2001.

[94] Coton, F. N., Wang, T., and Galbraith, R. A. M., "An Examination of Key Aerodynamic Modelling Issues Raised by the NREL Blind Comparison," *Wind Energy*, Vol. 5, 2002, pp. 199–212.

[95] Leishman, J. G., *Principles of Helicopter Aerodynamics* Cambridge University Press, 2000.

[96] Milne-Thomson, L. M., *Theoretical Aerodynamics* Dover, New York, 1973, Ch. 9, pp. 168–170.

[97] Crouse, G. L., and G, L. J., "A New Method for Improved Free-Wake Convergence in Hover and Low Speed Forward Flight," Proceedings of the 21st Aerospace Sciences Meeting & Exhibit, Reno, NV, January 11–14 1993.

[98] Bagai, A., and Leishman, J. G., "Rotor Free-Wake Modeling using a Relaxation Technique - Including Comparisons with Experimental Data," Proceedings of the 50th Annual National Forum of the American Helicopter Society, Washington, DC, May 1994.

[99] Johnson, W., *Helicopter Theory* Dover Publications, 1994, pp. 540–543.

[100] Prandtl, L., and Tietjens, O. G., *Fundamentals of Hydro- and Aero-Mechanics* McGraw-Hill, New York, 1934.

[101] Chorin, A. J., "Numerical Study of Slightly Viscous Flow," *Journal of Fluid Mechanics*, Vol. 57, 1973, pp. 785–796.

[102] Ananthan, S., and Leishman, J. G., "The Role of Filament Stretching in the Free-Vortex Modeling of Rotor Wakes," *Journal of the American Helicopter Society*, Vol. 49, No. 2, April 2004, pp. 176–191.

[103] Saffman, P. G., *Vortex Dynamics* Cambridge University Press, 1992, Ch. 11.

[104] Rankine, W. J. M., *Manual of Applied Mechanics* C. Griffen Co., London, 1858.

[105] Lamb, H., *Hydrodynamics* Cambridge University Press, 1932.

[106] Vatistas, G. H., Koezel, V., and Mih, W. C., "A Simpler Model for Concentrated Vortices," *Experiment in Fluids*, Vol. 11, 1991, pp. 73–76.

[107] Squire, H. B., "The Growth of a Vortex In Turbulent Flow," *Aeronautical Quarterly*, Vol. 16, August 1965, pp. 302–306.

[108] Cotel, A. J., and Breidenthal, R. E., "Turbulence Inside a Vortex," *Physics of Fluids*, Vol. 11, No. 10, October 1999, pp. 3026–3029.

[109] Mahalingam, R., and Komerath, N. M., "Measurements of the Near Wake of a Rotor in Forward Flight," Proceedings of the 36th Aerospace Sciences Meeting & Exhibit, Reno, NV, January 12–15 1998.

[110] Iversen, J. D., "Correlation of Turbulent Trailing Vortex Decay Data," *Journal of Aircraft*, Vol. 13, No. 5, May 1996, pp. 338–342.

[111] Gupta, S., and Leishman, J. G., "Stability of Methods in the Free-Vortex Wake Analysis of Wind Turbines," Proceedings of the 23rd ASME Wind Energy Symposium and the 42nd AIAA Aerospace Sciences Meeting, Reno, NV, Jan. 5–8 2004.

[112] Bhagwat, M. J., and Leishman, J. G., "Stability, Consistency and Convergence of Time-Marching Free-Vortex Rotor Wake Algorithms," *Journal of the American Helicopter Society*, Vol. 46, No. 1, 2001, pp. 59–70.

[113] Weissinger, J., "The Lift Distribution of Swept-Back Wings," *NACA TM 1120*, 1947.

[114] McCormick, B. W., Tangler, J. A., and Sherrieb, H. E., "Structure of Trailing Vortices," *Journal of Aircraft*, Vol. 5, No. 3, May-June 1968, pp. 260–267.

[115] Vermeer, L. J., J, N. S., and Crespo, A., "Wind Turbine Wake Aerodynamics," *Progress in Aerospace Sciences*, Vol. 39, 2003, pp. 467–510.

[116] Montgomerie, B., "The Influence of 3D Effects in Lift and Drag on the Performance of Stalled Horizontal Axis Wind Turbine Rotor," Proceedings of

8*th* IEA Symposium on Aerodynamics of Wind Turbines, Lyngby, Denmark, 1994, pp. 101–107.

[117] Corten, G. P., *Flow Separation on Wind Turbine Blades* PhD thesis, Utrecht University, January 2001.

[118] Viterna, L. A., and Janetzke, D. C., "Theoretical and Experimental Power from Large Horizontal-Axis Wind Turbines," NASA TM-82944, September 1982.

[119] Pierce, K., and Hansen, A. C., "Prediction of Wind Turbine Rotor Loads Using the Beddoes–Leishman Model for Dynamic Stall," *Journal of Solar Energy Engineering*, Vol. 117, 1995, pp. 200–204.

[120] Beddoes, T. S., "Representation of Aerofoil Behaviour," *Vertica*, Vol. 7, 1983, pp. 183–197.

[121] Schreck, S. J., and Robinson, M. C., "Dynamic Stall and Rotational Augmentation in Recent Wind Turbine Aerodynamic Experiments," Proceedings of 32nd AIAA Fluid Dynamics Conference and Exhibit, St. Louis, MS, June 24–26 2002.

[122] Tangler, J., "The Nebulous Art of Using Wind Tunnel Airfoil Data and Blade-Element Momentum Theory for Predicting Rotor Performance," Proceedings of 21st ASME Wind Energy Symposium and the 40th AIAA Aerospace Sciences Meeting, Reno, NV, January 14–17 2002.

[123] Duque, E. P. N., van Dam, C. P., Drodeur, R. R., and Chao, D. D., "Navier–Stokes Analysis of Time-Dependent Flows About a Wind Turbine," Proceedings of the 3rd ASME/JSME Joint Fluids Engineering Conference, San Francisco, CA, July 18–23 1999.

[124] Johansen, J., Sørenson, N. N., Michelsen, J. A., and Schreck, S., "Detached-Eddy Simulation of Flow around the NREL Phase-VI Blade," *Wind Energy*, Vol. 5, 2002, pp. 185–197.

[125] Leishman, J. G., and Beddoes, T. S., "A Generalized Method for Airfoil Unsteady Aerodynamic Behavior and Dynamic Stall Using the Indicial Method," Proceedings of the 42nd Annual Forum of the American Helicopter Society, Washington DC, June 2–4 1986, pp. 243–266.

[126] Voutsinas, S. G., Riziotis, V. A., Dimitris, D. G., and Chaviaropoulos, P. K., "Profile Stall Characteristics, Aerodynamic Damping and Design Implications for Wind Turbine Blades," Proceedings of the 18th ASME Wind Energy Symposium, Reno, NV, Jan. 11–14 1999.

[127] Thwaites, B., *Incompressible Aerodynamics* Dover Publications, 1987.

[128] Leishman, J. G., "Validation of Approximate Indicial Aerodynamic Functions for Two-Dimensional Subsonic Flow," *Journal of Aircraft*, Vol. 25, No. 10, Oct 1988.

[129] McCroskey, W. J., McAlister, K. W., and and Pucci, L. W. C. S. L., "An Experimental Study of Dynamic Stall on Advanced Airfoil Sections," NASA TM-84245, Vol. Vol. 1, 2 & 3, 1982.

[130] Lewis, R. I., *Vortex Element Methods for Fluid Dynamic - An Analysis of Engineering Systems* Cambridge University Press, 1991, pp. 148–150.

[131] Wood, D. H., and Li, D., "Assessment of Accuracy of Representing a Helical Vortex by Straight Segments," *AIAA Journal*, Vol. 40, No. 4, April 2002, pp. 647–651.

[132] Boersma, J., and Wood, D. H., "On the Self-Induced Motion of a Helical Vortex," *J. Fluid Mech.*, Vol. 384, 1999, pp. 263–280.

[133] Boersma, J., and Wood, D. H., "On the Motion of Multiple Helical Vortices," *J. Fluid Mech.*, Vol. 447, 2001, pp. 149–171.

[134] Lomax, H., Pulliam, T. H., and Zingg, D. H., *Fundamentals of Computational Fluid Dynamics* Springer, 2001, pp. 115–132.

[135] Bagai, A., and Leishman, J. G., "Rotor Free-Wake Modeling Using a Relaxation Technique-Including Comparisons with Experimental Data," *Journal of the American Helicopter Society*, Vol. 40, No. 3, 1995, pp. 29–41.

[136] Butterfield, C. P., Musial, W. P., and Simms, D. A., "Combined Experiment Phase I Final Report," NREL TP-257-4655, October 1992.

[137] Ramsay, R. R., Hoffman, M. J., and Gregorek, G. M., "Effects of Grit Roughness and Pitch Oscillations on the S809 Airfoil," NREL TP-442-7817, December 1995.

[138] Somers, D. M., "Design and Experimental Results for the S809 Airfoil," NREL SR-440-6918, January 1997.

[139] Eggleston, D. M., and Stoddard, F. S., *Wind Turbine Engineering Design* Van Nostrand Reinhold Company, New York, 1987.

[140] Laino, D. J., and Hansen, A. C., "User's Guide to the Wind Turbine Aerodynamics Computer Software AeroDyn," Windward Engineering , 2002.

[141] Gessow, A., "Review of Information on Induced Flow of a Lifting Rotor," *NACA TN 3238*, 1954.

[142] Washizu, K., Azuma, A., Koo, J., and Oka, T., "Experiments on a Model Helicopter Rotor Operating in the Vortex Ring State," *Journal of Aircraft*, Vol. 3, No. 3, 1966, pp. 225–230.

[143] Ramasamy, M., and Leishman, J. G., "A Generalized Model for Transitional Blade Tip Vortices," Proceedings of the 60th Annual Forum of American Helicopter Society, Baltimore, MD, June 7–10 2004.

[144] Li, H., Burggraf, O. R., and Conlisk, A. T., "Formation of a Rotor Tip Vortex," *Journal of Aircraft*, Vol. 39, No. 5, 2002, pp. 739–749.

[145] Grant, I., Parkin, P., and Wang, X., "Optical Vortex Tracking Studies of a Horizontal Axis Wind Turbine in Yaw Using Laser-Sheet Flow Visualization," *Experiments in Fluids*, Vol. 23, 1997, pp. 513–519.

[146] Grant, I., and Parkin, P., "A DPIV Study of the Trailing Vortex Elements from the Blades of a Horizontal Axis Wind Turbine in Yaw," *Experiments in Fluids*, Vol. 28, 2000, pp. 368–376.

[147] Laino, D. J., and Hansen, A. C., "Current Efforts Towards Improved Aerodynamic Modeling Using the AeroDyn Subroutines," Proceedings of 23rd Wind Energy Symposium and the 42nd AIAA Aerospace Sciences Meeting, Reno, NV, Jan. 5–8 2004.

[148] Jonkman, J. M., and Buhl, M., "FAST User's Guide," NREL TP-500-29798, June 2005.

[149] Jonkman, J. M., and Buhl, M., "New Developments for the NWTC's FAST Aeroelastic HAWT Simulator," Proceedings of 23rd Wind Energy Symposium and the 42nd AIAA Aerospace Sciences Meeting, Reno, NV, Jan. 5–8 2004.

[150] Elliot, A. S., "Analyzing the Rotor Dynamics with a General-Purpose Code," *Mechanical Engineering*, Vol. 12, December 1990, pp. 21–25.

[151] Sorenson, J. N., Mikkelsen, R., and Schreck, S., "Navier–Stokes Predictions of the NREL Phase VI Rotor in the NASA Ames 80 ft × 120 ft Wind Tunnel," *Wind Energy*, Vol. 5, 2002, pp. 151–169.

[152] Laino, D. J., Hansen, A. C., and Minnema, J. E., "Validation of AeroDyn Subroutines Using NREL Unsteady Aerodynamics Experiment Data," *Wind Energy*, Vol. 5, 2002, pp. 227–244.